

Graphene

Guest Editors: Rakesh K. Joshi, Masamichi Yoshimura,
and Ashok Kumar





Graphene

Journal of Nanomaterials

Graphene

Guest Editors: Rakesh K. Joshi, Masamichi Yoshimura,
and Ashok Kumar



Copyright © 2010 Hindawi Publishing Corporation. All rights reserved.

This is a special issue published in volume 2010 of “Journal of Nanomaterials.” All articles are open access articles distributed under the Creative Commons Attribution License, which permits unrestricted use, distribution, and reproduction in any medium, provided the original work is properly cited.

Editorial Board

- Katerina Aifantis, Greece
Nageh K. Allam, USA
Margarida Amaral, Portugal
Xuedong Bai, China
Enrico Bergamaschi, Italy
Theodorian Borca-Tasciuc, USA
C. Jeffrey Brinker, USA
Christian Brosseau, France
Xuebo Cao, China
Sang-Hee Cho, Republic of Korea
Shafiul Chowdhury, USA
Cui ChunXiang, China
Miguel A. Correa-Duarte, Spain
Shadi A. Dayeh, USA
Ali Eftekhari, USA
Claude Estournes, France
Alan Fuchs, USA
Lian Gao, China
Russell E. Gorga, USA
Hongchen Chen Gu, China
Mustafa O. Guler, Turkey
John Zhanhu Guo, USA
Smrati Gupta, Germany
Michael Harris, USA
Zhongkui Hong, USA
Michael Z. Hu, USA
David Hui, USA
Y.-K. Jeong, Republic of Korea
Sheng-Rui Jian, Taiwan
Wanqin Jin, China
Rakesh K. Joshi, India
Zhenhui Kang, China
- Fathallah Karimzadeh, Iran
Do Kyung Kim, Republic of Korea
Kin Tak Lau, Australia
Burtrand Lee, USA
Benxia Li, China
Jun Li, Singapore
Shijun Liao, China
Gong Ru Lin, Taiwan
J.-Y. Liu, USA
Jun Liu, USA
Tianxi Liu, China
Songwei Lu, USA
Daniel Lu, China
Jue Lu, USA
Ed Ma, USA
Gaurav Mago, USA
Sanjay R. Mathur, Germany
A. McCormick, USA
Vikas Mittal, UAE
Weihai Ni, Germany
Sherine Obare, USA
Edward Andrew Payzant, USA
Kui-Qing Peng, China
Anukorn Phuruangrat, Thailand
Ugur Serincan, Turkey
Huaiyu Shao, Japan
Donglu Shi, USA
Suprakas Sinha Ray, South Africa
Vladimir Sivakov, Germany
Marinella Striccoli, Italy
Bohua Sun, South Africa
Saikat Talapatra, USA
- Nairong Tao, China
Titipun Thongtem, Thailand
Somchai Thongtem, Thailand
Valeri P. Tolstoy, Russia
Tsung-Yen Tsai, Taiwan
Takuya Tsuzuki, Australia
Raquel Verdejo, Spain
Mat U. Wahit, Malaysia
Shiren Wang, USA
Yong Wang, USA
Cheng Wang, China
Zhenbo Wang, China
Jinquan Wei, China
Ching Ping Wong, USA
Xingcai Wu, China
Guodong Xia, Hong Kong
Zhi Li Xiao, USA
Ping Xiao, UK
Shuangxi Xing, China
Yangchuan Xing, USA
N. Xu, China
Doron Yadlovker, Israel
Ying-Kui Yang, China
Khaled Youssef, USA
Kui Yu, Canada
Haibo Zeng, China
Tianyou Zhai, Japan
Renyun Zhang, Sweden
Yanbao Zhao, China
Lianxi Zheng, Singapore
Chunyi Zhi, Japan

Contents

Graphene, Rakesh K. Joshi, Masamichi Yoshimura, and Ashok Kumar
Volume 2010, Article ID 915937, 1 page

Modelling of Graphene Nanoribbon Fermi Energy, Zaharah Johari, Mohammad Taghi Ahmadi, Desmond Chang Yih Chek, N. Aziziah Amin, and Razali Ismail
Volume 2010, Article ID 909347, 6 pages

Stable Aqueous Suspension and Self-Assembly of Graphite Nanoplatelets Coated with Various Polyelectrolytes, Jue Lu, Inhwan Do, Hiroyuki Fukushima, Ilsoon Lee, and Lawrence T. Drzal
Volume 2010, Article ID 186486, 11 pages

Chemical Functionalization of Graphene Nanoribbons, Narjes Gorjizadeh and Yoshiyuki Kawazoe
Volume 2010, Article ID 513501, 7 pages

Graphene Nanoribbon Conductance Model in Parabolic Band Structure, Mohammad Taghi Ahmadi, Zaharah Johari, N. Aziziah Amin, Amir Hossein Fallahpour, and Razali Ismail
Volume 2010, Article ID 753738, 4 pages

Preparation of Colloidal Dispersions of Graphene Sheets in Organic Solvents by Using Ball Milling, Weifeng Zhao, Furong Wu, Hang Wu, and Guohua Chen
Volume 2010, Article ID 528235, 5 pages

Positioning of the Fermi Level in Graphene Devices with Asymmetric Metal Electrodes, Bum-Kyu Kim, Eun-Kyoung Jeon, Ju-Jin Kim, and Jeong-O Lee
Volume 2010, Article ID 575472, 5 pages

Formulation of 2D Graphene Deformation Based on Chiral-Tube Base Vectors, Bohua Sun
Volume 2010, Article ID 402591, 7 pages

Isotope Effect on the Thermal Conductivity of Graphene, Hengji Zhang, Geunsik Lee, Alexandre F. Fonseca, Tammie L. Borders, and Kyeongjae Cho
Volume 2010, Article ID 537657, 5 pages

A New Strategy to Pretreat Carbon Nanofiber and Its Application in Determination of Dopamine, Dong Liu, Yang Liu, Haoqing Hou, and Tianyan You
Volume 2010, Article ID 659207, 6 pages

The Field Emission Properties of Graphene Aggregates Films Deposited on Fe-Cr-Ni alloy Substrates, Zhanling Lu, Wanjie Wang, Xiaotian Ma, Ning Yao, Lan Zhang, and Binglin Zhang
Volume 2010, Article ID 148596, 4 pages

Nanocomposite Materials of Alternately Stacked C₆₀ Monolayer and Graphene, Makoto Ishikawa, Shu Kamiya, Shoji Yoshimoto, Masaru Suzuki, Daisuke Kuwahara, Naruo Sasaki, and Kouji Miura
Volume 2010, Article ID 891514, 6 pages

Preparation of Bulk ¹³C-Enriched Graphene Materials, Leilei Tian, Xin Wang, Li Cao, Mohammed J. Meziani, Chang Yi Kong, Fushen Lu, and Ya-Ping Sun
Volume 2010, Article ID 742167, 5 pages



Characteristic Features of Stone-Wales Defects in Single-Walled Carbon Nanotube; Adsorption, Dispersion, and Field Emission, Seungkwang Roh, Jongtaek Lee, Mira Jang, Mingyeong Shin, Juone Ahn, Taehee Park, and Whikun Yi
Volume 2010, Article ID 398621, 6 pages

Simulated Nanoscale Peeling Process of Monolayer Graphene Sheet: Effect of Edge Structure and Lifting Position, Naruo Sasaki, Hideaki Okamoto, Shingen Masuda, Kouji Miura, and Noriaki Itamura
Volume 2010, Article ID 742127, 12 pages

Editorial

Graphene

Rakesh K. Joshi,¹ Masamichi Yoshimura,² and Ashok Kumar¹

¹ Nanotechnology Education and Research Center, University of South Florida, 4202 E. Fowler Avenue, Tampa, FL 33620, USA

² Nano High-Tech Research Center, Toyota Technological Institute, 2-12-1 Hisaka Tempaku-ku, Nagoya, Japan

Correspondence should be addressed to Rakesh K. Joshi, joshinano@gmail.com

Received 23 November 2010; Accepted 31 December 2010

Copyright © 2010 Rakesh K. Joshi et al. This is an open access article distributed under the Creative Commons Attribution License, which permits unrestricted use, distribution, and reproduction in any medium, provided the original work is properly cited.

Graphene is a two-dimensional semimetal with a tiny overlap between valence and conductance bands. It was discovered in 2004 by the group of Professor Andre Geim at Manchester. It is a one-atom-thick planar film of sp²-bonded carbon atoms which are densely packed in a honeycomb crystal lattice. It is the basic structural element of all other graphite materials. Graphene has remarkably high electron mobility at room temperature, as compared to those of silicon-based semiconductors. Since the identification of graphene in 2004, discoveries have been made to demonstrate graphene-based single-atom-layer transistors and chemical nanosensors for single-molecule gas detection. The electron mobility-related resistivity of graphene is about 35 percent less than that of copper, which is known to be the least resistive material at room temperature. Owing to its super mechanical-electronic properties, graphene is predicted to be a very promising material for widespread applications at various scales, ranging from macroaircraft to microdevices. Professor Andre Geim and Dr. Konstantin Novoselov were awarded the 2010 Nobel Prize in physics for their pioneering research on graphene.

This special issue is a collection of the articles on graphene research. The objective of this special issue is to bring together some selected examples of current research efforts related to the synthesis, characterization, and applications of graphene. We received research papers from the groups of many leading researchers worldwide. All the articles in this issue were peer reviewed by multiple reviewers. This issue publishes 14 accepted articles on various aspects of graphene research.

Acknowledgments

The editors would like to acknowledge and thank the authors, reviewers, and staff members of Hindawi Publishing Corporation for their contributions to this special issue. We highly appreciate the encouragement and support from the Editor-in-Chief Professor M. Hu and all the editors of the Journal of Nanomaterials.

*Rakesh K. Joshi
Masamichi Yoshimura
Ashok Kumar*

Research Article

Modelling of Graphene Nanoribbon Fermi Energy

**Zaharah Johari, Mohammad Taghi Ahmadi, Desmond Chang Yih Chek,
N. Aziziah Amin, and Razali Ismail**

*Department of Electronic Engineering, Faculty of Electrical Engineering, Technological University of Malaysia, Skudai,
81310 Johor Darul Takzim, Malaysia*

Correspondence should be addressed to Mohammad Taghi Ahmadi, ahmadi@ph@gmail.com

Received 30 December 2009; Accepted 16 March 2010

Academic Editor: Rakesh Joshi

Copyright © 2010 Zaharah Johari et al. This is an open access article distributed under the Creative Commons Attribution License, which permits unrestricted use, distribution, and reproduction in any medium, provided the original work is properly cited.

Graphene nanoribbon (GNR) is a promising alternative to carbon nanotube (CNT) to overcome the chirality challenge as a nanoscale device channel. Due to the one-dimensional behavior of plane GNR, the carrier statistic study is attractive. Research works have been done on carrier statistic study of GNR especially in the parabolic part of the band structure using Boltzmann approximation (nondegenerate regime). Based on the quantum confinement effect, we have improved the fundamental study in degenerate regime for both the parabolic and nonparabolic parts of GNR band energy. Our results demonstrate that the band energy of GNR near to the minimum band energy is parabolic. In this part of the band structure, the Fermi-Dirac integrals are sufficient for the carrier concentration study. The Fermi energy showed the temperature-dependent behavior similar to any other one-dimensional device in nondegenerate regime. However in the degenerate regime, the normalized Fermi energy with respect to the band edge is a function of carrier concentration. The numerical solution of Fermi-Dirac integrals for nonparabolic region, which is away from the minimum energy band structure of GNR, is also presented.

1. Introduction

Single layer of graphite which is also known as graphene has been discovered as a material with attractive low-dimensional physics, and possible applications in electronics [1–6]. A single-wall carbon nanotube (SWCNT) is a piece of rolled-up graphene sheet while a nanoribbon is an unrolled nanotube. Band-gap opening is expected by patterning narrow ribbons [7, 8] from Graphene which can be achieved by chemical means [9]. This Graphene nanoribbon (GNR) with quasi-one-dimensional structures and narrow widths ($< \sim 10$ nm) is predicted to be used as a channel for field effect transistors with high switching speed and excellent carrier mobility with ballistic transport behavior [9–14]. Armchair and zigzag GNRs show metallic or semiconducting electronic properties depending on the number of dimer lines, N which gives the width of the nanoribbon as depicted in Figures 1 and 2. The semiconducting property in armchair GNRs occurs when $N = 3p$ or $3p + 1$, where p is an integer [15]. The

width of the GNR, w_{GNR} , is proportional to N given by the expression

$$w_{\text{GNR}} = (N - 1) \frac{\sqrt{3}}{2} a_{\text{C-C}}, \quad (1)$$

where $a_{\text{C-C}} = 0.142$ nm is the lattice constant [16]. Quantum confinement effect results in similarity of semiconducting and metallic behaviors in both nanotube and nanoribbon configurations. A nanoribbon can be assumed as an unrolled single-wall nanotube that results in two different classes of GNRs depending on SWNTs unfolded way. One is by unzipping the SWNT along the axial direction through a row of atoms and then splitting the atom row onto both edges of the resulting GNR [17].

2. Graphene Nanoribbon Band Structure

The band energy throughout the entire Brillouin zone of graphene is given by [18]

$$E(\vec{k}) = \pm t \sqrt{1 + 4 \cos\left(\frac{k_x 3a_{C-C}}{2}\right) \cos\left(\frac{k_y \sqrt{3}a_{C-C}}{2}\right) + 4 \cos^2\left(\frac{k_y \sqrt{3}a_{C-C}}{2}\right)}, \quad (2)$$

where $a_{C-C} = 1.42 \text{ \AA}$ is carbon-carbon (C-C) bond length, $t = 2.7 \text{ eV}$ is the nearest neighbor C-C tight-binding overlap energy, and $k_{x,y,z}$ is the wave vector component [19, 20]. In low-energy limit [21] due to the approximation for the graphene band structure near the Fermi point, the $E(k)$ relation of the GNR is obtained as

$$E(\vec{k}) = \pm \frac{t3a_{C-C}}{2} \sqrt{k_x^2 + \beta^2}, \quad (3)$$

where β is the quantized wave vector [22] given as

$$\beta = \frac{2\pi}{a_{C-C}\sqrt{3}} \left(\frac{p_i}{N+1} - \frac{2}{3} \right), \quad (4)$$

where p_i is the subband index and N is the number of dimer lines which determine the width of the ribbon [21], and k_x is the wave vector along the length of the nanoribbon. The energy band gap of the GNR is then simplified to be

$$E_g = 3ta_{C-C}\beta. \quad (5)$$

By using (5) as the band gap, we can rewrite the band energy as [22]

$$E = \pm \frac{E_g}{2} \sqrt{\left(1 + \frac{k_x^2}{\beta^2}\right)}. \quad (6)$$

According to (6), the relationship between energy and wave vector is not parabolic. In the case of semiconducting GNR, the square root approximation can be employed to formulate the parabolic relation between energy and wave vector. Therefore the band energy in the low-energy limit ($k = 0$) is

$$E(k) \approx \frac{E_g}{2} + \frac{E_g}{4\beta^2} k_x^2, \quad (7)$$

$$E \approx \frac{E_g}{2} + \frac{\hbar^2 k_x^2}{2m^*}, \quad (8)$$

where m^* is the effective mass of GNR. The square root approximation leads to Fermi-Dirac integrals in the parabolic band structure for the carrier concentration, velocity, and current expression which is similar to the one-dimensional devices [22]. By representing the GNR energy band of (6) and (8) in Figure 3, it can be seen that the band structure is parabolic at certain range of energy in the E - k relationship. In the parabolic region it is sufficient to use the Fermi-Dirac integral for carrier statistic study. However in the nonparabolic part, it will lead to a different kind of Fermi integral.

By taking the derivatives of energy E over the wave vector k (dE/dk) for (8), the density of state (DOS) [22] for parabolic part of one-dimensional GNR band energy

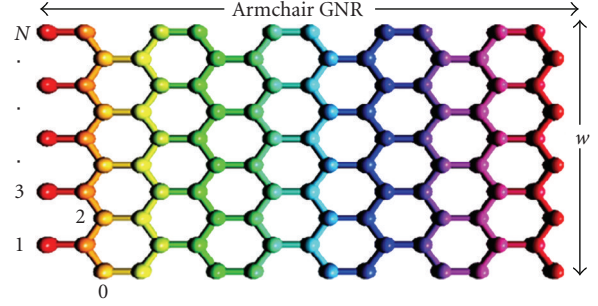


FIGURE 1: Armchair GNRs with dimer lines N and width w .

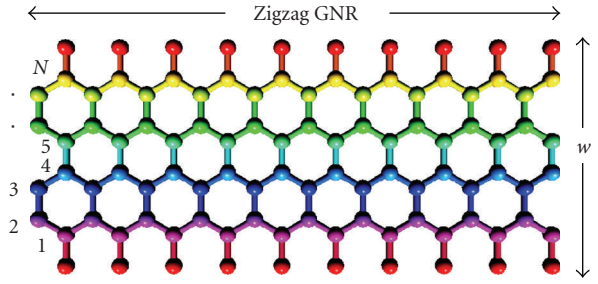


FIGURE 2: Zigzag GNRs with dimer lines N and width w .

incorporating the effect of electron-spin parameter ($g_s = 2$) [23] is given by

$$\text{DOS}_{\text{GNR}}(E) = \frac{\Delta n}{\Delta E \cdot L} = \frac{1}{2\pi} \left(\frac{2m^*}{\hbar^2} \right)^{1/2} \left(E - \frac{E_g}{2} \right)^{-1/2}, \quad (9)$$

where L is the length of the ribbon. By substituting $E_g/2$ with shifted conduction band energy E_C , this DOS equation can be readily applied to another one-dimensional material.

3. Result and Discussion

3.1. Carrier Statistics in Parabolic Band Structure. Carrier concentration is an essential parameter for semiconductor. The numbers of electrons/cm³ and holes/cm³ with energies between E and $E + dE$ have been established to be $\text{DOS}(E)f(E)d(E)$ and $\text{DOS}(E)[1 - f(E)]dE$.

Therefore the total carrier concentration in a band can be obtained by simply integrating the Fermi-Dirac distribution function over energy band as follows [23]:

$$n = \int_{E_C}^{E_{\text{top}}} \text{DOS}(E)f(E) dE, \quad (10)$$

$$p = \int_{E_{\text{bottom}}}^{E_V} \text{DOS}(E)[1 - f(E)] dE. \quad (11)$$

By substituting the density of state $\text{DOS}_{\text{GNR}}(E)$ and Fermi-Dirac distribution function $f(E)$ expressions into carrier concentration, we obtained [24]

$$n_D = N_C \mathcal{J}_{(D-2)/2}(\eta_D), \quad (12)$$

where D is dimensionality $D = 3$ (3D), 2 (2D), and 1 (1D), N_C is effective density of states, $N_C = (2m^*k_B T/\pi\hbar^2)^{1/2}$,

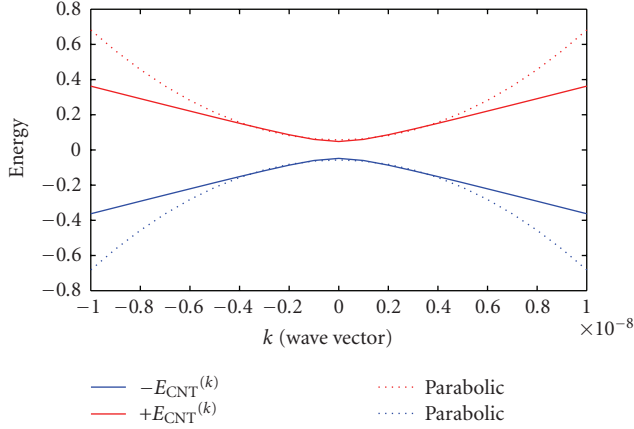


FIGURE 3: The band structure of GNR near the minimum energy is parabolic.

$\mathcal{J}_{(D-2)/2}$ is the Fermi-Dirac integral of order $(D-2)/2$, and normalized Fermi energy is $\eta_D = (E_F - E_{CD})/k_B T$. The Fermi-Dirac integral of order i is defined as

$$\mathcal{J}_i(\eta_D) = \frac{1}{\Gamma(i+1)} \int_0^\infty \frac{x^i}{e^{(x-\eta_D)} + 1} dx. \quad (13)$$

Under nondegenerate condition, the “1” from the denominator can be neglected and hence the Fermi integral reduces to

$$\mathcal{J}_i(\eta) \approx e^\eta. \quad (14)$$

In degenerate regime, the exponential part of (14) is very small because all the levels are occupied by electrons up to Fermi level. Thus, the occupation probability is 1 and the Fermi-Dirac integral can be solved analytically resulting in

$$\mathcal{J}_i(\eta_D) = \frac{1}{\Gamma(i+1)} \frac{\eta_D^{i+1}}{i+1}. \quad (15)$$

The inequalities adjacent to (14) are simultaneously satisfied if the Fermi level lies in the band gap more than $3K_B T$ from either band edge. Figure 4 shows the energy band diagram indicating the degenerate and nondegenerate regions. Conversely, if the Fermi level is within $3K_B T$ of either band edge or lies inside a band, the semiconductor is said to be degenerate. It should be noted that a nondegenerate positioning of the Fermi level makes $f(E) \approx e^{-((E-E_F)/K_B T)}$ for all conduction band energies and $1 - f(E) \approx e^{((E-E_F)/K_B T)}$ for all valence band energies for all dimensions.

The simplified form of the occupancy factors is a Maxwell-Boltzmann-type function that also describes, for example, the energy distribution of molecules in a high temperature. The simplified occupancy factors lead directly to the nondegenerate relationships. In closed-form relationships we find limited usage in device analysis since the nondegenerate relationships are only valid for an intrinsic and low-doped semiconductor [22]. Quasi-one-dimensional GNR in Figure 5 has two axis (x and z) directions that are less than De Broglie wave-length (one layer atomic thickness

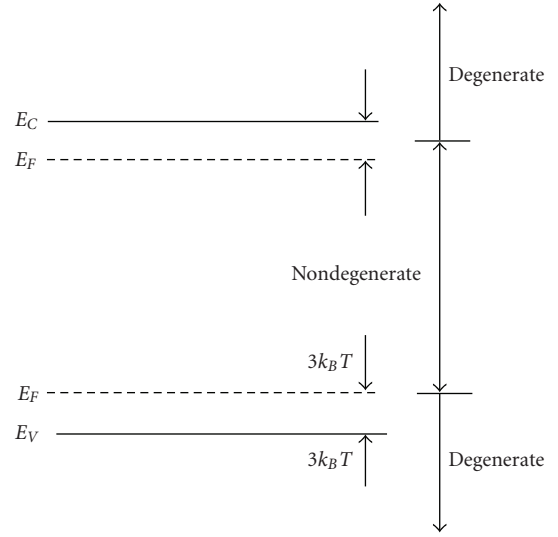


FIGURE 4: Energy band diagram showing degenerate and nondegenerate regions.

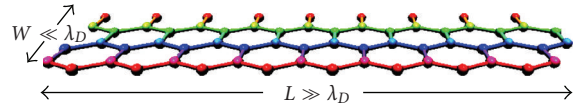


FIGURE 5: Cross-section of a rectangular one-dimensional GNR with $W \ll \lambda_D$ and $L \gg \lambda_D$.

with width less than 10 nm). However, GNR has length that is more than De Broglie wave-length, $L \gg \lambda_D$. The width is less than De Broglie wave-length $\ll \lambda_D$.

In nondegenerate limit condition, the carrier concentration of GNR can be expressed as

$$n_{\text{GNR(non degenerate)}} = N_C e^{-((E_C - E_F)/k_B T)}. \quad (16)$$

Here $E_C = E_{C0} + \epsilon_{0y} + \epsilon_{0z}$ is the shifted conduction band due to the confinement effect. This simplified distribution function is extensively used in determining the transport parameters. It is applicable for nondegenerately doped semiconductors and also GNR near the minimum band energy. However, most nanoelectronic devices today are degenerately doped [25, 26]. However, any design based on the Maxwellian distribution is not strictly correct and often leads to errors in the interpretation of the results.

For degenerate GNR we have

$$n_{\text{GNR(deg)}} = \left[\frac{8m^*(E_F - E_C)}{\pi^2 \hbar^2} \right]^{1/2}. \quad (17)$$

In quasi-one-dimensional semiconducting GNR, the Fermi-Dirac integral is a proportion of exponential of η in nondegenerate approximation and a proportion of $2/\sqrt{\pi} e^{1/2}$ in degenerate approximation as shown in Figure 6. This significant result proves that the Fermi-Dirac integral can be simplified into degenerate and nondegenerate approximation and therefore a simplified equation can be obtained.

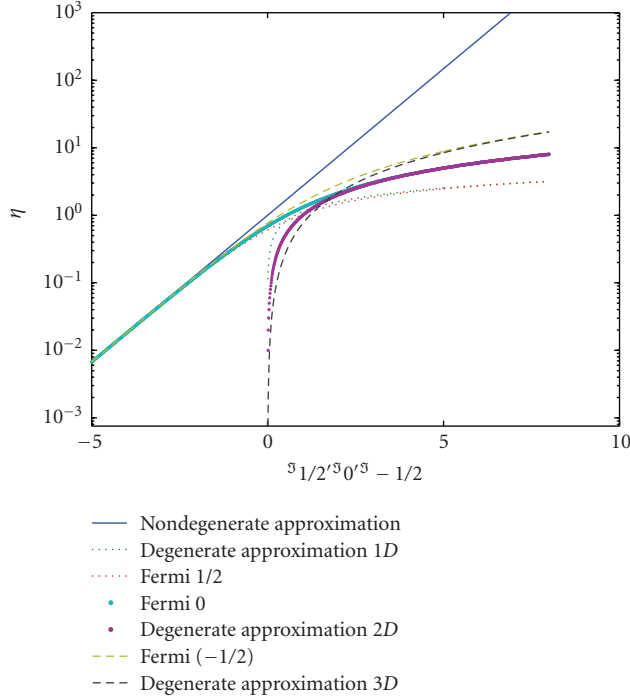


FIGURE 6: Comparison of Fermi-Dirac integral and Fermi $-1/2$, 0 , $1/2$ for Q3D bulk, Q2D, and Q1D devices, respectively [27].

Also shown in Figure 6 are those for $D = 3$ (bulk), 2 (quasi-2-dimensional), and 1 (quasi-1-dimensional). The normalized Fermi energy η_{Fd} as a function of normalized carrier concentration in the nondegenerate regime of GNR is given by [24]

$$(E_F - E_C)_{\text{non degenerate}} = k_B T \ln \left(\frac{n}{N}_d \right), \quad (18)$$

where $(E_F - E_C)_{\text{non degenerate}}$ is a weak (logarithmic) function of carrier concentration. It varies linearly with temperature in the nondegenerate (ND) regime. However, for strongly degenerate statistics, the Fermi energy is independent of temperature and it is a strong function of carrier concentration given by [24]

$$(E_F - E_C)_{\text{degenerate}} = \frac{\hbar^2}{m^*} 2\pi \left[\Gamma \left(\frac{d}{2} + 1 \right) n_d / 2 \right]^{2/d}. \quad (19)$$

The Fermi energy is proportional to n_d^2 for 1D nanostructure specifically for the GNR. Equations (18) and (19) are important as we would like to know the position of the Fermi level with respect to the carrier concentration in GNR. The higher doping concentration on GNR will lead to higher carrier concentration and hence Fermi level is further from conduction band.

3.2. Carrier Statistics in Nonparabolic Band Structure. As illustrated in Figure 3, the energy band is only parabolic near the low-energy limit in a range of $-0.5 < k < 0.5$. The non-parabolic part remains unsolved outside that range.

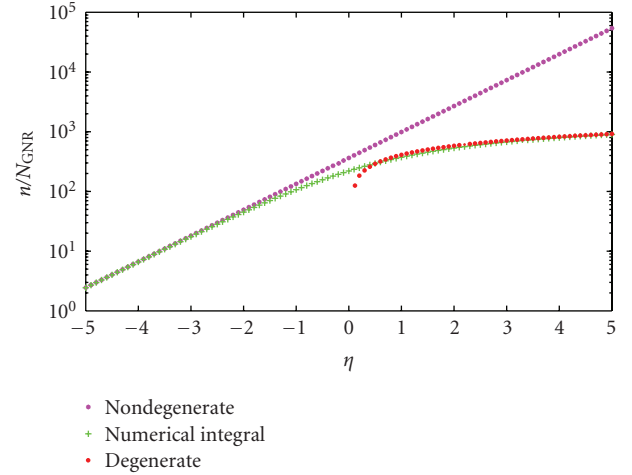


FIGURE 7: Comparison of the GNR Fermi-Dirac integral in degenerate and nondegenerate regimes in non-parabolic region. Also shown is the comparison with general equation ($W = 3.5663$, $m = 10$, $p = 21$, and $N = 30$).

The carrier concentration in the non-parabolic region is determined by

$$n_{\text{GNR}} = \int_{-\infty}^{\infty} \frac{1}{3\pi a_{c-c} t} \frac{E}{\sqrt{E^2 - (E_g/2)^2}} \frac{1}{e^{(E-E_F)/k_B T} + 1} dE. \quad (20)$$

However, this integral cannot be solved analytically. Rearranging (20) we obtained

$$n_{\text{GNR}} = N_C \int_{-\infty}^{\infty} \frac{(x + E_g/2k_B T)}{\sqrt{x^2 + x(E_g/k_B T)}} \left(\frac{1}{e^{x - \eta_{\text{FGNR}}} + 1} \right) dx, \quad (21)$$

where $N_C = k_B T / 3\pi a_{c-c} t$, $x = E - (E_g/2)/k_B T$, and $\eta_{\text{FGNR}} = E_F - (E_g/2)/k_B T$. N_C is the effective density of states in the nonparabolic region of the GNR. For the nondegenerate condition which neglected 1 in the denominator, (21) will be similar to the other one-dimensional devices which showed temperature dependence effect for the Fermi energy. By replacing the graphene nanoribbon Fermi integral with another integral M , the equation for electron concentration in non-parabolic region of the GNR will be simplified as

$$n_{\text{GNR}} = N_C M e^{\eta_{\text{GNR}}}, \quad (22)$$

where

$$M = \int_{E_C}^{E_{\text{top}}} \frac{x + E_G/2k_B T}{\sqrt{x^2 + xE_G/k_B T}} \left(\frac{1}{e^{x - \eta} + 1} \right) dx. \quad (23)$$

As the carrier occupancy probability is unity in the degenerate regime, the exponential part can be neglected, which leads to

$$n_{\text{GNR}} = N_C \int_0^{\eta} \frac{x + E_G/2k_B T}{\sqrt{x^2 + xE_G/k_B T}} dx. \quad (24)$$

Thus, the carrier concentration is a simple integral which can be solved analytically. Expanding (24)

$$n_{\text{GNR}} = N_C \int_0^\eta \frac{x}{\sqrt{x^2 + xE_G/k_B T}} dx + \int_0^\eta \frac{E_G/2k_B T}{\sqrt{x^2 + xE_G/k_B T}} dx. \quad (25)$$

By substituting x and η_{FGNR} into (25), the normalized Fermi energy is dependent on the carrier concentration and independent of temperature. Thus, the non-parabolic carrier concentration of the GNR can be expressed as

$$n_{\text{GNR}} = N_C \left(\sqrt{(E_F - E_C)^2 + (E_F - E_C)^2 E_G} \right). \quad (26)$$

In quasi-one-dimensional semiconducting nanoribbon the Fermi-Dirac integral is proportional to the exponential of η in nondegenerate approximation and it is proportional to carrier concentration in degenerate approximation. Figure 7 shows that the nanoribbon Fermi integral in non-parabolic region is closely approximated by the exponential of η when $\eta \leq -3$ for the nondegenerate regime. Thus GNR Fermi energy is a function of temperature that is independent of the carrier concentration in the nondegenerate regime. In the other strongly degenerate regime for ($\eta \geq 6$), the Fermi energy is a function of carrier concentration appropriate for given dimensionality and it is independent of temperature.

4. Conclusion

The modeling of carrier statistic in a both parabolic and non-parabolic region is presented. The one-dimensional GNR approaches degeneracy at relatively lower values of carrier concentration as compared to 2D and 3D structures. The Fermi energy with respect to the band edge of the GNR is a function of temperature but is independent of the carrier concentration in the nondegenerate regime. In the strongly degenerate regime, the Fermi energy is a function of carrier concentration but it is independent of temperature.

Acknowledgments

The authors would like to acknowledge the financial support from FRGS grant of the Ministry of Higher Education (MOHE), Malaysia. Mohammad Taghi Ahmadi is thankful to the Research Management Centre (RMC) of Universiti Teknologi Malaysia (UTM) for providing excellent research environment in which to complete this work.

References

- [1] A. K. Geim and K. S. Novoselov, "The rise of graphene," *Nature Materials*, vol. 6, no. 3, pp. 183–191, 2007.
- [2] K. S. Novoselov, A. K. Geim, S. V. Morozov, et al., "Electric field in atomically thin carbon films," *Science*, vol. 306, no. 5696, pp. 666–669, 2004.
- [3] C. Berger, Z. Song, X. Li, et al., "Electronic confinement and coherence in patterned epitaxial graphene," *Science*, vol. 312, no. 5777, pp. 1191–1196, 2006.
- [4] Y. Zhang, Y.-W. Tan, H. L. Stormer, and P. Kim, "Experimental observation of the quantum Hall effect and Berry's phase in graphene," *Nature*, vol. 438, no. 7065, pp. 201–204, 2005.
- [5] K. S. Novoselov, A. K. Geim, S. V. Morozov, et al., "Two-dimensional gas of massless Dirac fermions in graphene," *Nature*, vol. 438, no. 7065, pp. 197–200, 2005.
- [6] C. Berger, Z. Song, T. Li, et al., "Ultrathin epitaxial graphite: 2D electron gas properties and a route toward graphene-based nanoelectronics," *Journal of Physical Chemistry B*, vol. 108, no. 52, pp. 19912–19916, 2004.
- [7] Y.-W. Son, M. L. Cohen, and S. G. Louie, "Energy gaps in graphene nanoribbons," *Physical Review Letters*, vol. 97, no. 21, Article ID 216803, 4 pages, 2006.
- [8] H. Xiang, E. Kan, S.-H. Wei, M.-H. Whangbo, and J. Yang, "'Narrow' Graphene Nanoribbons Made Easier by Partial Hydrogenation," *Nano Letters*, vol. 9, no. 12, pp. 4025–4030, 2009.
- [9] M. Y. Han, B. Özyilmaz, Y. Zhang, and P. Kim, "Energy band-gap engineering of graphene nanoribbons," *Physical Review Letters*, vol. 98, no. 20, Article ID 206805, 4 pages, 2007.
- [10] D. A. Areshkin, D. Gunlycke, and C. T. White, "Ballistic transport in graphene nanostrips in the presence of disorder: importance of edge effects," *Nano Letters*, vol. 7, no. 1, pp. 204–210, 2007.
- [11] Z. Chen, Y.-M. Lin, M. J. Rooks, and P. Avouris, "Graphene nano-ribbon electronics," *Physica E*, vol. 40, no. 2, Article ID 0701599, pp. 228–232, 2007.
- [12] K. Nakada, M. Fujita, G. Dresselhaus, and M. S. Dresselhaus, "Edge state in graphene ribbons: nanometer size effect and edge shape dependence," *Physical Review B*, vol. 54, no. 24, pp. 17954–17961, 1996.
- [13] V. Barone, O. Hod, and G. E. Scuseria, "Electronic structure and stability of semiconducting graphene nanoribbons," *Nano Letters*, vol. 6, no. 12, pp. 2748–2754, 2006.
- [14] G. Liang, N. Neophytou, D. E. Nikonov, and M. S. Lundstrom, "Performance projections for ballistic graphene nanoribbon field-effect transistors," *IEEE Transactions on Electron Devices*, vol. 54, no. 4, pp. 677–682, 2007.
- [15] K. Nakada, M. Fujita, G. Dresselhaus, and M. S. Dresselhaus, "Edge state in graphene ribbons: nanometer size effect and edge shape dependence," *Physical Review B*, vol. 54, no. 24, pp. 17954–17961, 1996.
- [16] K. Wakabayashi, "Electronic and Magnetic Properties of Nanographite," in *Carbon-Based Magnetism—An Overview of the Magnetism of Metal Free Carbon-Based Compounds and Materials*, pp. 279–304, Elsevier, Amsterdam, The Netherlands, 2006.
- [17] Q. Yan, B. Huang, J. Yu, et al., "Intrinsic current-voltage characteristics of graphene nanoribbon transistors and effect of edge doping," *Nano Letters*, vol. 7, no. 6, pp. 1469–1473, 2007.
- [18] J. W. G. Wildöer, L. C. Venema, A. G. Rinzler, R. E. Smalley, and C. Dekker, "Electronic structure of atomically resolved carbon nanotubes," *Nature*, vol. 391, no. 6662, pp. 59–62, 1998.
- [19] R. A. Jishi, D. Inomata, K. Nakao, M. S. Dresselhaus, and G. Dresselhaus, "Electronic and lattice properties of carbon nanotubes," *Journal of the Physical Society of Japan*, vol. 63, no. 6, pp. 2252–2290, 1994.

- [20] R. F. Pierret, "Advanced semiconductor fundamentals," in *The Modular Series on Solid State Devices*, vol. 6, Prentice-Hall, Upper Saddle River, NJ, USA, 2nd edition, 2003.
- [21] S. Datta, *Quantum Transport Atom to Transistor*, Cambridge University Press, Cambridge, UK, 2005.
- [22] H. Zheng, Z. F. Wang, T. Luo, Q. W. Shi, and J. Chen, "Analytical study of electronic structure in armchair graphene nanoribbons," *Physical Review B*, vol. 75, no. 16, Article ID 165414, 6 pages, 2007.
- [23] H. M. Tien, N. H. Chau, and P. T. K. Loan, "Tight-binding calculations of band structure and conductance in graphene nano-ribbons," *Communications in Physics*, vol. 19, no. 1, pp. 1–8, 2009.
- [24] V. K. Arora, "Quantum engineering of nanoelectronic devices: the role of quantum emission in limiting drift velocity and diffusion coefficient," *Microelectronics Journal*, vol. 31, no. 11–12, pp. 853–859, 2000.
- [25] H. L. Hui, H. H. Ing, A. E. L. Chii, M. T. A. R. Ismail, and V. K. Arora, "The high-field drift velocity in degenerately-doped silicon nanowires," in *Proceedings of the 2nd IEEE International Nanoelectronics Conference (INEC '08)*, Shanghai, China, March 2008.
- [26] Q. Wan, J. Huang, A. Lu, and T. Wang, "Degenerate doping induced metallic behaviors in ZnO nanobelts," *Applied Physics Letters*, vol. 93, no. 10, Article ID 103109, 3 pages, 2008.
- [27] M. T. Ahmadi, R. Ismail, M. L.P. Tan, and V. K. Arora, "The ultimate ballistic drift velocity in carbon nanotubes," *Journal of Nanomaterials*, vol. 2008, Article ID 769250, 8 pages, 2008.

Research Article

Stable Aqueous Suspension and Self-Assembly of Graphite Nanoplatelets Coated with Various Polyelectrolytes

Jue Lu,^{1,2} Inhwan Do,¹ Hiroyuki Fukushima,¹ Ilsoon Lee,² and Lawrence T. Drzal¹

¹ Composite Materials and Structures Center, Michigan State University, East Lansing, MI 48824-1226, USA

² Department of Chemical Engineering and Materials Science, Michigan State University, East Lansing, MI 48824-1226, USA

Correspondence should be addressed to Ilsoon Lee, leeil@msu.edu and Lawrence T. Drzal, drzal@egr.msu.edu

Received 1 March 2010; Accepted 7 May 2010

Academic Editor: Rakesh Joshi

Copyright © 2010 Jue Lu et al. This is an open access article distributed under the Creative Commons Attribution License, which permits unrestricted use, distribution, and reproduction in any medium, provided the original work is properly cited.

Exfoliated graphite nanoplatelets (xGnPs) with an average thickness of 1–10 nm present an inexpensive alternative to carbon nanotubes in many applications. In this paper, stable aqueous suspension of xGnP was achieved by noncovalent functionalization of xGnP with polyelectrolytes. The surfactants and polyelectrolytes were compared with respect to their ability to suspend graphite nanoplatelets. The surface charge of the nanoplatelets was characterized with zeta potential measurements, and the bonding strength of the polymer chains to the surface of xGnP was characterized with Raman spectroscopy. This robust method opens up the possibility of using this inexpensive nanomaterial in many applications, including electrochemical devices, and leads to simple processing techniques such as layer-by-layer deposition. Therefore, the formation of xGnP conductive coatings using layer-by-layer deposition was also demonstrated.

1. Introduction

Considerable interest has been drawn in the layer-by-layer (LbL) self-assembly of nanosized carbon particles due to their excellent thermal, electrical, and mechanical properties [1]. Carbon nanotubes (CNTs) and fullerenes (also known as buckyball or C₆₀) have been intensively studied, and their possible applications in nanodevices [2, 3], quantum wires [4], ultrahigh-strength engineering fibers [5], sensors [6, 7], and support of electrocatalysts [4] are developing. Both carbon nanotubes and fullerenes are expensive, which hinders their application in industry. Recently, the two-dimensional carbon graphene has attracted great attention, due to its exceptionally high crystal and electronic quality [8, 9]. Growth of large area of high-quality graphene was developed on metal substrates [10], and individual graphene sheets can be also prepared by micromechanical cleavage [8]. Unfortunately, these approaches are technically complex and difficult for mass production. In addition, these two-dimensional crystals cannot theoretically exist in the free state [8]. The most commonly used nano sized form of graphene is graphite nanoplatelets, which are a few layers of graphene sheets stacked together and are produced by the exfoliation of graphite via an acid intercalation, followed by

ultrasonic irradiation to isolated graphite nanosheets [11]. Research in our group at MSU has led to a process that can successfully produce exfoliated graphite nanoplatelets (xGnPTM), which are 1–10 nm in thickness and from 100 to 1000 nm in diameter. The surface of the graphite nanoplatelets is pure graphene where the carbon is in a sp² configuration. This presents a uniformly homogeneous and moderately energetic surface that has been shown to be an excellent nucleating surface for both polar and nonpolar polymers. Furthermore, these graphite nanoplatelets possess the high electric conductivity of graphene. With an expected cost on the order of \$5/pound, these nanoplatelets could be a suitable substitute for carbon nanotubes and fullerenes for most applications. So far, graphite nanoplatelets are most commonly used in composite application due to their good mechanical properties and electrical conductivity [12–14]. Recently, we have demonstrated that xGnP can be an inexpensive alternative to carbon nanotubes and carbon black as an advantageous support for fuel cell applications, which has the highest thermal-oxidation resistance and the highest degree of graphitization [15]. In addition, xGnP and xGnP-supported electrocatalysts have shown significant catalytic effect toward hydrogen peroxide, resulting highly sensitive and quickly responding glucose biosensors [16, 17].

The major challenge for these hydrophobic carbon nanostructures is their dispersion in an aqueous medium. Several approaches have been studied for the production of aqueous suspension of carbon nanotubes. Chemical modification of the graphene surface is common, such as acid treatment, which imparts $-\text{COOH}$ groups at the broken links or at the ends of nanotubes [18, 19]. However, such chemical modification can disrupt the electronic conjugation in carbon nanotubes which inevitably deteriorate the electrical properties of the nanotubes. Another common method is to suspend carbon nanotubes in various surfactants or charged polymers accompanied by the physical processes, which involves high-shear homogenization and ultrasonication [20]. This method became universal for carbon nanotube dispersion because it is easy to control, and most importantly, it preserves the integrity of carbon nanotubes. The functionalized carbon nanotubes are used to construct thin films for various applications.

Since Decher's pioneering work in 1997 [21], the LbL assembly method has been well studied to create highly tuned, functional thin films with nanometer-level thickness [1]. In LbL assembly, oppositely charged polymers are alternately adsorbed on the surface by the electrostatic force, although possible hydrogen bonding, hydrophobic interaction, and van der Waals interactions could also be used. Considerable work has been done on self-assembly of carbon nanotubes. This approach can solve the dispersion problems of carbon nanotubes in polymer matrix, one of the big challenges of the traditional composite processing method. In addition, LbL assembly was also used to incorporate carbon nanotubes in the construction of chemical sensors and biosensors, due to their high electrocatalytic effect, fast electron transfer, rate and large working surface area [22]. Several groups have reported the preparation of self-assembled carbon films using graphite oxide nanoplatelets [23–26]. However, the oxidation of graphite reduced the original conductivity of graphite. To restore the conductivity of the carbon films, the graphite oxide needs to be reduced to the original state by either chemical or electrochemical methods, which is not cost effective. In addition, this additional process may inhibit their use in biosensor application due to the enzyme stability during the reduction process.

In this paper, we report the achievement of stable aqueous dispersions of graphite nanoplatelets and their self-assembly. Since graphite nanoplatelets are not stable in aqueous solution due to the hydrophobic characteristics of graphene sheets and their significant hydrophobic interactions which form agglomerates in aqueous solution. Much effort has been devoted to achieve a stable suspension of graphite nanoplatelets with various surfactants and polyelectrolytes (PEs). In addition, by modifying the charge of polyelectrolytes on the graphite sheet, the agglomeration of graphite nanoplatelets can be possibly prevented by electrostatic or strong repulsive forces due to the surface charge induced by the polyelectrolytes during the self-assembly process. The morphologies of the graphite monolayer and multilayer films have been characterized by the optical microscopy (OM), scanning electron microscopy (SEM) and

atomic force microscopy (AFM). Additionally, the resistance and transmittance of these films were also measured.

2. Experimental Procedures

2.1. Materials. Poly(diallyldimethylammonium chloride) (PDAC), sulfated poly(styrene) (SPS), and branched poly ethyleimine (PEI) were purchased from Aldrich. The weight average molecular weights (M_w) of PDAC, SPS, and PEI were $\sim 100,000$ – $200,000$, $70,000$, and $750,000$, respectively. Polyacrylic acid (PAA) ($M_w = 90,000$) was purchased from Polysciences Inc. Poly(3,4-ethylenedioxythiophene) poly(styrene sulfonate) (PEDT/SPS) (Baytron P V407) was received as a sample from Bayer Corp. and used as received. The surfactants, sodium dodecylbenzene sulfonate (SDBS) and sodium dodecyl sulfate (SDS) were purchased from Aldrich and used as received. Microscope glass slides were purchased from Corning. All aqueous solutions in the processes were prepared using deionized (DI) water ($>18.1 \text{ M}\Omega$) supplied by a Barnstead Nanopur Diamond-UV purification unit equipped with a UV source and final $0.2 \mu\text{m}$ filter. All procedures were done at room temperature.

2.2. Preparation of Polyelectrolyte and Surfactant Solutions. Aqueous polyelectrolyte solutions were prepared containing either 20 mM PDAC or 10 mM SPS in 0.1 M NaCl. PEI and PAA solution was prepared containing 0.1 wt% polymer in DI water, and the pH value of the solution was not adjusted. The solutions were filtered with $0.22 \mu\text{m}$ cellulose acetate membrane filter system from Corning to remove particulates. Other solutions with surfactants (SDBS and SDS) were prepared containing 0.1 wt% surfactants in DI water.

2.3. Preparation of Graphite Suspension. 0.1 g of xGnP was dispersed in 100 mL polyelectrolyte solution by sonication with an output power of 23 W for 30 minutes. The suspension was stirred for 24 hours. The excess polyelectrolyte was removed by filtering through $0.2 \mu\text{m}$ membrane followed by DI water washing for three times. The polyelectrolyte-coated xGnP was redispersed to 100 mL DI water by mild sonication (output power: 10 W) for 10–15 minutes. The pH value of the suspension with PEI-coated xGnP was adjusted to be between 5.0–6.0.

2.4. Layer-by-Layer Self-Assembly Procedure. To prepare xGnP/polyelectrolyte multilayers, anionic PEs-xGnP such as SPS-xGnP were alternately assembled with PDAC, and cationic PEs-xGnP, such as PEI-xGnP with SPS. First, the glass slides were cleaned twice in an ultrasonic unit, first with a commercially available detergent (Alconox, Alconox Inc.) for 20 minutes and then without for 10 minutes. Slides were dried under a N_2 gas stream and then treated with oxygen plasma for 10 minutes at 150 mTorr vacuum to activate negative surface charges on the glass. The multilayers of xGnP were prepared using a Microm DS 50 Slide Stainer purchased from Richard-Allan Scientific. The pretreated glass slides were immersed in the PDAC solution

for 20 minutes, followed by two 5-minutes rinses in DI water. Then the glass slides were immersed in graphite suspension for 30 min, followed by three 2-minutes rinses in DI water. The immersion time in xGnP is considered sufficient since longer time did not increase the surface coverage of xGnP. The sequence was repeated until the desired number of bilayers was formed. The substrates were dried naturally.

2.5. Characterization of xGnP and Polymer-Modified xGnP. Transmission electron microscopy (TEM) investigation was carried out with JEOL 100CX and JEOL 2200FS operating at a voltage of 100 keV and 200 keV for the morphology of xGnP. Specimens were prepared by ultrasonically dispersing the sample powders in acetone for 15 minutes, applying the powder suspension onto lacey carbon-coated Cu grids and drying them in air at ambient temperature. An X-ray photoelectron spectroscopy spectrum (XPS, Physical Electronics 5400 ESCA) was used to study the surface of xGnP and polymer modified xGnP. UV-vis absorption measurement was taken on a Perkin Elmer UV/Vis/NIR spectrometer (model Lambda 900). Thermogravimetric analysis (TGA) was performed using a TGA 2950 (TA instruments) from 25°C to 580°C at a heating rate of 10.0°C/min under an air flow. Approximately 10 mg of xGnP was used.

For Raman measurements, the xGnP thin films were prepared by filtering a certain amount of xGnP and polymer-coated xGnP on cellulose ester membrane with a pore size of 0.2 μm , and drying for a few days. The films were peeled off from the membrane before Raman measurement. The Raman characterization was carried out on a micro-Raman system with a laser wavelength of 532 nm and an intensity of 14.5 mW.

Both Zeta potential and particle size of xGnP were analyzed with Brookhaven Instruments ZetaPALS, which utilizes phase analysis light scattering (PALS) to determine the electrophoretic mobility of charged colloidal suspensions. The velocities of the charged particles were measured and the electrophoretic mobility was determined by dividing the measured velocity by the electric field strength. The zeta potential was determined from the electrophoretic mobility using the Smoluchowski equation. Before measurement, the polymer coated graphite nanoplatelets were suspended in DI water by sonication. The particle size was also analyzed with ZetaPALS incorporated with a 90Plus particle sizer. Since the principles of dynamic light scattering assume the particles to be spherical, only relative values of particle size were obtained. Each value of particle size is the average of ten measurements of the sample. For comparison, AcoustoSizer IIs (Colloidal Dynamics) was also used for measuring the particle size of xGnP. 120 mL of xGnP suspension with 1 wt% solid content was used.

2.6. Multilayers Characterizations. The morphology of single and multilayer films of xGnP on glass slides was characterized using scanning electron microscopy (SEM, JEOL 6300F). A layer of osmium was coated with a pure osmium coater (NEOC-AN, MEIWA SHOJI CO. LTD, JAPAN) for 20 s for enhanced conductivity before SEM measurements.

The morphology of multilayer was also characterized using atomic force microscopy (AFM, a Nanoscope IV version from Veeco Instruments (Santa Barbara, CA)) in tapping mode. The surface resistance of xGnP multilayer was measured with a Camry Instruments Femtostat Station, and the transmittance was measured with Perkin Elmer Lambda 900 UV/Vis/NIR spectrometer.

3. Results and Discussions

Graphite has a layered structure with hybridized carbon atoms in an sp^2 configuration, and different layers are held together by van der Waals forces. Exfoliation of graphite is achieved by intercalation compounds which tend to exfoliate graphite upon heating due to the fast evaporation of intercalantes. A process was developed in our lab to produce exfoliated graphite nanoplatelets from a sulfuric acid-based intercalated graphite by microwave and sonication process, followed by a milling process to further reduce the particle size to approximately 1 μm . BET surface area analysis showed an area of approximately 100 m^2/g for the produced exfoliated graphite nanoplatelets [27]. Since a hypothetical monolayer graphite would exhibit a specific surface area close to 2700 m^2/g , and an interlayer spacing of 0.335 nm is assumed [28], the average thickness of graphite nanoplatelets was estimated to be 1–10 nm, which was further confirmed by TEM observation. As shown in Figure 1, the top view of xGnP shows clean surface of xGnP. It seems graphene sheets with different size are stacking together. Side view of xGnP clearly shows about 30 layers of atomic sheets stacking together, which counts to the thickness up to 10 nm.

To eliminate the need to search wide availability of surfactants and polyelectrolytes, the literature results of their ability for solubilizing carbon nanotubes were adapted in this work. Therefore, a series of good surfactants and polyelectrolytes for carbon nanotubes were chosen to test for their ability to suspend and then self-assemble xGnP on the charged glass slides. They include sodium dodecylbenzene sulfonate (SDBS), sodium dodecyl sulfate (SDS), sulfated poly(styrene) (SPS), poly(acrylic acid) (PAA), and a conductive polymer blend: poly(3,4-ethylenedioxythiophene) poly(styrene sulfonate) (PEDT/SPS) was also used. In addition, a couple of positive polyelectrolytes, poly(diallyldimethylammonium chloride) (PDAC) and branched polyethyleimine (PEI) were also tested. Table 1 shows the summary of quick trial-and-error experiments. xGnP was dispersed in solution with the surfactants or polyelectrolytes and their stability was checked after 24 hours. The suspension with SDBS and SDS was relatively stable but self-assembly of xGnP resulted poor surface coverage of particles. Therefore, further study was not conducted on these surfactants. PDAC and PAA also showed poor dispersing ability. It was found that SPS and PEDT/SPS coated xGnP showed good stability in water. This is possibly due to the edge-to-face interactions between the graphitic surface and the aromatic rings of the polymer [29]. PEI is also a good suspending agent due to the hydrophobic interaction between PEI and uncharged graphitic surface [30].

TABLE 1: General performance of surfactants and polyelectrolytes on the solubilization of xGnP and layer-by-layer deposition thereafter.

		Suspension After 24 hours	Layer-by-layer deposition
Surfactants	SDS	Partially settle down	Poor
	SDBS	Partially settle down	Poor
Polyelectrolytes	PDAC	Mostly settle down	Poor
	PEI	Stable	Good
	SPS	Stable	Very good
	PEDT/SPS	Stable	Good
	PAA	Mostly settle down	Poor

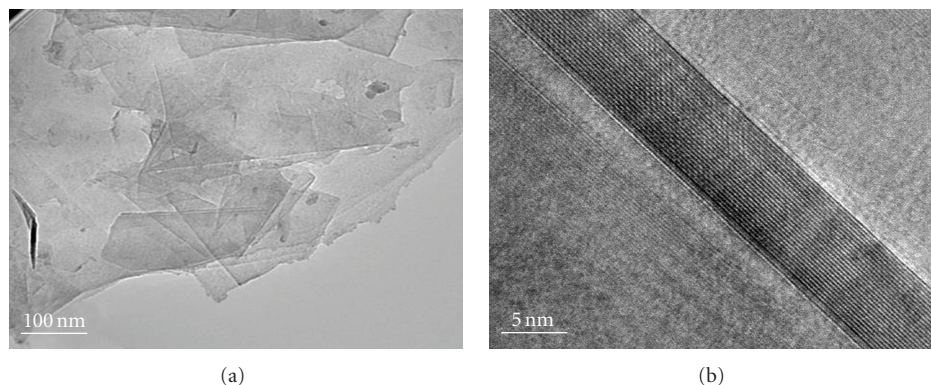


FIGURE 1: Typical TEM images of xGnP: (a) top view and (b) side view.

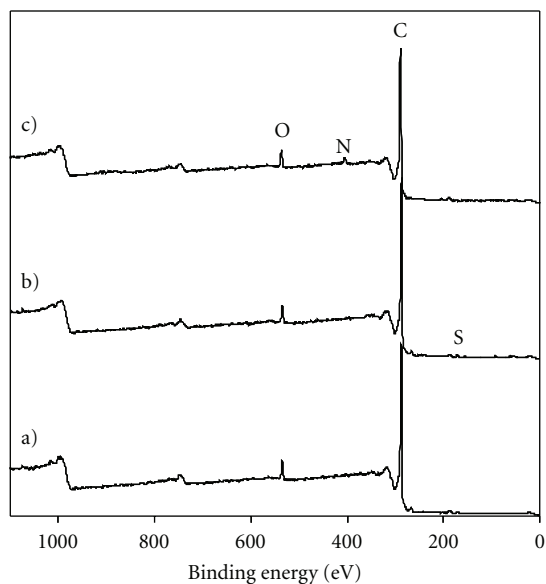


FIGURE 2: X-ray photoelectron spectroscopy spectra of xGnP before (a) and after SPS (b) and PEI (c) modification.

XPS was used to study the surface of xGnP before and after polymer coating. As shown in Figure 2, the surface of xGnP mainly contains C1s which shows peaks in the range of 280–290 eV. Small amount of oxygen is also shown which has an O1s peak at 540 eV. The oxygens mostly come from the edge group of the xGnP sheets such as carboxyl, hydroxyl, and carbonyl groups. There is also some Zr shown mainly

due to the contamination of zirconium ball during the milling process. The SPS coated xGnP shows its characteristic peaks of S2p at 167.3 eV, corresponding to sulfone. PEI coated xGnP shows N1s peak at 401 eV. Therefore, XPS clearly shows the bonding of the polyelectrolyte to the graphite surface. Table 2 shows the detailed concentration of atoms for xGnP with and without polymer coatings. The amount of polymer coated on the surface is low. TGA was used to directly measure the amount of polymer coated on the xGnP. As shown in Figure 3, graphite is thermally stable in ambient air environments up to 500°C, and then it slightly decomposed at elevated temperature. The SPS coated xGnP shows a gradual loss due to the residue water, and a major degradation starts at approximately 360°C. Instead, both PEI and PDAC coated xGnP show the major degradation approximately at 200°C, which are much less thermally stable than SPS coated xGnP. It is clear that SPS has higher amount of coating on xGnP than PEI and PDAC, which is approximately 5 wt%. Stankovich et al. claimed that ~40 wt% of SPS is coated on graphite nanoplatelets when dispersing nanoplatelets with a thickness of ~4 nm [29]. Various concentrations of SPS and coating times were used to increase the coverage of polymer on xGnP, but no increase in SPS content on xGnP was observed.

The surface charges of polyelectrolytes coated xGnP and unmodified xGnP were characterized using a zeta potential analyzer. The zeta potential describes the nature of the electrostatic potential near the surface of a suspended particle. In general, agglomeration of particles could be avoided by electrostatic repulsion above certain surface potentials, which is approximately ± 35 mV; and, the higher the absolute

TABLE 2: Atomic concentration of the surface of xGnP before and after PE modification.

	C1s	O1s	S2p	N1s	Zr3d
xGnP	92.38	6.38			0.25
SPS-xGnP	94.31	4.51	0.76		0.22
SPS-xGnP redispersed*	91.71	6.44	0.79		0.20
PEI-xGnP	91.84	4.73		3.19	0.25
PEI-xGnP redispersed*	90.69	5.79		3.24	0.28

*The xGnP was redispersed in DI water with mild sonication for 10–15 minutes, and then filtrated and dried before XPS measurement.

TABLE 3: Zeta potential of xGnP before and after the noncovalent attachment of polymers.

Materials	Zeta potential (mV)
xGnP	-32.33 ± 1.90
SPS-xGnP	-68.6 ± 0.75
PEDT/SPS-xGnP	-52.25 ± 1.49
PDAC-xGnP	49.39 ± 0.45
PEI-xGnP	48.56 ± 1.01

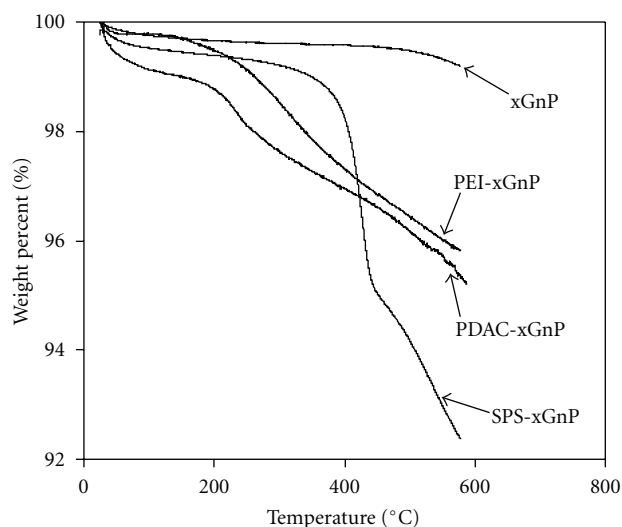


FIGURE 3: Thermogravimetric analysis of xGnP and polyelectrolytes modified xGnP.

value of the zeta potential, the more stable the particle suspension will be. In addition, the high surface charge of the modified graphite may count the strong van der Waals force between graphite nanoplatelets to prevent agglomeration during self-assembly. As shown in Table 3, the zeta potential for the unmodified xGnP was measured to be -32.33 mV, which is consistent with the literature value for the graphite particles [31]. The high absolute value of zeta potential for xGnP is possibly attributed to the naturally existing functional groups at the edges, such as carboxylic acid, hydroxyl, and so forth. The SPS and PEDT/SPS coated xGnP are kept negatively charged in aqueous solution, but the absolute value of zeta potential is increased to 68 mV for SPS coated xGnP, which confirms the significant adsorption of

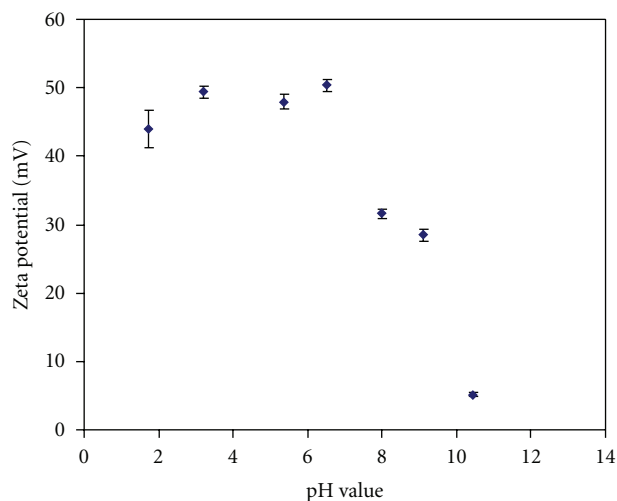


FIGURE 4: Zeta potential versus pH value for PEI coated xGnP.

SPS at the graphite surface. The zeta potential of PEDT/SPS coated xGnP is slightly lower (-52.25 mV), which is possibly due to the PEDT component in the conductive blend. For PDAC or PEI coated xGnP, the sign of the zeta potentials changed from negative to positive, and the magnitude of the positive zeta potential increased. By a simple comparison of the absolute values of zeta potential, the SPS coated xGnP suspension shows better stability than xGnP coated with other polyelectrolytes. The zeta potentials of PEI coated nanoplatelets varied with the pH value of the solution, thus the suspension stability varied. As shown in Figure 4, the zeta potential of PEI coated xGnP keeps relatively constant at a value of 48 mV when the pH is below 7, because the PEI molecules are mostly protonated which results strong repulsive force between the charged segments (pK_a of PEI is greater than 8.0). When the pH value is above 7, the zeta potential significantly decreases with increasing pH value due to uncharged PEI molecules. At the pH value of 10.5, the PEI coated xGnP has no net charge. The stability of xGnP suspension is fully correlated with the zeta potential of particles. Figure 5 shows the PEI coated xGnP dispersed in DI water with adjustment to the varied pH values after sitting for 24 hours. The suspension was relatively stable when the pH value is close to 7 or below. However, when the pH value is above 10, the graphite nanoplatelets completely settle out of solution.

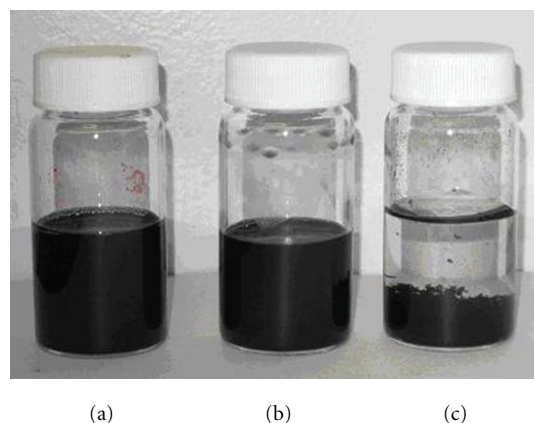


FIGURE 5: The stability of PEI coated xGnP at different solution pH values. (a) 5.33, (b) 7.16, and (c) 10.46.

The stability of xGnP suspension was further quantified by measuring the concentration difference of suspension and corresponding particles size before and after sitting for 48 hours. As discussed before, when the zeta potential of particle is above 35 mV, the repulsive force between particles can overcome the attractive van der Waals force, and the agglomeration of particles can be prevented. For graphite nanoplatelets, zeta potential may not fully characterize the stability of suspension, because the high zeta potential could mostly be attributed to the edge effect, and the large hydrophobic basal plane can be attracted by each other. In addition, the surface charge is limited and may not fully account for the particle size. The comparison of the xGnP concentration before and after allowing the suspension to sit for 48 hours is a good indication of the stability. For both SPS and PEI coated xGnP, approximately 45% of xGnP still remain in the solution and the other settles down. The top layer suspension is very stable, no further sedimentation occurs after a week. The analysis of average particle size by dynamic light scattering gives further insight on this. The average particle size of xGnP was measured to be 911.3 ± 47.8 nm. Although the principles of dynamic light scattering assume the particles measured to be spherical, the measured particle size of xGnP is close to the one observed with microscopic technique. In addition, a different technique was used to measure the particle size using AcoustoSizer IIs (Colloidal Dynamics), which uses electroacoustic signal to determine the dynamic mobility of the particles in a colloidal suspension. It gave a similar particle size for xGnP (data not shown). The particle size distribution shows that xGnP has approximately 30% which has a particle size above $1 \mu\text{m}$ (data not shown). In the top solution after sitting for 48 hours, the average particle size was measured to be 442.1 ± 13.1 nm, and 98% of particle is below 634.9 nm, meaning that most big particles are eliminated. We have also looked at the particle size of xGnP for a highly stable supernatant after centrifuge, which shows a value of 200.9 ± 6.2 nm. Therefore, the stability of xGnP suspension is determined by both surface charge and particle size.

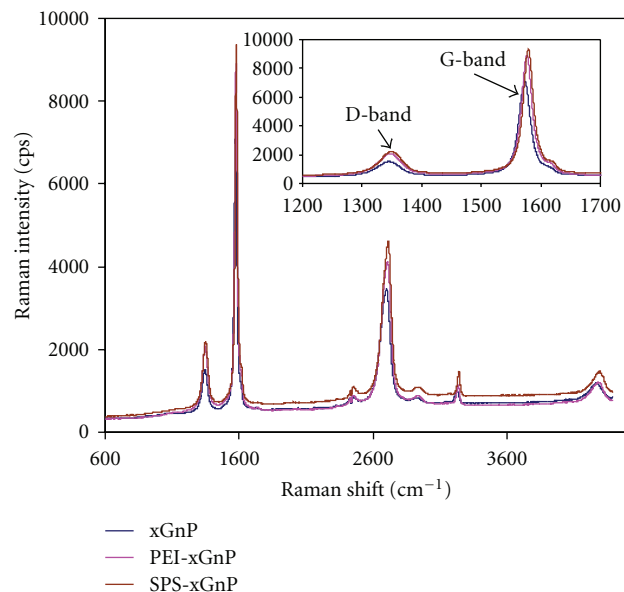


FIGURE 6: Raman spectra of xGnP before and after modification with polyelectrolytes (inset: enlargement of D-band and G-band).

The bonding strength of the polymer chains to the surface of xGnP can be measured by Raman spectrometry, because the presence of the polymer can affect the movement of carbon atoms [32]. The Raman spectra of xGnP and polymer coated xGnP are shown in Figure 6. The xGnP shows typical bands of graphite in the presence of disorder [33, 34]. The band at 1575 cm^{-1} is so called G-band resulting from the doubly degenerate zone center E_{2g} mode [33]. The peak in the $1300\text{--}1400 \text{ cm}^{-1}$ region is the disorder peak known as the D-band, which is attributed to scattering from sp^2 carbons containing defects. The peak between 2700 and 2800 cm^{-1} is D^* mode, which is an overtone of the D band [33]. By inspecting the spectra before and after polymer coating, it was found that both the intensity and spectral position of D band and G band have changed. In the presence of both PEI and SPS, the D band is slightly shifted to higher wave numbers, approximately $2\text{--}4 \text{ cm}^{-1}$, and the position of the G band is shifted $3\text{--}6 \text{ cm}^{-1}$ higher. The intensity and sharpness of the D band and G band increase; in addition, the ratio of the intensity of D band to that of the G-band slightly increases from 0.21 for xGnP to 0.23 for both PEI and SPS coated xGnP. Although the change in Raman spectra is not significant, it clearly indicates a typical noncovalent modification of the graphene sheet [32]. The upshift of the D and G band is possibly due to the hydrophobic and van der Waals forces between the polymer and the graphite sheet, which increase the energy necessary for vibrations to occur. And the slight increase in disorder structure after polymer coating is possibly due to the remaining carbon atoms from the polymer coating [32] and the field disturbance and physical strain in the graphene sheet caused by the interactions with the polymers. It was also noticed that the peak shift and intensity increase in Raman spectrum for SPS coated xGnP is more significant

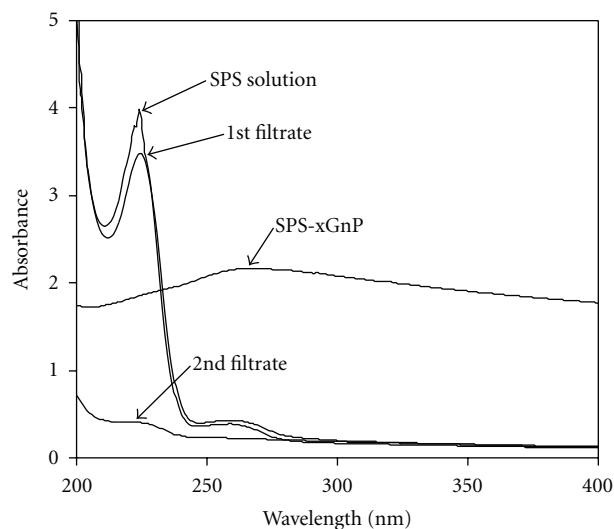


FIGURE 7: The UV-Vis spectra of SPS, SPS-xGnP and the filtrates obtained during the filtration process.

than those for PEI coated xGnP, which implies that SPS has a stronger interaction force with the graphene surface than PEI. This is possibly due to the molecular similarity of SPS to the graphene structure. At a high solution pH, where PEI is unprotonated, hydrophobic or Van der Waals forces could be the main driving force. During adsorption, PEI chains can be arranged on the hydrophobic basal plane in an extended conformation [35]. Although single molecules were found on the graphite surface, it is more possible for agglomerations form due to the lack of repulsive force between the molecules [30].

Most work reported so far regarding the self-assembly of carbon nanotubes using polymer noncovalent bonding involving the simple dispersion of carbon nanotubes in polyelectrolyte solution by sonication with no further purification [36, 37]. In this work, we found that the excess polyelectrolyte in the xGnP suspension plays a significant role in the self-assembly process. LbL assembly typically involves diffusion and adsorption processes, in which size matters. With the excess free polyelectrolytes, the surface coverage of xGnP on the glass slide was low. Therefore, it is necessary to remove the excess PEs that was not attached to xGnP. The stability of the adsorbed PE chains on graphite during filtration, the subsequent rinsing with water and redispersion utilizing sonication were examined with UV-vis spectroscopy and XPS. As shown in Figure 7, the spectrum of SPS shows a typical absorption peak at 222 nm, and the peak height of 1st filtrate after coating with xGnP decreased, indicating some SPS is deposited on xGnP. The SPS coated xGnP was rinsed with DI water for three times, and then redispersed in DI water by mild sonication. The second filtrate shows a very small peak at 222 nm, which could result from the incomplete wash or dissociation of polymer due to sonication. Surprisingly, there is no SPS peak showing in the spectrum of SPS-xGnP, which is possible due to the extremely low concentration

of xGnP in the sample. XPS was further used to confirm that SPS remains on the xGnP after the washing and sonication process. As shown in Table 2, the S2p atom content for SPS-xGnP after redispersing with sonication is close to the one before, indicating there is no loss of SPS from xGnP during washing and redispersion. The same result is observed for PEI-xGnP, indicated by the N1s content.

LbL self-assembly is a versatile technique to produce robust films with precise control on the film thickness and properties. With their one dimensional nanometer size, electrostatically charged PE coated surface, and their ability to form a stable colloidal dispersion, the PE modified graphite nanoplatelets are ideal candidates for multilayer self-assembly. SPS coated xGnP combined with PDAC was used to demonstrate the LbL assembly process. Optical microscopy images (not shown) of a single bilayer of PDAC/SPS coated xGnP show that the surface coverage of xGnP is low, possibly due to the large particle size, limiting the diffusion and repulsive electrostatic forces. With further multilayer growth, more graphite particles fill into the gaps or stack on the existing particles. At 10 bilayers, the surface became visibly black. Figures 8 and 9 show the SEM images of 4 and 10 xGnP bilayers, respectively. At low magnification, Figure 8(a) shows most agglomerates of graphite particle, and they seem isolated. At high magnification (Figures 8(b) and 8(c)), it is clear that these graphite agglomerates are bridged with graphene platelets with nanometer thicknesses. The edges of agglomerates and nanoplatelets are curled or folded which disrupts the packing of xGnP. Figure 9 shows a relatively dense packing of xGnP at 10 bilayers, but with the varying size and shape of the platelets, the surface of multilayer film is very rough.

The AFM image in Figure 10 shows a clear layered structure of graphene sheets, and all the nanoplatelets are stacking together and relatively close to one another. The roughness analysis of the AFM image shows a very rough surface of the multilayer film, and the section analysis shows that the thickness of 10 bilayers is in the range of 400 to 800 nm, which is much thicker than the theoretical value of 10 bilayers. xGnP/polyelectrolytes multilayers can also be fabricated with PEI-xGnP and SPS as the counter ion. It was found the surface coverage of xGnP was much lower than SPS-xGnP/PDAC multilayers (images not shown), which is possible due to the lower surface charge of PEI-xGnP, limiting their ability to be adsorbed on the surface.

One possible application of xGnP thin film is as an inexpensive conductive coating. Thus, the resistance and transmittance of xGnP multilayers were measured. Figure 11 shows the resistance of the glass slides coated with PDAC/SPS coated xGnP multilayer. The $\log(\text{resistance})$ at 1 Hz for the glass slide is 11.13, which is nonconductive. Glass slides coated with PDAC/SPS coated xGnP are non conductive until 4 bilayers, indicating that a percolation threshold is reached. This result is consistent with the OM and SEM observation. The resistance of the films continually decreases with more multilayers deposited on the surface. The $\log(\text{resistance})$ at 1 Hz reaches 4.85 for 10 PDAC/SPS-xGnP bilayer film. Recently, transparent conductive carbon

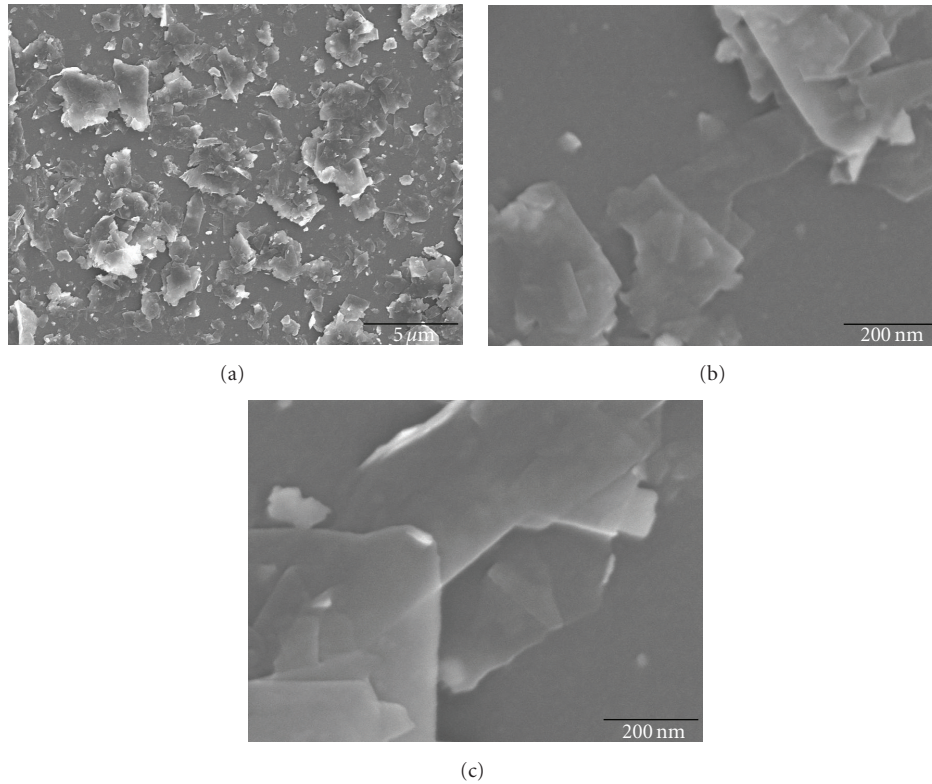


FIGURE 8: SEM images of 4 bilayers of PDAC/SPS-xGnP (a) low magnification (scale bar: $5\ \mu\text{m}$), (b) and (c) high magnification (scale bar: 200 nm).

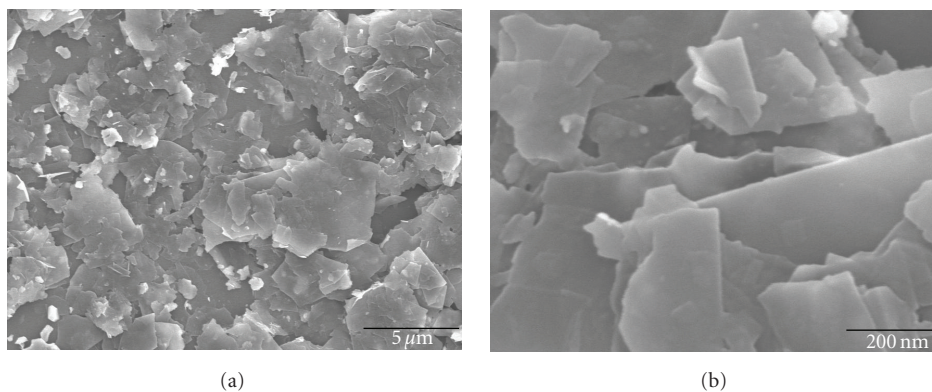


FIGURE 9: SEM images of 10 bilayers of PDAC/SPS-xGnP (a) low magnification (scale bar: $5\ \mu\text{m}$), and (b) high magnification (scale bar: 200 nm).

nanotube films have attracted much attention due to their possible application in modern technology, such as video displays, solar cells, lasers, optical communication devices, and solid state lighting [36, 38–40]. We are pursuing the replacement of carbon nanotubes with inexpensive xGnP in these applications. Figure 12 shows the transmittance of xGnP multilayers which were measured by the UV-vis spectrometer at 500 nm wavelength. Unfortunately, the increase in the conductivity of the film is accompanied with a dramatic decrease in the transmittance of the glass slides. The transmittance of the glass slide coated on both sides

is 11.89% when the surface is conductive (4 bilayers), and the transmittance decreases to 2.74% at 10 bilayers. The loss of transmittance suffers from the way that graphite deposited on the surface; curled and turned-in edges of the sheets, and the agglomeration of nanoplatelets cause the high thickness of the layers. Further work is being conducted to increase the conductivity and transmittance of xGnP containing films using different preparation techniques, such as Langmuir-Blodgett methods and filtration methods. Patterned conductive multilayered xGnP composite film was also developed for applications in electronic devices [41].

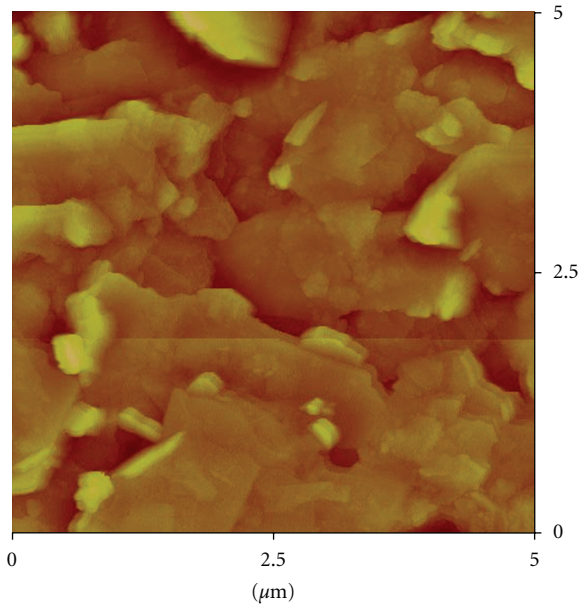


FIGURE 10: Height AFM image of 10 bilayers of PDAC/SPS-xGnP (color scale: black to bright yellow, 1200 nm).

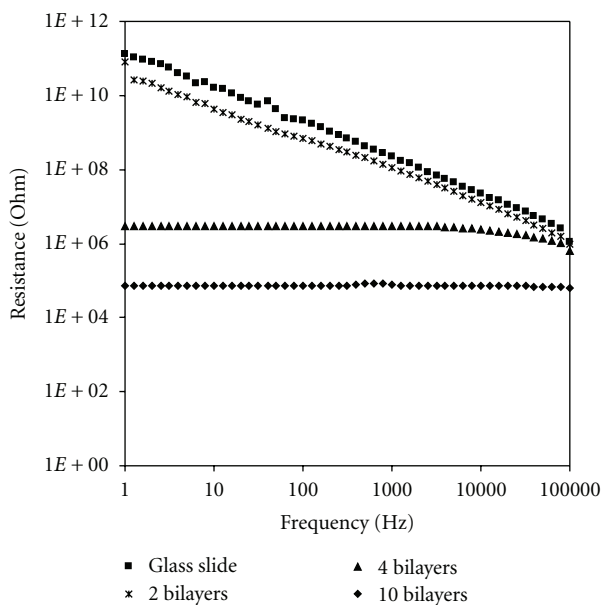


FIGURE 11: Resistance measurement of glass slide and xGnP multilayers.

4. Conclusions

In summary, we have achieved the stable aqueous suspension of graphite nanoplatelets, which are an inexpensive nanomaterial, by the noncovalent functionalization with polyelectrolytes. A variety of surfactants and polyelectrolytes have been compared for their ability to suspend graphite nanoplatelets. This noncovalent method is better for preserving the mechanical and electrical properties of graphite platelets compared to the traditional oxidation methods.

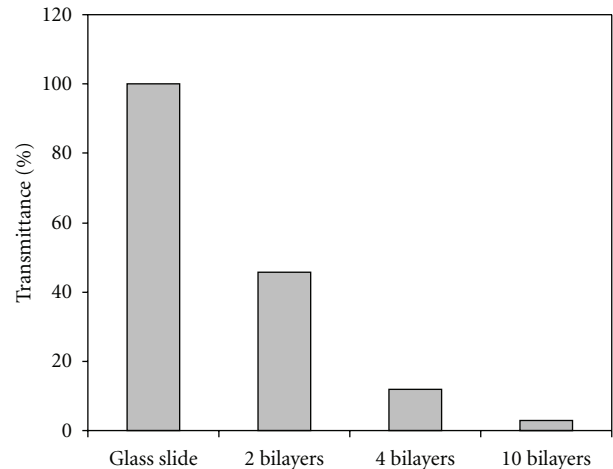


FIGURE 12: Transmittance of glass slides coated on both sides with various bilayers of PDAC/SPS-xGnP.

This robust method opens up the possibility of using these inexpensive nanomaterials in many applications, including electrochemical devices, and provides the way to processing techniques such as LbL deposition. We have demonstrated that conductive coating can be achieved by LbL assembly of polyelectrolyte-functionalized graphite nanoplatelets. Multilayer PDAC/SPS-xGnP film deposition reached the percolation threshold in only 4 cycles, resulting in a conductive thin film. The resistance of the film was lowered with more deposition cycles. However, the average roughness of these multilayer films was high, and the thickness of films was higher than theoretically estimated. This occurred because the edges of graphite nanoplatelets fold which affects the dense packing of the nanoplatelets; in addition, the nanoplatelets tend to overlap with each other. This also attributes to the low surface resistance and transmittance of xGnP films. Further work is on going to increase the film conductivity and transmittance using different processing methods, such as Langmuir-Blodgett and filtration.

Acknowledgment

The funding from the National Science Foundation (CBET-0609164, CMMI-0832730), the University Research Corridor, the Michigan Economic Development Corporation, and the MSU Foundation to support this research is greatly appreciated.

References

- [1] P. T. Hammond, "Form and function in multilayer assembly: new applications at the nanoscale," *Advanced Materials*, vol. 16, no. 15, pp. 1271–1293, 2004.
- [2] K. Ishibashi, S. Moriyama, D. Tsuya, T. Fuse, and M. Suzuki, "Quantum-dot nanodevices with carbon nanotubes," *Journal of Vacuum Science and Technology A*, vol. 24, no. 4, pp. 1349–1355, 2006.
- [3] M. Lee, J. Im, B. Y. Lee et al., "Linker-free directed assembly of high-performance integrated devices based on nanotubes and

- nanowires,” *Nature Nanotechnology*, vol. 1, no. 1, pp. 66–71, 2006.
- [4] K. Lee, J. Zhang, H. Wang, and D. P. Wilkinson, “Progress in the synthesis of carbon nanotube- and nanofiber-supported Pt electrocatalysts for PEM fuel cell catalysis,” *Journal of Applied Electrochemistry*, vol. 36, no. 5, pp. 507–522, 2006.
 - [5] C. Lynam, S. E. Moulton, and G. G. Wallace, “Carbon-nanotube biofibers,” *Advanced Materials*, vol. 19, no. 9, pp. 1244–1248, 2007.
 - [6] Y. Lin, W. Yantasee, and J. Wang, “Carbon nanotubes (CNTs) for the development of electrochemical biosensors,” *Frontiers in Bioscience*, vol. 10, pp. 492–505, 2005.
 - [7] C. M. Welch and R. G. Compton, “The use of nanoparticles in electroanalysis: a review,” *Analytical and Bioanalytical Chemistry*, vol. 384, no. 3, pp. 601–619, 2006.
 - [8] A. C. Ferrari, J. C. Meyer, V. Scardaci et al., “Raman spectrum of graphene and graphene layers,” *Physical Review Letters*, vol. 97, no. 18, Article ID 187401, 4 pages, 2006.
 - [9] A. K. Geim and K. S. Novoselov, “The rise of graphene,” *Nature Materials*, vol. 6, no. 3, pp. 183–191, 2007.
 - [10] X. Li, W. Cai, J. An et al., “Large-area synthesis of high-quality and uniform graphene films on copper foils,” *Science*, vol. 324, no. 5932, pp. 1312–1314, 2009.
 - [11] D. D. L. Chung, “Exfoliation of graphite,” *Journal of Materials Science*, vol. 22, no. 12, pp. 4190–4198, 1987.
 - [12] W.-X. Chen, J. Y. Lee, and Z. Liu, “Preparation of Pt and PtRu nanoparticles supported on carbon nanotubes by microwave-assisted heating polyol process,” *Materials Letters*, vol. 58, no. 25, pp. 3166–3169, 2004.
 - [13] H. Fukushima, “Graphite nanoreinforcements in polymer nanocomposites,” in *PhD Dissertation in Department of Chemical Engineering and Materials Science*, Michigan State University, East Lansing, Mich, USA, 2003.
 - [14] S. Stankovich, D. A. Dikin, G. H. B. Dommett et al., “Graphene-based composite materials,” *Nature*, vol. 442, no. 7100, pp. 282–286, 2006.
 - [15] I.-H. Do, “Metal decoration of exfoliated graphite nanoplatelets (xGnP) for fuel cell applications,” in *PhD Dissertation in Department of Chemical Engineering and Materials Science*, Michigan State University, East Lansing, Mich, USA, 2006.
 - [16] J. Lu, I. Do, L. T. Drzal, R. M. Worden, and I. Lee, “Nanometal-decorated exfoliated graphite nanoplatelet based glucose biosensors with high sensitivity and fast response,” *ACS Nano*, vol. 2, no. 9, pp. 1825–1832, 2008.
 - [17] J. Lu, L. T. Drzal, R. M. Worden, and I. Lee, “Simple fabrication of a highly sensitive glucose biosensor using enzymes immobilized in exfoliated graphite nanoplatelets Nafion membrane,” *Chemistry of Materials*, vol. 19, no. 25, pp. 6240–6246, 2007.
 - [18] W. Zhao, C. Song, and P. E. Pehrsson, “Water-soluble and optically pH-sensitive single-walled carbon nanotubes from surface modification,” *Journal of the American Chemical Society*, vol. 124, no. 42, pp. 12418–12419, 2002.
 - [19] E. T. Mickelson, I. W. Chiang, J. L. Zimmerman et al., “Solvation of fluorinated single-wall carbon nanotubes in alcohol solvents,” *Journal of Physical Chemistry B*, vol. 103, no. 21, pp. 4318–4322, 1999.
 - [20] V. C. Moore, M. S. Strano, E. H. Haroz et al., “Individually suspended single-walled carbon nanotubes in various surfactants,” *Nano Letters*, vol. 3, no. 10, pp. 1379–1382, 2003.
 - [21] G. Decher, “Fuzzy nanoassemblies: toward layered polymeric multicomposites,” *Science*, vol. 277, no. 5330, pp. 1232–1237, 1997.
 - [22] X. Wang, H.-X. Huang, A.-R. Liu et al., “Layer-by-layer assembly of single-walled carbon nanotube-poly(viologen) derivative multilayers and their electrochemical properties,” *Carbon*, vol. 44, no. 11, pp. 2115–2121, 2006.
 - [23] T. Cassagneau and J. H. Fendler, “High density rechargeable lithium-ion batteries self-assembled from graphite oxide nanoplatelets and polyelectrolytes,” *Advanced Materials*, vol. 10, no. 11, pp. 877–881, 1998.
 - [24] T. Cassagneau, F. Guérin, and J. H. Fendler, “Preparation and characterization of ultrathin films layer-by-layer self-assembled from graphite oxide nanoplatelets and polymers,” *Langmuir*, vol. 16, no. 18, pp. 7318–7324, 2000.
 - [25] N. A. Kotov, I. Dékány, and J. H. Fendler, “Ultrathin graphite oxide-polyelectrolyte composites prepared by self-assembly: transition between conductive and non-conductive states,” *Advanced Materials*, vol. 8, no. 8, pp. 637–641, 1996.
 - [26] N. I. Kovtyukhova, P. J. Ollivier, B. R. Martin, et al., “Layer-by-layer assembly of ultrathin composite films from micron-sized graphite oxide sheets and polycations,” *Chemistry of Materials*, vol. 11, no. 3, pp. 771–778, 1999.
 - [27] L. T. Drzal and H. Fukushima, “Expanded graphite and products produced therefrom,” 2004, US Patent application 20040127621.
 - [28] W. N. Reynolds, *Physical Properties of Graphite*, Elsevier, Amsterdam, The Netherlands, 1968.
 - [29] S. Stankovich, R. D. Piner, X. Chen, N. Wu, S. T. Nguyen, and R. S. Ruoff, “Stable aqueous dispersions of graphitic nanoplatelets via the reduction of exfoliated graphite oxide in the presence of poly(sodium 4-styrenesulfonate),” *Journal of Materials Chemistry*, vol. 16, no. 2, pp. 155–158, 2006.
 - [30] M. Schneider, M. Brinkmann, and H. Möhwald, “Adsorption of polyethylenimine on graphite: an atomic force microscopy study,” *Macromolecules*, vol. 36, no. 25, pp. 9510–9518, 2003.
 - [31] V. K. Paruchuri, A. V. Nguyen, and J. D. Miller, “Zeta-potentials of self-assembled surface micelles of ionic surfactants adsorbed at hydrophobic graphite surfaces,” *Colloids and Surfaces A*, vol. 250, no. 1–3, pp. 519–526, 2004.
 - [32] V. A. Sinani, M. K. Gheith, A. A. Yaroslavov et al., “Aqueous dispersions of single-wall and multiwall carbon nanotubes with designed amphiphilic polycations,” *Journal of the American Chemical Society*, vol. 127, no. 10, pp. 3463–3472, 2005.
 - [33] S. Reich and C. Thomsen, “Raman spectroscopy of graphite,” *Philosophical Transactions of the Royal Society A*, vol. 362, no. 1824, pp. 2271–2288, 2004.
 - [34] F. Tuinstra and J. L. Koenig, “Raman spectrum of graphite,” *Journal of Chemical Physics*, vol. 53, no. 3, pp. 1126–1130, 1970.
 - [35] J. Park and P. T. Hammond, “Polyelectrolyte multilayer formation on neutral hydrophobic surfaces,” *Macromolecules*, vol. 38, no. 25, pp. 10542–10550, 2005.
 - [36] M. Palumbo, K. U. Lee, B. T. Ahn et al., “Electrical investigations of layer-by-layer films of carbon nanotubes,” *Journal of Physics D*, vol. 39, no. 14, pp. 3077–3085, 2006.
 - [37] H. Paloniemi, M. Lukkarinen, T. Ääritalo et al., “Layer-by-layer electrostatic self-assembly of single-wall carbon nanotube polyelectrolytes,” *Langmuir*, vol. 22, no. 1, pp. 74–83, 2006.
 - [38] T. M. Barnes, X. Wu, J. Zhou et al., “Single-wall carbon nanotube networks as a transparent back contact in CdTe solar cells,” *Applied Physics Letters*, vol. 90, no. 24, Article ID 243503, 3 pages, 2007.

- [39] A. Schindler, J. Brill, N. Fruehauf, J. P. Novak, and Z. Yan IV, "Solution-deposited carbon nanotube layers for flexible display applications," *Physica E: Low-Dimensional Systems and Nanostructures*, vol. 37, no. 1-2, pp. 119–123, 2007.
- [40] Z. Wu, Z. Chen, X. Du et al., "Transparent, conductive carbon nanotube films," *Science*, vol. 305, no. 5688, pp. 1273–1276, 2004.
- [41] T. R. Hendricks, J. Lu, L. T. Drzal, and I. Lee, "Intact pattern transfer of conductive exfoliated graphite nanoplatelet composite films to polyelectrolyte multilayer platforms," *Advanced Materials*, vol. 20, no. 10, pp. 2008–2012, 2008.

Review Article

Chemical Functionalization of Graphene Nanoribbons

Narjes Gorjizadeh and Yoshiyuki Kawazoe

Institute for Materials Research, Tohoku University, Sendai 980-8577, Japan

Correspondence should be addressed to Narjes Gorjizadeh, narjes@imr.edu

Received 31 May 2010; Accepted 28 June 2010

Academic Editor: Rakesh Joshi

Copyright © 2010 N. Gorjizadeh and Y. Kawazoe. This is an open access article distributed under the Creative Commons Attribution License, which permits unrestricted use, distribution, and reproduction in any medium, provided the original work is properly cited.

We review the electronic properties of graphene nanoribbons functionalized by various elements and functional groups. Graphene nanoribbons are strips of graphene, the honeycomb lattice of carbon with sp^2 hybridization. Basically nanoribbons can be classified into two categories, according to the geometry of their edge, armchair, and zigzag, which determine their electronic structure. Due to their fascinating electronic and magnetic properties many applications has been suggested for these materials. One of the major methods to use graphene nanoribbons in future applications is chemical functionalization of these materials to make an engineering on their band gap. In this review, we introduce various types of modifying graphene nanoribbons to meet their promising applications.

1. Introduction

After discovery of graphene [1], it has been considered as basic material for the future nanoelectronic devices. Its unique properties, such as massless Dirac fermion behavior [2–4], half-integer quantum Hall effect [2, 5], and high-carrier mobility [2] make it a promising candidate for application in nanoelectronics and spintronics devices [2, 5–9]. Graphene nanoribbons can be constructed as strips of graphene, with quasi1D structures. So far, Nanoribbons with widths up to 2 nm have been fabricated experimentally [10–12]. Geometrically, two main types of nanoribbons with two edge shapes can be cut from a hexagonal lattice of graphene: zigzag edge and armchair edge [13–16]. Different types of ribbons are specified by their edge geometry and width. The width is labeled by an integer which counts the number of carbon chains between the two edges. Figure 1 shows the two types of ribbons with their width indices. The two ribbon characteristics, that is, edge geometry and width, are the key parameters which determine the electronic properties of the ribbons [7, 17–19].

The earliest theoretical studies of graphene nanoribbons, using a simple tight-binding method, predicted that 1/3 of the armchair nanoribbons, whose width index N satisfies $N = 3M - 1$ (M is an integer), are metallic [17], and another

2/3 are semiconductor with band gaps depending on their width, while all zigzag nanoribbons are metallic, a similar behavior as carbon nanotubes (CNTs). A characteristic peak in the density of states (DOS) of zigzag nanoribbons near and slightly below Fermi energy is also predicted [16, 20]. But recently the first principle studies based on spin polarized density functional theory (DFT) revealed that all graphene nanoribbons are semiconductors at their ground state with band gaps which depend on their width and edge geometry, closing at infinite width, that is, infinite graphene [7, 21]. Meanwhile zigzag nanoribbons have localized edge states which are ferromagnetically ordered, but with opposite spin orientation at the two edges which makes them antiferromagnetically coupled. The magnetism in zigzag nanoribbon, a pure carbon system, which arises from π -orbitals of carbon localized at the edge is specially notable [22]. These properties, along with the ballistic electronic transport, and quantum Hall effect [2, 5], cause graphene nanoribbons to be promising candidates for building blocks of future nanoelectronic and spintronic devices [1, 2, 5–7, 23–30] and also chemical sensors [31–33] and electrochemical switches [34].

In order to achieve their potential for these applications it is essential to have a better understanding of the electronic structure of graphene nanoribbons and have ability

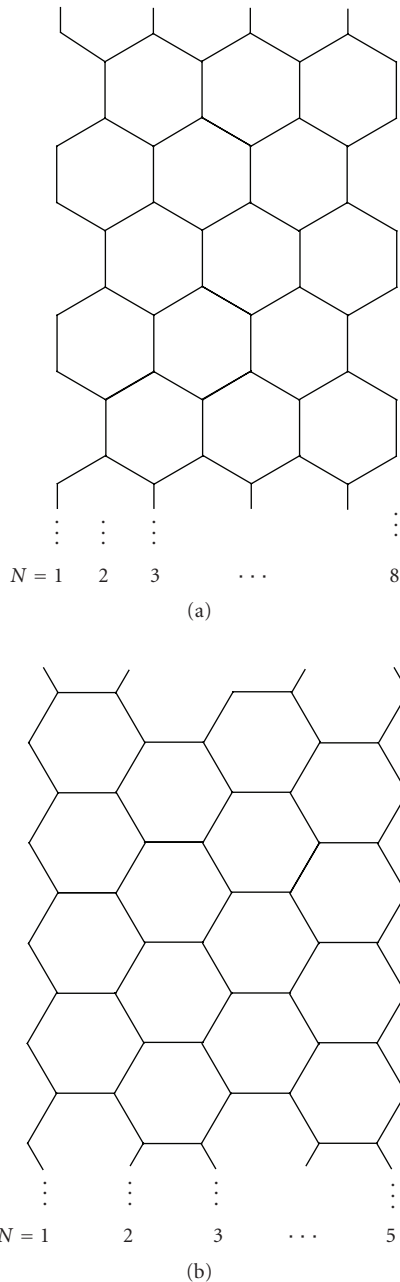


FIGURE 1: Graphene nanoribbons with armchair (a) and zigzag (b) edges. In each case, index N denotes the width of the ribbon, and ribbon axis is the vertical direction.

to control them. Modification of electronic structure of nanoribbons by chemical functionalization is an effective way to make them efficient for their applications [35–39].

Moreover, various junctions can be constructed by connecting nanoribbons of different widths and types with perfect atomic interface, and electronic device can be integrated on them by selective chemical functionalization on a single nanoribbon sheet [38, 40]. Yan et al. [41] illustrated that nanoribbon-based devices can be made with the atomic-perfect-interface junctions and with controlled doping through edge termination.

So far many theoretical studies have been done to functionalize graphene nanoribbons to manipulate their electronic properties. Here we review different ways of chemical functionalization of nanoribbons and their properties.

2. Functionalization of Graphene Nanoribbons

Electronic structure of graphene nanoribbons can be modified by several types of functionalization, such as functionalization by s -type, p -type, and d -type elements [38, 42–44], or by functional groups. Modification of the edge of the ribbon, or substitution of one or more carbons of the ribbon or adsorption of one atom or a functional group are different options of functionalization which have been all investigated theoretically and some of them has been observed experimentally.

2.1. Edge Modification. Nanoribbons intrinsically have dangling bonds at the edges whose linear combinations form some of the eigenstates near the Fermi energy, and hence determine the ribbon properties. These dangling bonds also provide active sites for chemical bonding, making the ribbons suitable for chemical modification. Since the unique properties of the ribbons are associated with their edge states, edge modification can significantly affect and control electronic and magnetic properties of the ribbons [37, 45, 46]. By functionalization of the edges with various atoms, from s -type to d -type transition metals, and by functional groups, we can obtain various electronic properties. In fact, the same ribbon can become semiconductors with wide range of band gaps, metallic, ferromagnetic (FM) and anti-ferromagnetic (AF) or half-metallic by appropriate chemical functionalization. Experimentally, the edge dangling bonds of the graphene sheets and ribbons can be saturated by hydrogen through specific hydrogenation procedures.

The first step in modification of nanoribbon is to saturate one of the edges by an element or functional group while the other edge is saturated by H. It was demonstrated by theoretical calculations that different functional groups at the edge of nanoribbons can significantly affect their electronic structure close to Fermi level [37]. Decoration of one edge of zigzag nanoribbons by two H atoms while the other has one H turns the antiferromagnetic nanoribbon into ferromagnetic [47]. Single-edge functionalization of zigzag ribbons leads to half-semiconductors with different band gaps for each spin and can also result in a spin-polarized half-semiconductor or in a semiconductor-metal transition [48]. Modification of one or both edges of zigzag nanoribbon with functional groups $-O$, $-F$, $-OH$, $-NH_2$, $-CH$, $-BH$, and $-B$ was also investigated [35, 37, 39, 45]. Figure 2 depicts schematic picture of a zigzag nanoribbon with three types of edge saturation.

In zigzag nanoribbons the atoms of one edge are ferromagnetically ordered, but the two edges are antiferromagnetically coupled, and the band structure of the two spin channels are degenerate. Applying an electric field across a zigzag ribbon results in lifting the spin degeneracy by reducing the band gap for one spin channel while widening

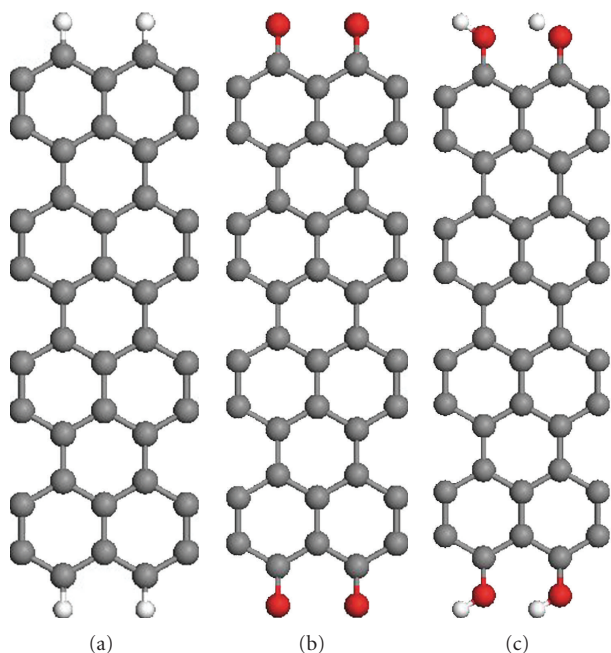


FIGURE 2: Zigzag nanoribbon with edge saturation by (a) H (b) O and (c) OH. Gray atoms are C, white atoms are H and red atoms are O.

the gap of the other spin channel [6, 7], which makes the ribbon half-metallic [49]. In half-metals one spin channel has metallic behavior, while the other one has energy band gap. This phenomena provides a spin selective behavior for nanoribbons which is a promise for spintronics applications. It was theoretically predicted that in these nanoribbons edge oxidation can have significant effect in designing efficient and robust spintronic devices based on nanoribbons [45]. Nanoribbons with fully oxidized edges turn half-metallic at low-electric field (0.2 V/\AA), while for fully or partially hydrogenated ribbons the field intensity needed to switch the system to half metallic regime is (0.4 V/\AA) [45].

Besides electric field, the degeneracy of spin channels can be broken by chemical modifications also. Modifying one edge of the nanoribbon with electron donating groups and the other edge with electron accepting groups is a sufficient way to generate large potential difference between the two edges [44]. This way the corresponding potential shift of band structure of spin up and spin down are different and the system may become half metallic. Kan et al. [44] have shown that replacing the terminating H atoms of one edge of zigzag ribbon by NO_2 groups and the other edge with CH_3 groups turns the ribbon into half-metal. Wu et al. [42] also suggested that half-metallicity can be realized in zigzag nanoribbons while one edge is modified with OH and the other edge is decorated with NO_2 or SO_2 .

Chemical modification of armchair nanoribbons is also effective to engineer their band gaps. Saturation of the edge of armchair nanoribbons by B attachment as a bridge between edge carbon atoms in the planar direction (Figure 3(b)) results in metallic behavior of the system, while N attached at the same geometry widens the gap

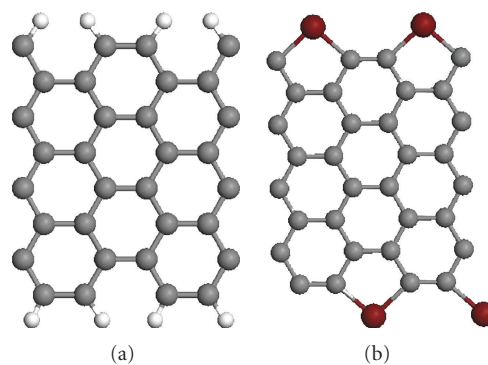


FIGURE 3: Armchair nanoribbon with edge saturation by (a) H and (b) B.

of the ribbon [38]. However, substitution of both edges by B or N keeps the ribbon substantially unchanged [48], while full half-metallicity can be achieved by substitution of one edge carbon by B atoms and the other edge by N atoms [50]. Decorating the edge of armchair nanoribbons, which are nonmagnetic semiconductors, in the position of Figure 3(b) by transition metals provides ferromagnetic or antiferromagnetic states depending on the type of the decorated atom [38]. However, edge functionalization of armchair ribbon by functional group NH_2 does not alter the electronic properties of the nanoribbon since the impurity states are located far away from the Fermi level [48].

2.2. Substitution. Substitution of one or more carbons of the nanoribbon by introducing impurities to the system is another effective way to control the electronic properties of the nanoribbons. Intrinsically B and N impurities play the role of p-type and n-type doping in carbon-based materials. But in nanoribbons the doping process is extremely sensitive to the dopant position and density, type and width of the ribbon [40, 51, 52]. If B(N) substitution occurs in the center of the armchair ribbons, the defect states appear close to the bottom (top) of the conduction (valance) band of the pristine ribbon, but the Fermi energy is shifted in the conduction (valance) band, resulting in a semiconductor-metal transition, rather than doping [48]. However by B and N substitution at the ribbon edges, the impurity levels are always very far from the Fermi energy and the electronic properties of the ribbon are substantially unchanged [48], while substitution of edge atoms in zigzag nanoribbons induce semiconductor-metal transition for high impurity densities, but do not give impurity levels close to the top or bottom of the gap [48].

Zheng et al. [50] have shown that zigzag nanoribbons can be either semiconducting, half metallic, or metallic by controlling the distance of the N or B impurity atoms to the edge. In these ribbons half metallicity can be achieved by substitution of one edge carbon with B atoms and the other edge with N atoms [50]. Half-metallicity can be also achieved by replacing middle zigzag chains of a zigzag nanoribbon by B-N chains (Figure 4) [53]. Replacing periodically the

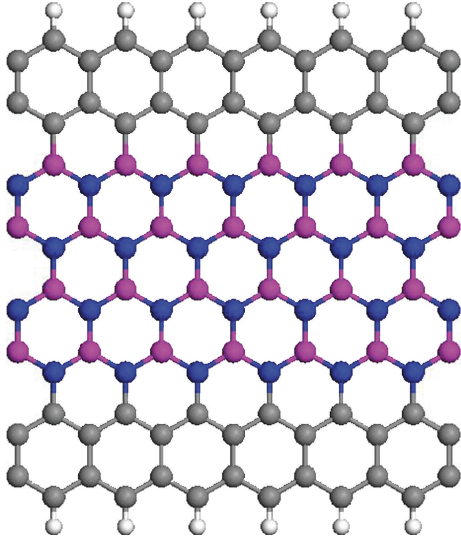


FIGURE 4: Hydrogen saturated zigzag nanoribbon. The middle zigzag chains of carbon are substituted by B–N chains.

armchair chains across the zigzag nanoribbon by B–N chain will also result in half metallicity [54].

2.3. Adsorption. Substitution of N and B has been shown to have significant effect on the electronic structure of nanoribbons. However controlling the doping site and density is a key factor in achieving the desired properties. Adsorption of additional atoms or functional groups is another effective way to modify the electronic structure of nanoribbons. Yu et al. [55] have shown that the properties of armchair nanoribbons can be strongly modified by adsorption of N atoms at the edge. First principle calculations of B, C, and N adsorbed atoms on zigzag nanoribbons have also revealed that these adatoms convert the antiferromagnetic ribbon into ferromagnetic with high magnetic moment [46]. These adatoms prefer the sites near the edge of the ribbon. On the other hand, NO_2 and NH_2 which act as strong acceptors and donors on graphene surface can modify the electronic structure of zigzag nanoribbons in the gap vicinity when adsorbed at the edge, but do not act as a dopant [48].

However, adsorption of transition metals on armchair nanoribbons turns the nonmagnetic ribbon into a magnetic metal [56]. Depending on the width of the ribbon and type of adsorbed transition metals, armchair nanoribbon can either become a metal or a semiconductor with ferromagnetic or antiferromagnetic spin alignment. Fe or Ti adsorption makes certain armchair nanoribbons half-metallic [56]. Adsorption of Ni atom on zigzag nanoribbons was also investigated [57]. The most stable position of the adsorbed Ni is at the edge site, which reduces the magnetic moments of both Ni atom and the edge C due to hybridization of d orbitals of Ni with p orbitals of C [57]. First principle studies of adsorption of Ni_n and Fe_n clusters ($n = 1-4$) on zigzag nanoribbons shows that clusters also prefer the edge sites, and the system is more stable in antiferromagnetic coupling of the zigzag edges [57].

Zigzag nanoribbons can also become half-metallic by deposition of the ferroelectric material polyvinylidene fluoride (PVDF) on them [43]. PVDFs generate the electrostatic potential on the nanoribbon because of their strong dipole moments. The dipole direction of PVDFs is changeable by an external electric field, and switching between half-metallic and insulating states in nanoribbon may be achieved [43].

The possibility of chemical doping and related chemical sensor properties of graphene have been demonstrated experimentally. NO_2 molecule is found to be a strong acceptor in experimental observations [32].

3. Conductance

Understanding the effect of chemical functionalization and edge topology on charge transport in graphene junctions is an important issue. So far various theoretical studies of the influence of edge geometry and chemical modifications on the transport properties of nanoribbons have been reported [48]. Simulations of electronic transport of realistic edge disordered armchair nanoribbons predicts that transport properties strongly depend on the geometry of the reconstructed edge profile and local defect chemical reactivity [58].

Quantum transport calculations of B doped armchair nanoribbons by substitution of carbons with B by various doping rates indicates that depending on the energy of the charge carrier, the transport can vary from quasiballistic to a strongly localized regime, as a result of strong electron-hole asymmetry induced by chemical doping [34]. The occurrence of quasibound states related to B impurities results in mobility gaps as large as 1 eV, due to strong electron-hole asymmetrical backscattering phenomena, which opens new ways to overcome current limitations of graphene-based devices through the fabrication of chemically doped graphene nanoribbons [34].

Martins et al. [59] also show that substitutional B atoms at the ribbon edge acts as scattering centers for the electronic transport along the ribbon which breaks the symmetry of spin-up and spin-down channels. Transport of one of the spin channels is reduced more strongly, which gives rise to spin-polarized transport by suitable doping [59].

First principle calculations show that presence of B and N impurities in armchair nanoribbons results in resonant backscattering, whose features are strongly dependent on the symmetry and the width of nanoribbon, as well as the position and dopants [51]. Energies of the quasibound states are strongly dependent on the position of the impurity with respect to the edges. When B is placed at the exact center of the ribbon the transmission at the first plateau is insensitive to the presence of the impurity, while B impurity at the edge reduces the conductance due to the quasibound states induced by the impurity [51].

Ab-initio calculations of conductance in armchair nanoribbons with joint attachment of OH/H and phenyl groups on their surface also shows that transport properties depend on the adsorption sites [60]. If OH bond is located at the ribbon edge, conductance is not affected. The same result is obtained for NH_2 adsorption at the edge of armchair

ribbons [48]. But when the OH bond is shifted out of the edge, the conductance is typically disturbed, and a rapid decay in conductance is obtained by increasing the defect density [60]. Dependence of Conductance on the defect site and its distance from the edge was also reported by [61].

Conductance measurements of nanoribbons has been also experimentally afforded [62]. All these studies opens the way to manipulate graphene nanoribbon-based devices and development of new applications based on functionalized nanoribbons.

4. Summary and Perspectives

Graphene nanoribbon has a great potential to be used in the future electronic applications. Working on desirable properties by modifying nanoribbons by appropriate elements or functional groups helps us find the suitable form of graphene nanoribbon for each application. Modification with various types of elements and functional groups can give us a variety of properties, such as semiconducting with a wide range of band gap, metallic, ferromagnetic, antiferromagnetic, half-metallic, half-semiconducting, all obtained from the same nanoribbon. Modification of the edge or using an adsorbate or substitution of carbons of the nanoribbon with an appropriate host are different options to meet the desired property from the nanoribbon. Applicability of each option would be proven by experiments.

Acknowledgments

The authors would like to express their sincere thanks to the crew of the Center for Computational Materials Science, Institute for Materials Research, for their support of the Hitachi SR11000 (model K2) supercomputer system and also Global COE program of Tohoku University for financial support.

References

- [1] K. S. Novoselov, A. K. Geim, S. V. Morozov, et al., "Electric field in atomically thin carbon films," *Science*, vol. 306, no. 5696, pp. 666–669, 2004.
- [2] K. S. Novoselov, A. K. Geim, S. V. Morozov et al., "Two-dimensional gas of massless Dirac fermions in graphene," *Nature*, vol. 438, no. 7065, pp. 197–200, 2005.
- [3] M. I. Katsnelson, K. S. Novoselov, and A. K. Geim, "Chiral tunnelling and the Klein paradox in graphene," *Nature Physics*, vol. 2, no. 9, pp. 620–625, 2006.
- [4] A. K. Geim and K. S. Novoselov, "The rise of graphene," *Nature Materials*, vol. 6, no. 3, pp. 183–191, 2007.
- [5] Y. Zhang, Y.-W. Tan, H. L. Stormer, and P. Kim, "Experimental observation of the quantum Hall effect and Berry's phase in graphene," *Nature*, vol. 438, no. 7065, pp. 201–204, 2005.
- [6] Y.-W. Son, M. L. Cohen, and S. G. Louie, "Half-metallic graphene nanoribbons," *Nature*, vol. 444, no. 7117, pp. 347–349, 2006.
- [7] Y.-W. Son, M. L. Cohen, and S. G. Louie, "Energy gaps in graphene nanoribbons," *Physical Review Letters*, vol. 97, no. 21, Article ID 216803, 4 pages, 2006.
- [8] B. Obradovic, R. Kotlyar, F. Heinz, et al., "Analysis of graphene nanoribbons as a channel material for field-effect transistors," *Applied Physics Letters*, vol. 88, no. 14, Article ID 142102, 3 pages, 2006.
- [9] Z. Li, H. Qian, J. Wu, B.-L. Gu, and W. Duan, "Role of symmetry in the transport properties of graphene nanoribbons under bias," *Physical Review Letters*, vol. 100, no. 20, Article ID 206802, 4 pages, 2008.
- [10] M. C. Lemme, T. J. Echtermeyer, M. Baus, and H. Kurz, "A graphene field-effect device," *IEEE Electron Device Letters*, vol. 28, no. 4, pp. 282–284, 2007.
- [11] X. Li, X. Wang, L. Zhang, S. Lee, and H. Dai, "Chemically derived, ultrasmooth graphene nanoribbon semiconductors," *Science*, vol. 319, no. 5867, pp. 1229–1232, 2008.
- [12] P. Gallagher, K. Todd, and D. Goldhaber-Gordon, "Disorder-induced gap behavior in graphene nanoribbons," *Physical Review B*, vol. 81, no. 11, Article ID 115409, 8 pages, 2010.
- [13] Y. Niimi, T. Matsui, H. Kambara, K. Tagami, M. Tsukada, and H. Fukuyama, "Scanning tunneling microscopy and spectroscopy of the electronic local density of states of graphite surfaces near monoatomic step edges," *Physical Review B*, vol. 73, no. 8, Article ID 085421, 8 pages, 2006.
- [14] Y. Kobayashi, K.-I. Fukui, T. Enoki, K. Kusakabe, and Y. Kaburagi, "Observation of zigzag and armchair edges of graphite using scanning tunneling microscopy and spectroscopy," *Physical Review B*, vol. 71, no. 19, Article ID 193406, 4 pages, 2005.
- [15] F. Sols, F. Guinea, and A. H. C. Neto, "Coulomb blockade in graphene nanoribbons," *Physical Review Letters*, vol. 99, no. 16, Article ID 166803, 4 pages, 2007.
- [16] Y. Niimi, T. Matsui, H. Kambara, K. Tagami, M. Tsukada, and H. Fukuyama, "Scanning tunneling microscopy and spectroscopy studies of graphite edges," *Applied Surface Science*, vol. 241, no. 1–2, pp. 43–48, 2005.
- [17] M. Fujita, K. Wakabayashi, K. Nakada, and K. Kusakabe, "Peculiar localized state at zigzag graphite edge," *Journal of the Physical Society of Japan*, vol. 65, no. 7, pp. 1920–1923, 1996.
- [18] R. Saito, M. Fujita, G. Dresselhaus, and M. S. Dresselhaus, "Electronic structure of chiral graphene tubules," *Applied Physics Letters*, vol. 60, no. 18, pp. 2204–2206, 1992.
- [19] D. J. Klein, "Graphitic polymer strips with edge states," *Chemical Physics Letters*, vol. 217, no. 3, pp. 261–265, 1994.
- [20] K. Sasaki, S. Murakami, and R. Saito, "Stabilization mechanism of edge states in graphene," *Applied Physics Letters*, vol. 88, no. 11, Article ID 113110, 3 pages, 2006.
- [21] L. Pisani, J. A. Chan, B. Montanari, and N. M. Harrison, "Electronic structure and magnetic properties of graphitic ribbons," *Physical Review B*, vol. 75, no. 6, Article ID 064418, 9 pages, 2007.
- [22] K. Wakabayashi, M. Fujita, H. Ajiki, and M. Sigrist, "Electronic and magnetic properties of nanographite ribbons," *Physical Review B*, vol. 59, no. 12, pp. 8271–8282, 1999.
- [23] Y. Zhang, Z. Jiang, J. P. Small, et al., "Landau-level splitting in graphene in high magnetic fields," *Physical Review Letters*, vol. 96, no. 13, Article ID 136806, 4 pages, 2006.
- [24] O. Hod and G. E. Scuseria, "Electromechanical properties of suspended graphene nanoribbons," *Nano Letters*, vol. 9, no. 7, pp. 2619–2622, 2009.
- [25] X. Lü, Y. Zheng, H. Xin, and L. Jiang, "Spin polarized electron transport through a graphene nanojunction," *Applied Physics Letters*, vol. 96, no. 13, Article ID 132108, 3 pages, 2010.
- [26] L. Zhu, J. Wang, T. Zhang, et al., "Mechanically robust tri-wing graphene nanoribbons with tunable electronic and magnetic properties," *Nano Letters*, vol. 10, no. 2, pp. 494–498, 2010.

- [27] Y. Yang and R. Murali, "Impact of size effect on graphene nanoribbon transport," *IEEE Electron Device Letters*, vol. 31, no. 3, pp. 237–239, 2010.
- [28] T. Ozaki, K. Nishio, H. Weng, and H. Kino, "Dual spin filter effect in a zigzag graphene nanoribbon," *Physical Review B*, vol. 81, no. 7, Article ID 075422, 5 pages, 2010.
- [29] K. Pi, W. Han, K. M. McCreary, A. G. Swartz, Y. Li, and R. K. Kawakami, "Manipulation of spin transport in graphene by surface chemical doping," *Physical Review Letters*, vol. 104, no. 18, Article ID 187201, 4 pages, 2010.
- [30] O. V. Zazyev and M. I. Katsnelson, "Magnetic correlations at graphene edges: basis for novel spintronics devices," *Physical Review Letters*, vol. 100, no. 4, Article ID 047209, 4 pages, 2008.
- [31] F. Schedin, A. K. Geim, S. V. Morozov et al., "Detection of individual gas molecules adsorbed on graphene," *Nature Materials*, vol. 6, no. 9, pp. 652–655, 2007.
- [32] T. O. Wehling, K. S. Novoselov, S. V. Morozov et al., "Molecular doping of graphene," *Nano Letters*, vol. 8, no. 1, pp. 173–177, 2008.
- [33] S. Alwarappan, A. Erdem, C. Liu, and C.-Z. Li, "Probing the electrochemical properties of graphene nanosheets for biosensing applications," *Journal of Physical Chemistry C*, vol. 113, no. 20, pp. 8853–8857, 2009.
- [34] B. Biel, F. Triozon, X. Blase, and S. Roche, "Chemically induced mobility gaps in graphene nanoribbons: a route for upscaling device performances," *Nano Letters*, vol. 9, no. 7, pp. 2725–2729, 2009.
- [35] M. Maruyama, K. Kusakabe, S. Tsuneyuki, K. Akagi, Y. Yoshimoto, and J. Yamauchi, "Magnetic properties of nanographite with modified zigzag edges," *Journal of Physics and Chemistry of Solids*, vol. 65, no. 2-3, pp. 119–122, 2004.
- [36] M. Maruyama and K. Kusakabe, "Theoretical prediction of synthesis methods to create magnetic nanographite," *Journal of the Physical Society of Japan*, vol. 73, no. 3, pp. 656–663, 2004.
- [37] D. Gunlycke, J. Li, J. W. Mintmire, and C. T. White, "Altering low-bias transport in zigzag-edge graphene nanostrips with edge chemistry," *Applied Physics Letters*, vol. 91, no. 11, Article ID 112108, 3 pages, 2007.
- [38] N. Gorjizadeh, A. A. Farajian, K. Esfarjani, and Y. Kawazoe, "Spin and band-gap engineering in doped graphene nanoribbons," *Physical Review B*, vol. 78, no. 15, Article ID 155427, 6 pages, 2008.
- [39] M. H. Wu, Y. Pei, and X. C. Zeng, "Planar tetracoordinate carbon strips in edge decorated graphene nanoribbon," *Journal of the American Chemical Society*, vol. 132, no. 16, pp. 5554–5555, 2010.
- [40] B. Huang, Q. Yan, G. Zhou et al., "Making a field effect transistor on a single graphene nanoribbon by selective doping," *Applied Physics Letters*, vol. 91, no. 25, Article ID 253122, 3 pages, 2007.
- [41] Q. Yan, B. Huang, J. Yu, et al., "Intrinsic current-voltage characteristics of graphene nanoribbon transistors and effect of edge doping," *Nano Letters*, vol. 7, no. 6, pp. 1469–1473, 2007.
- [42] M. H. Wu, X. Wu, and X. C. Zeng, "Exploration of half metallicity in edge-modified graphene nanoribbons," *Journal of Physical Chemistry C*, vol. 114, no. 9, pp. 3937–3944, 2010.
- [43] Y.-L. Lee, S. Kim, C. Park, J. Ihm, and Y.-W. Son, "Controlling half-metallicity of graphene nanoribbons by using a ferroelectric polymer," *ACS Nano*, vol. 4, no. 3, pp. 1345–1350, 2010.
- [44] E.-J. Kan, Z. Li, J. Yang, and J. G. Hou, "Half-metallicity in edge-modified zigzag graphene nanoribbons," *Journal of the American Chemical Society*, vol. 130, no. 13, pp. 4224–4225, 2008.
- [45] O. Hod, V. Barone, J. E. Peralta, and G. E. Suseria, "Enhanced half-metallicity in edgeoxidized zigzag graphene nanoribbons," *Nano Letters*, vol. 7, no. 8, pp. 2295–2299, 2007.
- [46] E. Kan, H. Xiang, F. Wu, C. Lee, J. Yang, and M.-H. Whangbo, "Ferrimagnetism in zigzag graphene nanoribbons induced by main-group adatoms," *Applied Physics Letters*, vol. 96, no. 10, Article ID 102503, 3 pages, 2010.
- [47] B. Xu, J. Yin, Y. D. Xia, X. G. Wan, K. Jiang, and Z. G. Liu, "Electronic and magnetic properties of zigzag graphene nanoribbon with one edge saturated," *Applied Physics Letters*, vol. 96, no. 16, Article ID 163102, 3 pages, 2010.
- [48] F. Cervantes-Sodi, G. Csányi, S. Piscanec, and A. C. Ferrari, "Edge-functionalized and substitutionally doped graphene nanoribbons: electronic and spin properties," *Physical Review B*, vol. 77, no. 16, Article ID 165427, 13 pages, 2008.
- [49] J.-H. Park, E. Vescovo, H.-J. Kim, C. Kwon, R. Ramesh, and T. Venkatesan, "Direct evidence for a half-metallic ferromagnet," *Nature*, vol. 392, no. 6678, pp. 794–796, 1998.
- [50] X. H. Zheng, X. L. Wang, T. A. Abtew, and Z. Zeng, "Building half-metallicity in graphene nanoribbons by direct control over edge states occupation," *Journal of Physical Chemistry C*, vol. 114, no. 9, pp. 4190–4193, 2010.
- [51] B. Biel, X. Blase, F. Triozon, and S. Roche, "Anomalous doping effects on charge transport in graphene nanoribbons," *Physical Review Letters*, vol. 102, no. 9, Article ID 096803, 4 pages, 2009.
- [52] S. S. Yu, W. T. Zheng, Q. B. Wen, and Q. Jiang, "First principle calculations of the electronic properties of nitrogen-doped carbon nanoribbons with zigzag edges," *Carbon*, vol. 46, no. 3, pp. 537–543, 2008.
- [53] S. Dutta, A. K. Manna, and S. K. Pati, "Intrinsic half-metallicity in modified graphene nanoribbons," *Physical Review Letters*, vol. 102, no. 9, Article ID 096601, 4 pages, 2009.
- [54] E.-J. Kan, X. Wu, Z. Li, X. C. Zeng, J. Yang, and J. G. Hou, "Half-metallicity in hybrid BCN nanoribbons," *Journal of Chemical Physics*, vol. 129, no. 8, Article ID 084712, 5 pages, 2008.
- [55] S. S. Yu, W. T. Zheng, and Q. Jiang, "Electronic properties of nitrogen-atom-adsorbed graphene nanoribbons with armchair edges," *IEEE Transactions on Nanotechnology*, vol. 9, no. 2, pp. 243–247, 2010.
- [56] H. Sevinçli, M. Topsakal, E. Durgun, and S. Ciraci, "Electronic and magnetic properties of 3d transition-metal atom adsorbed graphene and graphene nanoribbons," *Physical Review B*, vol. 77, no. 19, Article ID 195434, 7 pages, 2008.
- [57] V. A. Rigo, T. B. Martins, A. J. R. da Silva, A. Fazzio, and R. H. Miwa, "Electronic, structural, and transport properties of Ni-doped graphene nanoribbons," *Physical Review B*, vol. 79, no. 7, Article ID 075435, 9 pages, 2009.
- [58] S. M. M. Dubois, A. López-Bezanilla, A. Cresti et al., "Quantum transport in graphene nanoribbons: effect of edge reconstruction and chemical reactivity," *ACS Nano*, vol. 4, no. 4, pp. 1971–1976, 2010.
- [59] T. B. Martins, R. H. Miwa, A. J. R. da Silva, and A. Fazzio, "Electronic and transport properties of boron-doped graphene nanoribbons," *Physical Review Letters*, vol. 98, no. 19, Article ID 196803, 4 pages, 2007.
- [60] A. López-Bezanilla, F. Triozon, and S. Roche, "Chemical functionalization effects on armchair graphene nanoribbon transport," *Nano Letters*, vol. 9, no. 7, pp. 2537–2541, 2009.

- [61] N. Gorjizadeh, A. A. Farajian, and Y. Kawazoe, "The effects of defects on the conductance of graphene nanoribbons," *Nanotechnology*, vol. 20, no. 1, Article ID 015201, 6 pages, 2009.
- [62] M. Y. Han, B. Özyilmaz, Y. Zhang, and P. Kim, "Energy band-gap engineering of graphene nanoribbons," *Physical Review Letters*, vol. 98, no. 20, Article ID 206805, 4 pages, 2007.

Research Article

Graphene Nanoribbon Conductance Model in Parabolic Band Structure

**Mohammad Taghi Ahmadi, Zaharah Johari, N. Aziziah Amin,
Amir Hossein Fallahpour, and Razali Ismail**

Department of Electronic Engineering, Faculty of Electrical Engineering, Universiti Teknologi Malaysia, Skudai 81310, Johor Darul Takzim, Malaysia

Correspondence should be addressed to Mohammad Taghi Ahmadi, ahmadiph@gmail.com

Received 15 April 2010; Accepted 15 June 2010

Academic Editor: Rakesh K. Joshi

Copyright © 2010 Mohammad Taghi Ahmadi et al. This is an open access article distributed under the Creative Commons Attribution License, which permits unrestricted use, distribution, and reproduction in any medium, provided the original work is properly cited.

Many experimental measurements have been done on GNR conductance. In this paper, analytical model of GNR conductance is presented. Moreover, comparison with published data which illustrates good agreement between them is studied. Conductance of GNR as a one-dimensional device channel with parabolic band structures near the charge neutrality point is improved. Based on quantum confinement effect, the conductance of GNR in parabolic part of the band structure, also the temperature-dependent conductance which displays minimum conductance near the charge neutrality point are calculated. Graphene nanoribbon (GNR) with parabolic band structure near the minimum band energy terminates Fermi-Dirac integral base method on band structure study. While band structure is parabola, semiconducting GNRs conductance is a function of Fermi-Dirac integral which is based on Maxwell approximation in nondegenerate limit especially for a long channel.

1. Introduction

Graphene consist of a single sheet of carbon atom bonded in sp² of hexagonal lattice structure offers a numbers of fascinating possibilities in electronics application [1, 2]. Graphene is a gapless two dimensional material which its confinement introduce one dimensional Graphene nanoribbon with a width less than the De-Broglie wavelength as illustrated in Figure 1. The formation of band gap in GNR resulted from the confinement of electron that form standing waves along the chiral vector [3, 4]. The band gap of the GNR formed that depends on its width and chirality leads to different carrier transport phenomena [5, 6]. GNR band structure shows electronic properties of metallic and semiconducting just like the CNT [7]. GNR also share similar properties with single wall CNTs (SWNTs) [8] that have a mean free path in a range of micrometer [9, 10] as well as carrying higher carrier densities. Unlike CNTs, GNRs has simpler fabrication process owing to excellent future electronic devices like transistor and interconnect [11, 12]. Theoretical study on GNR [13–15] is still at the

beginning stage and the conductance phenomena based on band structure are still unexplored. In this paper, physical model of GNR conductance presented as a function of normalized Fermi energy.

2. Conductance Modeling

Applying the Taylor expansion on graphene band energy near the Fermi point, the $E(k)$ relation of the GNR is obtained as [16]

$$E(\vec{k}) = \pm \frac{t3a_{C-C}}{2} \sqrt{k_x^2 + \beta^2}, \quad (1)$$

where β is quantized wave vector given by [17]

$$\beta = \frac{2\pi}{a_{C-C}\sqrt{3}} \left(\frac{p_i}{N+1} - \frac{2}{3} \right) \quad (2)$$

here p_i is the subband index and N is the number of dimmer lines which determine the width of the ribbon [17] and k_x

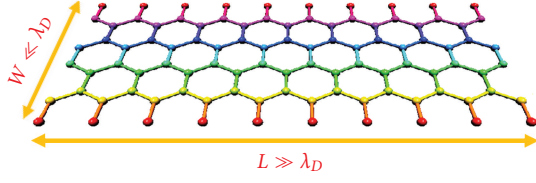


FIGURE 1: A prototype one-dimensional GNR with $W \ll \lambda_D$ and $L \gg \lambda_D$ for rectangular cross-section.

is the wave vector along the length of the nanoribbon. The energy band gap can be assumed as

$$E_g = 3ta_{cc}\beta. \quad (3)$$

Therefore, the modified energy relation is

$$E = \pm \frac{E_g}{2} \sqrt{\left(1 + \frac{k_x^2}{\beta^2}\right)}. \quad (4)$$

Equation (5) which indicates relationship between energy and wave vector is not parabolic, however, Square root approximation in corporate with Taylor expansion leads to parabolic relation between energy and wave vector [18, 19]

$$E(k) \approx \frac{E_g}{2} + \frac{E_g}{4\beta^2} k_x^2, \quad (5)$$

$$E \approx \frac{E_g}{2} + \frac{\hbar^2 k_x^2}{2m^*}, \quad (6)$$

where m^* is the effective mass of GNR. Plotting the GNR energy band of (5) and (7) in Figure 2, it is obviously shown that the band structure is parabolic at certain range of energy in E - k relationship. In parabolic part of the band energy, the wave vector can be extracted as

$$k = \sqrt{\frac{4E}{3a_{cc}t} - 2\beta^2}. \quad (7)$$

Based on this wave vector, number of actual modes $M(E)$ at a given energy which is dependent on the subbands location can be calculated. If the related energy includes the bottom of the conduction band, then parabolic approximation of band diagram can be used, then the mode density $M(E)$ increases with energy. In the valence band, information related to the subbands are more difficult, because the coupled multiple bands that are increasing and difficult dispersion relations are needed.

By taking the derivatives wave vector k over the energy $E(dk/dE)$ of (8), the number of the mode $M(E)$ is written as

$$M(E) = \frac{\Delta E}{\Delta k \cdot L} = \frac{3at}{2L} \left(\frac{4E}{3at} - 2\beta^2\right)^{1/2}, \quad (8)$$

where L is the length of the nanoribbon. Now taking into consideration of spin degeneracy, the number of conducting channels can be finalized as

$$M(E) = 2 \frac{\Delta E}{\Delta k \cdot L} = \frac{3at}{L} \left(\frac{4E}{9at} - 2\beta^2\right)^{1/2}. \quad (9)$$

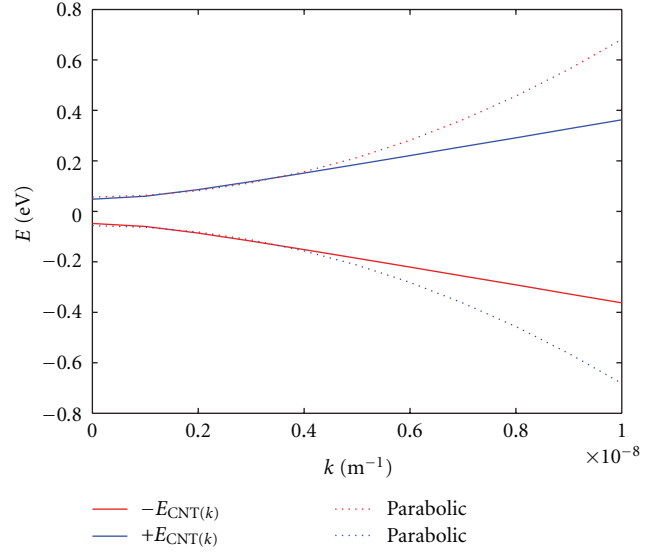


FIGURE 2: The band structure of GNR near the minimum energy is parabolic.

A region of lowest G with respect to *gate voltage* in bulk graphene is calculated and matches to the minimum conductivity at the charge neutrality point, $V_g = V_{\text{Dirac}}$. That is a fundamental constant proportional to the Planck's constant and electron charge

$$G_0 = \frac{2q^2}{h}, \quad (10)$$

where q is electron charge and h is Plank constant. In fact, levels of up spin and down spin in the small channels naturally with same energy as a degenerate level result in the minimum conductance two times larger than this amount which is equal to $2G_0$. In the bad contact, conductance measured is always lower than this value. Based on the Landauer formula, the conductance on large channel can follow the ohmic scaling law but in the smaller size needs to apply two possible corrections on this law, firstly, interface resistance which is independent of the length. Secondly, conductance related to the width nonlinearly which depends on the number of the modes in the conductor that is quantized parameter, in Landauer formula, both of these features are corporate and conductance is

$$G = \frac{2q^2}{h} \int_{-\infty}^{+\infty} dEM(E)T(E) \left(-\frac{df}{dE}\right), \quad (11)$$

where T is average probability of injected electron at one end will transmit to the other end, in our ballistic channel, this parameter is equal to one [20]. Replacement by the number of subbands (mode numbers) corporate with Fermi-Dirac distribution function conductance is related to the length of nanoribbon as well

$$G = \frac{3q^2}{h} \frac{at}{L} (3at)^{1/2} \int_{-\infty}^{+\infty} \left(E - \frac{2\beta^2}{3at}\right)^{1/2} d\left(-\frac{1}{1 + e^{(E-E_F)/k_B T}}\right). \quad (12)$$

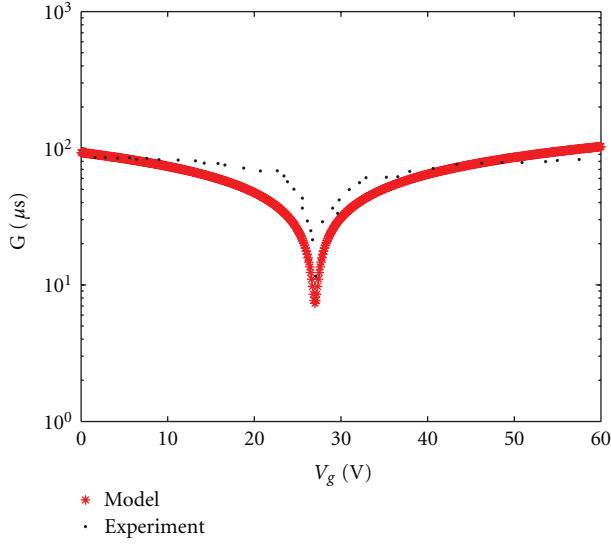


FIGURE 3: Comparison between GNR conductance model (Solid line) and experimental data (dotted line) displays good agreement between theoretical model and experimental data.

Temperature effect on nanoribbon conductance can be seen by changing the boundary of integral as follow

$$G = \frac{3q^2(3\pi a^3 t^3 k_B T)^{1/2}}{hL} \times \left[\int_0^{+\infty} \frac{x^{-1/2}}{(1/(1+e^{-x-\eta}))} dx + \int_0^{+\infty} \frac{x^{-1/2}}{(1/(1+e^{x+\eta}))} dx \right], \quad (13)$$

where $x = (E - E_g)/k_B T$ and normalized Fermi energy is $\eta = (E_F - E_g)/k_B T$. Presenting Fermi-Dirac integral form of conductance is useful to understand the role of degenerate and nondegenerate regimes.

$$G = \frac{3q^2(3\pi a^3 t^3 k_B T)^{1/2}}{hL} [\mathcal{J}_{-1/2}(\eta) + \mathcal{J}_{-1/2}(-\eta)]. \quad (14)$$

GNR conductance model presented on (14) indicates minimum conductance near the charge neutrality point which is in good agreements with experimental results as shown in Figure 3. The presented model here provides possibility towards emerging grapheme-based quantum devices.

Low conductance with respect to the gate voltage indicates minimum conductivity at the charge neutrality point (known as Dirac point), in the neighborhood of the charge-neutrality, point resistance is higher and carriers follow linear energy-momentum dispersion relations.

Unlike the three-dimensional graphene, GNRs show a decrease in minimum conductance more than an order of magnitude at low temperatures as shown in Figure 4. Also the defeat of G near the Dirac point recommends the energy gap in the GNR. However, significant shift of the minimum conductance at Dirac point may be effect on reduction of carrier mobility in graphene. The temperature-dependent conductance in GNRs, compare to that of the

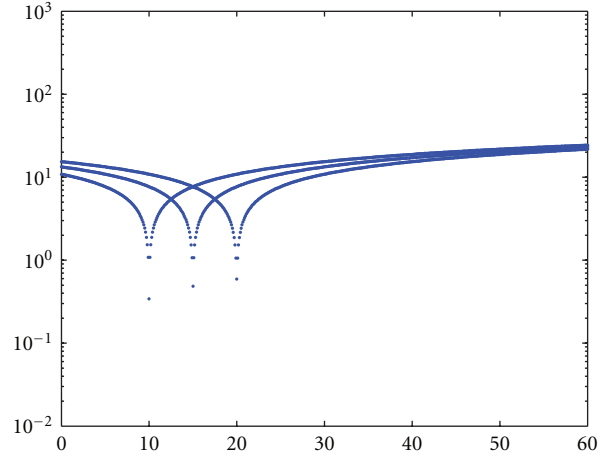


FIGURE 4: Conductance of GNRs as a function of gate voltage is plotted at different temperatures.

three-dimensional graphene samples, where conductance at Dirac point changes less with variation of temperature from 0K to 300 K shows different performance [3].

Nondegenerate approximation on Fermi-Dirac integral can be used when Fermi level in band gap is far from conduction and valence band age more than $3k_B T$. If the Fermi level lies inside the valance or conduction band or located $3k_B T$ in the interior of the band edge, degenerate approximation has to be used. Moreover, GNR length effect can be discussed in terms of degeneracy phenomena, by increasing the length of GNR, nondegenerate approximation will be dominant similar to the conventional long channel device. In the nondegenerate limit, Fermi-Dirac integral can be converted into the exponential equation as

$$G = \frac{3q^2(3\pi a^3 t^3 k_B T)^{1/2}}{hL} [e^{(\eta)} + e^{(-\eta)}]. \quad (15)$$

Reduction of nondegenerate mobility near the Dirac point can be seen by dotted line in Figure 5, also it is shown as a gap region appears for $25 < V_g < 30$ V. Near the Dirac point but outside of the gap region, the conductance balances with the width of the GNR. In the other word, narrower GNRs demonstrate the greatest dominance of minimum conductance at Dirac point [3].

As a device channel, the active GNR width contributes in charge transport, a narrower GNR with possible larger band gap makes them as a semiconducting device component [21]. However, in order to apply the GNR remarkable electrical appearance in nanoelectronic production, a band gap is highly required in graphene, therefore, strong demand is being made to explore the electrical properties of one-dimensional graphene nanostructures. The Fermi level variation and number of conduction modes that contribute to the transport in GNRs also are governed by bias voltage between the source and drain contacts [3–6].

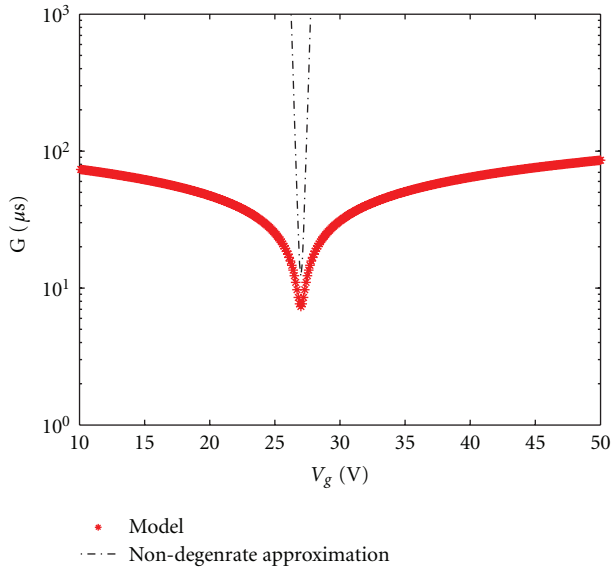


FIGURE 5: Nondegenerate approximations (dotted black line) near the Dirac point on comparison with real conductance (red line).

3. Conclusion

Based on quantum confinement effect granting parabolic band structure in semiconductor GNRs, conductance is a function of Fermi-Dirac integral which is based on Maxwell approximation in nondegenerate limit. GNR conductance at Dirac point illustrates minimum conductance at charge neutrality point which depends on temperature. Based on the presented model, GNR minimum conductance decreases by decreasing the temperature. Reduction of nondegenerate mobility near the charge neutrality point can be related to the minimum conductance near the Dirac point, however, outside of the Dirac point, the conductance balances with the width of the GNR.

Acknowledgments

The work is supported by postdoctoral fellowship scheme for the project “Nanoscale device modeling and simulation”, faculty of Electrical Engineering, managed by the UTM Research Management Center (RMC). The authors would like to thank the MOSTI and RMC for cordially sponsoring this work.

References

- [1] K. S. Novoselov, A. K. Geim, S. V. Morozov, et al., “Electric field in atomically thin carbon films,” *Science*, vol. 306, no. 5696, pp. 666–669, 2004.
- [2] K. S. Novoselov, A. K. Geim, S. V. Morozov et al., “Two-dimensional gas of massless Dirac fermions in graphene,” *Nature*, vol. 438, no. 7065, pp. 197–200, 2005.
- [3] M. Y. Han, B. Özyilmaz, Y. Zhang, and P. Kim, “Energy band-gap engineering of graphene nanoribbons,” *Physical Review Letters*, vol. 98, no. 20, Article ID 206805, 4 pages, 2007.
- [4] Z. Chen, Y.-M. Lin, M. J. Rooks, and P. Avouris, “Graphene nano-ribbon electronics,” *Physica E*, vol. 40, no. 2, pp. 228–232, 2007.
- [5] C. Stampfer, J. Güttinger, F. Molitor, D. Graf, T. Ihn, and K. Ensslin, “Tunable Coulomb blockade in nanostructured graphene,” *Applied Physics Letters*, vol. 92, no. 1, Article ID 012102, 3 pages, 2008.
- [6] F. Sols, F. Guinea, and A. H. C. Neto, “Coulomb blockade in graphene nanoribbons,” *Physical Review Letters*, vol. 99, no. 16, Article ID 166803, 4 pages, 2007.
- [7] C. Berger, Z. Song, T. Li et al., “Ultrathin epitaxial graphite: 2D electron gas properties and a route toward graphene-based nanoelectronics,” *Journal of Physical Chemistry B*, vol. 108, no. 52, pp. 19912–19916, 2004.
- [8] C. Berger, Z. Song, X. Li et al., “Electronic confinement and coherence in patterned epitaxial graphene,” *Science*, vol. 312, no. 5777, pp. 1191–1196, 2006.
- [9] B. Obradovic, R. Kotlyar, F. Heinz et al., “Analysis of graphene nanoribbons as a channel material for field-effect transistors,” *Applied Physics Letters*, vol. 88, no. 14, Article ID 142102, 3 pages, 2006.
- [10] K. Nakada, M. Fujita, G. Dresselhaus, and M. S. Dresselhaus, “Edge state in graphene ribbons: nanometer size effect and edge shape dependence,” *Physical Review B*, vol. 54, no. 24, pp. 17954–17961, 1996.
- [11] T. Ohta, A. Bostwick, T. Seyller, K. Horn, and E. Rotenberg, “Controlling the electronic structure of bilayer graphene,” *Science*, vol. 313, no. 5789, pp. 951–954, 2006.
- [12] R. Van Noorden, “Moving towards a graphene world,” *Nature*, vol. 442, no. 7100, pp. 228–229, 2006.
- [13] N. M. R. Peres, A. H. C. Neto, and F. Guinea, “Erratum: conductance quantization in mesoscopic graphene,” *Physical Review B*, vol. 73, no. 23, Article ID 239902, 1 pages, 2006.
- [14] D. Gunlycke, D. A. Areshkin, and C. T. White, “Semiconducting graphene nanostrips with edge disorder,” *Applied Physics Letters*, vol. 90, no. 14, Article ID 142104, 3 pages, 2007.
- [15] J. Fernández-Rossier, J. J. Palacios, and L. Brey, “Electronic structure of gated graphene and graphene ribbons,” *Physical Review B*, vol. 75, no. 20, Article ID 205441, 8 pages, 2007.
- [16] M. Lundstrom and J. Guo, *Nanoscale Transistors*, Springer, New York, NY, USA, 2006.
- [17] S. Thornhill, N. Wu, Z. F. Wang, Q. W. Shi, and J. Chen, “Graphene nanoribbon field-effect transistors,” in *Proceedings of the IEEE International Symposium on Circuits and Systems (ISCAS ’08)*, pp. 169–172, Seattle, Wash, USA, May 2008.
- [18] M. T. Ahmadi, A. H. Fallahpour, V. Kouhdaragh, K. Dagahi, and R. Ismail, “Band structure effect on Carbon Nanotube Fermi energy,” *International Review of PHYSICS*, vol. 3, no. 44, pp. 224–227, 2009.
- [19] M. T. Ahmadi, R. Ismail, M. L. P. Tan, and V. K. Arora, “The ultimate ballistic drift velocity in carbon nanotubes,” *Journal of Nanomaterials*, vol. 2008, no. 1, Article ID 769250, 8 pages, 2008.
- [20] S. Datta, *Electronic Transport in Mesoscopic Systems*, Cambridge University Press, Cambridge, UK, 2002.
- [21] A. Naeemi and J. D. Meindl, “Conductance modeling for graphene nanoribbon (GNR) interconnects,” *IEEE Electron Device Letters*, vol. 28, no. 5, pp. 428–431, 2007.

Research Article

Preparation of Colloidal Dispersions of Graphene Sheets in Organic Solvents by Using Ball Milling

Weifeng Zhao, Furong Wu, Hang Wu, and Guohua Chen

Institute of Polymer & Nanomaterials, Huaqiao University, Quanzhou, Fujian 362021, China

Correspondence should be addressed to Guohua Chen, hdcgh@hqu.edu.cn

Received 1 June 2010; Accepted 8 July 2010

Academic Editor: Rakesh Joshi

Copyright © 2010 Weifeng Zhao et al. This is an open access article distributed under the Creative Commons Attribution License, which permits unrestricted use, distribution, and reproduction in any medium, provided the original work is properly cited.

A top-down method was developed for producing colloidal dispersions of graphene sheets. Graphite nanosheets comprising hundreds of carbon layers were dispersed and gently ball-milled to exfoliate into graphene in a variety of organic solvents. After 30 hours of the shear-force-dominated grinding and a subsequent 4000 r.p.m. of centrifugation, single- and few-layer graphene sheets were readily prepared and homogeneously and stably suspended in the good solvent medium which possesses a surface tension value close to 40 mJ m^{-2} , such as in *N,N*-dimethylformamide, at a concentration up to 0.08 mg ml^{-1} , achieving a yield higher than 32.0 wt%. The graphene materials in the colloidal suspension were characterized using scanning and transmission electron microscopy and atomic force microscopy.

1. Introduction

With a strictly 2D structure and novel electronic and mechanical properties, graphene has rapidly become an amazing form of carbon that may be used as active components in a wide range of applications such as field-effect transistors [1], transparent conductors [2], liquid crystal displays [3], electromechanical resonators [4], composites [5], energy storage, and photovoltaic devices [6, 7]. To accelerate the use of graphene and tailor its properties, homogeneous colloidal suspensions of individual graphene sheets are always expected, for various processing of the graphene materials such as film and paper depositions, surface modifications and functionalization chemistry of the edges, and defects of graphene sheets are preferred to be conducted in the liquid phase. The key point for creating graphene suspension is overcoming the enormous van der Waals-like forces between graphite layers to yield a complete exfoliation of graphite flakes and dispersing the resulted graphene sheets stably in a liquid media.

In recent years, sonication has been extensively used as an exfoliation and dispersion strategy to produce colloidal suspensions of graphene sheets in a liquid phase [8–11]. The starting materials vary from pristine graphite to graphite

derivatives (e.g., graphite oxide [12, 13]). This procedure has been successful in various solvents with a surface tension value $40\text{--}50 \text{ mJ m}^{-2}$ which are good media for graphite exfoliation [8, 14], especially with the aid of a third, dispersant phase, such as surfactants and polymers [9, 10]. However, for the dispersions of unfunctionalized graphene sheets without surfactants or stabilizers in common solvents, the concentrations attainable are still low ($\leq 0.03 \text{ mg ml}^{-1}$) [8, 14]. This might be probably due to some limitations of sonication in graphite exfoliation. In fact, it has been found that excessive sonication cannot lead to higher yield of graphenes but destruct the graphene sheets [8, 9]. Herein, ball-milling was used to exfoliate graphite in a wide variety of organic solvents including ethanol, formamide, acetone, tetrahydrofuran (THF), tetramethylen (TMU), *N,N*-dimethylformamide (DMF), and *N*-methylpyrrolidone (NMP) to create colloidal dispersions of unfunctionalized graphene sheets. The wet ball-milling experiments were carried out in a planetary mill which mainly exerts shear forces on the materials [15]. Moreover, the rotating tray of the planetary mill was controlled at a low speed to further limit the shock forces applied by the ball impact. Due to the weak van der Waals-like coupling between graphite layers, the graphene sheets in graphite can slide easily with respect to one another under the applied shear forces, creating

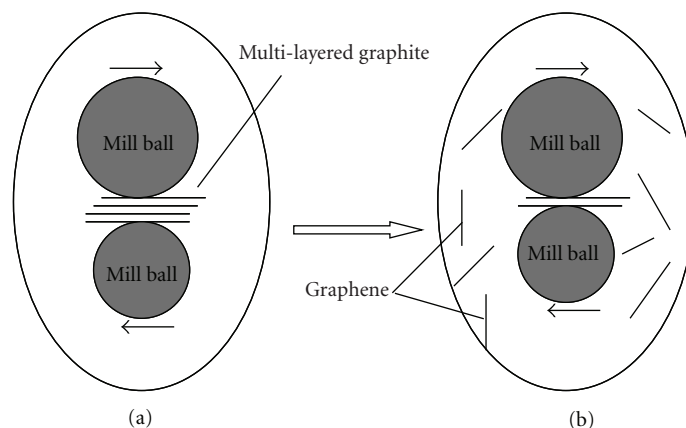


FIGURE 1: Schematic illustration for the creation of graphene from multilayered graphite by using wet ball-milling: (a) GNs dispersed in solvent are delaminated by mill balls in grinding process; (b) graphene sheets are formed *in situ* in solvent. The arrows indicate the shear forces applied to graphite platelets.

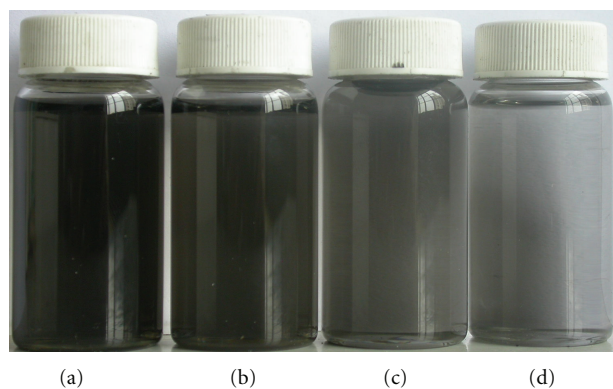


FIGURE 2: Dispersions of graphene materials in TMU (a), NMP (b), DMF (c), THF (d) after 4000 r/min of centrifugation. All of the samples have been kept quietly for six months.

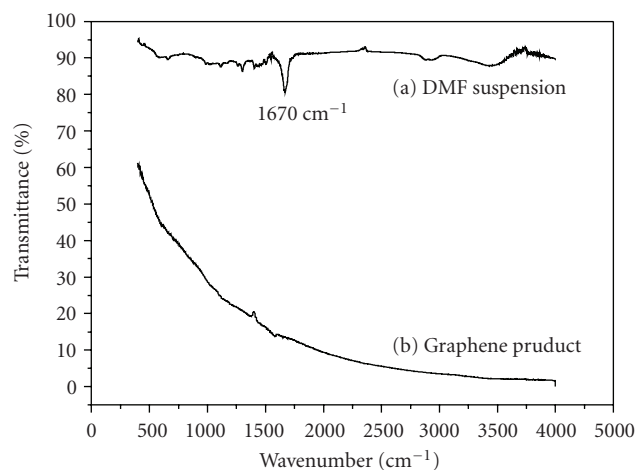


FIGURE 3: FTIR spectra for DMF-based graphene suspension (a) and dried graphene product (b).

isolated graphene sheets in the solvent media *in situ*, as illustrated in Figure 1.

2. Experimental

2.1. Preparation Procedure. The starting material, graphite nanosheets (GNs), was prepared by sonicating expanded graphite in an ethanol solution of water as reported in the literature [16]. All the organic solvents are of AR grade. In a typical procedure for wet grinding, 0.02 g of dried GNs were dispersed in 80 mL of an organic solvent (anhydrous DMF, e.g.) by a mechanical stirring, introduced with zirconia balls (2.0–2.5 mm in diameter, 200 g of weight) into a poly(tetrafluoroethylene) vial, and milled in a planetary mill at a mild rotation speed 300 r. p.m. to ensure the shear stress is dominant. After ball-milling for 30 hours, the obtained dark dispersion was placed quietly to let large pieces subside completely, and then was subjected to centrifugation at 4000 r.p.m. for 30 min to remove any macroscopic aggregates using a TGL-10B centrifuge, giving a black suspension with

single- and few-layer graphene sheets stably suspended in the good solvent (Figure 2).

2.2. Characterization. Absorbance was recorded on a UV-visible spectrophotometer (UV-1600, China) using a quartz cell with a path length of 10 mm at room temperature. Transmission electron microscopy (TEM) was performed on a JEM-2010 JEOL transmission electron microscope at an accelerating voltage of 300 kV. TEM specimens were prepared by either drop-casting graphenes from the supernatant or loading the microtomed epoxy composite slices of the as-obtained graphene powder onto copper grids coated with carbon film. Images of scanning electron microscopy (SEM) were acquired on graphene powder without golden coating using a LEO 1530 field-emitting scanning electron microscope (Germany) at the operating voltage of 20 KV. Fourier transform infrared spectroscopy (FTIR) of was recorded from KBr pellets on a FTIR-84005 spectrometer (Japan).

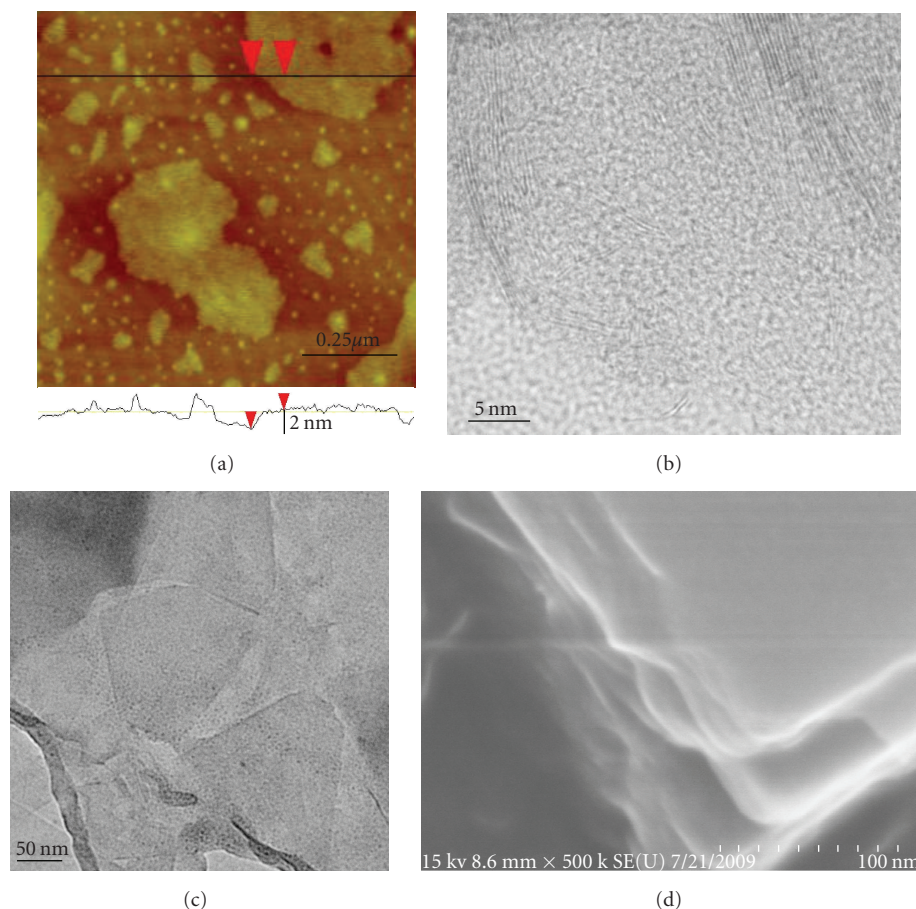


FIGURE 4: Supernatant graphene sheets in DMF. (a) AFM image of the supernatant graphene deposited on a mica substrate, followed with the corresponding height cross-section along the line in the image; the height difference between red arrows is ~ 1.8 nm. (b, c) HRTEM image of separated graphene sheets embedded in polymer slice (b) and isolated flat graphene flakes solution-dropped on TEM grid, from which scrolled edges were observed (c). (d) SEM images of restacked graphene sheets forming a paper-like layered structure.

3. Results and Discussion

Our starting material, GNs, has a nanoscale thickness ranging from 30 to 80 nm, while the lateral size appears much larger, which is of $5\text{--}20\ \mu\text{m}$. The features of nanometer sized thickness and outstanding surface area are advanced in improving the solvent-graphene layer interaction, should make the GNs exfoliate into few- even single-layered graphenes with great efficiency and speed.

The shear-force-type wet ball-milling/4000 r.p.m of centrifugation creates a homogeneous, highly stable, dark suspension of graphene in the good solvents as shown in Figure 2. What is notable is that the as-prepared dispersions are very stable at room temperature; sedimentation can hardly occur within nearly three weeks of quiet placement except for slight aggregations. The agglomerated graphene particles remaining well suspended in solvent could be readily re-dispersed by a simple diluting, for a high concentration will lead to gelation over time. Furthermore, in a low concentration suspension, no aggregations were observed after being placed quietly for long periods of time (at least six months), indicating an entire dispersion of individual graphene sheets. After evaporating solvent under vacuum

and repeated washing with ethanol, dried powder sample with a high purity were obtained for characterizations and for plotting standard curves of absorption. As shown in Figure 3, no DMF absorption features are observed in the graphene product FTIR spectrum which appears featureless, indicating a complete removal of the residual organics by repeated washing.

Figure 4(a) displays the typical AFM image of isolated graphene sheets evaporated from their dilute dispersion on freshly cleaved mica support. Topographic heights of the sheets estimated from the cross-sectional profile were found in the range of $0.8\text{--}1.8$ nm, an indicative of single- and few-layer graphenes. High-resolution transmission electron microscopy (HRTEM) is also a powerful technique used extensively to provide definitive identification of graphene materials. The cross-sections of graphene sheet show predominantly one line for a single-layer graphene, and several condensed dark lines for a few-layer sheet. HRTEM images of the supernatant materials in slice clearly give their cross-sections by a direct visualization (Figure 4(b)). Individual one dark lines with a thickness ~ 0.5 nm (corresponding to single atom carbon layers) can be readily identified. Few-layer graphene sheets composing two or several dark lines

TABLE 1: Fraction of graphene remaining after centrifugation.

Solvent	Surface tension (mJ m^{-2})	Remaining after 4000 r.p.m. of centrifugation	
		Concentration ($\mu\text{g/ml}$)	wt% remaining
NMP	41	88.9	35.56
TMU	34.7	88.28	35.31
DMF	35.2	96.67	38.67
THF	26.4	76.03	30.41
Acetone	23.7	66.6	26.64
Ethanol	22.27	10.32	4.128
Formamide	58.35	3.67	1.468

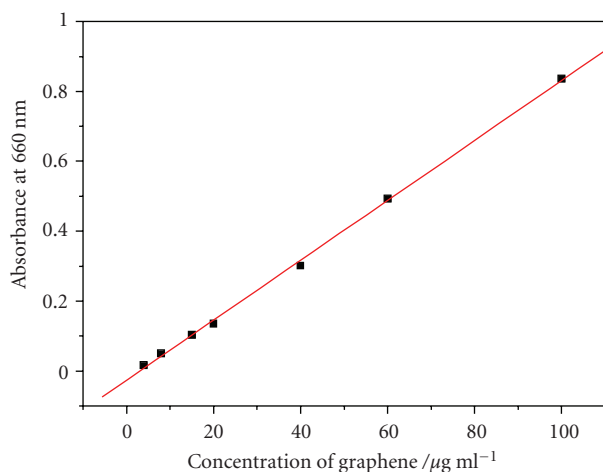


FIGURE 5: Plot of optical density at 660 nm versus graphene concentration. The straight line is a linear least squares fit of the experimental points.

were observed. Typically flat sheets deposited onto grid show a lateral size about 100–200 nm which is similar to that observed from the AFM image, and scroll on edges at times (Figure 4(c)). Due to the high-specific surface area, the graphene sheets have a significant tendency to restack, forming a paper-like layered structure when the solvent was evaporated (Figure 4(d)).

The good stability of the graphene suspensions enables the weight content of supernatant graphenes to be monitored using UV-vis spectroscopy, providing a reliable way to determine the graphene yield. As such, the as-prepared purified graphene samples from DMF were carefully weighted and readily redispersed in NMP with an agitation and a followed sonication of less than 1 min, giving a stable and homogeneous dispersion. The absorption spectra of the graphene NMP suspensions with different concentrations were then measured. It was found that the absorbance was well in line with the relative graphene contents in NMP, obeying Beer's law perfectly in the given range of concentration. By plotting the optical absorption values at 660 nm of wavelength versus concentrations, a standard curve was generated, with an R value of 0.999 (Figure 5.). According to Beer's law, the extinction coefficient was determined to be $1020 \text{ Lg}^{-1}\text{m}^{-1}$. Linear relationship between the absorbance and the relative

concentrations of graphene at other wavelength, 270 nm for example, has also been observed, which strictly follows Beer's law too. The results suggest that the graphene samples had been re-dispersed well in NMP medium before the absorption measurements.

By measuring the absorbance of the as-centrifuged graphene suspensions at 660 nm wavelength which matches the standard curve, the concentration of the supernatant graphene could then be calculated. Table 1 lists the contents of graphene remaining in solvents of different surface tensions after centrifugation at 4000 r.p.m. According to literatures [8, 17, 18], the values of surface tensions of graphene layers close to 40 mJ m^{-2} . In the good solvents with the surface tensions matches that of graphene sheets, such as DMF, NMP, and TMU, the graphene concentrations up to 0.08 mg ml^{-1} are significant higher compared with the case of ethanol and formamide where less than 5.0% of the materials remained. Colloidal suspension of single- and few-layer graphene sheets with a concentration $\sim 0.096 \text{ mg ml}^{-1}$ has been achieved in DMF, and the mass fraction remaining after centrifugation—which is also the yield for graphene—reaches higher than 38.0 wt%.

4. Conclusions

An effective method for creating colloidal suspensions of graphene sheets without the use of surfactants/stabilizers was proposed via exfoliating GNs in organic liquid media using wet ball-milling process. In the good solvents for graphite exfoliation including DMF, NMP, and TMU, suspensions of single- and few-layer graphene sheets can be produced facily at a significantly high yield without any recycling. The ability to provide stable suspensions of graphene sheets in organic solvents with such a high concentration should facilitate the processing of graphene materials remarkably. We believe that either theoretical investigations or practical applications related to graphene, such as functionalization chemistry of the sheet edges, and graphene surface modification will benefit a lot from this bulk exfoliation technique.

Acknowledgments

This work was funded by National Natural Science Foundation of China (nos. 20574025, 50373015) and Natural Science Foundation of Fujian Province (no. E0820001).

References

- [1] B. Obradovic, R. Kotlyar, F. Heinz et al., "Analysis of graphene nanoribbons as a channel material for field-effect transistors," *Applied Physics Letters*, vol. 88, no. 14, Article ID 142102, 2006.
- [2] G. Eda, G. Fanchini, and M. Chhowalla, "Large-area ultrathin films of reduced graphene oxide as a transparent and flexible electronic material," *Nature Nanotechnology*, vol. 3, no. 5, pp. 270–274, 2008.
- [3] P. Blake, P. D. Brimicombe, R. R. Nair et al., "Graphene-based liquid crystal device," *Nano Letters*, vol. 8, no. 6, pp. 1704–1708, 2008.
- [4] J. S. Bunch, A. M. van der Zande, S. S. Verbridge et al., "Electromechanical resonators from graphene sheets," *Science*, vol. 315, no. 5811, pp. 490–493, 2007.
- [5] S. Stankovich, D. A. Dikin, G. H. B. Dommett et al., "Graphene-based composite materials," *Nature*, vol. 442, no. 7100, pp. 282–286, 2006.
- [6] M. D. Stoller, S. Park, Y. Zhu, J. An, and R. S. Ruoff, "Graphene-based ultracapacitors," *Nano Letters*, vol. 8, no. 10, pp. 3498–3502, 2008.
- [7] Z. Liu, Q. Liu, Y. Huang et al., "Organic photovoltaic devices based on a novel acceptor material: graphene," *Advanced Materials*, vol. 20, no. 20, pp. 3924–3930, 2008.
- [8] Y. Hernandez, V. Nicolosi, M. Lotya et al., "High-yield production of graphene by liquid-phase exfoliation of graphite," *Nature Nanotechnology*, vol. 3, no. 9, pp. 563–568, 2008.
- [9] X. Li, X. Wang, L. Zhang, S. Lee, and H. Dai, "Chemically derived, ultrasmooth graphene nanoribbon semiconductors," *Science*, vol. 319, no. 5867, pp. 1229–1232, 2008.
- [10] X. Li, G. Zhang, X. Bai et al., "Highly conducting graphene sheets and Langmuir-Blodgett films," *Nature Nanotechnology*, vol. 3, no. 9, pp. 538–542, 2008.
- [11] W. Gu, W. Zhang, X. Li et al., "Graphene sheets from worm-like exfoliated graphite," *Journal of Materials Chemistry*, vol. 19, no. 21, pp. 3367–3369, 2009.
- [12] S. Park, J. An, I. Jung et al., "Colloidal suspensions of highly reduced graphene oxide in a wide variety of organic solvents," *Nano Letters*, vol. 9, no. 4, pp. 1593–1597, 2009.
- [13] S. Stankovich, D. A. Dikin, R. D. Piner et al., "Synthesis of graphene-based nanosheets via chemical reduction of exfoliated graphite oxide," *Carbon*, vol. 45, no. 7, pp. 1558–1565, 2007.
- [14] C. E. Hamilton, J. R. Lomeda, Z. Sun, J. M. Tour, and A. R. Barron, "High-yield organic dispersions of unfunctionalized graphene," *Nano Letters*, vol. 9, no. 10, pp. 3460–3462, 2009.
- [15] M. V. Antisari, A. Montone, N. Jovic, E. Piscopiello, C. Alvani, and L. Pilloni, "Low energy pure shear milling: a method for the preparation of graphite nano-sheets," *Scripta Materialia*, vol. 55, no. 11, pp. 1047–1050, 2006.
- [16] G. Chen, D. Wu, W. Weng, and C. Wu, "Exfoliation of graphite flake and its nanocomposites," *Carbon*, vol. 41, no. 3, pp. 619–621, 2003.
- [17] S. D. Bergin, V. Nicolosi, P. V. Streich et al., "Towards solutions of single-walled carbon nanotubes in common solvents," *Advanced Materials*, vol. 20, no. 10, pp. 1876–1881, 2008.
- [18] S. D. Bergin, Z. Sun, D. Rickard, P. V. Streich, J. P. Hamilton, and J. N. Coleman, "Multicomponent solubility parameters for single-walled carbon nanotube-solvent mixtures," *ACS Nano*, vol. 3, no. 8, pp. 2340–2350, 2009.

Research Article

Positioning of the Fermi Level in Graphene Devices with Asymmetric Metal Electrodes

Bum-Kyu Kim,¹ Eun-Kyoung Jeon,¹ Ju-Jin Kim,¹ and Jeong-O Lee²

¹Department of Physics, Institute of Physics and Chemistry, Chonbuk National University, Jeonju 561-756, Republic of Korea

²Fusion-Biotechnology Research Center, Korea Research Institute of Chemical Technology, Daejeon 305-600, Republic of Korea

Correspondence should be addressed to Ju-Jin Kim, jujinkim@chonbuk.ac.kr

Received 15 June 2010; Accepted 7 July 2010

Academic Editor: Rakesh Joshi

Copyright © 2010 Bum-Kyu Kim et al. This is an open access article distributed under the Creative Commons Attribution License, which permits unrestricted use, distribution, and reproduction in any medium, provided the original work is properly cited.

To elucidate the effect of the work function on the position of the Dirac point, we fabricated graphene devices with asymmetric metal contacts. By measuring the peak position of the resistance for each pair of metal electrodes, we obtained the voltage of the Dirac point V_g^{Dirac} (V) from the gate response. We found that the position of V_g^{Dirac} (V) in the hybrid devices was significantly influenced by the type of metal electrode. The measured shifts in V_g^{Dirac} (V) were closely related to the modified work functions of the metal-graphene complexes. Within a certain bias range, the Fermi level of one of the contacts aligned with the electron band and that of the other contact aligned with the hole band.

1. Introduction

The electrical properties of nanosized devices are significantly influenced by the characteristics of the electrical contacts in the devices. In devices in which a carbon nanotube (CNT) conducting channel is in contact with a metal, the carrier type of the device (*hole* or *electron*) can be selected by appropriate positioning of the Fermi level at the interface between the metal and the CNT channel [1–4]. The Schottky barrier at the metal electrode/semiconducting channel interface is determined by the energy difference between the metal work function and the electron affinity of the channel. Metal electrodes with low work functions are typically used for electron injection into the conduction band whereas metal electrodes with high work functions are adequate for hole injection into the valence band. In practice, however, it is difficult to find appropriate electrode metals with optimal work functions that are suitable for use with particular conducting channels [5, 6]. If the work function of the metal electrode could be varied systematically, it would be possible to precisely tailor the electrical properties of a device, thereby modifying the energy level alignment near the electrode/semiconductor interface.

On the other hand, substitutional impurity doping techniques used in the conventional bulk semiconductor

industry encounter many challenges when applied to carbon-based nanodevices, such as CNTs and graphene devices, due to the nonuniformity of the doping and the perfect covalent bonding structure of the carbon nanostructures. Precise control over the electrical properties of CNT devices is essential for future electronic device development [7]. As an alternative to impurity doping, contact doping may be used to modify the barrier height between carbon-based conducting channels and metal electrodes. Charge transport in most CNT field-effect transistors (FETs) is strongly influenced by the Schottky barrier between the nanotubes and the contact electrode. Under normal conditions, CNT-FETs fabricated to date have shown only *p*-type operation [8]. The reason why CNT-FETs exhibit characteristic *p*-type behavior has long been a topic of debate [9, 10]. Previously, hole doping by environmental oxygen molecules was believed to be the principal cause of the *p*-type behavior of CNT-FETs [11, 12]. However, it is now generally agreed that *p*-type behavior arises from the low-lying Schottky barrier for hole transport at a high work function metal-CNT interface [13]. The position of the Fermi level at the interface between the metal electrode and the CNT channel should be a key parameter governing the transport characteristics in these devices.

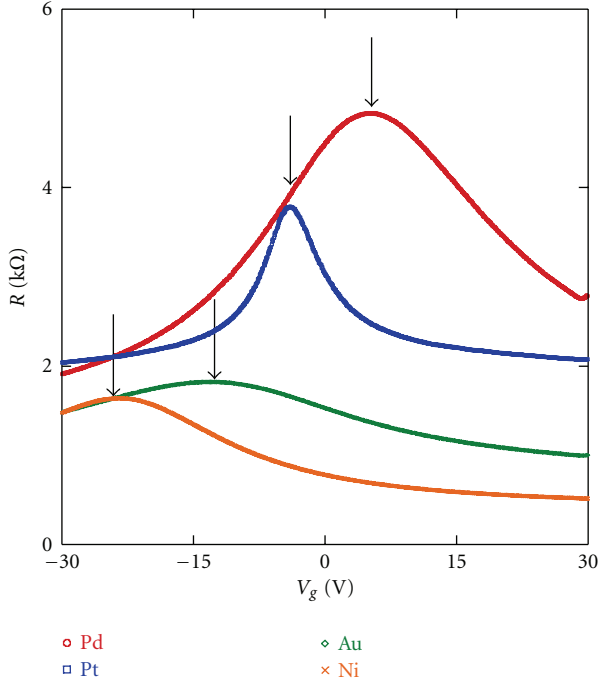


FIGURE 1: Two-probe electronic transfer characteristics measured in graphene transistors with various metal contacts. The arrows indicate the positions of the Dirac point voltages, V_g^{Dirac} (V). The specific values of V_g^{Dirac} (V) were +1.26 V (Pd), -3.92 V (Pt), -13.12 V (Au), and -24.33 V (Ni).

Because graphene is a zero-gap semiconductor with a linear dispersion relation near the Fermi level [14], graphene devices with metal electrodes may show Fermi level positioning effects similar to those observed in CNT devices. By adjusting the Fermi level pinning position, we can intentionally select whether the charge carrier passing through the contact barrier is an *electron* or *hole*. The controlled adjustment of the Dirac point is not only of scientific interest but also is employed in the fabrication of graphene-based devices. Previous studies have modulated the Dirac point by varying the concentration of external dopants or by applying an electrostatic bias [15, 16]. However, this type of Dirac point adjustment arises from channel doping, not from Fermi level positioning effects.

In previous transport experiments, the position of the Dirac point has appeared to be arbitrary. The effects of metal contact, edges, defects, and adsorbed species were thought to be intertwined in some nonlinear fashion and, therefore, were difficult to separate [17–21]. The effects of the metal contacts were particularly intriguing because most transport measurements are expected to depend fundamentally on the metal-graphene interface [22, 23]. In the present paper, we investigated the role of the metal work function on the position of the Dirac charge neutrality point V_g^{Dirac} (V) by measuring the gate transfer characteristics of graphene transistors with asymmetric metal contacts. A variety of metal electrodes that bind physically or chemically to graphene were employed as contact electrodes, and we confirmed that

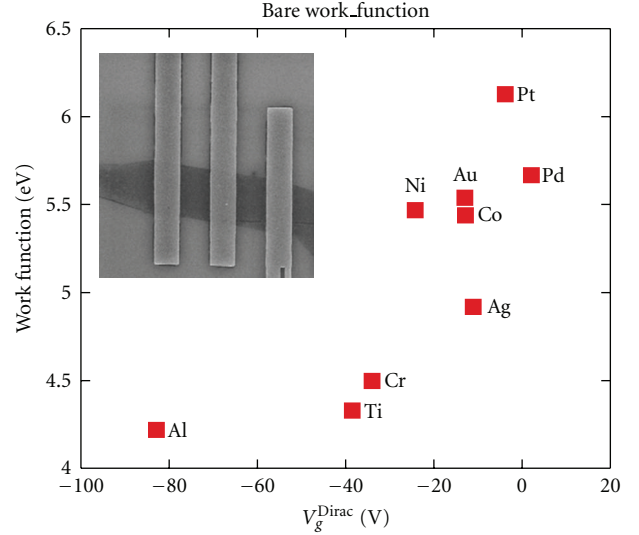


FIGURE 2: Averaged voltages of Dirac points in the gate response as a function of the metal work function. Inset: scanning electron micrograph image of a typical graphene field effect transistor used in this experiment.

the Dirac point V_g^{Dirac} (V) could be modified by varying the metal work function and the metal-graphene interaction. By employing asymmetric metal electrodes, we demonstrated that it was possible to simultaneously inject different types of charge carrier into the same graphene channel.

2. Experimental

Graphene sheets were micromechanically cleaved from a highly oriented pyrolytic graphite (HOPG) sample. Graphene devices were prepared on a heavily doped Si substrate with a 300 nm thick, thermally grown SiO_2 layer. Once a suitable graphene sheet was characterized by optical microscopy and atomic force microscopy, deep UV lithography and electron-beam (e-beam) lithography were used to generate electrode patterns on the selected graphene sheet. To minimize chemical contamination, we used only a PMMA resist during the fabrication process. Source and drain electrodes were formed by depositing one of a variety of metals with different work functions by either sputtering (for Co, Ni, Ti, Cr, Pd, or Au) or electron-beam evaporation techniques (for Pt, Ag, Au, Ti, Pd, or Al). The film deposition technique did not significantly affect the position of the Dirac point. Devices with hetero-metallic contacts were subjected to two identical e-beam lithography procedures. To discriminate the effect of metal work function, all fabrication parameters were kept constant as much as possible, and the same fabrication process and device layout were used. The inset of Figure 2 shows a scanning electron microscopy image of a typical graphene transistor with metal electrodes. A heavily doped Si substrate was used as a back gate to control the carrier concentration in the graphene devices, and the channel lengths of the devices were kept at approximately $2 \mu\text{m}$.

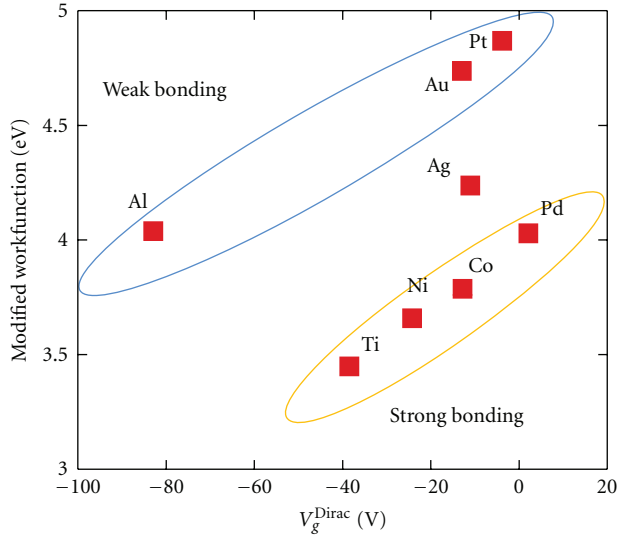


FIGURE 3: Position of the Dirac point in the gate response in relation to the modified work function of a metal-graphene complex. Two classes of metal—those that physisorb and those that chemisorb onto graphene—are clearly distinguished, with the exception of Ag.

3. Results and Discussion

First, we address the transport characteristics of the graphene devices with symmetric source and drain contact electrodes. The channel doping effects due to the adsorption of molecules on the surfaces of the graphene channel were minimized by preparing all devices under identical fabrication conditions, with the only difference being the identity of the metal electrode. We measured the gate-dependent resistance of the graphene devices, as shown in Figure 1. The positions of the resistance peaks designated by arrows correspond to the Dirac points at the metal-graphene interfaces, and these positions depended on the type of metal electrode. Only the Pd-contact device showed a positive peak voltage, implying that the Fermi level was aligned with the hole band of the graphene channel. In contrast, other materials (Pt, Au, and Ni) showed a negative Dirac peak voltage.

The relation between the peak position and the metal electrode was inferred by plotting the average voltage of the Dirac point V_g^{Dirac} (V) of the gate response as a function of the bare metal work function, as shown in Figure 2. V_g^{Dirac} (V) was obtained from the average value measured in 4–6 devices. Because the metal contact, as an electron reservoir, determines the Fermi level of the graphene, V_g^{Dirac} (V) may be related to the metal work function. At first glance, V_g^{Dirac} (V) appears to be closely correlated with the magnitude of the bare metal work function [24]. However, some deviations from the expected values are readily identified, especially for contact materials with good wetting properties, such as Ti, Cr, and Co. Because the density of states in graphene is much lower than that in an electrode metal, even small amounts of electron transfer near the interface will significantly shift the Fermi level [22]. Thus, the interface charge transfer between the metal and graphene is another governing parameter

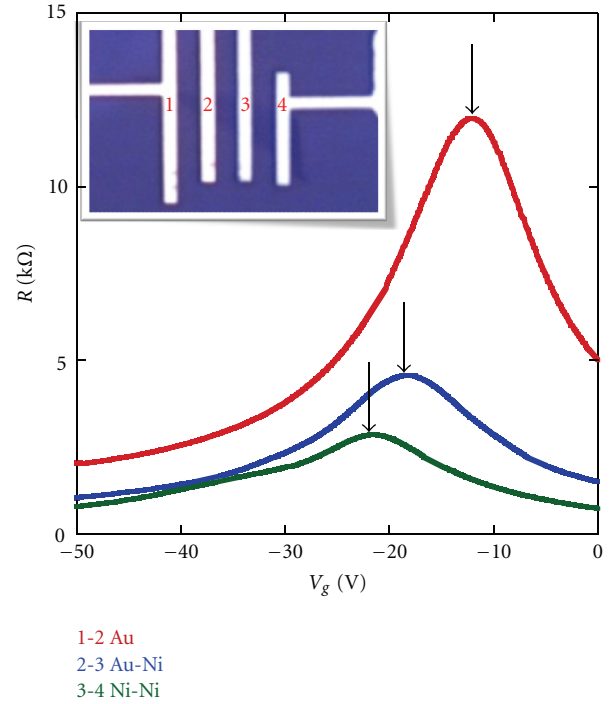


FIGURE 4: Gate response curves measured from a symmetric Au-contact graphene device (1-2), a Ni-contact device (3-4), and an asymmetric-contact device containing Ni and Au contacts (2-3). Inset: Optical microscope image of graphene with asymmetric hetero-metal electrodes (Au, Ni).

for the Fermi level alignment, particularly in regards to the good wetting properties of the metal electrode to the graphene channel. Accordingly, we classified the metals into two groups: those physisorbed onto graphene (Al, Au, and Pt) and those chemisorbed onto graphene (Ti, Ni, Co, and Pd). In previous theoretical studies [22, 23], the electronic structure of the metal surface in contact with the graphene over layer was investigated, and the movement of the Fermi level of graphene was obtained with respect to the work function of the metal-graphene complex.

We replotted the average V_g^{Dirac} (V) of the gate response as a function of the “modified work function” of the metal-graphene complex, as shown in Figure 3. The modified work function values in Figure 3 were derived from [22, 23]. When plotted in this way, V_g^{Dirac} (V) could be separated into two groups—physisorbed (weak bonding) metal electrodes and chemisorbed (strong bonding) metal electrodes—with the exception of Ag. Within each of these groups, the movement of the Dirac point of the gate response was almost directly proportional to the work function of the metal-graphene complex. The Ag-contact device, which did not fall into either group, appeared to show a much stronger binding behavior than what would be predicted by theoretical calculations [22]. The deviation of the Ag electrode device from the expected behavior may originate from some other type of strong bonding near the interface. Further theoretical and experimental studies are required to understand the discrepancy of this system.

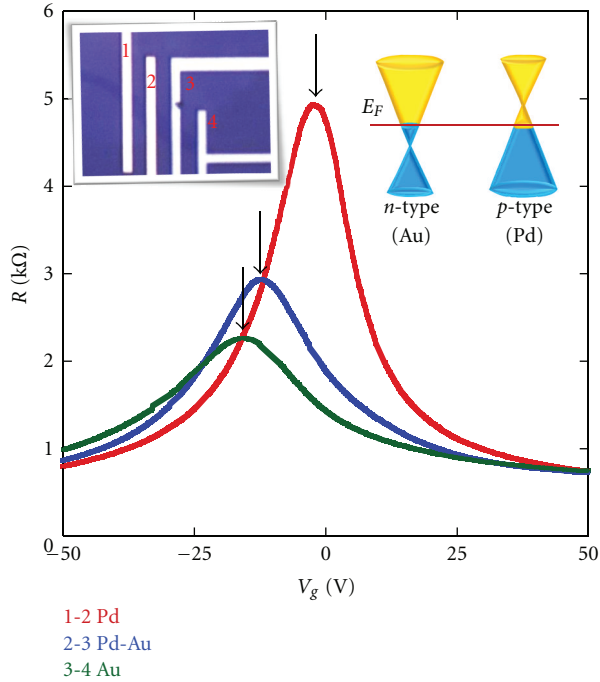


FIGURE 5: Gate response curves for a symmetric Pd-contact graphene device (1-2), an Au-contact device (3-4), and an asymmetric-contact device with Pd and Au electrodes (2-3). Inset: an optical microscope image of graphene with asymmetric hetero-metal electrodes (Pd, Au).

Next, we employed asymmetric hetero-metal electrodes (Au, Ni) and (Pd, Au) in graphene devices to more clearly observe the effects of the metal work functions. Within a single device, we fabricated 4 electrodes using two different types of metal, as shown in Figures 4 and 5. Figure 4 compares the I - V_g characteristics measured from a symmetric Au-contact graphene device, an Ni-contact device, and an asymmetric-contact device containing Ni and Au electrodes. The measured V_g^{Dirac} (V) values for the three measurement configurations were -12.08 V, -21.51 V, and -18.28 V, respectively. As shown, the Dirac point of the Au–Ni-contact graphene device was situated between that of the Au-contact device and that of the Ni-contact graphene device, confirming that the work function of the contact metal indeed significantly influenced the electronic properties of graphene. A Pd electrode with a large V_g^{Dirac} (V) and an Au electrode were paired to fabricate a bipolar contact device: one contact injected electrons, and the other injected holes through the respective contact barriers.

Figure 5 shows the gate response curves of the graphene device containing Pd and Au hybrid contacts. The measured V_g^{Dirac} (V) values for the three measurement configurations were -2.38 V (Pd–Pd), -12.27 V (Pd–Au), and -13.98 V (Au–Au), respectively. The V_g^{Dirac} (V) of Pd–Pd in this particular device was slightly smaller than the value ($+1.97$ V) measured for the averaged symmetric devices, as shown in Figure 2. The Pd–Au-contact graphene devices were situated between the Au-contact device and the Pd-contact graphene

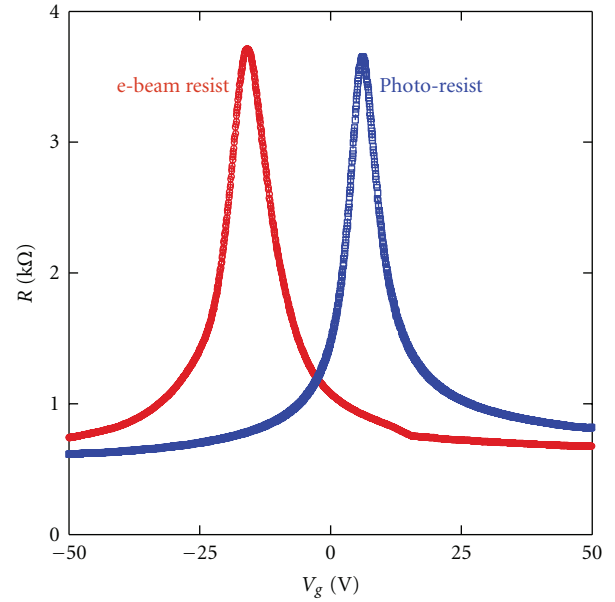


FIGURE 6: Gate response of the resistance of graphene devices produced using different resists (e-beam resist or photoresist) in the fabrication process.

device. Within the gate bias range from -2.38 V to -13.98 V, the Fermi level for the Au contact side aligned at the electron band. On the other hand, the Fermi level for the Pd contact side was positioned at the hole band, as shown in the right inset of Figure 6. Transport measurements within this bias range may detect interesting phenomena originating from the mixed type of charge carriers in the graphene conducting channel.

Another interesting experimental observation to note is the effect of the polymeric resist on the movement of the Dirac point. When we fabricated graphene devices using a different type of resist solution (a AZ5214 photoresist instead of the PMMA electron beam resist used for the previous measurements), the resulting devices showed Dirac point voltages that were shifted by 10 V in the positive direction (see Figure 6). Note that the global shape of the gate response curve and the resistance did not depend on the resist used. The gate response curve shifted in a parallel direction while maintaining the curve shape commonly observed in CNT devices, which is known to arise from channel doping and not from contact modification [2]. Doping at the graphene channel surface originated from the chemical composition of the photoresist. Note that the previous experiments used the e-beam resist (PMMA) to fabricate the graphene devices. The sensitivity to the type of resist may be one reason why the V_g^{Dirac} (V) appeared to be arbitrarily positioned in previous transport experiments [18–20]. Annealing processes commonly used for graphene devices may help remove the residual chemical species from the photoresist, which could minimize channel doping effects [25]. After removing the channel doping by the proper techniques, the position of the Dirac point at the interface between the metal electrode and

the graphene should be governed by the work function of the metal-graphene complex.

4. Summary

We have studied the positioning of the Dirac point in graphene devices with asymmetric metal electrodes by measuring the transport properties of the devices. We found that the positioning of V_g^{Dirac} (V) in hetero-metal contact devices was strongly influenced by the modified work function values of the metal-graphene complexes. The asymmetric metal contact electrodes showed Fermi levels that were aligned at one contact with the electron band and at the other contact with the hole band, within a certain bias range. This result demonstrates that it is possible to simultaneously inject different types of charge carriers into the same graphene channel. Finally, we found that the type of the resist shifted V_g^{Dirac} (V) significantly via channel doping.

Acknowledgments

This paper was supported by the Chonbuk National University and the National Research Foundation of Korea (R01-2008-000-11425-0 and KRF-2008-313-C00319).

References

- [1] Y. Noshu, Y. Ohno, S. Kishimoto, and T. Mizutani, "N-type carbon nanotube field-effect transistors fabricated by using Ca contact electrodes," *Applied Physics Letters*, vol. 86, no. 7, Article ID 073105, 3 pages, 2005.
- [2] H.-S. Kim, B.-K. Kim, J.-J. Kim, J.-O. Lee, and N. Park, "Controllable modification of transport properties of single-walled carbon nanotube field effect transistors with in situ Al decoration," *Applied Physics Letters*, vol. 91, no. 15, Article ID 153113, 3 pages, 2007.
- [3] C. W. Lee, K. Zhang, H. Tantang et al., "Tuning of electrical characteristics in networked carbon nanotube field-effect transistors using thiolated molecules," *Applied Physics Letters*, vol. 91, no. 10, Article ID 103515, 2007.
- [4] S. Alwarappan, G. Liu, and C.-Z. Li, "Simultaneous detection of dopamine, ascorbic acid, and uric acid at electrochemically pretreated carbon nanotube biosensors," *Nanomedicine*, vol. 6, no. 1, pp. 52–57, 2010.
- [5] H.-S. Kim, E.-K. Jeon, J.-J. Kim et al., "Air-stable n-type operation of Gd-contacted carbon nanotube field effect transistors," *Applied Physics Letters*, vol. 93, no. 12, Article ID 123106, 2008.
- [6] Z. Zhang, X. Liang, S. Wang et al., "Doping-free fabrication of carbon nanotube based ballistic CMOS devices and circuits," *Nano Letters*, vol. 7, no. 12, pp. 3603–3607, 2007.
- [7] V. Derycke, R. Martel, J. Appenzeller, and Ph. Avouris, "Controlling doping and carrier injection in carbon nanotube transistors," *Applied Physics Letters*, vol. 80, no. 15, p. 2773, 2002.
- [8] R. Martel, T. Schmidt, H. R. Shea, T. Hertel, and Ph. Avouris, "Single- and multi-wall carbon nanotube field-effect transistors," *Applied Physics Letters*, vol. 73, no. 17, pp. 2447–2449, 1998.
- [9] S. Heinze, J. Tersoff, and Ph. Avouris, "Electrostatic engineering of nanotube transistors for improved performance," *Applied Physics Letters*, vol. 83, no. 24, pp. 5038–5040, 2003.
- [10] J. Appenzeller, J. Knoch, V. Derycke, R. Martel, S. Wind, and Ph. Avouris, "Field-modulated carrier transport in carbon nanotube transistors," *Physical Review Letters*, vol. 89, no. 12, Article ID 126801, 4 pages, 2002.
- [11] P. G. Collins, K. Bradley, M. Ishigami, and A. Zettl, "Extreme oxygen sensitivity of electronic properties of carbon nanotubes," *Science*, vol. 287, no. 5459, pp. 1801–1804, 2000.
- [12] A. Bachtold, P. Hadley, T. Nakanishi, and C. Dekker, "Logic circuits with carbon nanotube transistors," *Science*, vol. 294, no. 5545, pp. 1317–1320, 2001.
- [13] R. Martel, V. Derycke, C. Lavoie et al., "Ambipolar electrical transport in semiconducting single-wall carbon nanotubes," *Physical Review Letters*, vol. 87, no. 25, Article ID 256805, 4 pages, 2001.
- [14] R. Saito, M. Fujita, G. Dresselhaus, and M. S. Dresselhaus, "Electronic structure of graphene tubules based on C60," *Physical Review B*, vol. 46, no. 3, pp. 1804–1811, 1992.
- [15] F. Schedin, A. K. Geim, S. V. Morozov et al., "Detection of individual gas molecules adsorbed on graphene," *Nature Materials*, vol. 6, no. 9, pp. 652–655, 2007.
- [16] J. B. Oostinga, H. B. Heersche, X. Liu, A. F. Morpurgo, and L. M. K. Vandersypen, "Gate-induced insulating state in bilayer graphene devices," *Nature Materials*, vol. 7, no. 2, pp. 151–157, 2007.
- [17] I. Gierz, C. Riedl, U. Starke, C. R. Ast, and K. Kern, "Atomic hole doping of graphene," *Nano Letters*, vol. 8, no. 12, pp. 4603–4607, 2008.
- [18] D. B. Farmer, G.-M. Roksana, V. Perebeinos et al., "Chemical doping and electron-hole conduction asymmetry in graphene devices," *Nano Letters*, vol. 9, no. 1, pp. 388–392, 2009.
- [19] Y. Dan, Y. Lu, N. J. Kybert, Z. Luo, and A. T. C. Johnson, "Intrinsic response of graphene vapor sensors," *Nano Letters*, vol. 9, no. 4, pp. 1472–1475, 2009.
- [20] R. Nouchi, M. Shiraishi, and Y. Suzuki, "Transfer characteristics in graphene field-effect transistors with Co contacts," *Applied Physics Letters*, vol. 93, no. 15, Article ID 152104, 2008.
- [21] S. Alwarappan, A. Erdem, C. Liu, and C.-Z. Li, "Probing the electrochemical properties of graphene nanosheets for biosensing applications," *Journal of Physical Chemistry C*, vol. 113, no. 20, pp. 8853–8857, 2009.
- [22] G. Giovannetti, P. A. Khomyakov, G. Brocks, V. M. Karpan, J. van den Brink, and P. J. Kelly, "Doping graphene with metal contacts," *Physical Review Letters*, vol. 101, no. 2, Article ID 026803, 2008.
- [23] N. Park, B.-K. Kim, J.-O. Lee, and J.-J. Kim, "Influence of metal work function on the position of the Dirac point of graphene field-effect transistors," *Applied Physics Letters*, vol. 95, Article ID 243105, 3 pages, 2009.
- [24] H. B. Michaelson, "The work function of the elements and its periodicity," *Journal of Applied Physics*, vol. 48, no. 11, pp. 4729–4733, 1977.
- [25] K. Nagashio, T. Nishimura, K. Kita, and A. Toriumi, "Systematic investigation of the intrinsic channel properties and contact resistance of monolayer and multilayer graphene field-effect transistor," *Japanese Journal of Applied Physics*, vol. 49, no. 5, part 1, Article ID 051304, 6 pages, 2010.

Research Article

Formulation of 2D Graphene Deformation Based on Chiral-Tube Base Vectors

Bohua Sun

Department of Mechanical Engineering, Cape Peninsula University of Technology, P.O. Box 1906, Bellville 7535, City of Cape Town, South Africa

Correspondence should be addressed to Bohua Sun, sunb@cput.ac.za

Received 12 May 2010; Accepted 13 June 2010

Academic Editor: Rakesh Joshi

Copyright © 2010 Bohua Sun. This is an open access article distributed under the Creative Commons Attribution License, which permits unrestricted use, distribution, and reproduction in any medium, provided the original work is properly cited.

The intrinsic feature of graphene honeycomb lattice is defined by its chiral index (n, m) , which can be taken into account when using molecular dynamics. However, how to introduce the index into the continuum model of graphene is still an open problem. The present manuscript adopts the continuum shell model with single director to describe the mechanical behaviors of graphene. In order to consider the intrinsic features of the graphene honeycomb lattice—chiral index (n, m) , the chiral-tube vectors of graphene in real space have been used for construction of reference unit base vectors of the shell model; therefore, the formulations will contain the chiral index automatically, or in an explicit form in physical components. The results are quite useful for future studies of graphene mechanics.

1. Introduction

A one-atom-thick layer of graphite called graphene is the “mother” of all graphitic forms. Graphene is a 2D building material for carbon materials of all other dimensionalities. It can be wrapped up to 0D buckyballs, rolled into 1D nanotubes, or stacked into 3D graphite [1–3]. Figure 1 is a famous picture taken from [3].

The graphene has attracted attention because of its unusual two-dimensional structure and potential for applications. Owing to its exceptional mechanical properties and low mass density, graphene is an ideal material for use in nanoelectromechanical systems (NEMS), which are of great interest both for fundamental studies of mechanics at the nanoscale and for a variety of applications, including force, position, mass, and gas sensing [4].

Graphene research has developed at a truly relentless pace. Several papers appear every day; comprehensive reviews have been done by the graphene pioneers [2, 3]. Geometrically, the graphene can be considered as an “almost” 2D material due to its very small thickness at only one-atom. The 2D feature of the graphene makes it possible to directly use well-formulated 2D continuum shell model to simulate its deformation, vibration, and buckling [1–3].

Although many features of the graphene can be described by relativistic quantum mechanics and molecular dynamics, the continuum modeling is still useful and crucial for rational device design and interpretation of experimental results. Because experiments at the nanoscale are extremely difficult and atomistic modelling remains prohibitively expensive for large-sized atomic system, it has been accepted that continuum models will continue to play an essential role in the study of carbon nanotube [5]. The validity of using continuum models for nanotube and graphene has been supported by both experimental results and molecular-dynamics simulation, all previous investigations on nanotube have indicated that the laws of continuum mechanics are still valid to some extent even in nanoscale. The success of continuum models to nanotube gives us confidence to predict that continuum modelling is going to be also valid for graphene mechanics analysis [6, 7].

Within the frame of classic continuum mechanics, there is a well-formulated branch-theory of shell [8–14]. It deals with a special 3D continuum shell; its thickness is very much smaller than its width and length. The deformation of the thinner 3D shell can be considered as a 2D middle surface with a small thickness, and all off-middle surface quantities can be presented in terms of middle surface. In this way, the

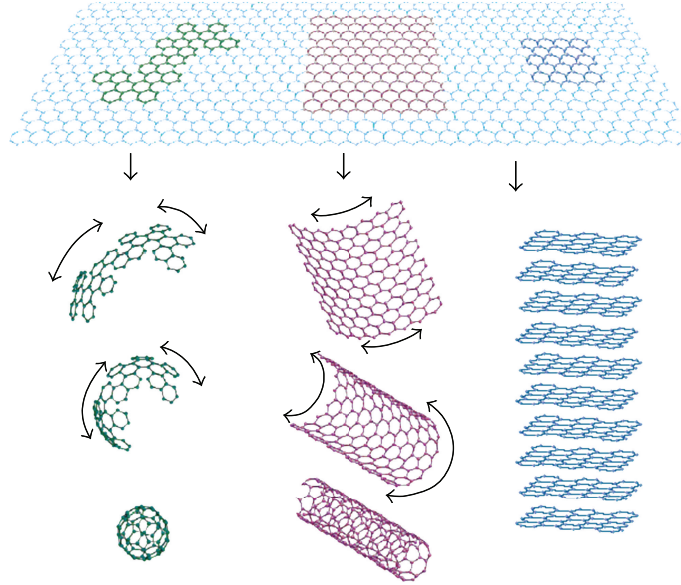


FIGURE 1: Mother of all graphitic forms. Graphene is a 2D building material for carbon materials of all other dimensionalities. It can be wrapped up into 0D buckyballs, rolled into 1D nanotubes or stacked into 3D graphite.

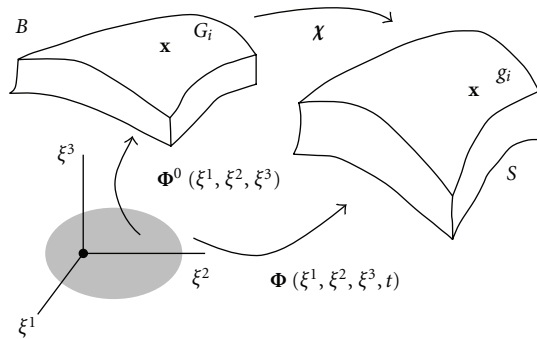


FIGURE 2: Paramterization of the reference and current configurations B and S ; the deformation mapping and basis vectors.

3D thinner shell problem is being converted into a 2D surface problem with a small thickness. Based on this understanding, it is to believe that the shell theory should be the best continuum mechanics model for graphene mechanics.

Regarding the mechanics modeling of the graphene, most of literature considered the graphene as a 2D pre-stretched membrane with zero thickness [15–18], and some considered the graphene bending properties [19–22]. Since monolayer graphene is very thin, to some extent the membrane theory could be very simple and quite good estimate model, but for tiny and delicate NEMS devices, any small thing must be taken into account as it might has a significant impact on graphene, for instance, graphene's thickness [3, 6].

Although graphene's thickness is very small, one layer graphene thickness is 0.335 nm [5], but it cannot be ignored as zero, because the thickness plays a key role to supply a bending stiffness. The graphene should be modelled as a very thinner 3D object by shell theory [8–14].

The current shell theory [8–14] can be directly applied to the deformation analysis of nanostructures, for instance, [7, 22]. Reference [22] considered the effects of surface tension on the elastic properties of nanostructures, and [7] discussed a promised nanomaterials nanotorus. However, how to introduce the chiral index (n, m) into continuum model of the graphene is still an open problem. The present manuscript adopts the continuum shell model with single director to describe the mechanical behaviors of graphene. In order to consider the intrinsic features of the graphene honeycomb lattice-chiral index (n, m) , the chiral-tube vectors of graphene in real space have been used for construction of reference unit base vectors of the shell model; therefore, the formulations will contain the chiral index automatically, or in explicit form in physical components. The results are quite useful for future studies of graphene mechanics.

The paper is organized as follows. Some elasticity concepts and kinematics of a deformable surface will be introduced in Section 2; the parameterization of single director shell and deformation mode will be demonstrated in Sections 3 and 4. The basis vectors will be established in Section 5. The deformation gradient for both with and without predeformation will be formulated in Sections 6 and 7. The explicit form of the chiral index (n, m) in the physical components will be shown in the Section 8.

2. Some Elasticity Concepts

2.1. Configuration, Deformation, and Parametrization. Let B represent the stress-free or reference placement of the physical body with boundary ∂B . Points of B are indentified by $\mathbf{X} \in B$. Let B be parametrized by the one to one point

mapping function Φ , such that $B = \{\mathbf{X} = \Phi(\xi^1, \xi^2, \xi^3) \in R^3 \mid (\xi^1, \xi^2, \xi^3) \in \Omega\}$ where $\Omega \subset R^3$ is the parametric image of the body under the inverse mapping Φ^{-1} . Denote the deformed configuration of the body by S with the boundary of S given by ∂S . Points in S are identified by $\mathbf{x} \in S$. The time-dependent configurations are parametrized by one to one point mapping function Φ , such that $S = \{\mathbf{x} = \Phi(\xi^1, \xi^2, \xi^3, t) \in R^3 \mid (\xi^1, \xi^2, \xi^3) \in \Omega, t \in [0, T], \mathbf{x}|_{\partial S} = \bar{\mathbf{x}}\}$ where $\Phi(\xi^1, \xi^2, \xi^3, t)|_{t=0} \equiv \Phi^0(\xi^1, \xi^2, \xi^3)$ and $\bar{\mathbf{x}}$ is the prescribed placement of points on the boundary ∂S where the placement is given. The deformation mapping $\chi : \mathbf{X} \in B \rightarrow \mathbf{x} \in S$ is given parametrically by $\chi(\mathbf{X}, t) = \Phi \circ \Phi^0^{-1}$. Note that $\chi(\mathbf{X}, 0) = \mathbf{1}$ is the identity mapping.

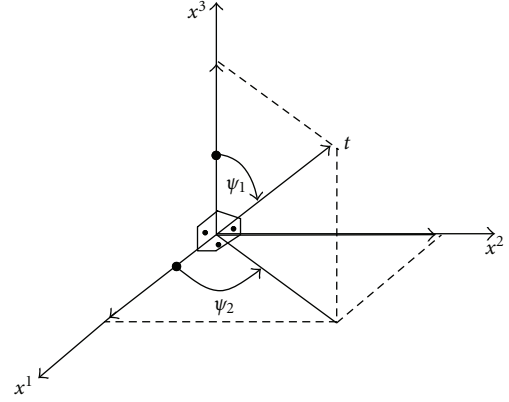


FIGURE 3: Parameterization of single director.

2.2. Tangent Basis Vectors and the Deformation Gradient. By differentiating the mapping function \mathbf{x} with respect to curvilinear coordinate (convected coordinate) function $\xi^i (i = 1, 2, 3)$, the tangent basis vectors are obtained $\mathbf{g}_i(\xi^1, \xi^2, \xi^3, t) = \mathbf{x}_{,i}(\xi^1, \xi^2, \xi^3, t)$. The fact that the tangent basis vectors are linearly independent is expressed by the relationship $\mathbf{g}_1 \cdot (\mathbf{g}_2 \times \mathbf{g}_3) > 0$. The reference or undeformed tangent basis vectors \mathbf{G}_i are obtained by particularizing the current basis vectors to $t = 0$, hence $\mathbf{G}_i = \mathbf{X}_{,i}(\xi^1, \xi^2, \xi^3)$. The dual basis vectors \mathbf{g}^i and \mathbf{G}^i are defined by the orthogonality condition $\mathbf{g}^i \cdot \mathbf{g}_j = \delta^i_j$, $\mathbf{G}^i \cdot \mathbf{G}_j = \delta^i_j$. The deformation gradient is the mapping $\mathbf{F} : R^3 \rightarrow R^3$ and is obtained by taking the material gradient of the deformation mapping χ as $\mathbf{F} = T\chi \in GL_+(3)$, where $GL_+(3) = \{\mathbf{F} \in R^{3 \times 3} \mid \det(\mathbf{F}) > 0\}$. In terms of the parametrization, \mathbf{F} is given by $\mathbf{F} = T\chi = \Delta \mathbf{x} \Delta \mathbf{X}^{-1}$. Using the above relations, the deformation gradient \mathbf{F} can be given in terms of the current tangent basis vectors and the reference dual basis vectors by $\mathbf{F} = \mathbf{g}_i \otimes \mathbf{G}^i$ or in a coordinate format as $\mathbf{F} = F^j_i \mathbf{g}_i \otimes \mathbf{G}^j$, where $F^j_i = \partial x^j / \partial X^i$, with relations $\mathbf{F}^T = \mathbf{G}^i \otimes \mathbf{g}_i$, $\mathbf{F}^{-1} = \mathbf{G}_i \otimes \mathbf{g}^i$, and $\mathbf{F}^{-T} = \mathbf{g}^i \otimes \mathbf{G}_i$. Then, the determinant of the deformation gradient J is given by $J = \det \mathbf{F} = j/j^0$, $j = \det \Delta \mathbf{x} = \mathbf{g}_1 \cdot (\mathbf{g}_2 \times \mathbf{g}_3)$, $j^0 = \det \Delta \mathbf{X} = \mathbf{G}_1 \cdot (\mathbf{G}_2 \times \mathbf{G}_3)$. Since the current and reference tangent basis vectors are linearly independent, so have $j^0 > 0$, $j > 0$, $J > 0$.

3. Parameterization of Graphene Shell Model

The variable pair (\mathbf{r}, \mathbf{d}) is chosen normally as kinematic variable, in which \mathbf{r} is the position vector and \mathbf{d} is the director field of mid-surface. Since they are vectors, so the calculations corresponding to these quantities also operate in vector space.

The reasonable parameterization of director field plays a central role in development of shell models. The director field is decomposed into a positive magnitude parameter λ and the inextensible component or unit director field \mathbf{t} , $\mathbf{d} = \lambda \mathbf{t}$, where $\lambda = |\mathbf{d}|$, $\mathbf{t} \cdot \mathbf{t} = 1$, $\mathbf{t} = \mathbf{d}/\lambda$. The unit director field \mathbf{t} is parameterized by two independent angles, that is, $\mathbf{t} = \mathbf{t}(\psi_1, \psi_2) = \{\sin \psi_1 \cos \psi_2 \sin \psi_1 \sin \psi_2 \cos \psi_1\}$. The advantage of this kind of representation of \mathbf{t} is that the variational calculation is very simple, for instance, $\delta \mathbf{t} = \mathbf{t}_{,1} \delta \psi_1 + \mathbf{t}_{,2} \delta \psi_2$.

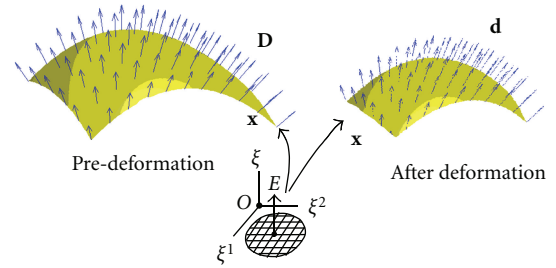


FIGURE 4: Single director shell model middle surface and director field.

4. Single Director Kinematic Modelling of Graphene

The variable pair (\mathbf{r}, \mathbf{d}) is chosen normally as kinematic variable, in which \mathbf{r} is the position vector and \mathbf{d} is the director field of deformed mid-surface and denoting \mathbf{R} and \mathbf{D} being the position vector and single director on the middle surface of undeformed configuration.

According to the long tradition of shell research [8–14], the single director field in reference or undeformed configuration can be written as

$$\mathbf{X} = \mathbf{R}(\xi^1, \xi^2, t) + \xi \mathbf{D}(\xi^1, \xi^2, t). \quad (1)$$

The single director field in current configuration can be written as

$$\mathbf{x} = \mathbf{r}(\xi^1, \xi^2, t) + \xi \mathbf{d}(\xi^1, \xi^2, t). \quad (2)$$

Thus, the points in the body are identified as the mid-surface mapping \mathbf{r} or \mathbf{R} plus the distance ξ along the director \mathbf{d} or \mathbf{D} .

The deformation mode of shell is such that points initially defined along straight fibers, that is, identified as the distance ξ above or below the mid-surface along the line defined by the initial director \mathbf{D} , remain a straight fibers. From the physical point of view, the solution to the shell problem, under the single director kinematic assumption, can be considered as the solution for the shell mid-surface plus the solution for the director which orients points along thickness fibers.

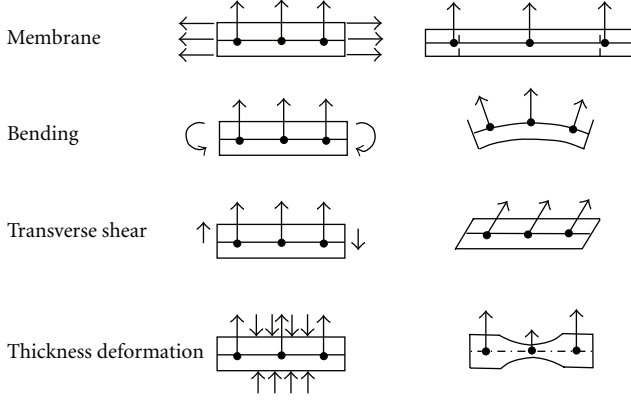


FIGURE 5: Deformation mode of the single director shell model.

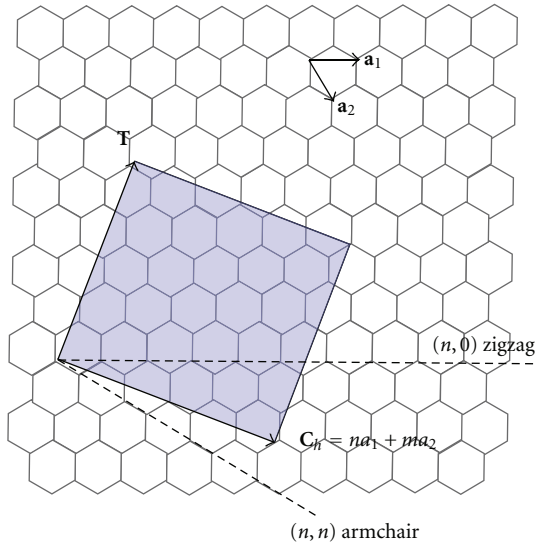


FIGURE 6: The (n, m) nanotube naming scheme can be thought of as a vector (C_h) in an infinite graphene sheet that describes how to “roll up” the graphene sheet to make the nanotube. T denotes the tube axis, and a_1 and a_2 are the unit vectors of graphene in real space. http://en.wikipedia.org/wiki/Carbon_nanotube.

Let us now check, from geometric understanding, whether the single director kinematic assumption could capture the main characteristics of shell deformation. Finite membrane stretch is captured by the deformation of the mid-surface map \mathbf{r} ; finite bending strains are modeled by the spatial gradient of the director \mathbf{d} ; transverse shear strain is accounted for by measuring the relative rotation of the director \mathbf{d} with respect to the normal to the mid-surface. The thickness change can be represented by the difference of magnitude of initial and current director.

5. Establishment of Unit Base Vectors in the Reference State (Undeformed Graphene Sheet)

The way the graphene sheet is wrapped is represented by a pair of indices (n, m) called the chiral vector. The integers n and m denote the number of unit vectors along two directions in the honeycomb crystal lattice of graphene. If $m = 0$, the nanotubes are called “zigzag”. If $n = m$, the nanotubes are called “armchair”. Otherwise, they are called “chiral”.

The orthogonal base vectors in the reference state of the grapheme can be defined as follows: let \mathbf{a}_1 be a base vector \mathbf{e}_1 , normal base vector of the grapheme plane is $\mathbf{e}_3 = \mathbf{a}_1 \times \mathbf{a}_2 / |\mathbf{a}_1 \times \mathbf{a}_2| = (2/\sqrt{3})(\mathbf{a}_1 \times \mathbf{a}_2)$, and then $\mathbf{e}_2 = (2/\sqrt{3})\mathbf{a}_2 - (1/\sqrt{3})\mathbf{a}_1$. The chiral vector C_h can be expressed as follows in terms of orthogonal base vectors: $C_h = (n + (\sqrt{3}/2)m)\mathbf{e}_1 + (\sqrt{3}/2)m\mathbf{e}_2$. The tube axes vector T is orthogonal to the chiral vectors, that is, $T \cdot C_h = 0$, then we have $T = (\sqrt{3}/2)m\mathbf{e}_1 - (n + (\sqrt{3}/2)m)\mathbf{e}_2$. The no-orthogonal base vectors $\{\mathbf{a}_1, \mathbf{a}_2, \mathbf{e}_3\}$ can be represented by orthogonal base vectors $\{\mathbf{e}_1, \mathbf{e}_2, \mathbf{e}_3\}$.

Since T and C_h are orthogonal each other, we can form another chiral-tube base vectors $\{C_h, T, E\}$, where the normal vector or single director field in undeformed grapheme plane is $E = C_h \times T = (n^2 + m\sqrt{3})\mathbf{e}_3$.

Up to now, from unit vectors of grapheme in real space, we have formulated two base vectors $\{\mathbf{e}_1, \mathbf{e}_2, \mathbf{e}_3\}$ and $\{C_h, T, E\}$. In order to capture more information about the deformed grapheme sheet, we will try to formulate its shell model based on the chiral-tube base vectors $\{C_h, T, E\}$; this work has not been found in the literature. For tensor calculation, we introduce E^i to represent the chiral-tube base vectors as follows:

$$E^1 = C_h, \quad E^2 = T, \quad E^3 = E. \quad (3)$$

Corresponding to the chiral-tube unit base vectors $\{C_h, T, E\}$, we can define three axes $\xi^i (i = 1, 2, 3)$, for instance, the any point in the graphene plane can be expressed as follows: $\xi^1 C_h + \xi^2 T = \xi^1 E^1 + \xi^2 E^2$ and any point out of the graphene plane is $\xi^2 = \xi^1 E^1 + \xi^2 E^2 + \xi E$.

6. Tangent Basis and Deformation Gradient of Graphene without Predeformation

If the grapheme sheet has no any predeformation, it will be like a plane. Since $E_{,\alpha} = \partial E / \partial \xi^\alpha = 0$, we have the tangent basis vectors in the undeformed configuration as follows:

$$G_\alpha = E_\alpha, \quad G_3 = E_3. \quad (4)$$

After the deformation, the convected tangent basis vectors in current graphene shell configuration is defined by

$$\mathbf{g}_\alpha = \mathbf{x}_{,\alpha} = \mathbf{r}_{,\alpha} + \xi \mathbf{d}_{,\alpha}, \quad \mathbf{g}_3 = \mathbf{x}_{,3} = \mathbf{d}. \quad (5)$$

The dual basis vectors are also defined by the relationships $\mathbf{g}^i \cdot \mathbf{g}_j = \delta_j^i$ and $E^l \cdot E_j = \delta_j^l$.

Then, tangent of deformation or deformation gradient F can be defined by

$$F = \mathbf{g}_i \otimes G^i = \mathbf{r}_{,\alpha} \otimes E^\alpha + \mathbf{d} \otimes E^3 + \xi \mathbf{d}_{,\alpha} \otimes E^\alpha. \quad (6)$$

If we put $\xi = 0$ in (5), then the basis vectors of the mid-surface in the current configuration can be obtained; $\mathbf{a}_i = \mathbf{g}_i|_{\xi=0}$ that is,

$$\mathbf{a}_\alpha = \mathbf{r}_{,\alpha}, \quad \mathbf{a}_3 = \mathbf{d}, \quad (7)$$

and the corresponding dual basis vectors in the mid-surface are defined by $\mathbf{a}^i \cdot \mathbf{a}_j = \delta_j^i$.

7. Deformation Gradient of Graphene with Pre-Deformation

If 2D graphene is being wrapped up to 0D nanodot, 1D nanotube, 3D stacked graphite, or been prestressed and then undergo deformation, it means that the graphene got pre-deformation.

After the pre-deformation, the convected tangent basis vectors in predeformation configuration are defined by

$$\bar{\mathbf{G}}_\alpha = \mathbf{X}_{,\alpha} = \mathbf{R}_{,\alpha} + \xi \mathbf{D}_{,\alpha}, \quad \bar{\mathbf{G}}_3 = \mathbf{X}_{,3} = \mathbf{D}. \quad (8)$$

The dual basis vectors are also defined by the relationships $\bar{\mathbf{G}}^i \cdot \bar{\mathbf{G}}_j = \delta_j^i$.

The predeformation gradient \mathbf{F}_{pre} will be

$$\mathbf{F}_{\text{pre}} = \bar{\mathbf{G}}_i \otimes \mathbf{G}^i = \mathbf{R}_{,\alpha} \otimes \mathbf{E}^\alpha + \mathbf{D} \otimes \mathbf{E}^3 + \xi \mathbf{D}_{,\alpha} \otimes \mathbf{E}^\alpha. \quad (9)$$

The after deformation gradient \mathbf{F}_{def} will be

$$\mathbf{F}_{\text{after}} = \mathbf{g}_i \otimes \bar{\mathbf{G}}^i = \mathbf{r}_{,\alpha} \otimes \bar{\mathbf{G}}^\alpha + \mathbf{d} \otimes \bar{\mathbf{G}}^3 + \xi \mathbf{d}_{,\alpha} \otimes \bar{\mathbf{G}}^\alpha. \quad (10)$$

According to the superposition of deformation gradient, the total deformation gradient will be

$$\begin{aligned} \mathbf{F}_{\text{Total}} &= \mathbf{F}_{\text{def}} \mathbf{F}_{\text{pre}} = (\mathbf{g}_i \otimes \bar{\mathbf{G}}^i) (\bar{\mathbf{G}}_j \otimes \mathbf{G}^j) = \mathbf{g}_i \otimes \mathbf{G}^i \\ &= \mathbf{r}_{,\alpha} \otimes \mathbf{E}^\alpha + \mathbf{d} \otimes \mathbf{E}^3 + \xi \mathbf{d}_{,\alpha} \otimes \mathbf{E}^\alpha. \end{aligned} \quad (11)$$

The associated Jacobian determinants are given by

$$J = \det(\mathbf{F}) = \frac{j}{j^0}, \quad j = \mathbf{g}_1 \times \mathbf{g}_2 \cdot \mathbf{g}_3, \quad j^0 = \mathbf{E}_1 \times \mathbf{E}_2 \cdot \mathbf{E}_3, \quad (12)$$

and from (8) and (9), and if we denote the director field gradient as

$$\mathbf{d}_{,\alpha} = \kappa_\alpha^\beta \mathbf{a}_\beta + \kappa_\alpha^3 \mathbf{d}, \quad \mathbf{D}_{,\alpha} = K_\alpha^\beta \mathbf{A}_\beta + K_\alpha^3 \mathbf{D}. \quad (13)$$

then, we have

$$\begin{aligned} j &= \hat{j}(1 + 2\xi h + \xi^2 \kappa), \quad \hat{j} = j|_{\xi=0} = \mathbf{r}_{,1} \times \mathbf{r}_{,2} \cdot \mathbf{d}, \\ \bar{j} &= \tilde{j}(1 + 2\xi H + \xi^2 K), \quad \tilde{j} = \bar{j}|_{\xi=0} = \mathbf{R}_{,1} \times \mathbf{R}_{,2} \cdot \mathbf{D}, \end{aligned} \quad (14)$$

where $h = (1/2)(\kappa_1^1 + \kappa_2^2)$, $\kappa = \kappa_1^1 \kappa_2^2 - \kappa_2^1 \kappa_1^2$ can be thought of as the mean and Gaussian curvature in the deformed configuration, and $H = (1/2)(K_1^1 + K_2^2)$, $K = K_1^1 K_2^2 - K_2^1 K_1^2$ can be thought of as mean and Gaussian curvature in the pre-deformation configuration. Since no deformation in the

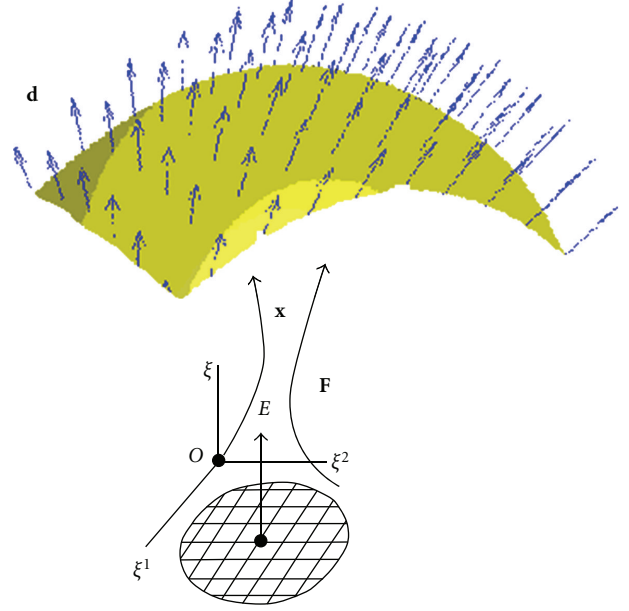


FIGURE 7: The graphene sheet without pre-deformation.

undeformed graphene plane exists, so both its mean and Gaussian curvature are zero.

For instance, the cylindrical pre-deformation [21], $x_1 = R \sin(2\pi(X_1/L))$, $x_2 = X_2$, $x_3 = R - R \cos(2\pi(X_1/L))$, where L is the width of the graphene sheet before rolling and R is the nanotube radius. The pre-deformation gradient in this case is

$$\mathbf{F}_{\text{pre}} = \begin{pmatrix} \frac{2\pi R}{L} \cos\left(2\pi \frac{X_1}{L}\right) & 0 & 0 \\ 0 & 1 & 0 \\ \frac{2\pi R}{L} \sin\left(2\pi \frac{X_1}{L}\right) & 0 & 0 \end{pmatrix}. \quad (15)$$

8. Physical Components of Some Quantities in Terms of Chiral Index (n, m)

The chiral index (n, m) is an intrinsic parameter of graphene. With our chiral-tube basis vectors, the influence of the chiral index (n, m) has been introduced into deformation gradient and can be shown explicitly in physical components.

Before going to discuss the physical components of tensor, let us here make a remark about the physical components of physical quantities. We should remember that the tensor (vector) components of a physical quantity which is referred to a particular curvilinear coordinate system may or may not have the same physical dimensions. In this case a great convenience arises because we would like to keep our freedom in choosing arbitrary curvilinear coordinates. For this reason, we must distinguish the tensor components from the ‘‘physical components’’, which must have uniform physical dimensions, but they do not transfer conveniently under coordinate transformations.

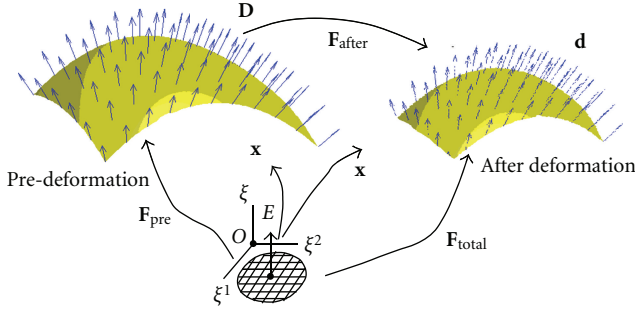


FIGURE 8: The grapheme with pre-deformation.

First of all, let us consider the physical components of a vector $\mathbf{u} = u^i \mathbf{g}_i = \mathbf{u} \cdot \mathbf{g}^i$. It is clearly that the base vectors \mathbf{g}_i and \mathbf{g}^i are in general not unit vectors. In fact, their lengths are $|\mathbf{g}_i| = \sqrt{\mathbf{g}_i \cdot \mathbf{g}_i} = \sqrt{g_{ii}}$, $|\mathbf{g}^i| = \sqrt{\mathbf{g}^i \cdot \mathbf{g}^i} = \sqrt{g^{ii}}$, i not in summation. Then $\hat{\mathbf{g}}_i = \mathbf{g}_i / \sqrt{g_{ii}}$, $\hat{\mathbf{g}}^i = \mathbf{g}^i / \sqrt{g^{ii}}$ are unit vectors. With the notation of the unit vectors, the vector can be rewritten as

$$\mathbf{u} = u^i \mathbf{g}_i = u^i \sqrt{g_{ii}} \hat{\mathbf{g}}_i \equiv \hat{u}^i \hat{\mathbf{g}}_i = u_i \mathbf{g}^i = u_i \sqrt{g^{ii}} \hat{\mathbf{g}}^i \equiv \hat{u}_i \hat{\mathbf{g}}^i, \quad (16)$$

where $\hat{u}^i = u^i \sqrt{g_{ii}}$, $\hat{u}_i = u_i \sqrt{g^{ii}}$ will have the same physical dimensions. It is seen that \hat{u}^i are the components of \mathbf{u} resolved in the direction of unit vectors $\hat{\mathbf{g}}_i$ which are tangent to the coordinate lines, and that \hat{u}_i are the components of \mathbf{u} resolved in the direction of unit vectors $\hat{\mathbf{g}}^i$ which are perpendicular to the coordinate planes. So the components \hat{u}^i and \hat{u}_i are called the physical components of the vector \mathbf{u} , and $\hat{\mathbf{g}}_i$ and $\hat{\mathbf{g}}^i$ are physical base vectors. This means that that the physical components of a vector \mathbf{u} can be defined as the components of \mathbf{u} resolved in the directions of a set of unit vectors which are parallel either to the set of base vectors or to the set of reciprocal base vectors.

Similarly, for the reference or undeformed state, then $\hat{\mathbf{E}}_i = \mathbf{E}_i / \sqrt{G_{ii}}$, $\hat{\mathbf{E}}^i = \mathbf{E}^i / \sqrt{G^{ii}}$. For tensor calculation, we define the chiral-tube unit physical base vectors as

$$\hat{\mathbf{E}}_1 = \frac{\mathbf{C}_h}{|\mathbf{C}_h|}, \quad \hat{\mathbf{E}}_2 = \frac{\mathbf{T}}{|\mathbf{T}|}, \quad \hat{\mathbf{E}}_3 = \frac{\mathbf{E}_3}{|\mathbf{E}_3|}, \quad (17)$$

where $|\mathbf{C}_h| = \sqrt{\mathbf{C}_h \cdot \mathbf{C}_h} = \sqrt{(n + (\sqrt{3}/2)m)^2 + ((\sqrt{3}/2)m)^2}$, $|\mathbf{T}| = \sqrt{(n + (\sqrt{3}/2)m)^2 + ((\sqrt{3}/2)m)^2}$, and $|\mathbf{E}_3| = (n^2 + m\sqrt{3})$. It is indicated in (14) that chiral index has been included into the physical components of base vectors. Since all quantities and variables must be established on the base vectors, all of them will be represented by the chiral index. This is the beauty of this work. For "zigzag" with $m = 0$, we have $\hat{\mathbf{E}}_1 = \mathbf{C}_h/n$, $\hat{\mathbf{E}}_2 = \mathbf{T}/n$, $\hat{\mathbf{E}}_3 = \mathbf{E}_3/n^2$; for "armchair" with $n = m$, we have

$$\hat{\mathbf{E}}_1 = \frac{2\mathbf{C}_h}{(n\sqrt{7+2\sqrt{3}})}, \quad \hat{\mathbf{E}}_2 = \frac{2\mathbf{T}}{n\sqrt{7+2\sqrt{3}}}, \quad (18)$$

$$\hat{\mathbf{E}}_3 = \frac{\mathbf{E}_3}{n^2(1+\sqrt{3})}.$$

Using the above physical component in (14), for instance, the 2nd Piola-stress tensor of the shell model can be written in physical component form:

$$\begin{aligned} \mathbf{S} &= J\mathbf{F}^{-1}\boldsymbol{\sigma}\mathbf{F}^{-T} = J\sigma^{ij}\mathbf{E}_i \otimes \mathbf{E}_j \\ &= J\sigma^{ij}\sqrt{E_{ii}}\sqrt{G_{jj}}\hat{\mathbf{E}}_i \otimes \hat{\mathbf{E}}_j \equiv \hat{\mathbf{S}}^{ij}\hat{\mathbf{E}}_i \otimes \hat{\mathbf{E}}_j. \end{aligned} \quad (19)$$

Similarly, all other quantities can be explicitly expressed in terms of the chiral index (n, m) .

9. Conclusion

This paper investigates the possibility of introducing the chiral index (n, m) into the deformation formulation of graphene continuum shell model. For this purpose, we established a chiral-tube basis vectors from graphene unit vectors in real space and formulated graphene deformation gradient for both with and without predeformation. The importance of the chiral index on the deformation and stress has been shown explicitly in the physical components.

Acknowledgments

This work was supported by South Africa National Research Foundation. This support is gratefully acknowledged. The author would like to express his thankfulness to the constructive comments and insightful suggestions given by three anonymous referees.

References

- [1] A. K. Geim and K. S. Novoselov, "The rise of graphene," *Nature Materials*, vol. 6, no. 3, pp. 183–191, 2007.
- [2] A. K. Geim, "Graphene: status and prospects," *Science*, vol. 324, no. 5934, pp. 1530–1534, 2009.
- [3] A. K. Geim and K. S. Novoselov, "The rise of graphene," *Nature Materials*, vol. 6, no. 3, pp. 183–191, 2007.
- [4] B. Sun and X. M. Henry Huang, "Mechanical nano-resonators at ultra-high frequency and their potential applications," *South Africa Journal of Science*, vol. 104, pp. 169–171, 2008.
- [5] C. Q. Ru, "Axially compressed buckling of a doublewalled carbon nanotube embedded in an elastic medium," *Journal of the Mechanics and Physics of Solids*, vol. 49, no. 6, pp. 1265–1279, 2001.
- [6] Y. Wu, M. Huang, F. Wang et al., "Determination of the young's modulus of structurally defined carbon nanotubes," *Nano Letters*, vol. 8, no. 12, pp. 4158–4161, 2008.
- [7] B. Sun, "Deformation, vibration, and buckling of nanotorus," *Journal of Nanomaterials*. In press.
- [8] W. Z. Chien, "The intrinsic theory of thin shells and plates, I," *Quarterly of Applied Mathematics*, vol. 1, pp. 297–327, 1943.
- [9] W. Z. Chien, "The intrinsic theory of thin shells and plates, II," *Quarterly of Applied Mathematics*, vol. 2, pp. 120–135, 1944.
- [10] W. T. Koiter, "On the nonlinear theory of thin elastic shells," *Proceedings of the Koninklijke Nederlandse Akademie van Wetenschappen. Series B*, vol. 69, pp. 1–54, 1966.
- [11] P. M. Naghdi, *The Theory of Shells, Handbuch der Physik*, vol. 2, Springer, Berlin, Germany, 1972, edited by C. Truesdell.
- [12] J. L. Sanders, "Non-linear theories for thin shells," *Quarterly of Applied Mathematics*, vol. 21, pp. 21–36, 1963.

- [13] J. C. Simo and D. D. Fox, "On a stress resultant geometrically exact shell model. Part I: formulation and optimal parametrization," *Computer Methods in Applied Mechanics and Engineering*, vol. 72, no. 3, pp. 267–304, 1989.
- [14] B. Sun and R. Liu, "Single director shell model without complex geometric concepts," *Advance in Mechanics*, vol. 35, no. 2, pp. 181–194, 2003.
- [15] C. Lee, X. Wei, J. W. Kysar, and J. Hone, "Measurement of the elastic properties and intrinsic strength of monolayer graphene," *Science*, vol. 321, no. 5887, pp. 385–388, 2008.
- [16] J. Atalaya, A. Isacsson, and J. M. Kinaret, "Continuum elastic modeling of graphene resonators," *Nano Letters*, vol. 8, no. 12, pp. 4196–4200, 2008.
- [17] J. S. Bunch, S. S. Verbridge, J. S. Alden et al., "Impermeable atomic membranes from graphene sheets," *Nano Letters*, vol. 8, no. 8, pp. 2458–2462, 2008.
- [18] B. I. Yakobson, C. J. Brabec, and J. Bernholc, "Nanomechanics of carbon tubes: instabilities beyond linear response," *Physical Review Letters*, vol. 76, pp. 2511–2514, 1996.
- [19] M. Arroyo and T. Belytschko, "Finite crystal elasticity of carbon nanotubes based on the exponential Cauchy-Born rule," *Physical Review B*, vol. 69, no. 11, Article ID 115415, 11 pages, 2004.
- [20] Y. Huang, J. Wu, and K. C. Hwang, "Thickness of graphene and single-wall carbon nanotubes," *Physical Review B*, vol. 74, no. 24, Article ID 245413, 2006.
- [21] Q. Lu and R. Huang, "Nonlinear mechanics of single-atom-layer graphene sheets," *International Journal of Applied Mechanics*, vol. 1, no. 3, pp. 443–467, 2009.
- [22] Z.-Q. Wang, Y.-P. Zhao, and Z.-P. Huang, "The effects of surface tension on the elastic properties of nano structures," *International Journal of Engineering Science*, vol. 48, no. 2, pp. 140–150, 2010.

Research Article

Isotope Effect on the Thermal Conductivity of Graphene

Hengji Zhang,¹ Geunsik Lee,¹ Alexandre F. Fonseca,²
Tammie L. Borders,³ and Kyeongjae Cho^{1,4}

¹ Department of Physics, University of Texas at Dallas, Richardson, TX 75080, USA

² Departamento de Física, Instituto de Ciências Exatas (ICEx), Universidade Federal Fluminense, 27213-350, Volta Redonda, RJ, Brazil

³ Department of Chemistry, University of North Texas, Denton, TX 76203, USA

⁴ Department of Materials Science and Engineering, University of Texas at Dallas, Richardson, TX 75080, USA

Correspondence should be addressed to Kyeongjae Cho, kjcho@utdallas.edu

Received 1 June 2010; Accepted 7 July 2010

Academic Editor: Rakesh Joshi

Copyright © 2010 Hengji Zhang et al. This is an open access article distributed under the Creative Commons Attribution License, which permits unrestricted use, distribution, and reproduction in any medium, provided the original work is properly cited.

The thermal conductivity (TC) of isolated graphene with different concentrations of isotope (C_{13}) is studied with equilibrium molecular dynamics method at 300 K. In the limit of pure C_{12} or C_{13} graphene, TC of graphene in zigzag and armchair directions are ~ 630 W/mK and ~ 1000 W/mK, respectively. We find that the TC of graphene can be maximally reduced by $\sim 80\%$, in both armchair and zigzag directions, when a random distribution of C_{12} and C_{13} is assumed at different doping concentrations. Therefore, our simulation results suggest an effective way to tune the TC of graphene without changing its atomic and electronic structure, thus yielding a promising application for nanoelectronics and thermoelectricity of graphene-based nano device.

1. Introduction

Since it was fabricated in 2004 [1], graphene, a monolayer of sp²-bonded network of carbon atoms, has attracted much attention for its unique electronic properties [2]. Meanwhile, both recent theory and experiment studies [3, 4] have revealed that isolated graphene has shown an unusual high thermal transport capability, which is of great importance in thermal management of nanoelectronics. Different from conventional metallic materials, thermal energy carriers for graphene are mainly in the form of phonon vibrations [3–5], and phonon contribution to TC is approximately 50 times larger than electron contribution at room temperature [3], which suggests that electron thermal transport is negligible in our case. Furthermore, the electronic contribution to TC would be independent of isotope effect as C_{13} is electronically identical to C_{12} . For these reasons, we will study only the phonon contribution to TC in this paper.

In addition to utilizing its high TC, another possible application of graphene has been investigated for thermoelectric energy conversion [6], where low TC but high electric conductivity for graphene is required for obtaining high thermoelectric efficiency. Such efficiency is expressed

as $ZT = (\sigma S^2/\kappa)T$, where σ is the electric conductivity, S is the Seebeck coefficient, and κ is the thermal conductivity. To achieve high ZT for graphene, a general scheme is to minimize κ while keeping σ and S less changed. One practical method is to dope the graphene with the stable isotope C_{13} since electronic structure of graphene is unchanged in this doping. In a pure crystal, one without defects or dislocations, phonon scattering in the presence of different isotopes has been strongly correlated with changes in thermal conductivity. Similar to the observation for isotope effects on TC of Ge, diamond, and boron nitride nanotubes [7, 8], it is interesting to check how effectively isotope-doping method will reduce TC of Graphene.

Modeling of thermal transport can be achieved by using Boltzmann transport equation (BTE) [9, 10], or molecular dynamics (MD) simulations [11]. In BTE method, the single mode relaxation time (SMRT) approximation is a commonly used technique involving the assignment of the relaxation time to different phonon scattering mechanisms. The relaxation time can be either fitted to the experimental TC value [12] or determined from MD simulations [10]. In MD simulation approach, TC can be predicted from either nonequilibrium MD [13], where a temperature is applied

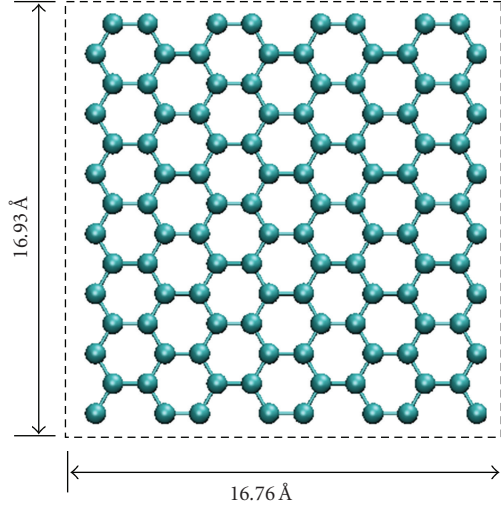


FIGURE 1: Structure of graphene unit cell with 112 carbon atoms.

across the simulation cell, or equilibrium MD [14], where the so-called Green-Kubo method is used to compute TC from heat current fluctuations. One advantage for MD method is that there is no assumption needed for phonon interactions. As long as the phonon dispersion and anharmonicity of the potential are accurate, MD method provides a robust way to accurately compute thermal transport.

In Section 2, we introduce Green-Kubo method and describe the simulation procedures to compute TC. In Section 3, we show the isotope effects on thermal transport of graphene, and discuss the reason for TC reduction and its possible application for thermoelectric application. Section 4 presents a summary and conclusions.

2. Green-Kubo MD Simulation Method

The Green-Kubo formula [14] derived from linear response theory can express thermal conductivity tensor in terms of equilibrium heat current-current autocorrelation in the form

$$\kappa_{\alpha\beta} = \frac{1}{\Omega k_B T^2} \int_0^{\tau_m} \langle \vec{J}_\alpha(\tau) \cdot \vec{J}_\beta(0) \rangle d\tau, \quad (1)$$

where Ω is the system volume defined as the area of graphene multiplied with van der Waals thickness (3.35 Angstrom), k_B is the Boltzmann constant, T is the system temperature, and τ_m is the time required to be longer than the time for current-current correlations to decay to zero [11]. $J_{\alpha,\beta}$ is denoted as the heat flux in α or β direction, its expression is commonly defined as

$$\vec{J} = \frac{d}{dt} \sum_i \vec{r}_i(t) E_i(t), \quad (2)$$

$$E_i = \frac{1}{2} m v_i^2 + \phi_i, \quad (3)$$

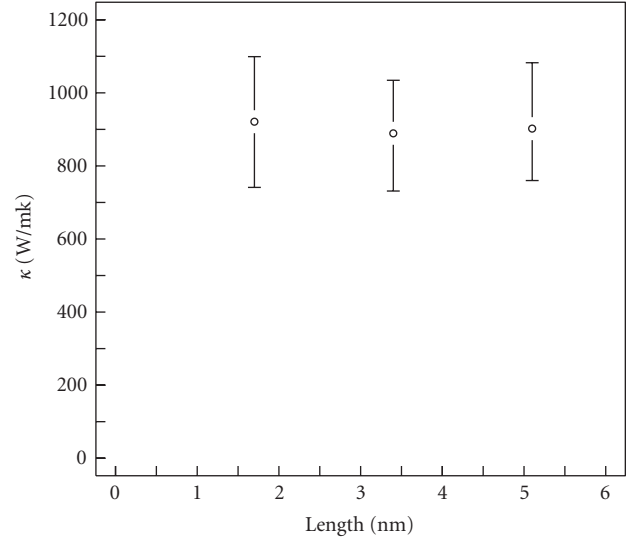


FIGURE 2: Graphene TC convergence tests with different unit cell boundary lengths. κ is the average of TC in zigzag and armchair directions.

where \vec{r}_i , v_i , and E_i are the position, velocity and site energy of atom i , respectively. ϕ_i is the potential energy at site i . Then, we use Hardy's definition [15],

$$\vec{J} = \sum_i \left[E_i \vec{v}_i + \frac{1}{2} \sum_{j \neq i} \vec{r}_{ij} (\vec{F}_{ij} \cdot \vec{v}_i) \right], \quad (4)$$

where $\vec{r}_{ij} = \vec{r}_i - \vec{r}_j$ and F_{ij} is the force exerted on atom i by atom j . One merit of Hardy's definition is that it is independent of pair-wise or many-body potential formulas. Based on the above equations, heat current at each step is recorded on disk as a quantity defined by atom positions, velocities, and interatomic forces, which can be extracted from atomistic simulations. The last step is to compute TC tensor with the known heat current in (1).

In the equilibrium MD simulations, we used the second generation REBO carbon potential for its accuracy in describing bond strength and anharmonicity of carbon materials [16]. A unit cell of graphene, with a periodic boundary condition as shown in Figure 1, has been thermalized to 300 K for 200 ps with Berendsen thermostats. Afterwards, the heat current of graphene is recorded every 2 fs in nine microcanonical ensemble simulations with uncorrelated initial conditions. Each microcanonical simulation needs to run up to 10 ns to obtain converged TC value. Compared with nonequilibrium molecular dynamics (NEMD), the Green-Kubo method is indeed less computationally efficient; however, it is free of troubles such as finite size and boundary effects, which are commonly unavoidable in NEMD.

3. Results and Discussion

We computed the TC of mass defect-free graphene as 630 W/mk and 1000 W/mk in armchair and zigzag direction,

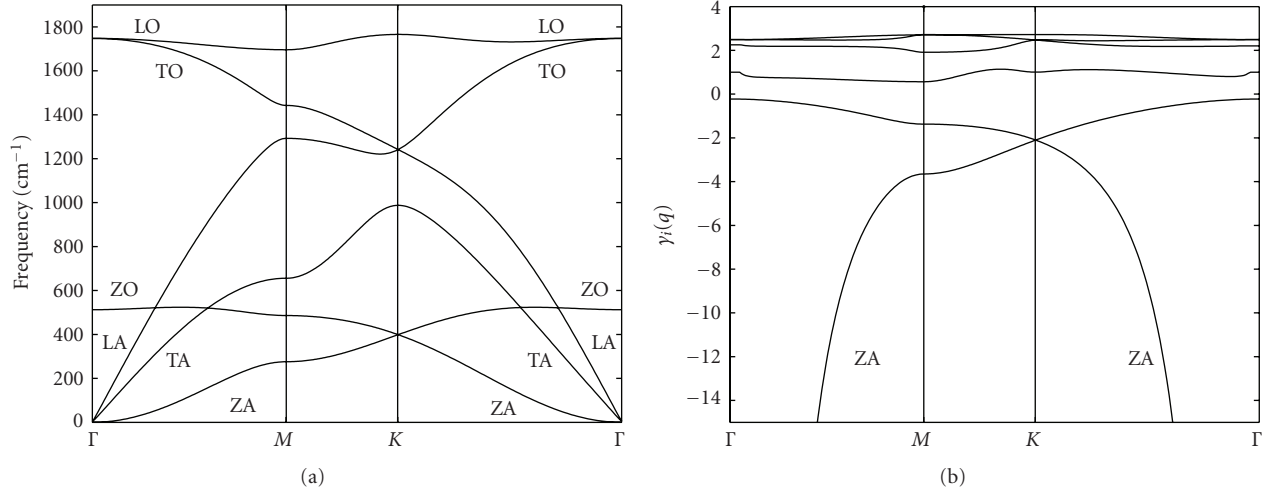


FIGURE 3: (a) Phonon dispersions for C_{12} graphene and (b) Grüneisen parameters of graphene as a function of q momentum for each vibration mode. ΓM and ΓK represent armchair and zigzag directions of graphene. Phonon dispersion for graphene is calculated with PHON code [17] for REBO carbon potential.

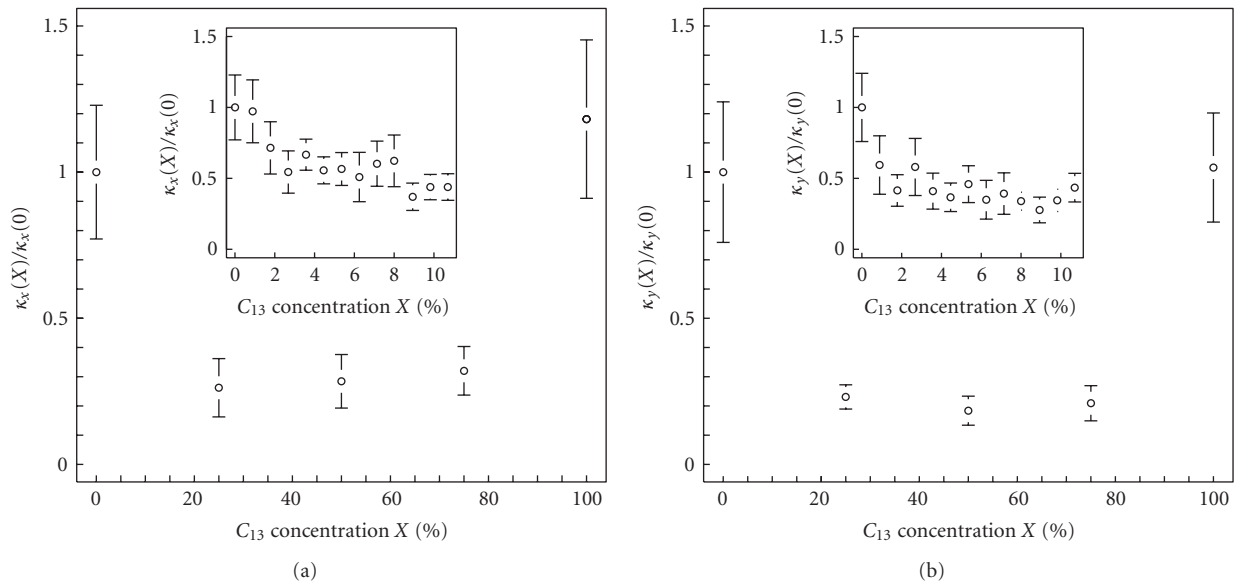


FIGURE 4: Normalized Graphene TC as a function of C_{13} concentration (a) TC in armchair direction (b) TC in zigzag direction. The inset shows TC as a function of C_{13} for low concentration. The normalizing factors κ_x and κ_y are the values for pure graphene, 630 W/mK and 1000 W/mK, respectively.

respectively. This is lower than the reported experimental data [4, 5]. The reason has to do with the discrepancies on phonon dispersion between experiment measurement and theoretical data predicted with original REBO potential [18]. Although the absolute TC of graphene is overall underestimated in our simulation, the relative difference of TC caused by isotope mass defect is still physically meaningful, and the normalized TC reduction seen in Figure 4 properly reflects the isotope effect on TC of graphene.

One primary test done before studying isotope effects on thermal transport is the convergence test for graphene with different unit cell periodic boundary lengths. As shown

in Figure 2, we have tested three cases with the boundary length of 1.6, 3.4, and 5.1 nm respectively, and the converged result suggests that the majority contribution from different phonon vibration modes are well included in our simulations. Then, to be efficient, we choose the 1.6 nm unit cell as the structure for the following simulations.

The first thing we learned from the simulations is that TC of pure C_{12} or C_{13} graphene in zigzag direction is $\sim 58\%$ greater than that in armchair direction. This can be conceptually explained from the acoustic phonon dispersion and Grüneisen parameter of graphene calculated with REBO potential as shown in Figure 3. In the SMRT approximation,

the BTE method can express TC as a summation of each phonon mode contribution, $\kappa = \sum_i \sum_q \kappa_i(\vec{q})$ and $\kappa_i = C_i(\vec{q})v_i^2(\vec{q})\tau^{ph}(\vec{q})$ where i and \vec{q} represent phonon modes and wave momentum, and $C_i(\vec{q})$ is the specific heat of the phonons, which is constant in the classical case. v_i is the group velocity for mode i , τ^{ph} is the relaxation time, and T is the temperature. From Figure 3(a), we notice that both out-of-plane acoustic (ZA) and transverse acoustic (TA) modes in zigzag direction have apparently larger group velocity than that in armchair direction, longitudinal acoustic (LA) modes group velocity in both directions is quite similar. Then, from Figure 3(b), the Grüneisen parameter, which is plotted as a function of phonon mode i and momentum q , shows a smaller difference in zigzag and armchair directions for each vibration mode. As the Grüneisen parameters for LA, TA, and ZA are similar, it is reasonable to assume that the relaxation times for phonon vibration in zigzag and armchair direction are the same. Based on the above analysis, we conclude that the difference in the TC between zigzag and armchair directions mainly comes from their different group velocities.

In the isotope effect study, we generated a wide range of graphene samples with different C_{13} concentrations randomly distributed, since it is a more realistic possible configuration after the synthesis of graphene. Recently, Mingo et al. have proposed a possible method to generate isotope clusters in graphene, and theoretically demonstrated TC reduction using nonequilibrium Green's function method [19]. Figure 4 shows the normalized graphene TC values as a function of C_{13} concentration in armchair and zigzag directions, and the maximum TC reduction for graphene can be made between 25% and 75% of the C_{13} atomic concentrations.

The explanation of the almost “parabolic” shape of TC in Figure 4 can be found in an earlier important relation derived by Klemens [20]. As it is commonly accepted, the longer the phonon mean free path is, the larger TC would be. Klemens found that, for isotope scattering, the mean free path is proportional to $g^{-1}T^{-4}$, where $g = \sum_i C_i[(M_i^2 - (\sum C_i M_i))/(\sum C_i M_i)^2]^2$ and T is the temperature. C_i and M_i represent the concentration and the mass of the constituent isotope atoms, respectively. Thus, the mean free path directly has to do with the g factor, which is the mass variation of isotope atoms. In our simulation, g factor reaches its maximum for around 50% of C_{13} , so there we have the minimum phonon mean free path and the minimum TC. As C_{13} atomic concentration approaches to zero or 100%, g becomes smaller, phonon free path is larger, and TC increases. It will not get to infinity because of the Umklapp and other phonon scattering mechanisms.

Among various methods that modulate the TC of graphene, the isotope-doping method provides an efficient way to improve thermoelectric efficiency, since isotope atoms do not change the electronic structure of graphene, the electric conductivity, and the Seebeck coefficient remains the same after the C_{13} doping. As our simulations suggest, κ in armchair and zigzag directions can be reduced by up to 80%, which means an improvement of the ZT by a factor of 5 since

ZT is inversely proportional to TC. Recently, two important simulation studies were carried out on ZT of armchair [21] and zigzag [22] graphene nanoribbons (GNRs). In both works, the authors looked for defect and disordered structures that minimize TC while keep electric conductivity less changed, thus maximizing the ZT. Compared with this, the isotope-doping method appears to be another attractive method that would promote ZT even further for GNRs when it is combined with those methods [21, 22]. We believe our results can motivate new experiments to check the efficiency of isotope-doping method for thermoelectric application.

4. Conclusion

In summary, we have studied isotope effect on TC of isolated graphene with equilibrium MD methods. Our simulation results suggest that TC of graphene can be effectively reduced by up to 80% in armchair and zigzag directions for isotope concentrations as low as 25%. The phenomenon that mass defect can reduce TC is explained with the relation between phonon mean free path and mass variation of the isotope mixtures [20]. Finally, our study shows that doping graphene with carbon isotope C_{13} could be a practical way to reduce TC without changing its electric property, thus promoting thermoelectric coefficient.

Acknowledgments

The authors are grateful to support from Lockheed Martin. G. Lee acknowledges support from SWAN, and A. F. Fonseca acknowledges partial support from the Brazilian agency CNPq. We thank Rodney Ruoff for suggesting to study isotope effect in graphene. The authors also appreciate discussions with Davide Donadio and Giulia Galli.

References

- [1] K. S. Novoselov, A. K. Geim, S. V. Morozov et al., “Electric field in atomically thin carbon films,” *Science*, vol. 306, no. 5696, pp. 666–669, 2004.
- [2] A. K. Geim and K. S. Novoselov, “The rise of graphene,” *Nature Materials*, vol. 6, no. 3, pp. 183–191, 2007.
- [3] K. Saito, J. Nakamura, and A. Natori, “Ballistic thermal conductance of a graphene sheet,” *Physical Review B*, vol. 76, no. 11, Article ID 115409, 2007.
- [4] J. H. Seol, I. Jo, A. L. Moore et al., “Two-dimensional phonon transport in supported graphene,” *Science*, vol. 328, no. 5975, pp. 213–216, 2010.
- [5] A. A. Balandin, S. Ghosh, W. Bao et al., “Superior thermal conductivity of single-layer graphene,” *Nano Letters*, vol. 8, no. 3, pp. 902–907, 2008.
- [6] D. Dragoman and M. Dragoman, “Giant thermoelectric effect in graphene,” *Applied Physics Letters*, vol. 91, no. 20, Article ID 203116, 2007.
- [7] D. T. Morelli, J. P. Heremans, and G. A. Slack, “Estimation of the isotope effect on the lattice thermal conductivity of group IV and group III-V semiconductors,” *Physical Review B*, vol. 66, no. 19, Article ID 195304, 9 pages, 2002.
- [8] C. W. Chang, A. M. Fennimore, A. Afanasiev et al., “Isotope effect on the thermal conductivity of boron nitride

- nanotubes,” *Physical Review Letters*, vol. 97, no. 8, Article ID 085901, 2006.
- [9] A. J. H. McGaughey and M. Kaviani, “Quantitative validation of the Boltzmann transport equation phonon thermal conductivity model under the single-mode relaxation time approximation,” *Physical Review B*, vol. 69, no. 9, Article ID 094303, 12 pages, 2004.
- [10] D. Donadio and G. Galli, “Thermal conductivity of isolated and interacting carbon nanotubes: comparing results from molecular dynamics and the Boltzmann transport equation,” *Physical Review Letters*, vol. 99, no. 25, Article ID 255502, 2007.
- [11] P. K. Schelling, S. R. Phillpot, and P. Keblinski, “Comparison of atomic-level simulation methods for computing thermal conductivity,” *Physical Review B*, vol. 65, no. 14, Article ID 144306, 12 pages, 2002.
- [12] S. E. Lemehov, V. Sobolev, and P. Van Uffelen, “Modelling thermal conductivity and self-irradiation effects in mixed oxide fuels,” *Journal of Nuclear Materials*, vol. 320, no. 1-2, pp. 66–76, 2003.
- [13] J. Hu, X. Ruan, and Y. P. Chen, “Thermal conductivity and thermal rectification in graphene nanoribbons: a molecular dynamics study,” *Nano Letters*, vol. 9, no. 7, pp. 2730–2735, 2009.
- [14] A. S. Henry and G. Chen, “Spectral phonon transport properties of silicon based on molecular dynamics simulations and lattice dynamics,” *Journal of Computational and Theoretical Nanoscience*, vol. 5, no. 2, pp. 141–152, 2008.
- [15] R. J. Hardy, “Energy-flux operator for a lattice,” *Physical Review*, vol. 132, no. 1, pp. 168–177, 1963.
- [16] D. W. Brenner, O. A. Shenderova, J. A. Harrison, S. J. Stuart, B. Ni, and S. B. Sinnott, “A second-generation reactive empirical bond order (REBO) potential energy expression for hydrocarbons,” *Journal of Physics Condensed Matter*, vol. 14, no. 4, pp. 783–802, 2002.
- [17] The PHONON package of D. Alfe, 2008, <http://chianti.geol.ucl.ac.uk/~dario/phon>.
- [18] L. Lindsay and D. A. Brodio, “Optimized Tersoff and Brenner empirical potential parameters for lattice dynamics and phonon thermal transport in carbon nanotubes and graphene,” *Physical Review B*, vol. 81, Article ID 205441, 6 pages, 2010.
- [19] N. Mingo, K. Esfarjani, D. A. Broido, and D. A. Stewart, “Cluster scattering effects on phonon conduction in graphene,” *Physical Review B*, vol. 81, no. 4, Article ID 045408, 6 pages, 2010.
- [20] P. G. Klemens, “The scattering of low-frequency lattice waves by static imperfections,” *Proceedings of the Physical Society A*, vol. 68, no. 12, pp. 1113–1128, 1955.
- [21] Y. Ouyang and J. Guo, “A theoretical study on thermoelectric properties of graphene nanoribbons,” *Applied Physics Letters*, vol. 94, no. 26, Article ID 263107, 2009.
- [22] H. Sevinçli and G. Cuniberti, “Enhanced thermoelectric figure of merit in edge-disordered zigzag graphene nanoribbons,” *Physical Review B*, vol. 81, Article ID 113401, 2010.

Research Article

A New Strategy to Pretreat Carbon Nanofiber and Its Application in Determination of Dopamine

Dong Liu,¹ Yang Liu,¹ Haoqing Hou,² and Tianyan You¹

¹ State Key Laboratory of Electroanalytical Chemistry, Changchun Institute of Applied Chemistry, Chinese Academy of Sciences, 5625 Renmin Street, Changchun, Jilin 130022, China

² College of Chemistry and Chemical Engineering, Jiangxi Normal University, Nanchang 330027, China

Correspondence should be addressed to Tianyan You, youty@ciac.jl.cn

Received 31 May 2010; Accepted 18 July 2010

Academic Editor: Rakesh Joshi

Copyright © 2010 Dong Liu et al. This is an open access article distributed under the Creative Commons Attribution License, which permits unrestricted use, distribution, and reproduction in any medium, provided the original work is properly cited.

A novel sonochemical process, using hydrogen peroxide in a laboratory ultrasonic bath, was employed to pretreat the carbon nanofiber (CNF) for creating oxygen-rich groups on the surface of CNF. After the sonochemical process, the CNF showed good hydrophilicity and high electrochemical activity. Compared to normal pretreatment process, this sonochemical process is timesaving and effective for dispersion and functionalization of CNF. The resulting CNF showed high catalytic activity toward the oxidation of DA. A carbon paste electrode modified by CNF (CPE-CNF) was used to determine the dopamine (DA) in the presence of ascorbic acid (AA). The detection limit is 0.05 μM , with the linear range from 0.05 μM to 6.4 μM .

1. Introduction

Carbonaceous materials, especially carbon nanotube (CNT), attracted great research interests, and lots of investigations have been done in the field of chemical biosensors and fuel cells. Comparing with CNT, carbon nanofiber (CNF) exhibits unique mechanical and catalytic properties, high electrical conductivity, and chemical stability. However, due to the hydrophobicity of CNF surface, the pristine CNF is difficult to be dispersed in the water. As a result, it is necessary to treat CNF for improving the hydrophilicity. Acidic mixture solution is mostly used to treat CNF. So far, the functionalization is carried out by the pretreatment of CNF in HCl, HNO₃, and KOH for improving its hydrophilicity [1]. As for CNT, a sonochemical process has already been developed to treat CNT in the acidic mixture solution to create oxygen-rich groups for depositing metal nanoparticle [2], which is found to be timesaving and effective. Except for the acidic mixture solution, hydrogen peroxide (H₂O₂) solution is also used to modify the CNT [3]. The results indicated that the aldehydic groups formed on the CNT after treated with the H₂O₂ solution, but the hydroxyl bands (–OH) and the aldehydic groups (< C=O) formed after treated with the acidic mixture solution. Although the pretreatment

using acidic mixture solution has verified its feasibility, such a method is time-consuming and complicated. It is necessary to develop a new way to treat CNF for improving the hydrophilicity, which should be simple and effective.

Dopamine (DA) takes an important part in the functioning of the human metabolism, central nervous and renal systems [4]. DA possesses high electrochemical activity and has been widely studied by electroanalytical techniques [5]. However, ascorbic acid (AA) always coexists with DA in the human body, and the oxidation potential of AA is close to that of DA. As a result, it is difficult to determine these two species separately using conventional electrodes. A large number of attempts have already been made for the determination of DA sensitively and selectively. Lots of new materials, such as C₆₀-functionalized multiwalled carbon nanotube films [6], the boron-doped carbon nanotubes [7], polymer film [8], and self-assembled monolayer [9], were applied to detect DA in the presence of AA. Moreover, at a physiological pH, DA (pK_a = 8.9) is positively charged, yet AA (pK_a = 4.2) is negatively charged, when the electrode surface is negatively charged, DA can be adsorbed and detected selectively [10]. Some materials, such as nafion, clay [11], and polymeric films [12], were precoated on the surface of the electrode so as to make it negatively charged.

We applied H_2O_2 solution to treat CNF in a laboratory ultrasonic bath. Comparing with normal acid pretreatment, this method is timesaving, and the resulting CNF shows good hydrophilicity. The CNF-modified carbon paste electrode (CNF-CPE) shows high electrochemical activity and large effective electroactive surface area. The CNF-CPE exhibits good electrochemical catalysis toward DA in the presence of AA and it can detect DA sensitively and selectively. The CNF-CPE used for the detection of DA is effective and simple in comparison with other modified electrodes, which may be applied to the practical analysis of DA.

2. Experiment

2.1. Materials. Polyacrylonitrile (PAN), dimethylformamide (DMF), and graphite powder ($2\ \mu\text{m}$) were purchased from Aldrich. Mineral oil, 30% H_2O_2 , and AA were from Beijing Chemical Co. (China), DA from Alfa Aesar. All other reagents were of analytical grade. The phosphate buffer solution was made from Na_2HPO_4 and NaH_2PO_4 . All solutions were prepared by the double-distilled water. The electrochemical measurements were carried out on a CHI 832 electrochemical workstation (Shanghai, China) with a conventional three-electrode system composed of a platinum auxiliary, a Ag/AgCl (saturated KCl) reference, and a bare or modified carbon paste working electrode.

The surface potential of the treated CNF was estimated by zeta potential measurement (Malvern, Zetasizer ZEN3600). A measurement cell was filled by the suspension of CNF and the pH of the suspension was controlled by the addition of HCl solution. The surface of the CNF was analyzed by using X-ray photoelectron spectroscopy (Thermo, ESCALAB 250). A Fourier transform infrared spectrometry (FT-IR) measurement was performed with a Bruker VERTEX 70 spectrometer.

2.2. Preparation of CNF. Carbon nanofiber was made from carbonizing the electrospun PAN nanofibers as reported [13]. 2 mg CNF was put into 4 mL 30% H_2O_2 solution. First, the mixture solution was put in a laboratory ultrasonic bath at 50°C for 5 minutes to disperse the carbon nanofiber. Then it was stirred for 10 minutes. This mixing and dispersion process was repeated to break big carbon nanofiber aggregates. After then, the mixture solution was stirred for 2 hours to make sure that there was no H_2O_2 in the solution. The mixture was separated from the solution in a centrifuge at 9000 rpm and washed with 5.0 mL of deionized water five times. Finally, the CNF was dried at 80°C . The resulting CNF was dispersed in the water with a concentration of $1\ \text{mg mL}^{-1}$.

2.3. Preparation of Electrodes. The carbon paste electrode (CPE) was prepared by mixing graphite powder and mineral oil (70:30, w/w), and then the mixture was packed into a pipette tube (1.5 mm ID; 1.4 cm depth). Electrical contact was made by inserting a copper wire. The CNF-CPE was prepared by dropping $15\ \mu\text{L}$ CNF ($1\ \text{mg/mL}$) suspension on the surface of CPE and dried at room temperature. The

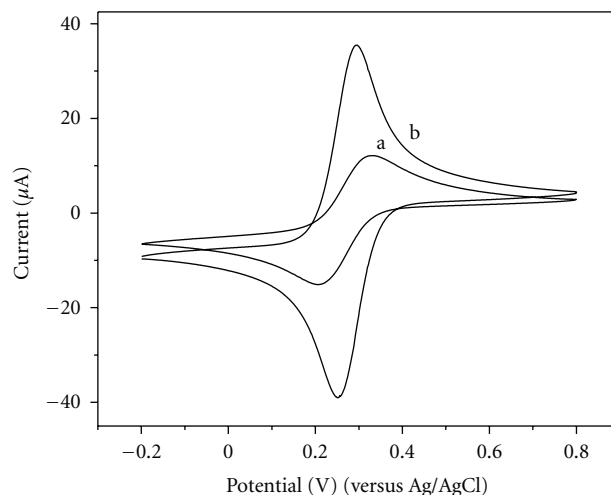


FIGURE 1: Cyclic voltammograms of 5 mM $\text{K}_3\text{Fe}(\text{CN})_6$ at the CPE (a) and CNF-CPE (b) Electrolyte, 0.5 M KCl; scan rate, $50\ \text{mVs}^{-1}$.

resulting CNF-CPE was rinsed carefully with double-distilled water before each measurement. For comparison, CPE which was prepared by the same method was used.

3. Results and Discussion

3.1. Characterization of CNF-CPE. The modified electrode prepared by a simple procedure was applied to investigate the electrochemical performance of CNF by using 5 mM $[\text{Fe}(\text{CN})_6]^{3-/4-}$ redox probe. The cyclic voltammogram for $[\text{Fe}(\text{CN})_6]^{3-/4-}$ at CPE (curve a) and CNF-CPE (curve b) was shown in Figure 1. At the CNF-CPE (curve b), a pair of well-defined redox peaks for $\text{Fe}(\text{CN})_6^{-3}/\text{Fe}(\text{CN})_6^{4-}$ appears at 296 mV and 253 mV, and the peak-to-peak separation is 44 mV, whereas at the bare CPE the peak-to-peak separation is over 119 mV (Figure 1, curve a). The result demonstrates that the use of CNF can increase the electron transfer rate. In contrast to anodic peak current of the bare CPE, that of CNF-CPE is increased by 2.1-fold, which reveals that the presence of CNF enlarged the effective electroactive surface area. Therefore, the use of CNF significantly improves the reversibility of the redox reaction and enlarges electroactive surface area of the modified electrode which is due to the high electric conductivity of CNF [13]. Although some investigations reveal that $\text{Fe}(\text{CN})_6^{-3}/\text{Fe}(\text{CN})_6^{4-}$ is not catalyzed by oxygen-rich groups, they do require a specific surface interaction [14, 15]. It comes to that $\text{Fe}(\text{CN})_6^{-3}/\text{Fe}(\text{CN})_6^{4-}$ is “surface-sensitive” but not “oxide-sensitive”. Meantime, some investigations reveal that the oxygen-rich groups, such as carboxyl and phenol surface groups, are able to adsorb platinum ion to the surface of CNF during Pt/CNF synthesis [16].

To confirm the presence of oxygen-rich groups, the ζ -potentials of the treated CNF were measured in aqueous solutions with various pH values. From the plots in Figure 2, it can be confirmed that the treated CNF is negatively charged in deionized water (pH ~ 7), which implies the

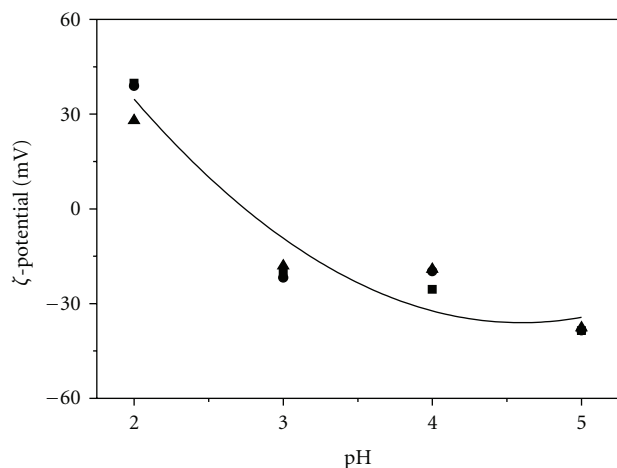


FIGURE 2: Values of ζ -potential for the water suspension of the treated CNF at different pH values.

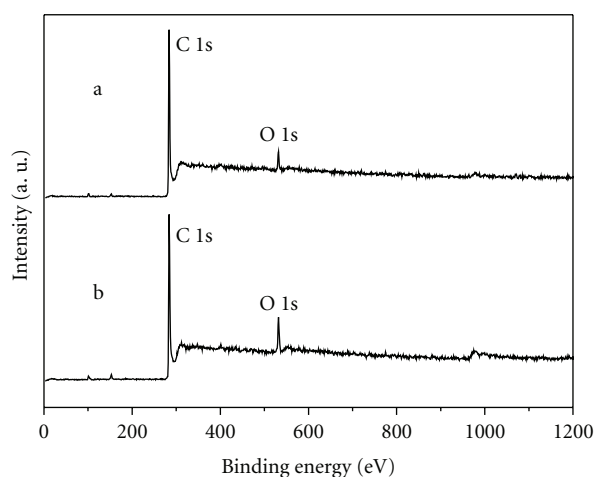


FIGURE 3: XPS scan spectrum of CNF (a) and treated CNF (b).

presence of oxygen-rich groups on the surface of the treated CNF [17], because it is well-known that the oxygen-rich groups formed on the carbon surface would make the surface negatively charged [17]. In addition, XPS was also studied as shown in Figure 3. The oxygen would present as oxygen-rich groups, such as carbonyl and carboxyl groups. The resulting O/C atomic ratio for the CNF is 0.0395, and for the treated CNF increases to 0.0889, indicating the pretreatment of CNF results in an increased amount of oxygen content [16]. Finally, a Fourier transform infrared (FT-IR) spectroscopy measurement was conducted for the treated CNF and the result is shown in Figure 4. The band at 1657 cm^{-1} and 1736 cm^{-1} can be assigned to carbonyl and carboxyl groups [18]. As for the band at 1546 cm^{-1} , the assignment is not settled [18]. From the above results, it can be concluded that oxygen-rich groups can be created after the treatment. In summary, the high electroactivity of CNF-CPE in this

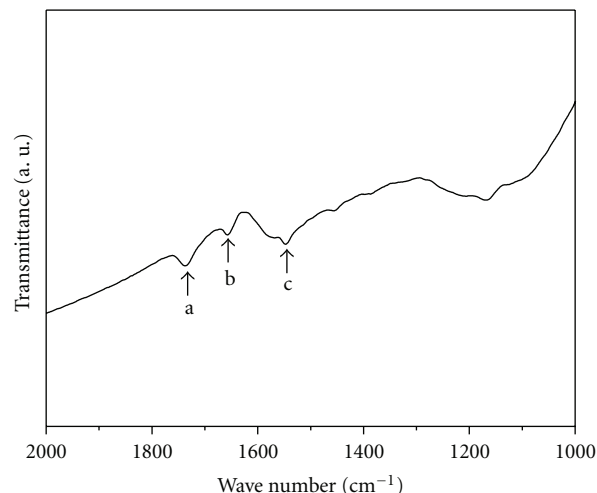


FIGURE 4: IR spectrum of the treated CNF. The three arrows in the figure indicate three IR peaks at 1736 (a), 1657 (b), and 1546 (c) cm^{-1} , respectively.

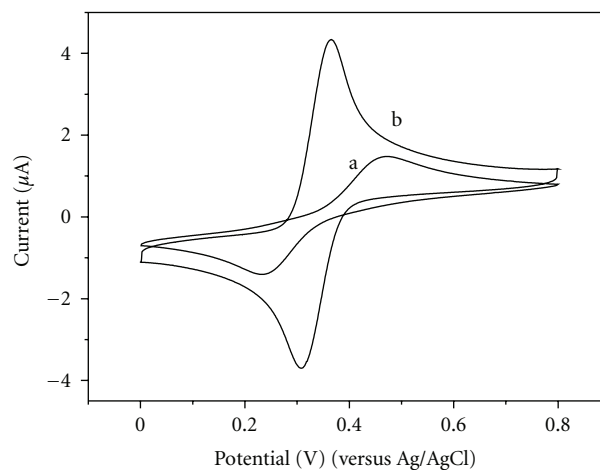


FIGURE 5: Cyclic voltammograms of DA (0.2 mM) at the CPE (a) and CNF-CPE (b) in 0.1 M PBS (pH 4.5). Scan rate, 50 mV s^{-1} .

experiment can be attributed to the unique surface of CNF resulting from the oxygen-rich groups on the surface.

3.2. Electrochemical Behavior of Dopamine at CNF-CPE. DA shows high electrochemical activity and has been widely studied by electroanalytical techniques. However, it is difficult to detect DA sensitively and selectively in the presence of AA. In addition, the electrode fouling leads to poor reproducibility and sensitivity, which is due to the adsorption of oxidation product [19]. CNF-CPE was used to investigate the electrochemical behavior of DA in PBS (pH 4.5) solution. Figure 5 shows cyclic voltammograms of DA in 0.1 M PBS at the bare CPE (curve a) and CNF-CPE (curve b). It can be observed that DA occurs quasi-reversibly with the anodic and cathodic peak potential at 473 mV and 233 mV at the bare CPE. The peak-to-peak separation is 224 mV , indicating the slow electron transfer at the bare CPE. However, the peak

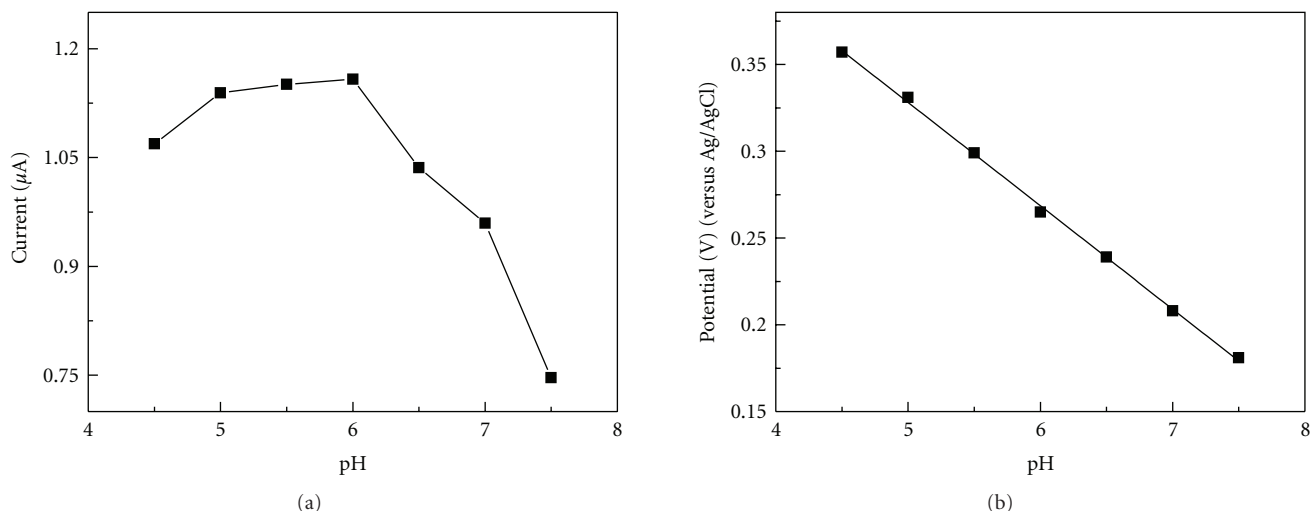


FIGURE 6: (a) Effect of pH value on the peak current of DA; (b) Effect of pH value on the anodic peak potential of DA.

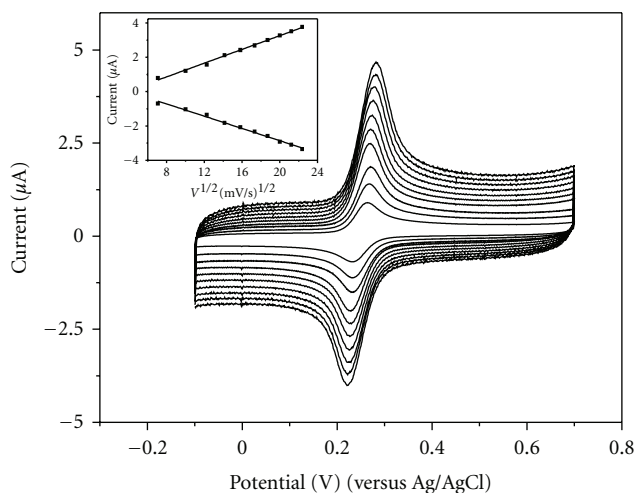


FIGURE 7: Cyclic voltammograms for the oxidation of DA at the CNF-CPE in 0.1 M PBS (pH 6.0). Scan rate: 50, 100, 150, 200, 250, 300, 350, 400, 450, and 500 mV s^{-1} . Inset plot shows the peak current versus square root of scan rate.

potential of DA oxidation exhibits more negative with the anodic and cathodic peak potential at 365 mV and 308 mV at the CNF-CPE. The peak-to-peak separation is 57 mV, which indicates that electron transfer is fast at the CNF-CPE. Furthermore, the redox current of DA at the CNF modified electrode is higher than that at the bare CPE, which demonstrates that CNF modified electrode has a remarkable catalytic activity to the redox process of DA in contrast to the bare CPE. The superior electrocatalytic activity of the CNF-CPE is mainly ascribed to the higher proportion of oxygen-functional groups presented on the surface of CNF, and large effective electroactive surface area. In addition, the oxygen-rich groups on the surface of CNF made the modified electrode negatively charged, while DA ($\text{pK}_a = 8.9$)

was positively charged in 0.1 M PBS (pH 4.5). Therefore, high redox current at the CNF-CPE can be attributed to the adsorption of DA.

In order to further investigate the electrochemical behavior of DA at CNF-CPE, the effect of pH value on the determination of DA at the CNF-CPE was carefully investigated by cyclic voltammograms in a wide pH range (pH 4.5–7.5). Figure 6(a) shows cyclic voltammograms of DA in 0.1 M PBS with different pH value at the CNF-CPE. It can be observed that the peak current of DA increases with a higher pH value until it reaches 6.0, and then it decreases with a higher pH value. In order to obtain high sensitivity, pH 6.0 was selected as an optimum pH value for the determination of DA. Figure 6(b) illustrates the relationship between the anodic peak potential (E_{pa}) of DA and the pH value of solution. It can be found that the anodic peak potential of DA shifts negatively as the increase of the pH value of solution and is linear with the pH value in the range from 4.5 to 7.5. The corresponding linear equations is $E_{pa} = -59.5\text{pH} + 0.626$ with a slope of 59.5 mV/pH ($r = 0.998$). It demonstrates that the redox of DA undergoes a two-electron and two-proton process, which is consistent with the previous reports [20].

Cyclic voltammograms was used to investigate the electrochemical behavior of DA with the different scan rate in the range from 50 to 500 mV s^{-1} . Figure 7 shows that the peak current of DA at the CNF-CPE is proportional to the scan rate in the range from 50 to 500 mV s^{-1} . It is found that the anodic and cathodic peak currents increase as the increase of the scan rate. The inset plot exhibits the corresponding plot of peak currents versus scan rate. The anodic and cathodic peak currents are linear with the square root of scan rate and the corresponding linear equations for anodic and cathodic peak currents are $i_a = 0.200v^{1/2} - 0.7396$ ($r = 0.995$) and $i_c = -0.1785v^{1/2} + 0.7119$ ($r = 0.992$), and indicates that the electrochemical oxidation of DA at the CNF-CPE is a diffusion-controlled process [7].

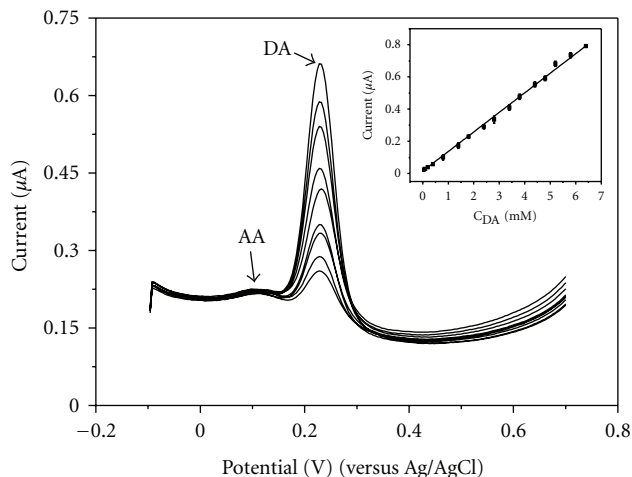


FIGURE 8: Differential pulse voltammograms at the CNF-CPE for AA ($5 \mu\text{M}$) in the presence of DA with different concentrations: (a) 0.4, (b) 0.6, (c) 0.8, (d) 1.0, (e) 1.4, (f) 1.8, (g) 2.0, (h) 2.4, and (i) $2.8 \mu\text{M}$. DPV measurements were performed from -0.1 to 0.7 V with the pulse amplitude of 50 mV and the pulse width of 50 ms. Inset plot shows the dependence of the response currents of the CNF-CPE electrode on the concentration of DA in 0.1 M PBS (pH 6.0).

3.3. Determination of Dopamine. Differential pulse voltammetry (DPV) was used for the detection of DA in the presence of AA. Figure 8 shows the DPV of DA with various concentrations in the presence of $5 \mu\text{M}$ AA at the CNF-CPE. It can be obtained that the anodic peak potential of DA and AA at 228 mV and 120 mV, and the peak-to-peak separation is about 110 mV. The oxidation current of DA shows a linear relationship with the DA concentration from $0.05 \mu\text{M}$ to $6.4 \mu\text{M}$. Moreover, the peak current of AA remains nearly unchanged with the increase of DA concentration, which demonstrates that the response of DA is not interfered in the presence of $5 \mu\text{M}$ AA. The inset plot in Figure 8 shows the corresponding results of the DPV curves of DA with different concentrations at the CNF-CPE. The linear regression equation for the response of DA can be expressed as I_p (nA) = $121.5c$ (μM) + 15.2 with a correlation coefficient of 0.998 . The detection limit is $0.05 \mu\text{M}$ at signal-to-noise ratio (SNR) of 3 , and the linear range is 0.05 to $6.4 \mu\text{M}$. The detection limit obtained in this work is lower than that at the cetylpyridinium bromide (CPB) modified SWCNTs [21] and thionine-nafion modified multiwalled carbon nanotube [22]. Comparing the linear range of dopamine obtained at the CNF-CPE with the previous reports [21, 22], the linear range at the CNF-CPE is not very wide, for the adsorption of DA at the CNF-CPE would affect the detection of dopamine.

The reproducibility and stability of the electrode were investigated. The reproducibility for $0.1 \mu\text{M}$ DA at the CNF-CPE was recorded with the RSD of 5.5% ($n = 3$). The DPV response of $4.8 \mu\text{M}$ DA at the CNF-CPE remained 96% after seven days. All the results above indicate that the CNF-CPE exhibits a good reproducibility and stability.

TABLE 1: Determination of DA in dopamine hydrochloride injection.

DA specified (μM)	Added (μM)	Found (μM)	Recovery (%)
2.1	0	1.8	—
2.1	1	3.3	106.4
2.1	2	4.2	102.4
2.1	3	4.6	92

3.4. Determination of DA in Dopamine Hydrochloride Injection. The method for analysis of DA was used in pharmaceutical product to verify the reliability. This CNF-CPE was applied to determine DA in dopamine hydrochloride injection (10 mg mL^{-1} per injection). First, the sample was diluted 10 times with double distilled water, and then appropriate amounts of the diluted sample were transferred into the electrochemical cell for the determination using DPV. The analytical results are summarized in Table 1. It can be observed that the recovery ranges from 92% to 106.4% , which is acceptable for practical analysis.

4. Conclusions

A new method was employed to pretreat the CNF, which was timesaving and effective. The resulting CNF showed good hydrophilic, high electrochemical activity, and large effective electroactive surface area, owing to the presence of the oxygen-rich groups. The electrochemical redox behavior of DA was improved obviously at the CNF-CPE. Furthermore, AA with high concentration did not alter the response of CNF-CPE toward the oxidation of DA. For the determination of DA, CNF-CPE showed good characteristics, high sensitivity and selectivity.

Acknowledgments

The authors are grateful for the financial support from the National Natural (no. 20875085) and Chinese Academy of Sciences (no. KJCX2-YW-H11).

References

- [1] L. Wu, X. Zhang, and H. Ju, "Detection of NADH and ethanol based on catalytic activity of soluble carbon nanofiber with low overpotential," *Analytical Chemistry*, vol. 79, no. 2, pp. 453–458, 2007.
- [2] S. Deng, G. Jian, J. Lei, Z. Hu, and H. Ju, "A glucose biosensor based on direct electrochemistry of glucose oxidase immobilized on nitrogen-doped carbon nanotubes," *Biosensors and Bioelectronics*, vol. 25, no. 2, pp. 373–377, 2009.
- [3] C. Xu, J. Chen, Y. Cui et al., "Influence of the surface treatment on the deposition of platinum nanoparticles on the carbon nanotubes," *Advanced Engineering Materials*, vol. 8, no. 1-2, pp. 73–77, 2006.
- [4] H. R. Zare, N. Rajabzadeh, N. Nasirizadeh, and M. Mazloum Ardakani, "Voltammetric studies of an oracet blue modified glassy carbon electrode and its application for the simultaneous determination of dopamine, ascorbic acid and uric acid,"

- Journal of Electroanalytical Chemistry*, vol. 589, no. 1, pp. 60–69, 2006.
- [5] Y. Xiao, C. Guo, C. M. Li et al., “Highly sensitive and selective method to detect dopamine in the presence of ascorbic acid by a new polymeric composite film,” *Analytical Biochemistry*, vol. 371, no. 2, pp. 229–237, 2007.
- [6] H. Zhu, W. Wu, H. Zhang, L. Fan, and S. Yang, “Highly selective and sensitive detection of dopamine in the presence of excessive ascorbic acid using electrodes modified with c_{60} -functionalized multiwalled carbon nanotube films,” *Electroanalysis*, vol. 21, no. 24, pp. 2660–2666, 2009.
- [7] C. Deng, J. Chen, M. Wang, C. Xiao, Z. Nie, and S. Yao, “A novel and simple strategy for selective and sensitive determination of dopamine based on the boron-doped carbon nanotubes modified electrode,” *Biosensors and Bioelectronics*, vol. 24, no. 7, pp. 2091–2094, 2009.
- [8] A. Ciszewski and G. Milczarek, “Polyeugenol-modified platinum electrode for selective detection of dopamine in the presence of ascorbic acid,” *Analytical Chemistry*, vol. 71, no. 5, pp. 1055–1061, 1999.
- [9] J. Kang, L. Zhuo, X. Lu, and X. Wang, “Electrochemical behavior of dopamine at a quercetin-SAM-modified gold electrode and analytical application,” *Journal of Solid State Electrochemistry*, vol. 9, no. 2, pp. 114–120, 2005.
- [10] P. R. Roy, T. Okajima, and T. Ohsaka, “Simultaneous electroanalysis of dopamine and ascorbic acid using poly (N,N-dimethylaniline)-modified electrodes,” *Bioelectrochemistry*, vol. 59, no. 1-2, pp. 11–19, 2003.
- [11] J.-M. Zen and P.-J. Chen, “A selective voltammetric method for uric acid and dopamine detection using clay-modified electrodes,” *Analytical Chemistry*, vol. 69, no. 24, pp. 5087–5093, 1997.
- [12] A. Doménech, H. García, M. T. Doménech-Carbó, and M. S. Galletero, “2,4,6-Triphenylpyrylium ion encapsulated into zeolite Y as a selective electrode for the electrochemical determination of dopamine in the presence of ascorbic acid,” *Analytical Chemistry*, vol. 74, no. 3, pp. 562–569, 2002.
- [13] J. Huang, D. Wang, H. Hou, and T. You, “Electrospun palladium nanoparticle-loaded carbon nanofibers and their electrocatalytic activities towards hydrogen peroxide and NADH,” *Advanced Functional Materials*, vol. 18, no. 3, pp. 441–448, 2008.
- [14] D. T. Fagan, I. F. Hu, and T. Kuwana, “Vacuum heat treatment for activation of glassy carbon electrodes,” *Analytical Chemistry*, vol. 57, no. 14, pp. 2759–2763, 1985.
- [15] P. Chen and R. L. McCreery, “Control of electron transfer kinetics at glassy carbon electrodes by specific surface modification,” *Analytical Chemistry*, vol. 68, no. 22, pp. 3958–3965, 1996.
- [16] A. J. Plomp, D. S. Su, K. P. D. Jong, and J. H. Bitter, “On the nature of oxygen-containing surface groups on carbon nanofibers and their role for platinum depositionsan XPS and titration study,” *Journal of Physical Chemistry C*, vol. 113, no. 22, pp. 9865–9869, 2009.
- [17] H. Orikasa, N. Inokuma, S. Okubo, O. Kitakami, and T. Kyotani, “Template synthesis of water-dispersible carbon nano ”test tubes” without any post-treatment,” *Chemistry of Materials*, vol. 18, no. 4, pp. 1036–1040, 2006.
- [18] C. Moreno-Castilla, M. V. López-Ramón, and F. Carrasco-Marín, “Changes in surface chemistry of activated carbons by wet oxidation,” *Carbon*, vol. 38, no. 14, pp. 1995–2001, 2000.
- [19] S. Hou, N. Zheng, H. Feng, X. Li, and Z. Yuan, “Determination of dopamine in the presence of ascorbic acid using poly (3,5-dihydroxy benzoic acid) film modified electrode,” *Analytical Biochemistry*, vol. 381, no. 2, pp. 179–184, 2008.
- [20] S. Jiao, M. Li, C. Wang, D. Chen, and B. Fang, “Fabrication of Fc-SWNTs modified glassy carbon electrode for selective and sensitive determination of dopamine in the presence of AA and UA,” *Electrochimica Acta*, vol. 52, no. 19, pp. 5939–5944, 2007.
- [21] Y. Zhang, Y. Pan, S. Su, L. Zhang, S. Li, and M. Shao, “A novel functionalized single-wall carbon nanotube modified electrode and its application in determination of dopamine and uric acid in the presence of high concentrations of ascorbic acid,” *Electroanalysis*, vol. 19, no. 16, pp. 1695–1701, 2007.
- [22] S. Shahrokhian and H. R. Zare-Mehrjardi, “Application of thionine-nafion supported on multi-walled carbon nanotube for preparation of a modified electrode in simultaneous voltammetric detection of dopamine and ascorbic acid,” *Electrochimica Acta*, vol. 52, no. 22, pp. 6310–6317, 2007.

Research Article

The Field Emission Properties of Graphene Aggregates Films Deposited on Fe-Cr-Ni alloy Substrates

Zhanling Lu,¹ Wanjie Wang,¹ Xiaotian Ma,¹ Ning Yao,² Lan Zhang,³ and Binglin Zhang³

¹ School of Materials Science and Engineering, Zhengzhou University, Zhengzhou 450001, China

² Materials Physics Laboratory of Education Ministry of China, Zhengzhou University, Zhengzhou 450052, China

³ Department of Engineering Mechanics, Zhengzhou University, Zhengzhou 450001, China

Correspondence should be addressed to Zhanling Lu, zllu@zzu.edu.cn

Received 31 May 2010; Accepted 21 June 2010

Academic Editor: Rakesh Joshi

Copyright © 2010 Zhanling Lu et al. This is an open access article distributed under the Creative Commons Attribution License, which permits unrestricted use, distribution, and reproduction in any medium, provided the original work is properly cited.

The graphene aggregates films were fabricated directly on Fe-Cr-Ni alloy substrates by microwave plasma chemical vapor deposition system (MPCVD). The source gas was a mixture of H₂ and CH₄ with flow rates of 100 sccm and 12 sccm, respectively. The micro- and nanostructures of the samples were characterized by Raman scattering spectroscopy, field emission scanning electron microscopy (SEM), and transparent electron microscopy (TEM). The field emission properties of the films were measured using a diode structure in a vacuum chamber. The turn-on field was about 1.0 V/μm. The current density of 2.1 mA/cm² at electric field of 2.4 V/μm was obtained.

1. Introduction

Graphene has grabbed appreciable attention due to its exceptional electronic and optoelectronic properties [1]. One of the potential applications of graphene is in field emission (FE) displays. Malesev et al. synthesized vertically aligned few-layer graphenes (FLGSs) using plasma-enhanced chemical vapor deposition (PECVD) on titanium substrate, and turn-on field of the field emission from the graphene layer was as low as 1 V/μm [2]. Qi et al. prepared FLGSs by radio-frequency PECVD on Si(100) substrates without any catalyst, and turn-on field of its emission was 3.91 V/μm [3]. We previously reported that nanocrystalline graphitic films on ceramic substrates by MPCVD using Fe-Ni-Cr layer as catalyst were deposited, the turn-on field of 1.26 V/μm was obtained [4].

In this paper, we present the field emission characteristics of the graphene aggregates films, which were synthesized by MPCVD directly on stainless steel substrate without any catalyst. The structure of the films was also studied.

2. Experiment

The Fe-Cr-Ni alloy substrates were polished with abrasive paper of W7 (particle size was about 15 μm) and then

ultrasonically cleaned with deionized water and acetone. The graphene films were deposited directly on the substrates without any catalyst by MPCVD. The source gas was a mixture of H₂ and CH₄ with flow rates of 100 sccm and 12 sccm, respectively. During the deposition, the total pressure of 6.0 KPa, substrate temperature of 700°C, and microwave power of 1600 W were kept for 10 mins.

The structure of deposited films were analyzed by Raman scattering, SEM, and TEM. The field emission properties were measured using a diode structure, which was placed in a vacuum chamber. The deposited film with area of 0.2 cm² was used as a cathode. The anode of an indium tin oxide (ITO-) coated glass was separated from the cathode by a mica spacer with thickness of 600 μm. The base pressure in the vacuum chamber was maintained below 1 × 10⁻⁴ Pa during the measurements. The voltage was stepped up from 0 to 2500 V.

3. Results and Discussion

The Raman spectrum of the sample was shown in Figure 1. The G- band appearing at 1583 cm⁻¹ originates from in-plane vibration of sp² carbon atoms and is a doubly degenerate (TO and LO) phonon mode (E_{2g} symmetry) at

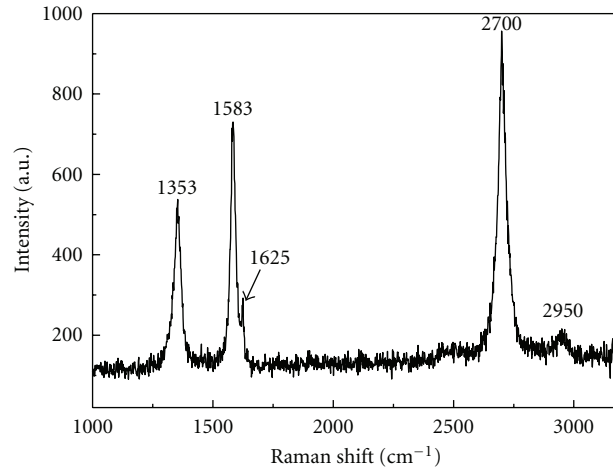


FIGURE 1: Raman shift of the as-grown sample.

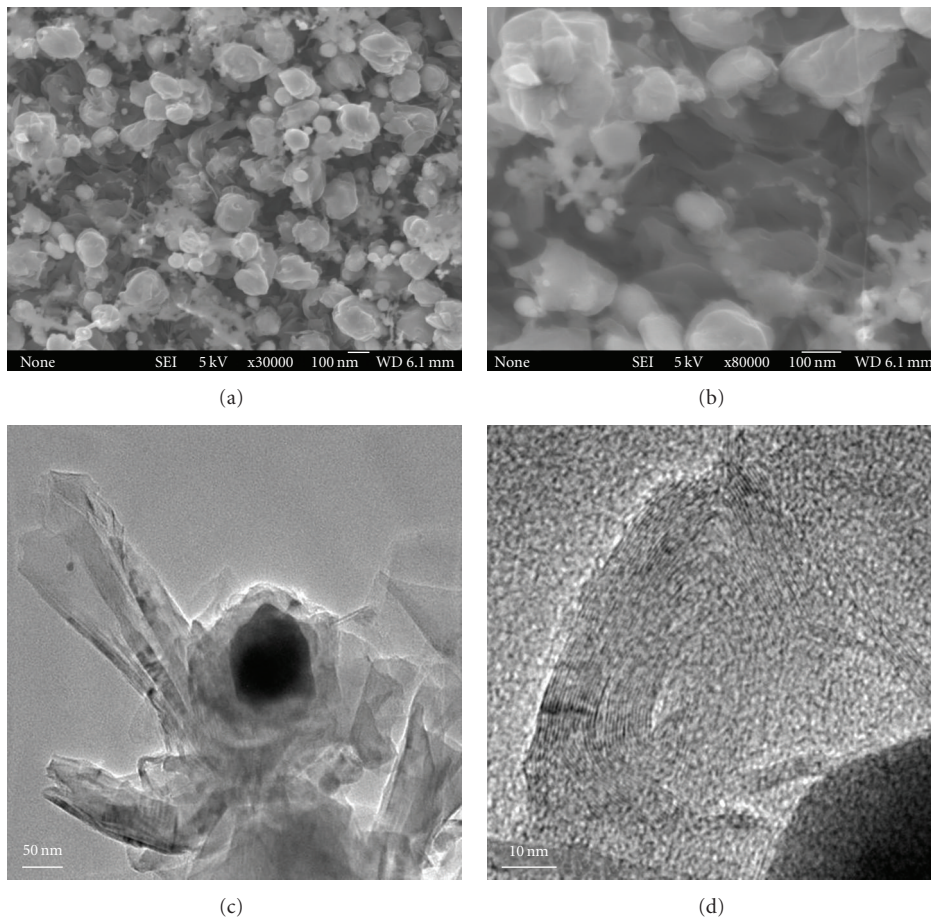


FIGURE 2: SEM and TEM images of the sample; (a) top-view SEM image of as-grown sample, (b) SEM of an enlarged image, (c) TEM image of agglomerated graphene sheets, and (d) HRTEM image of graphene sheet.

the Brillouin zone center. The band located at 1353 cm^{-1} corresponds to the D band of graphitic carbon species, which is a disorder-activated Raman mode and is associated with the TO branch near the K-point. The 2D band at 2700 cm^{-1} originates from a two-phonon double resonance Raman

process, and it is closely related to the band structure of graphene layers and is to be used to confirm the presence of graphene [5, 6]. The band at 1620 cm^{-1} , termed as D' , which arises from phonon scattering at the crystal-lattice defects. The band at 2950 cm^{-1} originates from D+G mode

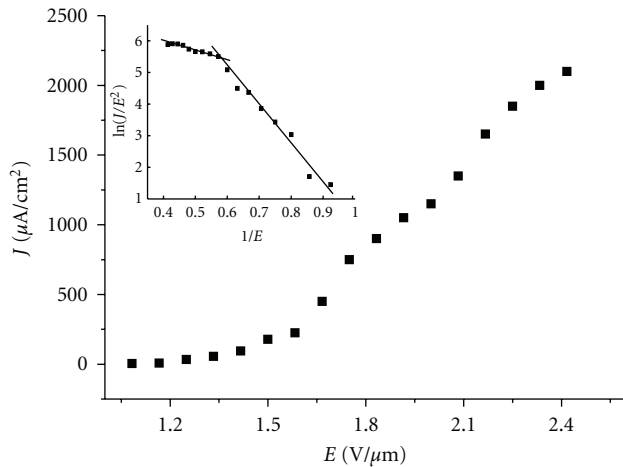


FIGURE 3: I-V curve and its F-N plot of the sample.

[7]. The Raman spectrum of the sample indicated that the deposited film was graphene film.

The morphology of the graphene film was shown in Figure 2. Figures 2(a) and 2(b) showed the top-view SEM images of as-grown sample, and it seemed to be consisted of petal-like clusters of graphene sheets. Such kind of film was named graphene aggregates film. The sizes of the clusters were about 100–300 nanometers. In order to further examine and confirm the nanostructure of the sample, TEM measurements were performed. To prepare TEM samples, the sample was ultrasonically treated in alcohol directly, then dropped onto holey grids. Figure 2(c) revealed the TEM image of agglomerated graphene sheets around an amorphous carbon particle, which may hint that the growth of the graphene sheets probably originated from amorphous carbon structure. In the experimental condition, the detailed growth mechanism of the agglomerated graphene needs further study. The layered structure shown in HRTEM image (Figure 2(d)) confirmed the structure of graphene. It also revealed the defects such as wrinkles and edge loops in graphene sheet.

The field emission characteristics of the graphene aggregates film were tested. The turn-on field of about $1.0 \text{ V}/\mu\text{m}$ and the current density of $2.1 \text{ mA}/\text{cm}^2$ at electric field of $2.4 \text{ V}/\mu\text{m}$ were obtained. Figure 3 showed the current versus voltage (I - V) curve of the field emission, and the corresponding Fowler-Nordheim (F-N) plot was inserted in Figure 3, which characterized the tunnel effect of the field emission from the graphene aggregates film. The F-N plot exhibited two different slopes at low-field region and high-field region. The current saturation of the emission and the slope deviation of the F-N plot at high-field region were observed in Figure 3. The same phenomena were observed for carbon nanotubes emitter, reported by Choi et al. [8]. In the present case, we suggested that the current saturation and F-N plot deviation were attributed to the same reason, which was adsorbate desorption effect, especially hydrogen-adsorbate desorption during the emission measurement. We had also reported the hydrogen desorption effect during

the emission measurement for amorphous carbon emitter [9]. During the graphene film deposition by CVD method, hydrogen atoms were adsorbed on the surface and edges of graphene aggregates to form the localized states near the Fermi level, which were responsible for the emission. During the emission measurement, the hydrogen adsorbates gradually desorbed, and the localized states disappeared, which probably led to the current saturation and F-N plot deviation phenomena.

The above measured results indicate that the graphene aggregates film was a good material for field electron emitter. The good field emission properties would be attributed to two possible mechanisms. (1) The graphene sheets were extending to a height of several hundreds of nanometers vertically aligned to their surfaces along the applied electric field, and the field sites of which would cause a large-field enhancement factor [10]. (2) The defects of the graphene sheet lowered electron affinity that provided a low-energy barrier and enhanced electron emission. Filleter et al. reported that energy barrier of single-layer graphene grown epitaxially on 6H-SiC (0001) had been determined to be $135 \pm 9 \text{ meV}$ by means of the Kelvin probe force microscopy [11], which was much lower than that of 4.5 eV for graphite.

4. Conclusion

In summary, we have demonstrated that the graphene film can be directly grown on stainless steel surface employing methane as the source gas in about a 10-min growth time. The growth temperature was about 700°C . The graphene aggregates emitter has a very low turn-on field of only about $1 \text{ V}/\mu\text{m}$ and an emission current density of $2.1 \text{ mA}/\text{cm}^2$ at an applied field of $2.4 \text{ V}/\mu\text{m}$. This promising field emission performance can be attributed to the electric field enhancement, and the defects induced low-work function of the graphene aggregates film.

References

- [1] W. Choi, I. Lahiri, R. Seelaboyina, and Y. S. Kang, "Synthesis of graphene and its applications: a review," *Critical Reviews in Solid State and Materials Sciences*, vol. 35, no. 1, pp. 52–71, 2010.
- [2] A. Malesevic, R. Kemps, A. Vanhulsel, M. P. Chowdhury, A. Volodin, and C. V. Haesendonck, "Field emission from vertically aligned few-layer graphene," *Journal of Applied Physics*, vol. 104, no. 8, Article ID 084301, 5 pages, 2008.
- [3] J. L. Qi, X. Wang, W. T. Zheng, H. W. Tian, C. Q. Hu, and Y. S. Peng, "Ar plasma treatment on few layer graphene sheets for enhancing their field emission properties," *Journal of Physics D*, vol. 43, no. 5, Article ID 055302, 6 pages, 2010.
- [4] J. Deng, L. Zhang, B. Zhang, and N. Yao, "The structure and field emission enhancement properties of nano-structured flower-like graphitic films," *Thin Solid Films*, vol. 516, no. 21, pp. 7685–7688, 2008.
- [5] Z. H. Ni, Y. Y. Wang, T. Yu, and Z. X. Shen, "Raman spectroscopy and imaging of graphene," *Nano Research*, vol. 1, no. 4, pp. 273–291, 2008.

- [6] L. M. Malard, M. A. Pimenta, G. Dresselhaus, and M. S. Dresselhaus, "Raman spectroscopy in graphene," *Physics Reports*, vol. 473, no. 5-6, pp. 51–87, 2009.
- [7] C. N. R. Rao, A. K. Sood, K. S. Subrahmanyam, and A. Govindaraj, "Graphene: the new two-dimensional nanomaterial," *Angewandte Chemie—International Edition*, vol. 48, no. 42, pp. 7752–7777, 2009.
- [8] Y. C. Choi, Y. M. Shin, D. J. Bae, S. C. Lim, Y. H. Lee, and B. S. Lee, "Patterned growth and field emission properties of vertically aligned carbon nanotubes," *Diamond and Related Materials*, vol. 10, no. 8, pp. 1457–1464, 2001.
- [9] Z.-L. Lu, C.-Q. Wang, Y. Jia, B.-L. Zhang, and N. Yao, "Electron emission degradation of nano-structured sp^2 -bonded amorphous carbon films," *Chinese Physics*, vol. 16, no. 3, pp. 843–847, 2007.
- [10] A. Y. Babenko, A. T. Dideykin, and E. D. Eidelman, "Graphene ladder: a model of field emission center on the surface of loose nanocarbon materials," *Physics of the Solid State*, vol. 51, no. 2, pp. 435–439, 2009.
- [11] T. Filleter, K. V. Emtsev, T. Seyller, and R. Bennewitz, "Local work function measurements of epitaxial graphene," *Applied Physics Letters*, vol. 93, no. 13, Article ID 133117, 2008.

Research Article

Nanocomposite Materials of Alternately Stacked C₆₀ Monolayer and Graphene

Makoto Ishikawa,¹ Shu Kamiya,² Shoji Yoshimoto,³ Masaru Suzuki,⁴ Daisuke Kuwahara,⁴ Naruo Sasaki,⁵ and Kouji Miura¹

¹Department of Physics, Aichi University of Education, Hirosawa 1, Igayacho, Kariya 448-8542, Japan

²Research Department, Taiho Kogyo Co., Ltd., 2-47 Hosoya-Cho, Toyota 471-8502, Japan

³Aichi Industrial Technology Institute, 1-157-1, Ondacho, Kariya 448-0013, Japan

⁴Department of Applied Physics and Chemistry, University of Electro-Communications, 1-5-1 Chohugaoka, Chofu, Tokyo 182-8585, Japan

⁵Department of Materials and Life Science, Faculty of Science and Technology, Seikei University, 3-3-1 Kichijoji-Kitamachi, Musashino, Tokyo 180-8633, Japan

Correspondence should be addressed to Kouji Miura, kmiura@aecc.aichi-edu.ac.jp

Received 17 May 2010; Accepted 4 August 2010

Academic Editor: Rakesh Joshi

Copyright © 2010 Makoto Ishikawa et al. This is an open access article distributed under the Creative Commons Attribution License, which permits unrestricted use, distribution, and reproduction in any medium, provided the original work is properly cited.

We synthesized the novel nanocomposite consisting alternately of a stacked single graphene sheet and a C₆₀ monolayer by using the graphite intercalation technique in which alkylamine molecules help intercalate large C₆₀ molecules into the graphite. Moreover, it is found that the intercalated C₆₀ molecules can rotate in between single graphene sheets by using ¹³C NMR measurements. This preparation method provides a general way for intercalating huge fullerene molecules into graphite, which will lead to promising materials with novel mechanical, physical, and electrical properties.

1. Introduction

C₆₀ intercalated graphite has previously been designed, and the electronic properties and stabilities have been studied theoretically [1]. It is also reported that the C₆₀ intercalated graphite may possess potential applications in semiconductor [2] and hydrogen storage device [3]. On the other hand, fullerene molecules, especially, C₆₀, also have unique lubrication effects, and they have been treated as a lubricant due to their spherical shape [4–6]. Up to now, we have studied C₆₀ monolayers confined by graphite flakes [7] and C₆₀ monolayers included among graphite [8–10], which, interestingly, exhibit ultralow friction, because quasi-freely rotating C₆₀ molecules act as molecular bearings. However, it is quite difficult to perform a mass production for intercalating C₆₀ molecules into graphite and to provide nanomaterials with a perfectly alternate stacking of C₆₀ monolayer and graphene in previous studies.

Here we show nanocomposite materials consisting alternately of a stacked single graphene sheet, by the graphite intercalation technique in which alkylamine molecules help intercalate large C₆₀ molecules into the graphite.

2. Experimental

First, graphite oxide (GO) was synthesized from graphite powder with an average size of 500 μm (Nippon Carbon Co., Ltd.) in accordance with the Hummers method [12] with some modifications, and the intercalation of octylamine into graphite (GO-OA) was performed as described previously in [13, 14]. Next, octylamine-intercalated graphite oxide (GO-OA) was added to fullerene solution (100 mg of C₆₀ dissolved in 100 mL toluene), and after that, the toluene used was evaporated at room temperature, leaving behind in the products (GO-OA-C₆₀). The C₆₀ fullerene used in this experiment was purchased from Frontier Carbon Co., Ltd in

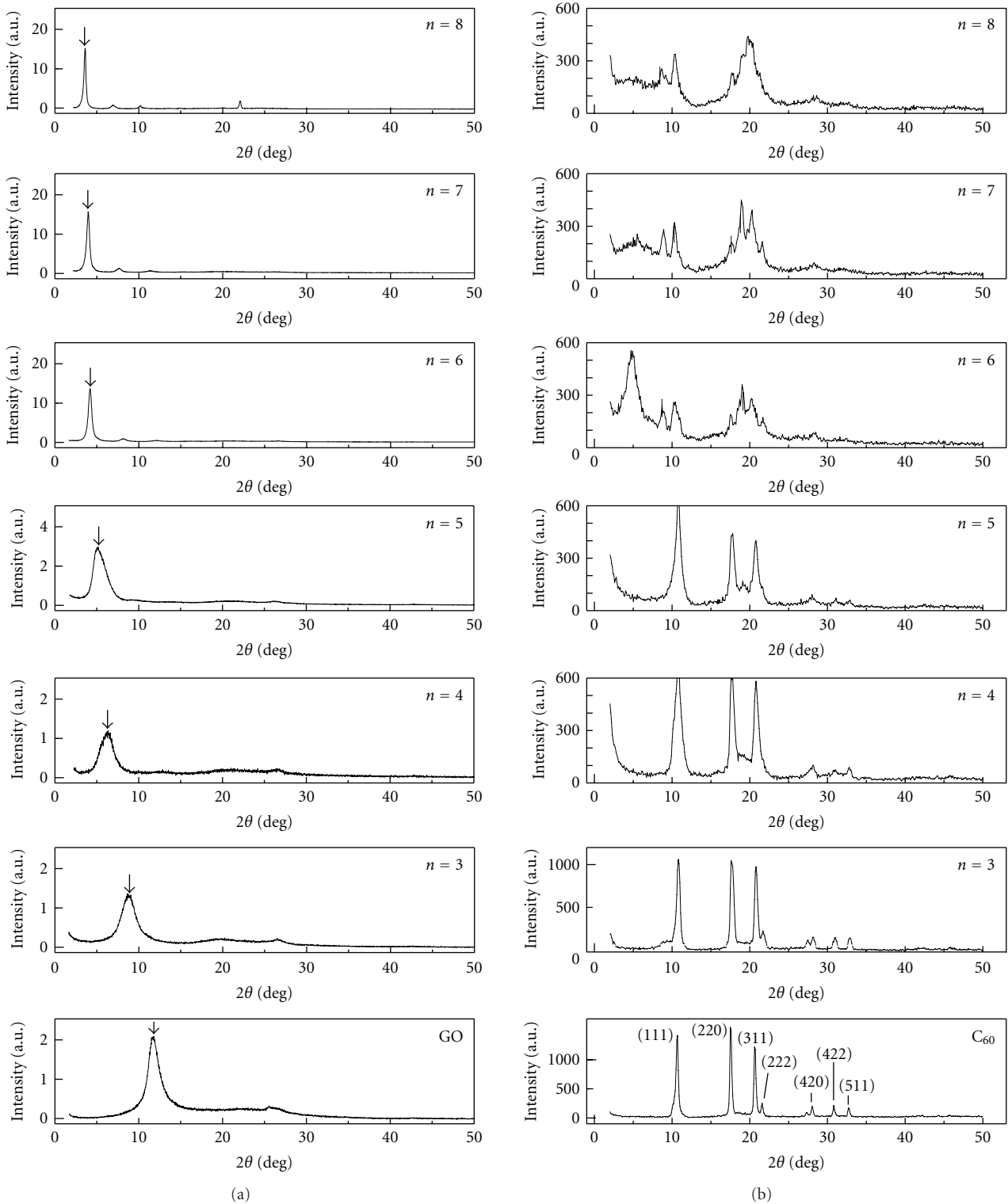


FIGURE 1: XRD intensity from as-prepared samples. (a) XRD intensity from graphite oxide (GO) and alkylamine-intercalated graphite oxides (GO-amine) with different chain lengths ($C_nH_{2n+1}NH_2$) ($n = 3-8$). The peaks of GO and GO-amine are indicated by the arrows in the figure. (b) XRD intensity from GO-amine with different chain lengths in C_{60} solution ($n = 3-8$).

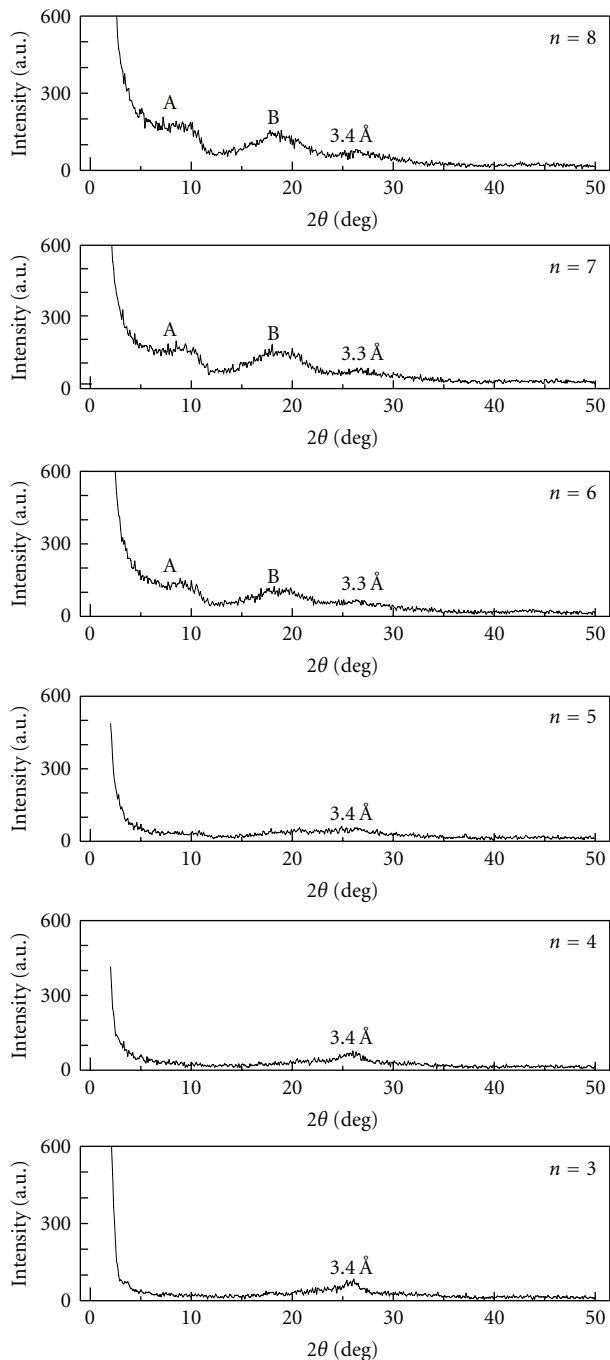


FIGURE 2: XRD intensity from the specimens heated for 80 minutes at 600°C under a high vacuum of 10^{-6} Torr for the GO- C_{60} specimens of Figure 1(b).

Japan. The products of GO-OA- C_{60} were treated with 0.1 N hydrochloric acid solution at room temperature for at least 30 minutes and dried in air at 80°C overnight to remove the octylamine, resulting in the C_{60} -intercalated graphite oxide (GO- C_{60}). Finally, in order to remove C_{60} powders that are not intercalated into the graphite, and moreover, to remove octylamines that are intercalated into the graphite, GO- C_{60} was heated for at least 80 minutes at 600°C under a high

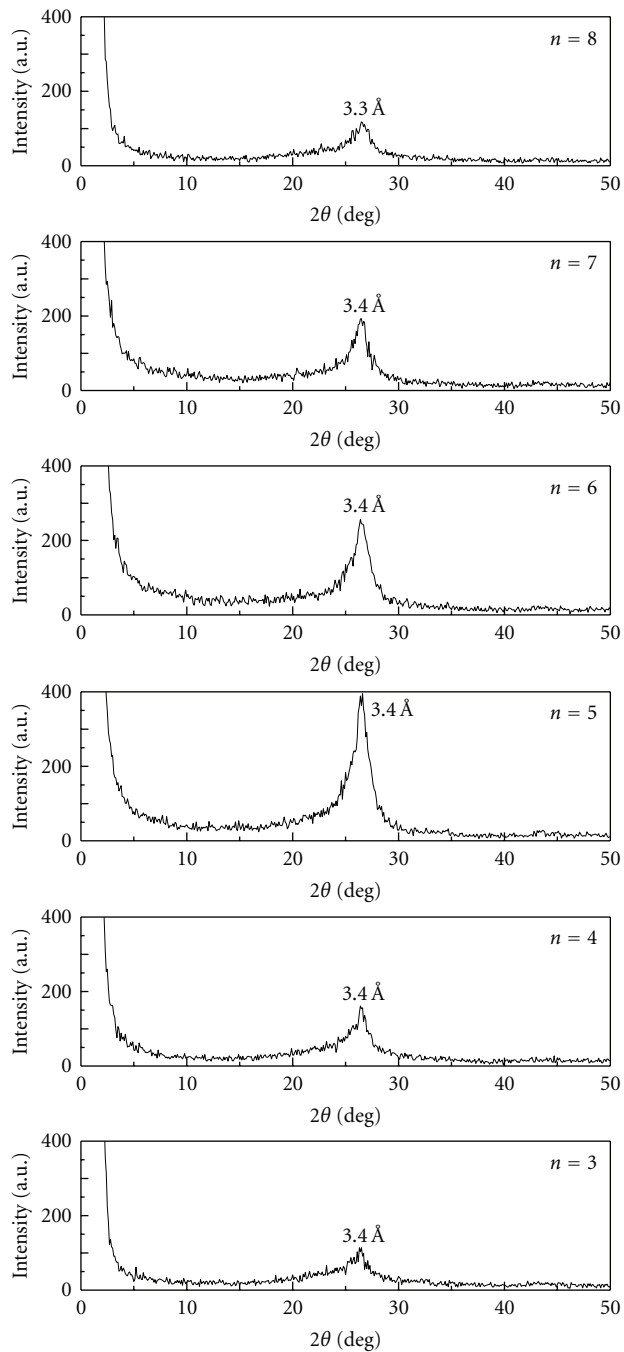


FIGURE 3: XRD intensity from the specimens heated for 80 minutes at 600°C under high vacuum of 10^{-6} Torr for alkylamine-intercalated graphite oxide (GO-amine).

vacuum of 10^{-6} Torr, which results in the nanocomposite consisting alternately of a stacked single graphene sheet and a C_{60} monolayer. All specimens were analyzed by using X-ray diffraction (Rigaku RINT 2200/PC diffractometer: $CuK\alpha$ radiation at 40 kV and 30 mA), FT-IR spectroscopy (FTIR: JASCO 480 Plus FT-IR spectrometer: the samples in KBr pellets), NMR (our original 7.1 T spectrometer with a Tecmag Apollo spectrometer and a Doty SuperSonic MAS

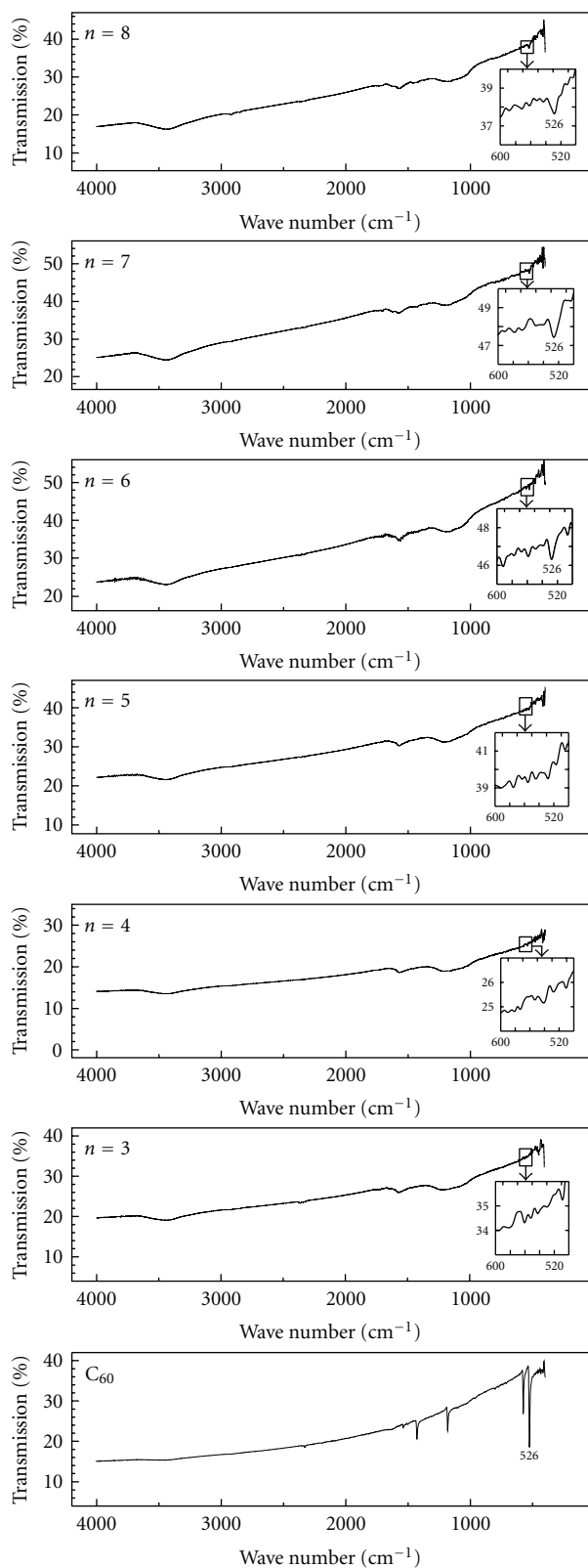


FIGURE 4: FT-IR spectra from the specimens of Figure 2. The C_{60} intermolecular IR-active (F_{1u}) modes are indicated in the inset of the figure.

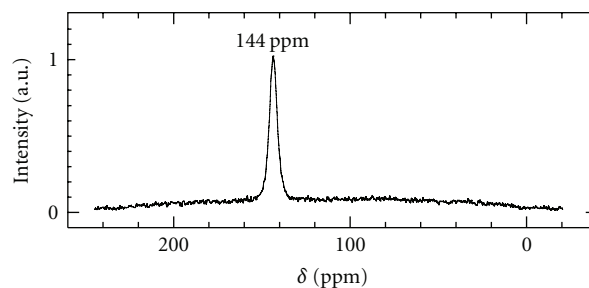


FIGURE 5: The ^{13}C NMR spectra for the specimens of Figure 2 at room temperature. Only one sharp line with a peak position of 144 ppm [11] was observed.

7 mm probe head), and high-resolution electron microscopy (JEM3100FEF: a lattice resolution of 0.1 nm when it is operated at an acceleration voltage of 300 kV).

3. Results and Discussion

Figure 1(a) shows the X-ray diffraction (XRD) intensity from graphite oxide (GO) and alkylamine-intercalated graphite oxide (GO-amine) with different alkyl chain lengths ($C_nH_{2n+1}NH_2$) ($n = 3$ to 8). The appearance of a peak in the GO of Figure 1(a) shows that the spacing between graphite oxide sheets is approximately 8 Å, which is identical to the published data [12]. It is found that the spacing between graphite oxide sheets in the case of the GO-amine ($n = 3$ to 8) increases with the increase in the length of the alkyl chain incorporated in the interlayer space of the GO. Figure 1(b) shows the XRD intensity from the GO-amine ($n = 3$ to 8) in C_{60} solution, which we call the C_{60} -intercalated graphite oxide (GO- C_{60}). It should be noted that there appear drastic changes in the XRD intensity between $n = 5$ and $n = 6$ in Figure 1(b), which indicates that C_{60} molecules are intercalated in the interlayer space of the GO by the driving force of alkylamine situated at between the graphene oxide sheets when the interlayer space is sufficiently larger than the C_{60} molecule. However, there exist many C_{60} powders which are not intercalated into the GO in these GO- C_{60} specimens because the stronger peaks, (111), (220), (311), (222), (331), (420), (422), and (511), of XRD intensity from C_{60} powders (JCPDS file No.44-0558) appear in the spectra of Figure 1(b). In order to remove C_{60} powders that are not intercalated into the GO, and moreover, to expel the alkylamines which are intercalated into the graphite, the GO- C_{60} specimens of Figure 1(b) were heated for 80 minutes at 600°C under a high vacuum of 10^{-6} Torr, as shown in Figure 2. It should be noted that $n = 6$, $n = 7$, and $n = 8$ have broad peaks of A and B corresponding to d -spacings of 9 Å and 4.6 Å, respectively, in addition to a broad peak of $d = 3.3$ Å corresponding to the spacing of graphite layers, although $n = 3$, $n = 4$, and $n = 5$ have only a single broad peak of $d = 3.3$ Å. Since the GO-amine reverts to the graphite layers when alkylamines leaves the GO-amine host after heating at up to 600°C, as shown in the XRD intensity of Figure 3, the graphene oxide layers in

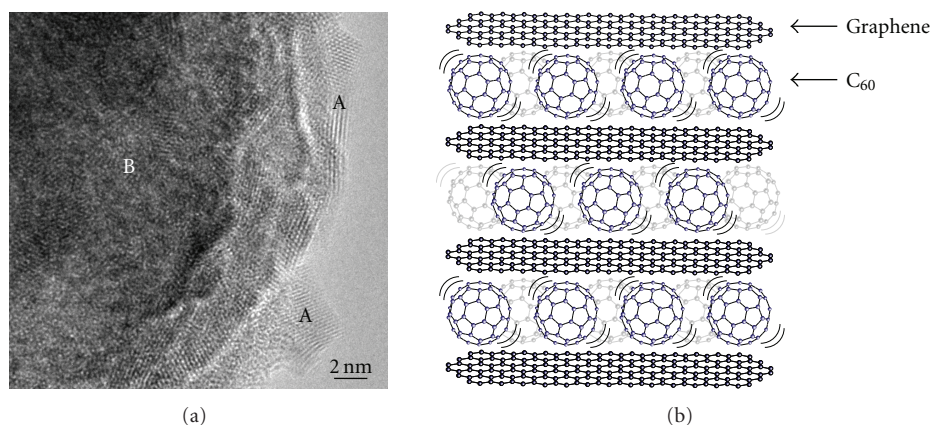


FIGURE 6: High-resolution electron microscope (HR-TEM) image and structure model of alternately stacked graphene sheets and C₆₀ monolayers. (a) High-resolution electron microscope (HR-TEM) image from the nanoribbon of the specimens of Figure 2. Graphene layers (area: A) and C₆₀ molecules between graphene sheets (area: B) are shown. (b) Structure model of alternately stacked graphene sheets and C₆₀ monolayers, where C₆₀ molecules can rotate between graphene sheets.

the GO-C₆₀, which do not include C₆₀ molecules, also revert to the graphite layers when alkylamines go out from it after heating. It is expected that the peaks of A and B ($n = 6$ to 8) in Figure 2 are due to the d -spacing between the graphenes intercalating the C₆₀ monolayer and their stacking faults (the disorder of the stacking) [15], respectively. However, since peak A is also widely distributed, the d -spacings between the graphenes intercalating the C₆₀ monolayer are considered to be widely distributed.

Figure 4 shows the FT-IR spectra from the specimens of Figure 2. This result is consistent with the conclusion based on Figure 2 that C₆₀ molecules can be intercalated into the GO with alkylamine chains longer than that of $n = 5$ because the FT-IR spectra from $n = 6$, $n = 7$, and $n = 8$ in Figure 4 exhibit the C₆₀ intermolecular IR-active (F_{1u}) modes [11] although those with the shorter alkylamine chains do not exhibit these modes. However, one mode of 526 cm^{-1} among IR-active (F_{1u}) modes only appears in these FT-IR spectra because the number of C₆₀ molecules included in the specimens is rather small.

The rotational dynamics of C₆₀ molecules between graphenes have been investigated by ¹³C NMR in the temperature range from room temperature to -80°C . We prepared C₆₀ materials 20–30% enriched in ¹³C in order to increase the ¹³C NMR signal. The present specimen was mixed with Na₂SO₄ in a weight ratio of 1:50 to avoid arcing in a NMR probe. The NMR experiments were performed at 75.4 MHz for ¹³C in an external field of 7.1 T by the pulse inversion recovery method. ¹³C NMR spectra were taken by Fourier transforming the signal following the $\pi/2$ pulse. The typical $\pi/2$ pulse width was 5.4 μs . It is well known that for C₆₀ molecules in solid C₆₀ at room temperature, large rotational motion averages out the chemical-shift anisotropy (CSA) and the ¹³C NMR spectra show motional narrowing of 2.5 ppm in width. In contrast, spectra broaden at low temperature and develop the CSA power pattern with a CSA tensor with the principle values $\delta_{11} = 213\text{ ppm}$, $\delta_{22} = 182\text{ ppm}$, and $\delta_{33} = 33\text{ ppm}$ [11].

Figure 5 shows the ¹³C NMR spectra for the specimens of Figure 2 at room temperature, where the ¹³C NMR spectrum at room temperature is the same as that at the temperature of -80°C . Only one sharp line with a peak position of 144 ppm was observed, and its line shape is a Gaussian-like function with an FWHM value of 5 ppm. The positions are in good agreement with the average principle values for C₆₀ molecules in solid C₆₀, and the linewidth is about one-twentieth narrower than that of the powder pattern [11]. These observations clearly demonstrate the lack of the polymerization [16] of C₆₀ molecules in the present material. Furthermore, the observed Gaussian-like line shape means a motional narrowing and that C₆₀ molecules rotate quasi-freely with a correlation time on the order of 10 ps. This correlation time is similar to that of the same case [17]. This means that no strong bonding such as chemical bonding between the graphenes and C₆₀ molecules is made, and C₆₀ molecules easily rotate for outer force.

It is possible that the specimens in the case of Figure 2 are broken into nanoribbons of nanometer thickness by ultrasonic vibration, which is analogous to the preparation method of the graphene nanoribbon. A high-resolution electron microscope (HR-TEM) image of the nanoribbon is shown in Figure 6(a). First, two parts of graphene layers (areas A) are shown in Figure 6(a). A missing rows of zigzag chains clearly appear in the graphene network, which indicates that the thickness of the specimen is on an atomic scale [18], and moreover, moire patterns formed by graphenes also appear in area A. It is expected that the contrast of area B originates from the C₆₀ molecules confined between graphene sheets, although we will discuss this contrast later in detail. Now we illustrate the structure model of C₆₀-intercalated graphite in Figure 6(b), that is, the nanocomposite consisting of alternately stacked graphene sheets and C₆₀ monolayers in which C₆₀ molecules can form a monolayer and rotate between graphene sheets.

4. Conclusion

At present, preliminary experiment indicates it is possible to intercalate huge fullerene molecules, such as C_{70} and $La@C_{82}$ larger than a C_{60} molecule into graphite. Hence it is expected that the unique structure comprising huge fullerene molecules intercalated into graphite will give rise to attractive novel applications such as superlubrication materials, variable nanocapacitance, nanoswitches, and hydrogen storage in the future. Moreover, since the tribological test of grease and oils with an additive of this nanocomposite powder exhibits excellent lubricating performance with an ultralow friction previously unattained, the structure and material properties are expected to be more attractive also from scientific and material points of view. These are examples of the application that shows the novel mechanical property, and the intercalated materials will lead to promising materials with novel mechanical, physical, and electrical properties.

Acknowledgments

This paper was supported by Grants-in-Aid for Scientific Research from the Japan Society for the Promotion of Science (nos. 16340089 and 18340087) and “Practical Application Research, Science and Technology Incubation Program in Advanced Regions”, Japan Science and Technology Agency.

References

- [1] S. Saito and A. Oshiyama, “Design of C_{60} -graphite cointercalation compounds,” *Physical Review B*, vol. 49, no. 24, pp. 17413–17419, 1994.
- [2] V. Gupta, P. Scharff, K. Risch, H. Romanus, and R. Müller, “Synthesis of C_{60} intercalated graphite,” *Solid State Communications*, vol. 131, no. 3–4, pp. 153–155, 2004.
- [3] A. Kuc, L. Zhechkov, S. Patchkovskii, G. Seifert, and T. Heine, “Hydrogen sieving and storage in fullerene intercalated graphite,” *Nano Letters*, vol. 7, no. 1, pp. 1–5, 2007.
- [4] R. Luthi, E. Meyer, H. Haefke, L. Howald, W. Gutmannsbauer, and H.-J. Guntherodt, “Sled-type motion on the nanometer scale: determination of dissipation and cohesive energies of C_{60} ,” *Science*, vol. 266, no. 5193, pp. 1979–1981, 1994.
- [5] Z. Y. Li, “Orientational order of ultrathin C_{60} films on graphite,” *Surface Science*, vol. 441, no. 2–3, pp. 366–372, 1999.
- [6] S. Okita, M. Ishikawa, and K. Miura, “Nanotribological behavior of C_{60} films at an extremely low load,” *Surface Science*, vol. 442, no. 1, pp. L959–L963, 1999.
- [7] K. Miura, S. Kamiya, and N. Sasaki, “ C_{60} molecular bearings,” *Physical Review Letters*, vol. 90, no. 5, Article ID 055509, 4 pages, 2003.
- [8] K. Miura, D. Tsuda, and N. Sasaki, “Superlubricity of C_{60} intercalated graphite films,” *e-Journal of Surface Science and Nanotechnology*, vol. 3, pp. 21–23, 2005.
- [9] K. Miura, D. Tsuda, N. Itamura, and N. Sasaki, “Superlubricity of fullerene intercalated graphite composite,” *Japanese Journal of Applied Physics Part 1*, vol. 46, no. 8A, pp. 5269–5274, 2007.
- [10] N. Itamura, K. Miura, and N. Sasaki, “Simulation of scan-directional dependence of superlubricity of C_{60} molecular bearings and graphite,” *Japanese Journal of Applied Physics*, vol. 48, no. 6, Article ID 060207, 3 pages, 2009.
- [11] R. Tycko, G. Dabbagh, R. M. Fleming, R. C. Haddon, A. V. Makhija, and S. M. Zahurak, “Molecular dynamics and the phase transition in solid C_{60} ,” *Physical Review Letters*, vol. 67, no. 14, pp. 1886–1889, 1991.
- [12] W. S. Hummers Jr. and R. E. Offeman, “Preparation of graphitic oxide,” *Journal of the American Chemical Society*, vol. 80, no. 6, p. 1339, 1958.
- [13] Y. Matsuo, T. Miyabe, T. Fukutsuka, and Y. Sugie, “Preparation and characterization of alkylamine-intercalated graphite oxides,” *Carbon*, vol. 45, no. 5, pp. 1005–1012, 2007.
- [14] C. Nethravathi and M. Rajamathi, “Delamination, colloidal dispersion and reassembly of alkylamine intercalated graphite oxide in alcohols,” *Carbon*, vol. 44, no. 13, pp. 2635–2641, 2006.
- [15] H.-K. Jeong, Y. P. Lee, R. J. W. E. Lahaye et al., “Evidence of graphitic AB stacking order of graphite oxides,” *Journal of the American Chemical Society*, vol. 130, no. 4, pp. 1362–1366, 2008.
- [16] A. M. Rao, P. Zhou, K.-A. Wang et al., “Photoinduced polymerization of solid C_{60} films,” *Science*, vol. 259, no. 5097, pp. 955–957, 1993.
- [17] K. Matsuda, Y. Maniwa, and H. Kataura, “Highly rotational C_{60} dynamics inside single-walled carbon nanotubes: NMR observations,” *Physical Review B*, vol. 77, no. 7, Article ID 075421, 2008.
- [18] Z. Liu, K. Suenaga, P. J. F. Harris, and S. Iijima, “Open and closed edges of graphene layers,” *Physical Review Letters*, vol. 102, no. 1, 015501, 4 pages, 2009.

Research Article

Preparation of Bulk ^{13}C -Enriched Graphene Materials

Leilei Tian,¹ Xin Wang,¹ Li Cao,¹ Mohammed J. Meziani,¹ Chang Yi Kong,^{1,2} Fushen Lu,¹ and Ya-Ping Sun¹

¹Department of Chemistry and Laboratory for Emerging Materials and Technology, Clemson University, Clemson, SC 29634-0973, USA

²Department of Materials Science and Chemical Engineering, Faculty of Engineering, Shizuoka University, 3-5-1 Johoku, Naka-ku, Hamamatsu 432-8561, Japan

Correspondence should be addressed to Ya-Ping Sun, syaping@clemson.edu

Received 29 May 2010; Accepted 18 July 2010

Academic Editor: Rakesh Joshi

Copyright © 2010 Leilei Tian et al. This is an open access article distributed under the Creative Commons Attribution License, which permits unrestricted use, distribution, and reproduction in any medium, provided the original work is properly cited.

Arc-discharge has been widely used in the bulk production of various carbon nanomaterials, especially for structurally more robust single-walled carbon nanotubes. In this paper, the same bulk-production technique was applied to the synthesis of significantly ^{13}C -enriched graphitic materials, from which graphene oxides similarly enriched with ^{13}C were prepared and characterized. The results demonstrate that arc-discharge is a convenient method to produce bulk quantities of ^{13}C -enriched graphene materials from relatively less expensive precursors (largely amorphous ^{13}C powders).

1. Introduction

Graphene nanosheets (GNs) consisting of a single or few layers of hexagonally arrayed sp^2 -bonded carbons in a two-dimensional lattice have attracted tremendous amount of recent attention for their interesting and/or unique properties, with a long list of predicted technological applications [1–10]. For example, individual GNs have been found to possess superior electronic properties arising from the confinement of electrons in two dimensions [3], and as a zero-bandgap semiconductor to feature long-range ballistic transport and high carrier mobility at room temperature [8, 11, 12]. GNs also exhibit excellent thermal transport properties [10], with their dispersion into polymeric matrices resulting in record-setting thermal conductive performances [13–15].

The preparation or production in larger quantities of GNs has been actively pursued in the research community [16, 17]. Among widely investigated methods are those based on the micromechanical cleavage of graphite [11], epitaxial growth [18], and chemical exfoliation of graphite [13, 19], especially the exfoliation through the route of graphene oxides (GOs) [20]. For structural characterization and other purposes, ^{13}C -enriched GNs (or GOs as precursors) are

particularly valuable. However, the ^{13}C -enrichment in bulk quantities of graphene materials has hardly been a routine task. There are only a few relevant studies in the literature (all based on the same sample source), despite their obviously high impact in the graphene research field [21–23]. The sample of ^{13}C -enriched graphite films in the available studies was synthesized by using cold-wall chemical vapor deposition (CVD) onto nickel substrate, with isotopically enriched methane as the ^{13}C source [22].

Beyond CVD, arc-discharge under inert atmosphere has been widely used in the bulk production of various carbon nanomaterials, including especially carbon nanotubes [24–28]. In fact, single-walled carbon nanotubes from arc-discharge production are generally structurally more robust [26, 27]. Therefore, it is desirable to apply the same bulk-production technique to the synthesis of graphite from amorphous carbon powders (such as commercially supplied ^{13}C powders). Here, we report the use of arc-discharge for the production of significantly ^{13}C -enriched graphitic materials, from which graphene oxides (GOs) similarly enriched with ^{13}C were prepared and characterized. The results demonstrate that arc-discharge is a convenient method to produce bulk quantities of ^{13}C -enriched graphene materials from relatively less expensive precursors (^{13}C powders).

2. Results and Discussion

The sample containing ^{13}C -enriched graphite was synthesized in an arc-discharge chamber. For the electrodes, the anode was a hollow graphite rod completely filled with a mixture of ^{13}C powder (largely amorphous) and graphite. The total ^{13}C content in the anode rod was targeted to be about 20%. The cathode was a solid graphite rod. In a helium atmosphere, the arc-discharge was at a high current to render a high temperature for the carbon evaporation, thus to facilitate the formation of more graphitic carbon materials. In principle, arc-discharge (or sometime called plasma arcing) creates a high-temperature (up to $3,000^\circ\text{C}$) condition that evaporates and ionizes the carbon electrode materials. The ultrahot carbon vapors and ions serve as precursors to spontaneously form the targeted nanostructures (fullerenes, carbon nanotubes, or graphite sheets) upon condensation in the arc-discharge chamber. In the experiment reported here, there was a significant amount of black deposit on the cathode, which was determined as being more graphitic than the soot-like material in the chamber according to thermogravimetric analysis (TGA). The deposit was collected as a sample containing ^{13}C -enriched synthetic graphite. According to spectral shifts in the Raman spectroscopy evaluation, the estimated ^{13}C content in the sample was on the order of 15%, slightly lower than the original ^{13}C loading in the anode rod.

The X-ray diffraction pattern for the ^{13}C -enriched sample was generally similar to that of the commercially supplied natural graphite (Figure 1), with diffraction peaks at 2θ of 26.2° , 42.7° , 54.0° , and 78.0° , corresponding to (002), (10), (004), and (110) diffractions, respectively, in the graphitic framework. However, the ^{13}C -enriched sample was likely more complex morphologically, as reflected in the significantly broader (002) diffraction peak (Figure 1), though the complexity should have little effect on the preparation of graphene oxides (GOs) in terms of the Hummers method [1, 29]. The extreme processing conditions associated with the Hummers method would push all surviving species toward the well-exfoliated GOs.

In the Hummers method treatment of the ^{13}C -enriched sample, the same experimental conditions as those for natural graphite were applied. A similarly homogeneous aqueous dispersion of GOs was obtained (Figure 2), which was stable over the duration of the project (several months).

The optically transparent aqueous dispersions were used in UV/vis absorption measurements. Shown in Figure 2 is a comparison of optical absorption spectra between GOs from precursor samples with and without the ^{13}C enrichment. Both spectra exhibited the characteristic absorption bands at 230 nm and 300 nm, corresponding to the well-established π - π^* (due to the remaining graphene structure) and n - π^* transitions in GOs, respectively [30], suggesting that the ^{13}C -enriched GOs were structurally similar to those from natural graphite.

The ^{13}C -enriched GOs from the Hummers method in aqueous dispersion were deposited onto a solid substrate for characterization by Raman spectroscopy. As shown in Figure 3, the Raman spectrum of the ^{13}C -enriched GOs

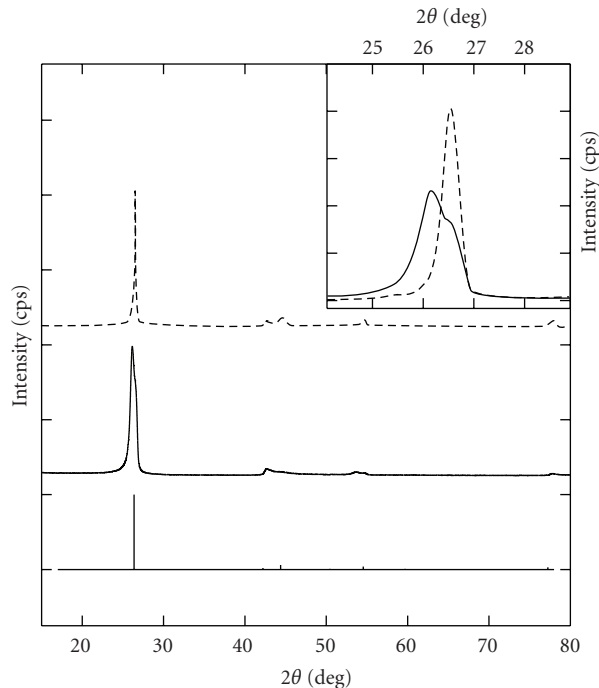


FIGURE 1: X-ray diffraction patterns of the ^{13}C -enriched sample produced in arc-discharge (solid line) and the as-supplied natural graphite (dashed line), along with the standard from JCPDS database.

featured the same G-band and D-band as those typically found in GOs from natural graphite (Figure 2) [31], except that the Raman bands of the ^{13}C -enriched GOs were at lower frequencies (due to ^{13}C being heavier than ^{12}C). The Raman results confirmed that the aqueous dispersion from the Hummers method was indeed a dispersion of ^{13}C -enriched GOs. More quantitatively, the Raman spectral shifts were used to estimate the ^{13}C content in the enriched sample. Under the assumption of same force constants for ^{12}C and ^{13}C bonds, the observed frequencies of a specific Raman mode for the ^{13}C -enriched sample (ω) and regular ^{12}C sample (ω_{12}) are related to the ^{13}C content in the enriched sample (x) as follows [32, 33]:

$$\omega = \omega_{12} \sqrt{\frac{m_{12}}{m_{12}(1-x) + m_{13}x}}, \quad (1)$$

where m_{12} and m_{13} are atomic masses of ^{12}C and ^{13}C , respectively. The Raman spectral shifts from different batches of GOs were slightly different, so were the shifts of G-band versus D-band between the ^{13}C -enriched and regular GOs. On average, however, the estimated ^{13}C content in the enriched sample was 18.5%, comparable with the targeted ^{13}C enrichment in the anode used in arc-discharge (about 20%).

The presence of GOs in the ^{13}C -enriched sample after Hummers method treatment was further confirmed and their morphology probed in electron microscopy analyses. The specimen of the ^{13}C -enriched GOs was prepared by depositing a few drops of a diluted aqueous dispersion

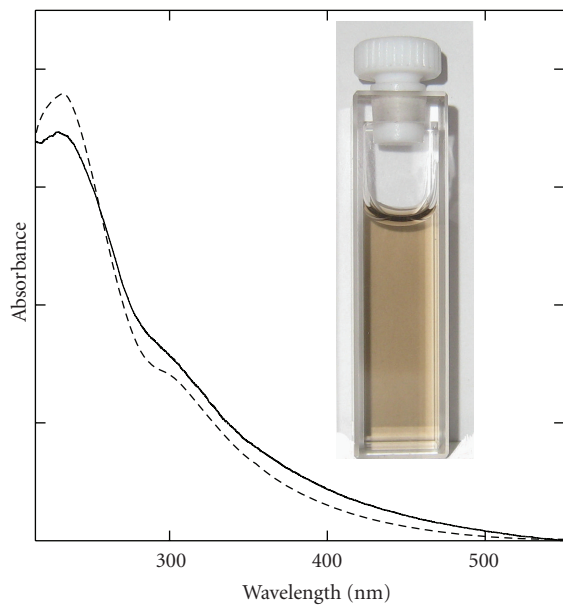


FIGURE 2: UV/vis absorption spectra of aqueous dispersions of the ^{13}C -enriched GOs (solid line, a photo of the dispersion in the inset) and GOs from the natural graphite (dashed line).

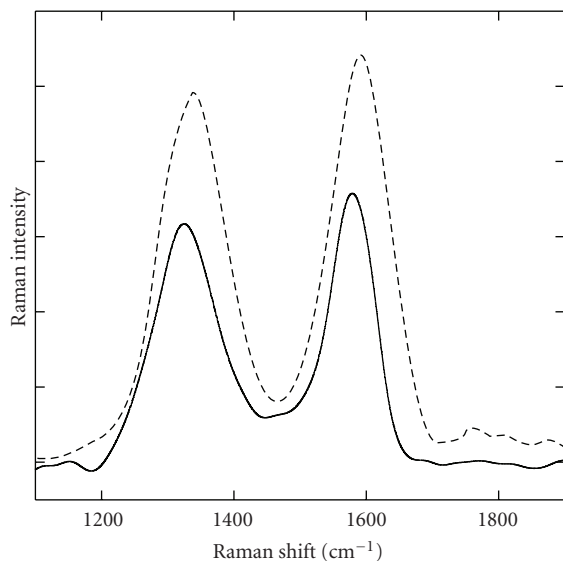


FIGURE 3: Raman spectra of the ^{13}C -enriched GOs (solid line) and GOs from the natural graphite (dashed line).

(~ 0.05 mg/mL) onto a holey carbon-coated copper grid, followed by drying under ambient conditions. With the use of a scanning transmission electron microscope (S-TEM), the images obtained for the specimen imaging modes (transmission and Z-contrast) exhibited consistently a primary morphology of well-exfoliated sheets, which appeared to be transparent to the electron beam (Figure 4). The ^{13}C -enriched GOs in TEM images were generally similar to those from natural graphite (Figure 4), except for the former appearing somewhat more wrinkled with less regular edges (Figure 4). While the TEM results alone

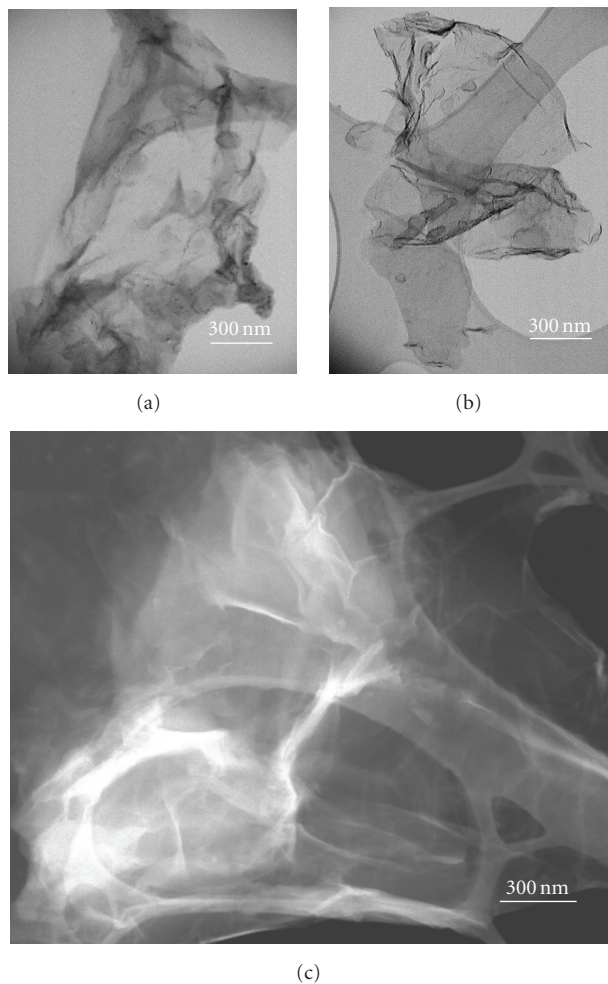


FIGURE 4: TEM images of the ^{13}C -enriched GOs (a) and GOs from the natural graphite (b) on holey carbon-coated copper grid; and the ^{13}C -enriched GOs in the Z-contrast mode (c).

were hardly sufficient for any conclusions, the possibility existed that the graphite material (as precursor to the GOs) from the arc-discharge production had a smaller grain size and contained more defects. Nevertheless, the production conditions were not optimized, thus still more rooms for significant improvements in arc-discharge production for structurally more robust graphite precursors.

The results presented above clearly demonstrate that ^{13}C -enriched GOs in bulk quantity can be obtained from the graphite precursor produced in an arc-discharge chamber. A major advantage of this production approach is the use of relatively less expensive ^{13}C powders as starting material. The overall yield from ^{13}C powders to GOs was on the order of 10% in terms of ^{13}C conversion, and improvements may be expected when the production conditions are optimized. The soot-like material (also with significant ^{13}C content) collected from arc-discharge chamber could be recycled (for graphite materials of lower ^{13}C enrichment). Another improvement to be pursued is the quality of the graphite precursor and the resulting GOs, as it is well-established that

arc-discharge is a preferred method to produce structurally more robust carbon nanotubes.

The correlation between the ^{13}C enrichment in the final GOs and that in the starting anode rod for arc-discharge is interesting and useful, as it may allow more predictable production of graphene materials of various targeted ^{13}C enrichment ratios for different applications. Efforts on such predictable production and on the optimization of production conditions are in progress.

3. Experimental Section

3.1. Materials. The graphite sample, referred to as “natural graphite”, was the surface-enhanced flake graphite (Grade 3805) supplied by Asbury Carbons. ^{13}C powders (largely amorphous, ^{13}C content 97%) were purchased from Icon Isotope, Inc. Fine-extruded graphite rods (carbon content >99.9%, 6.4 mm in diameter and ~30 cm in length) were acquired from Graphitestore.com, Inc. Sulfuric acid (93%), nitric acid (73%), hydrochloric acid (36%), hydrogen peroxide (35%), and phosphorus pentoxide (P_2O_5) were obtained from ACROS, ammonium persulfate ($(\text{NH}_4)_2\text{S}_2\text{O}_8$) from Aldrich, and potassium permanganate (KMnO_4) from Fisher Scientific. PVDF membrane filters (0.45 μm pore size) were supplied by Fisher Scientific, dialysis membrane tubing (MWCO ~ 3,500) by Spectrum Laboratories, and holey carbon-coated copper grids by SPI Supplies. Water was deionized and purified by being passed through a Labconco WaterPros water purification system.

3.2. Measurements. Thermogravimetric analysis (TGA) was performed on a TA Instruments Q500 analyzer. Optical absorption spectra were recorded on a Shimadzu UV-3600 UV/vis/NIR spectrophotometer. Raman spectra were obtained on a Jobin Yvon T64000 Raman spectrometer equipped with a Melles-Griot He-Ne laser (35 mW) for 632.8 nm excitation, a triple monochromator, an Olympus BX-41 microscopy, and a liquid nitrogen-cooled symphony detector. Transmission electron microscopy (TEM) images were acquired on Hitachi HD-2000 S-TEM systems.

3.3. Arc-Discharge. The arc-discharge production was carried out in a water-cooled stainless steel chamber equipped with an arc length controller (ALC-401, Jetline Engineering). For the anode, a commercially supplied graphite rod was cut in half to ~15 cm in length and then drilled to become hollow, with an inner diameter of ~4 mm. The hollow cavity was filled with a mixture of the natural graphite (0.54 g) and ^{13}C powders (0.64 g). The targeted ^{13}C content in the anode rod was ~20%. A solid graphite rod was used as cathode. The arc-discharge, under helium atmosphere (1 atm), was at a direct current of 70 A (28 V). The anode was consumed in about 40 min. The black deposit (~2 g) on the cathode containing ^{13}C -enriched graphite was collected.

3.4. Graphene Oxides. The Hummers method [29] with minor modification was used for the preparation of graphene oxides (GOs) from the arc-produced graphite sample.

Briefly, concentrated H_2SO_4 (10 mL) in a 500 mL flask was heated to 80°C, to which $(\text{NH}_4)_2\text{S}_2\text{O}_8$ (0.9 g) and P_2O_5 (0.9 g) were added. The mixture was stirred until the reagents were completely dissolved. The ^{13}C -enriched graphite sample (1 g) from the arc-discharge production was added, and the resulting mixture was heated at 80°C for 4.5 h. Upon being cooled to room temperature, the reaction mixture was diluted with water (250 mL) and kept for ~12 h. It was then filtrated and washed repeatedly with water, followed by drying in a vacuum oven. The solid sample was added to concentrated H_2SO_4 (40 mL) in a 500 mL flask cooled in an ice bath. To the mixture was added slowly KMnO_4 (5 g over 40 min), during which the temperature was kept at <10°C. The reaction mixture, with a change in color from black to greenish brown, was heated at 35°C for 2 h, followed by dilution with water (85 mL—Caution: the temperature must be kept at <35°C throughout) and further stirring for 2 h. The reaction mixture was poured into a large beaker, to which water (250 mL) and then aqueous H_2O_2 (30%, 10 mL) were added. Bubbles from the aqueous mixture along with a color change to brilliant yellow were observed. The mixture was allowed to settle for ~12 h. The clear supernatant was decanted, and the sediment was washed repeatedly with aqueous H_2SO_4 (5 wt%)- H_2O_2 (0.5 wt%) and HCl solution (10 wt%), followed by washing repeatedly with water until no layers observed in centrifuging. The sample was then dialyzed (MWCO ~ 3,500) against water for 7 days to yield a clean aqueous dispersion of GOs.

Acknowledgments

This work was made possible by financial support from the Air Force Office of Scientific Research (AFOSR) through the program of Dr. Charles Lee. X. Wang was supported by the American Chemical Society Petroleum Research Fund. L. Cao was supported by a *Susan G. Komen for the Cure* Postdoctoral Fellowship. C. Y. Kong was supported by the Excellent Young Researchers Overseas Visit Program of Japan Society for the Promotion of Science (JSPS). F. Lu was a participant in the Palmetto Academy, an education-training program managed by South Carolina Space Grant Consortium.

References

- [1] S. Stankovich, D. A. Dikin, G. H. B. Dommett et al., “Graphene-based composite materials,” *Nature*, vol. 442, no. 7100, pp. 282–286, 2006.
- [2] J. S. Bunch, A. M. Van Der Zande, S. S. Verbridge et al., “Electromechanical resonators from graphene sheets,” *Science*, vol. 315, no. 5811, pp. 490–493, 2007.
- [3] A. K. Geim and K. S. Novoselov, “The rise of graphene,” *Nature Materials*, vol. 6, no. 3, pp. 183–191, 2007.
- [4] D. A. Dikin, S. Stankovich, E. J. Zimney et al., “Preparation and characterization of graphene oxide paper,” *Nature*, vol. 448, no. 7152, pp. 457–460, 2007.
- [5] F. Schedin, A. K. Geim, S. V. Morozov et al., “Detection of individual gas molecules adsorbed on graphene,” *Nature Materials*, vol. 6, no. 9, pp. 652–655, 2007.

- [6] M. D. Stoller, S. Park, Z. Yanwu, J. An, and R. S. Ruoff, "Graphene-based ultracapacitors," *Nano Letters*, vol. 8, no. 10, pp. 3498–3502, 2008.
- [7] P. Blake, P. D. Brimicombe, R. R. Nair et al., "Graphene-based liquid crystal device," *Nano Letters*, vol. 8, no. 6, pp. 1704–1708, 2008.
- [8] K. I. Bolotin, K. J. Sikes, Z. Jiang et al., "Ultrahigh electron mobility in suspended graphene," *Solid State Communications*, vol. 146, no. 9–10, pp. 351–355, 2008.
- [9] H. A. Becerril, J. Mao, Z. Liu, R. M. Stoltenberg, Z. Bao, and Y. Chen, "Evaluation of solution-processed reduced graphene oxide films as transparent conductors," *ACS Nano*, vol. 2, no. 3, pp. 463–470, 2008.
- [10] A. A. Balandin, S. Ghosh, W. Bao et al., "Superior thermal conductivity of single-layer graphene," *Nano Letters*, vol. 8, no. 3, pp. 902–907, 2008.
- [11] K. S. Novoselov, A. K. Geim, S. V. Morozov et al., "Electric field in atomically thin carbon films," *Science*, vol. 306, no. 5696, pp. 666–669, 2004.
- [12] X. Du, I. Skachko, A. Barker, and E. Y. Andrei, "Approaching ballistic transport in suspended graphene," *Nature Nanotechnology*, vol. 3, no. 8, pp. 491–495, 2008.
- [13] L. M. Veca, M. J. Meziani, W. Wang et al., "Carbon nanosheets for polymeric nanocomposites with high thermal conductivity," *Advanced Materials*, vol. 21, no. 20, pp. 2088–2092, 2009.
- [14] A. Yu, P. Ramesh, X. Sun, E. Bekyarova, M. E. Itkis, and R. C. Haddon, "Enhanced thermal conductivity in a hybrid graphite nanoplatelet—carbon nanotube filler for epoxy composites," *Advanced Materials*, vol. 20, no. 24, pp. 4740–4744, 2008.
- [15] S. Wang, M. Tambraparni, J. Qiu, J. Tipton, and D. Dean, "Thermal expansion of graphene composites," *Macromolecules*, vol. 42, no. 14, pp. 5251–5255, 2009.
- [16] D. Li and R. B. Kaner, "Materials science—graphene-based materials," *Science*, vol. 320, no. 5880, pp. 1170–1171, 2008.
- [17] M. Segal, "Selling graphene by the ton," *Nature Nanotechnology*, vol. 4, no. 10, pp. 612–614, 2009.
- [18] C. Berger, Z. Song, X. Li et al., "Electronic confinement and coherence in patterned epitaxial graphene," *Science*, vol. 312, no. 5777, pp. 1191–1196, 2006.
- [19] S. Stankovich, D. A. Dikin, R. D. Piner et al., "Synthesis of graphene-based nanosheets via chemical reduction of exfoliated graphite oxide," *Carbon*, vol. 45, no. 7, pp. 1558–1565, 2007.
- [20] S. Park and R. S. Ruoff, "Chemical methods for the production of graphenes," *Nature Nanotechnology*, vol. 4, no. 4, pp. 217–224, 2009.
- [21] W. Cai, R. D. Piner, F. J. Stadermann et al., "Synthesis and solid-state NMR structural characterization of ^{13}C -labeled graphite oxide," *Science*, vol. 321, no. 5897, pp. 1815–1817, 2008.
- [22] X. Li, W. Cai, L. Colombo, and R. S. Ruoff, "Evolution of graphene growth on Ni and Cu by carbon isotope labeling," *Nano Letters*, vol. 9, no. 12, pp. 4268–4272, 2009.
- [23] W. Cai, R. D. Piner, Y. Zhu et al., "Synthesis of isotopically-labeled graphite films by cold-wall chemical vapor deposition and electronic properties of graphene obtained from such films," *Nano Research*, vol. 2, no. 11, pp. 851–856, 2009.
- [24] S. Iijima and T. Ichihashi, "Single-shell carbon nanotubes of 1-nm diameter," *Nature*, vol. 363, no. 6430, pp. 603–605, 1993.
- [25] B. Hornbostel, M. Haluska, J. Cech, U. Dettlaff, and S. Roth, *Carbon Nanotubes: Arc Discharge and Laser Ablation Synthesis of Singlewalled Carbon Nanotubes*, Springer, New York, NY, USA, 2006.
- [26] M. Keidar, "Factors affecting synthesis of single wall carbon nanotubes in arc discharge," *Journal of Physics D*, vol. 40, no. 8, article no. S18, pp. 2388–2393, 2007.
- [27] P. J. F. Harris, "Solid state growth mechanisms for carbon nanotubes," *Carbon*, vol. 45, no. 2, pp. 229–239, 2007.
- [28] T. Sugai, H. Yoshida, T. Shimada, T. Okazaki, H. Shinohara, and S. Bandow, "New synthesis of high-quality double-walled carbon nanotubes by high-temperature pulsed arc discharge," *Nano Letters*, vol. 3, no. 6, pp. 769–773, 2003.
- [29] W. S. Hummers Jr. and R. E. Offeman, "Preparation of graphitic oxide," *Journal of the American Chemical Society*, vol. 80, no. 6, p. 1339, 1958.
- [30] D. Li, M. B. Müller, S. Gilje, R. B. Kaner, and G. G. Wallace, "Processable aqueous dispersions of graphene nanosheets," *Nature Nanotechnology*, vol. 3, no. 2, pp. 101–105, 2008.
- [31] K. N. Kudin, B. Ozbas, H. C. Schniepp, R. K. Prud'homme, I. A. Aksay, and R. Car, "Raman spectra of graphite oxide and functionalized graphene sheets," *Nano Letters*, vol. 8, no. 1, pp. 36–41, 2008.
- [32] S. Fan, L. Liu, and M. Liu, "Monitoring the growth of carbon nanotubes by carbon isotope labelling," *Nanotechnology*, vol. 14, no. 10, pp. 1118–1123, 2003.
- [33] L. Liu and S. Fan, "Isotope labeling of carbon nanotubes and formation of ^{12}C - ^{13}C nanotube junctions," *Journal of the American Chemical Society*, vol. 123, no. 46, pp. 11502–11503, 2001.

Research Article

Characteristic Features of Stone-Wales Defects in Single-Walled Carbon Nanotube; Adsorption, Dispersion, and Field Emission

Seungkwang Roh,¹ Jongtaek Lee,² Mira Jang,² Mingyeong Shin,² Juone Ahn,² Taehee Park,² and Whikun Yi²

¹ Paju LCD Industrial Complex, Paju-city, Gyeonggi-do 413-779, Republic of Korea

² Department of Chemistry, Hanyang University, Haengdang-dong 17, Seoul 133-791, Republic of Korea

Correspondence should be addressed to Whikun Yi, wkyi@hanyang.ac.kr

Received 31 May 2010; Accepted 29 August 2010

Academic Editor: Rakesh Joshi

Copyright © 2010 Seungkwang Roh et al. This is an open access article distributed under the Creative Commons Attribution License, which permits unrestricted use, distribution, and reproduction in any medium, provided the original work is properly cited.

Adsorption behaviors of dodecanethiol ($C_{12}H_{25}SH$) molecules are investigated on the surface of single-walled carbon nanotubes (SWCNTs) with vibrational and X-ray photoelectron spectrometers. The active adsorption sites are proved as Stone-Wales (SW) defects (5–7 ring defects). The SW defect-removed SWCNTs formed by reacting nanotubes with allyl acrylate molecules are compared with pristine SWCNTs in dispersion and field emission. The former shows higher dispersion and field emission than the latter.

1. Introduction

Carbon nanotubes (CNTs) have a lot of defects such as, vacancies, metastable atoms, pentagons, heptagons, Stone-Wales (SW or a pair of 5–7 rings) defects, discontinuities of walls, and heterogeneous atoms [1–5]. According to a scanning tunneling microscopy (STM) observation, about 10% of the samples were found to exhibit stable defect features under extended scanning [6]. SW defects are stable and commonly present in CNTs and are believed to play key roles in the mechanical [7], electronic [8], and chemical [9] properties of CNTs.

In the studies of the interaction of CNTs with organic compounds, amines have attracted special attention [10–14]. Among these, the most extensively explored is the formation of amide derivatives between carboxylic groups on oxidized CNT tips and long-chain amines. Basiuk et al. [15] reported that infrared (IR) spectra of oxidized single-walled CNTs (SWCNTs) treated with amines under different conditions could not correspond to amide derivatives on SWCNT tips, because the very low concentration of the terminal groups relative to the whole sample mass resulted in a negligible contribution to the IR spectra. The bands detectable in the case of long-chain amines were thought

to correspond to amine molecules physisorbed because of strong hydrophobic interactions of their hydrocarbon chains with SWCNT walls. Our previous studies [16] investigated the adsorption behaviors of alkanethiol molecules on the surface of SWCNTs with vibrational spectrophotometer. We reported that alkanethiol molecules adsorbed strongly on the SWCNT surface and suggested that the active activation sites in the nanotube surface might be SW defects. According to the theoretical calculation by Zhou and Shi [17], it was found that the SW defects of the tube wall could reduce cohesive energies for some foreign atoms such as, H, C, N, O, F, and P. In other words, the heptagon rings generated during SWCNT synthesis can be good candidates for an adsorption of foreign molecules. More recently, first-principle calculations were performed to investigate the dependence of alkanethiol's interaction with SWCNTs on nanotube's type, curvature, and chirality [18]. They reported that the affinities of ethanethiol molecules for the semiconducting and metallic SWCNTs were rather close, about 10% stronger in the former case, and the binding energy of alkanethiol was increased for adsorption on large diameter CNTs.

In this study, we investigate the effect of SW defects for an adsorption of dodecanethiol (DT, $C_{12}H_{25}SH$) molecules onto SWCNT surface to get more advanced evidence on

active sites compared with our previous results. Moreover, after removing (or changing) SW defects from nanotube surface, the degree of dispersion and field emission (FE) of SWCNTs, respectively, was measured and compared with that of untreated pristine SWCNTs.

2. Experimental

SWCNTs and MWCNTs produced by arc-discharge process and thermal chemical vapor deposition (CVD) technique, respectively, were used for an adsorption of dodecanethiol (DT). Both nanotubes were oxidized thermally to remove carbon-containing materials, and subsequently sonicated in HNO_3 . Both CNTs were dispersed in ethanol by an ultrasonication for 8 h, sprayed on a glass, and then dried. The CNTs were immersed in the DT-containing ethanol solution for 1 min, and successively washed out several times with ethanol to remove physisorbed DT molecules from the surface of nanotubes. Adsorbed DT molecules were characterized by infrared (IR) and X-ray photoelectron spectrometer (XPS).

The removal (change) of 5–7 ring defects was carried out by reacting SWCNTs with methyl acrylate or octyl acrylate at 120°C (Diels-Alder reaction). Ultraviolet- (UV-) visible spectrometer was chosen to measure the degree of dispersion of SWCNTs in solvent. The field emission (FE) properties were measured using a two-parallel plate, that is, diode type, in a vacuum pressure of $\sim 1.0 \times 10^{-6}$ Torr at room temperature. Indium tin oxide (ITO) was used for two electrodes and the distance between them was kept at $300 \mu\text{m}$.

3. Results and Discussion

Figure 1 shows the vibrational spectra of pristine SWCNTs, methyl acrylate-treated defect-removed SWCNTs, and MWCNTs after an adsorption of DT molecules. In case of pristine SWCNTs, the spectrum contains strong two bands at 2856 and 2927 cm^{-1} which is assigned to symmetric and asymmetric stretching of $-\text{CH}_2-$ of adsorbed DT molecules, respectively. The shoulder around 2960 cm^{-1} is assigned to the asymmetrical stretching of CH_3 [19–21]. Our adsorption experiments were performed in liquid phase and through a consecutive washing condition. Therefore, our case would allow only the strong adsorption between DTs and SWCNTs, probably chemisorption.

The MWCNTs show no vibrational peaks of DTs, indicating that DTs are hardly adsorbed on the surface of MWCNTs. To understand the interactions between DT molecules and nanotube surface, we observed XPS spectra in the sulfur (2p) region of DT molecules. Figures 2(a) and 2(b) show an Mg $K\alpha$ -induced XPS spectrum of sulfur (2p) core levels of DT molecules on SWCNT and MWCNT surface, respectively. In general, the S (2p) spectra are composed of $2p_{3/2}$ and $2p_{1/2}$ peaks with an intensity of 2:1, as theoretically determined from the spin-orbit splitting effect [22–26]. Figure 2(a) shows two peaks at 162.8 eV ($\text{S}2p_{3/2}$) and 164.4 eV ($\text{S}2p_{1/2}$). Deconvolution of the sulfur (2p)

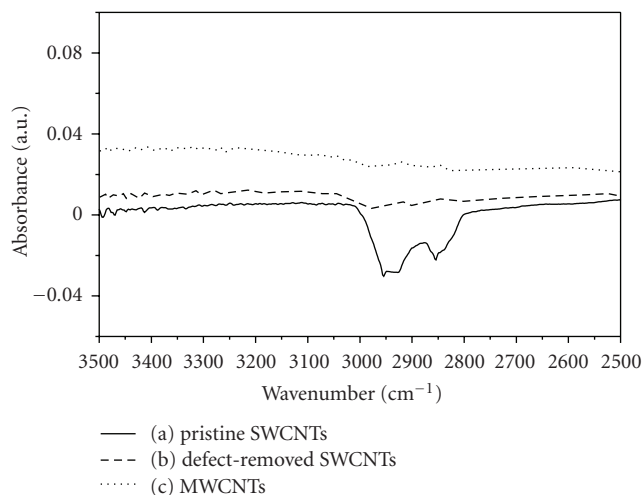


FIGURE 1: IR spectra after an adsorption of alkanethiol (DT) molecules for (a) pristine SWCNTs, (b) methyl acrylate-treated (defect-removed) SWCNTs, and (c) MWCNTs.

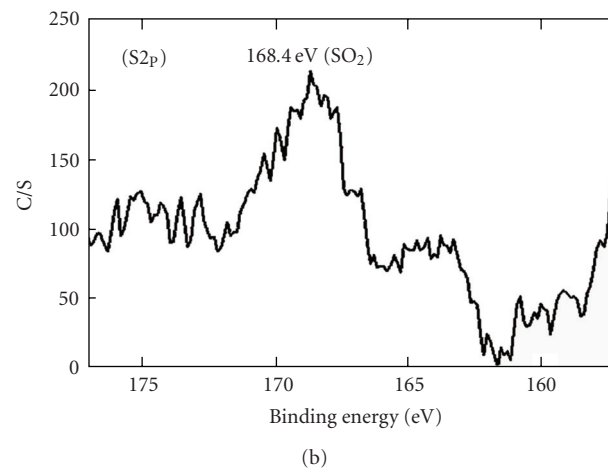
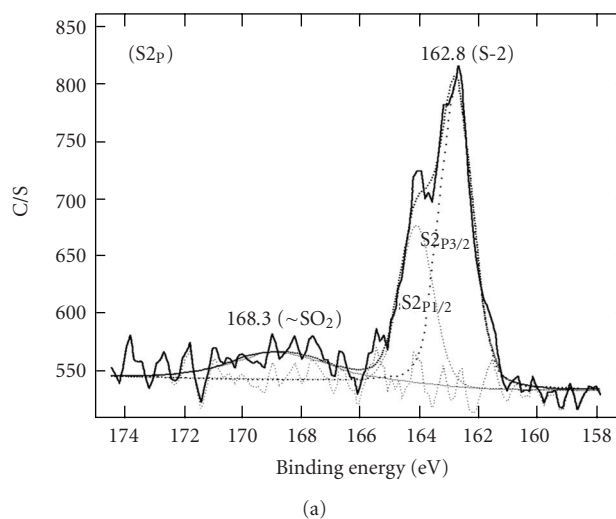


FIGURE 2: S2p XPS spectra of (a) DT-adsorbed SWCNTs and (b) DT-adsorbed MWCNTs.

emission line shape reveals the characteristic intensity ratio 2 : 1 with the peak separation of 1.2 eV. The binding energy of this state suggests the presence of a C-S bond, consistent with chemisorbed thiolate [23, 24, 26]. On the other hand, we cannot see $S2p_{3/2}$ and $S2p_{1/2}$ peaks on MWCNT surface (Figure 2(b)), which strongly suggests that there is no formation of thiolate species. In other words, DT molecules are not adsorbed on the MWCNT surface. The broad peak around 168.4 eV is believed due to sulfonate (or sulfoxide) species.

For the methyl acrylate-treated SWCNTs (Figure 1(b)), the two peaks at 2856 and 2927 cm^{-1} reduce drastically or almost disappear, which is the same result in our previous report [16]. We suggested that the active adsorption sites in SWCNTs might be SW defects for an adsorption of alkanethiols, thus DTs could not be adsorbed on the surface of SWCNTs after removal of SW defects artificially by reacting methyl acrylate ($\text{CH}=\text{CH}-\text{C}=\text{O}(\text{OCH}_3)$) with SWCNTs via Diels-Alder reaction in Scheme 1.

When we treated with methyl acrylate to remove SW defects, the reaction products were not evident since any characteristic vibrational peaks of the products were not found in the IR spectrum. It would be attributed by the small amount of the product sample.

We used octyl acrylate ($\text{CH}=\text{CH}-\text{C}=\text{O}(\text{OC}_8\text{H}_{17})$) instead of methyl acrylate to treat SWCNT surface. Octyl acrylate molecule has longer chain length and more carbon atoms inside than methyl acrylate, thus it is expected that vibrational spectrum due to long chain carbon atoms would be shown if octyl acrylate reacts with SWCNT surface through chemical reaction. Figure 3 represents the IR spectrum of octyl acrylate-treated SWCNTs. Inset shows IR spectrum of neat liquid sample of octyl acrylate molecules for comparison. We can see clearly the peaks at 2856 , 2927 , and 1725 cm^{-1} corresponding to symmetric and asymmetric stretching of $-\text{CH}_2-$, and conjugate $\text{C}=\text{O}$ stretching of octyl acrylate, respectively. The intensity of conjugated $\text{C}=\text{C}$ stretching mode at 1639 and 1618 cm^{-1} is reduced largely compared with the neat sample in inset. IR spectrum results strongly suggest that the 5–7 defects on SWCNTs react with octyl acrylate molecules via Diels-Alder reaction in Scheme 1. SWCNT tips are not considered here since terminated carboxyl ($-\text{COOH}$) or hydroxyl ($-\text{OH}$) groups hardly react with methyl acrylate.

Vibrational intensities of DT molecules are negligible on the surface of MWCNTs as shown in Figure 1(c). As elucidated in XPS results (Figure 2), DT molecules cannot adsorb on MWCNT surface chemically. This implies that the MWCNT surface has a relatively small number of 5–7 ring defects. According to theoretical examination [17], the energy barrier for bond rotation to form 5–7 defects from hexagonal rings is smaller in the tubes than in planar graphene because of the additional tubular strain. The above statements imply that an SWCNT has an advantage over an MWCNT to form 5–7 ring defects since the energy barrier for bond rotation in the SWCNT is smaller than in the MWCNT due to higher tubular strain. Consequently, the SWCNT has more chance to make 5–7 defects during synthesis than the MWCNT.

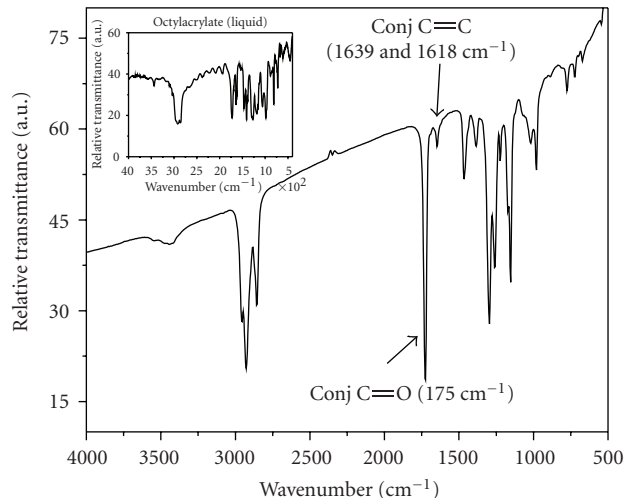


FIGURE 3: IR spectrum of octyl acrylate-treated SWCNTs. Inset represents vibrational spectrum of neat octyl acrylate.

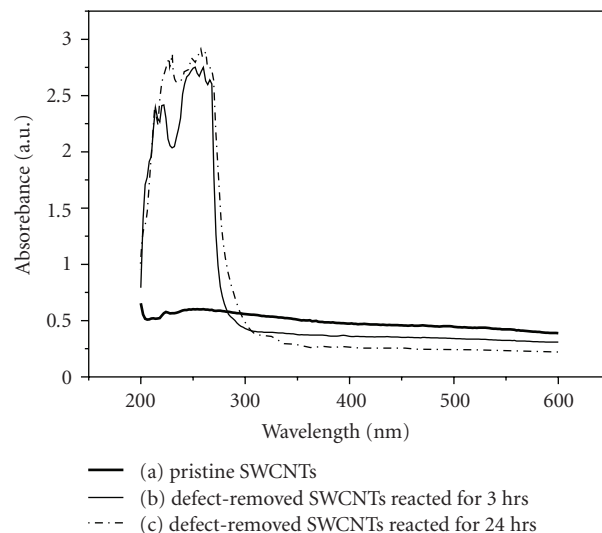


FIGURE 4: UV spectra of pristine SWCNTs (a), methyl acrylate-treated SWCNTs reacted for 3 hrs (b) and for 24 hrs (c).

Figure 4 shows UV-visible absorption spectra of pristine SWCNTs, methyl acrylate-treated SWCNTs (defect-removed SWCNTs) reacted for 3 hrs and 24 hrs in ethanol, respectively. More intense absorption from the spectra implies more stable homogeneous dispersion of SWCNTs in solvent [12, 14, 27]. Therefore, it can be said that the methyl acrylate-treated SWCNTs are dispersed more well rather than the pristine SWCNTs.

SWCNTs always form aggregates because of very strong van der Waals interaction between them. Keeping stable dispersion of SWCNTs in solvent is significant, and also a prerequisite for application as additives for reinforcement of composite materials. SWCNTs were solubilized in water with the aid of surfactant, purified and length-selected [28–30], but removing the surfactant afterwards was problematic.

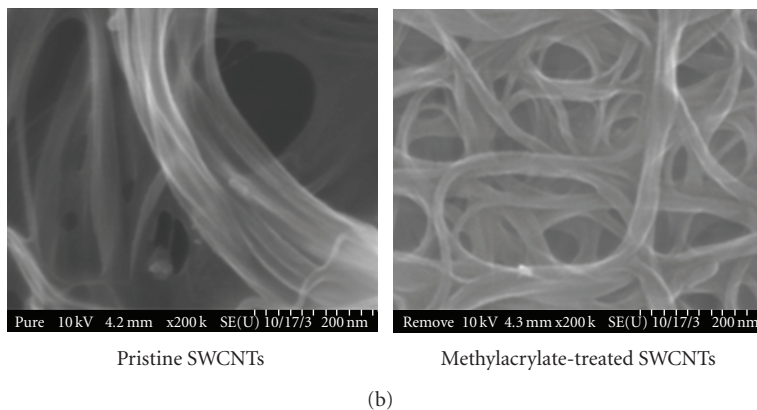
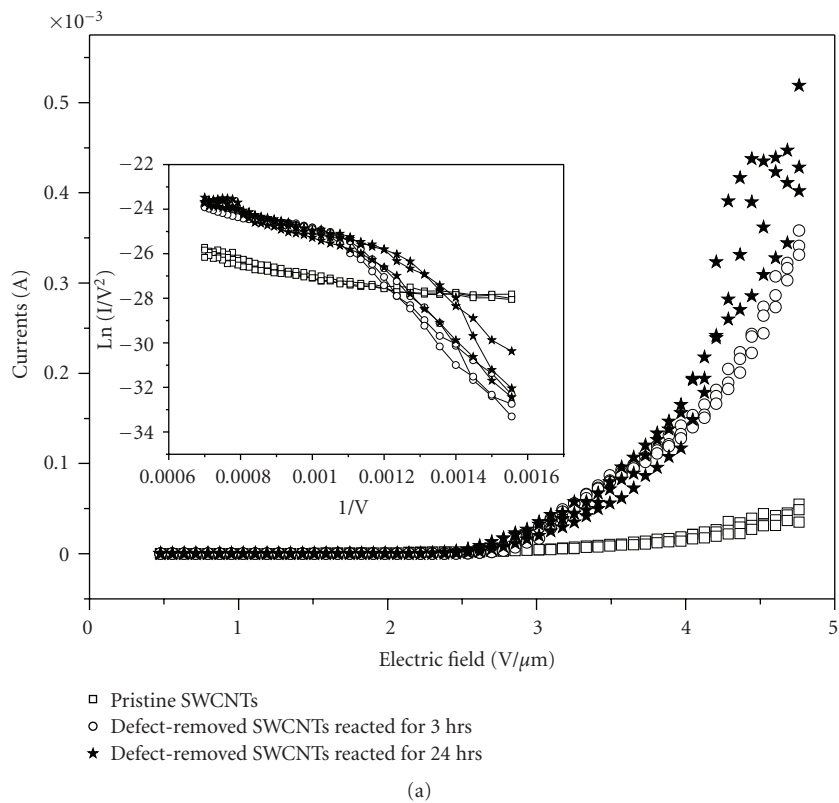
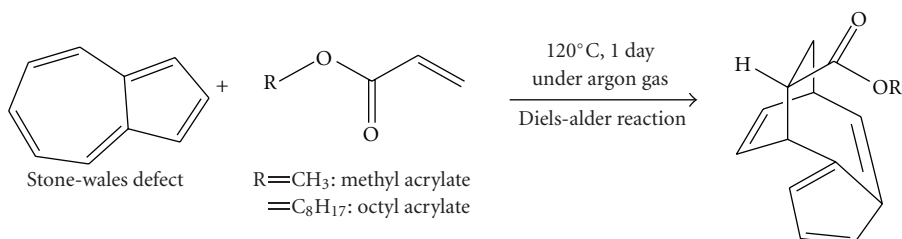


FIGURE 5: Field emission I-V curves (a) and SEM pictures (b) of pristine SWCNTs, methyl acrylate-treated SWCNTs reacted for 3 hrs and 24 hrs, respectively.



SCHEME 1: Diels-Alder reaction to remove (change) SW defects (5–7 ring defects) on the surface SWCNTs.

SWCNTs were also solubilized by functionalizing the end-caps with long aliphatic amines. The above approaches apparently work well, but have the disadvantage that the most convenient chemical handles further modification, and the acid-treated end-caps are tied-up by the solubilization functionality. Our method to remove ring defects is useful since it works well as shown in Figure 4. The interaction between SWCNTs is thought as a hydrophobic force. More stable homogeneous dispersion would be the results that the protruded acrylate molecules attached on the SWCNT surface can make SWCNTs to be exfoliated from the ropes.

We measured field emission (FE) current density of pristine SWCNTs, methyl acrylate-treated SWCNTs for 3 hrs and 24 hrs, respectively. Figure 5(a) shows that methyl acrylate-treated SWCNTs have higher FE current density than pristine SWCNTs, and also FE current behavior of methyl acrylate-treated SWCNTs is similar for both 3- and 24-hour-reacted sample in solvent. The turn-on field of each sample, V_{T-O} , which is defined as the macroscopic field to produce a current density of $10 \mu\text{A}/\text{cm}^2$, was obtained from the logarithmic plot of Figure 5(a). The turn-on field decreased from $3.57 \text{ V}/\mu\text{m}$ (pristine SWCNTs) to 2.8 and $2.73 \text{ V}/\mu\text{m}$ for 3 hrs and 24 hrs, respectively. The maximum emission current density gradually increased and reached $0.50 \text{ mA}/\text{cm}^2$ for the 24-hour-reacted defect-removed SWCNTs, about ten times higher than pristine SWCNTs ($0.05 \text{ mA}/\text{cm}^2$) at an electric field of $4.7 \text{ V}/\mu\text{m}$. The same explanations can be adopted for the enhanced FE current density, that is, the protruded acrylate molecules on the SWCNT surface can make SWCNTs exfoliate from the ropes as shown in Figure 5(b). The well separated SWCNTs reduce the screening effect [31], which leads to an emission decrease caused by neighboring tips when the distance between tips is too small.

4. Conclusion

In summary, Thiol-containing DT molecules can be adsorbed on the surface of SWCNTs, not MWCNTs, and the active adsorption sites are proved as 5–7 ring defects of the nanotube surface which can be removed (changed) by reacting with allyl acrylate molecules via Diels-Alder reaction. The defect-removed SWCNTs show higher degree of dispersion in solvent and enhanced FE currents compared with pristine SWCNTs.

Acknowledgment

The authors gratefully acknowledge the Korean Science and Engineering Foundation (KRF-2009-007-2914 and KRF-2010-001-6233).

References

- [1] F. Banhart, "Irradiation effects in carbon nanostructures," *Reports on Progress in Physics*, vol. 62, no. 8, pp. 1181–1221, 1999.
- [2] S. Iijima, T. Ichihashi, and Y. Ando, "Pentagons, heptagons and negative curvature in graphite microtubule growth," *Nature*, vol. 356, no. 6372, pp. 776–778, 1992.
- [3] O. Zhou, R. M. Fleming, D. W. Murphy et al., "Defects in carbon nanostructures," *Science*, vol. 263, no. 5154, pp. 1744–1747, 1994.
- [4] J.-C. Charlier, "Defects in carbon nanotubes," *Accounts of Chemical Research*, vol. 35, no. 12, pp. 1063–1069, 2002.
- [5] E. Saether, "Transverse mechanical properties of carbon nanotube crystals—part II: sensitivity to lattice distortions," *Composites Science and Technology*, vol. 63, no. 11, pp. 1551–1559, 2003.
- [6] M. Ouyang, J.-L. Huang, C. L. Cheung, and C. M. Lieber, "Atomically resolved single-walled carbon nanotube intramolecular junctions," *Science*, vol. 291, no. 5501, pp. 97–100, 2001.
- [7] K. M. Liew, X. Q. He, and C. H. Wong, "On the study of elastic and plastic properties of multi-walled carbon nanotubes under axial tension using molecular dynamics simulation," *Acta Materialia*, vol. 52, no. 9, pp. 2521–2527, 2004.
- [8] E. J. Duplock, M. Scheffler, and P. J. D. Lindan, "Hallmark of perfect graphene," *Physical Review Letters*, vol. 92, no. 22, Article ID 225502, 1 pages, 2004.
- [9] S. Picozzi, S. Santucci, L. Lozzi, L. Valentini, and B. Delley, "Ozone adsorption on carbon nanotubes: the role of Stone-Wales defects," *Journal of Chemical Physics*, vol. 120, no. 15, pp. 7147–7152, 2004.
- [10] S. S. Wong, E. Joselevich, A. T. Woolley, C. L. Cheung, and C. M. Lieber, "Covalently functionalized nanotubes as nanometresized probes in chemistry and biology," *Nature*, vol. 394, no. 6688, pp. 52–55, 1998.
- [11] S. S. Wong, A. T. Woolley, E. Joselevich, C. Li. C. , and C. M. Lieber, "Covalently-functionalized single-walled carbon nanotube probe tips for chemical force microscopy," *Journal of the American Chemical Society*, vol. 120, no. 33, pp. 8557–8558, 1998.
- [12] J. Chen, M. A. Hamon, H. Hu et al., "Solution properties of single-walled carbon nanotubes," *Science*, vol. 282, no. 5386, pp. 95–98, 1998.
- [13] M. A. Hamon, J. Chen, H. Hu et al., "Dissolution of single-walled carbon nanotubes," *Advanced Materials*, vol. 11, no. 10, pp. 834–840, 1999.
- [14] K. D. Ausman, R. Piner, O. Lourie, R. S. Ruoff, and M. Korobov, "Organic solvent dispersions of single-walled carbon nanotubes: toward solutions of pristine nanotubes," *Journal of Physical Chemistry B*, vol. 104, no. 38, pp. 8911–8915, 2000.
- [15] E. V. Basiuk, V. A. Basiuk, J.-G. Banuelos et al., "Interaction of oxidized single-walled carbon nanotubes with vaporous aliphatic amines," *Journal of Physical Chemistry B*, vol. 106, no. 7, pp. 1588–1597, 2002.
- [16] S. Roh, J. Oh, Y. Choi et al., "Adsorption of alkanethiol molecules onto carbon nanotube surface," *Journal of Vacuum Science and Technology B*, vol. 22, no. 3, pp. 1411–1415, 2004.
- [17] L. G. Zhou and S. Q. Shi, "Adsorption of foreign atoms on Stone-Wales defects in carbon nanotube," *Carbon*, vol. 41, no. 3, pp. 613–615, 2003.
- [18] J. Shakhs Emampour, M. D. Ganji, S. Mahmoudi, M. M. Taghavi, and M. Shokry, "Effect of curvature and chirality for alkanethiols interaction with single-walled carbon nanotubes: *ab initio* investigation," *Iranian Journal of Organic Chemistry*, vol. 4, pp. 256–260, 2009.
- [19] M. D. Porter, T. B. Bright, D. L. Allara, and C. E. D. Chidsey, "Spontaneously organized molecular assemblies. 4. Structural characterization of n-alkyl thiol monolayers on gold by optical ellipsometry, infrared spectroscopy, and electrochemistry," *Journal of the American Chemical Society*, vol. 109, no. 12, pp. 3559–3568, 1987.

- [20] R. G. Nuzzo, L. H. Dubois, and D. L. Allara, "Fundamental studies of microscopic wetting on organic surfaces. 1. Formation and structural characterization of a self-consistent series of polyfunctional organic monolayers," *Journal of the American Chemical Society*, vol. 112, no. 2, pp. 558–569, 1990.
- [21] M. Ulman, *An Introduction to Ultrathin Organic Films*, Academic Press, New York, NY, USA, 1991.
- [22] D. G. Castner, K. Hinds, and D. W. Grainger, "X-ray photoelectron spectroscopy sulfur 2p study of organic thiol and bisulfide binding interactions with gold surfaces," *Langmuir*, vol. 12, no. 21, pp. 5083–5086, 1996.
- [23] T. Ishida, M. Hara, I. Kojima et al., "High resolution X-ray photoelectron spectroscopy measurements of octadecanethiol self-assembled monolayers on Au(111)," *Langmuir*, vol. 14, no. 8, pp. 2092–2096, 1998.
- [24] T. Ishida, N. Choi, W. Mizutani et al., "High-resolution X-ray photoelectron spectra of organosulfur monolayers on Au(111): S(2p) spectral dependence on molecular species," *Langmuir*, vol. 15, no. 20, pp. 6799–6806, 1999.
- [25] F. Buckel, F. Effenberger, C. Yan, A. Götzhäuser, and M. Grunze, "Influence of aromatic groups incorporated in long-chain alkanethiol self-assembled monolayers on gold," *Advanced Materials*, vol. 12, no. 12, pp. 901–905, 2000.
- [26] C.-J. Zhong, R. C. Brush, J. Anderegg, and M. D. Porter, "Organosulfur monolayers at gold surfaces: reexamination of the case for sulfide adsorption and implications to the formation of monolayers from thiols and disulfides," *Langmuir*, vol. 15, no. 2, pp. 518–525, 1999.
- [27] J. L. Bahr, E. T. Mickelson, M. J. Bronikowski, R. E. Smalley, and J. M. Tour, "Dissolution of small diameter single-wall carbon nanotubes in organic solvents?" *Chemical Communications*, no. 2, pp. 193–194, 2001.
- [28] J. Liu, A. G. Rinzler, H. Dai et al., "Fullerene pipes," *Science*, vol. 280, no. 5367, pp. 1253–1256, 1998.
- [29] V. Krstic, G. S. Duesberg, J. Muster, M. Burghard, and S. Roth, "Langmuir-Blodgett films of matrix-diluted single-walled carbon nanotubes," *Chemistry of Materials*, vol. 10, no. 9, pp. 2338–2340, 1998.
- [30] G. S. Duesberg, J. Muster, V. Krstic, M. Burghard, and S. Roth, "Chromatographic size separation of single-wall carbon nanotubes," *Applied Physics A*, vol. 67, no. 1, pp. 117–119, 1998.
- [31] V. V. Zhirnov, E. I. Givargizov, and P. S. Plekhanov, "Field emission from silicon spikes with diamond coatings," *Journal of Vacuum Science and Technology B*, vol. 13, no. 2, pp. 418–421, 1995.

Review Article

Simulated Nanoscale Peeling Process of Monolayer Graphene Sheet: Effect of Edge Structure and Lifting Position

Naruo Sasaki,¹ Hideaki Okamoto,¹ Shingen Masuda,¹ Kouji Miura,² and Noriaki Itamura¹

¹Department of Materials and Life Science, Faculty of Science and Technology, Seikei University, 3-3-1 Kichijoji-Kitamachi, Musashino-shi, Tokyo 180-8633, Japan

²Department of Physics, Aichi University of Education, Hiroosawa 1, Igayacho, Kariya-shi, Aichi 448-8542, Japan

Correspondence should be addressed to Naruo Sasaki, naru@st.seikei.ac.jp

Received 1 June 2010; Accepted 4 August 2010

Academic Editor: Rakesh Joshi

Copyright © 2010 Naruo Sasaki et al. This is an open access article distributed under the Creative Commons Attribution License, which permits unrestricted use, distribution, and reproduction in any medium, provided the original work is properly cited.

The nanoscale peeling of the graphene sheet on the graphite surface is numerically studied by molecular mechanics simulation. For center-lifting case, the successive partial peelings of the graphene around the lifting center appear as discrete jumps in the force curve, which induce the arched deformation of the graphene sheet. For edge-lifting case, marked atomic-scale friction of the graphene sheet during the nanoscale peeling process is found. During the surface contact, the graphene sheet takes the atomic-scale sliding motion. The period of the peeling force curve during the surface contact decreases to the lattice period of the graphite. During the line contact, the graphene sheet also takes the stick-slip sliding motion. These findings indicate the possibility of not only the direct observation of the atomic-scale friction of the graphene sheet at the tip/surface interface but also the identification of the lattice orientation and the edge structure of the graphene sheet.

1. Introduction

Adhesion and peeling phenomena play important roles in connecting two objects regardless of whether they are inorganic, organic, or biological materials, which contributes to building up microscopic devices. The carbon nanostructures such as, carbon nanotube (CNT) and graphene have recently attracted great interests as the components of the electronic, magnetic, and optical devices. We have so far studied the peeling mechanics of the carbon nanotube (CNT) adsorbed onto the graphite surface both theoretically [1–3] and experimentally [4, 5]. It is clarified that the transition from the line- to the point-contact between the CNT and the graphite surface occurs during the peeling process [1–5]. The CNT on the sub-microscale has the same size as the spatulae of the microscopic hairs aligned on the gecko foot [6, 7]. Therefore the study of the peeling process of the nanoscale objects such as, CNT is useful for not only developing the gecko-foot-mimic adhesives [8] but also understanding the elementary process of adhesion.

On the other hand, since the success of its experimental isolation [9], the potential of various applications of the graphene such as, the components of the electronic devices

[10, 11] has been discussed by many researchers. There is also a possibility that its adhesion with the substrate is applied to the adhesive tape at nanoscale. Therefore the peeling mechanics of the graphene sheet is very important, which can be regarded as the elementary process of the macroscopic sticky tape such as, the gecko-foot-mimic adhesives [6–8] or that of the microscopic extension of the crack in the fracture process. In our preliminary experiments, we have already succeeded in peeling the multilayered graphene plate with a thickness of several μm by using atomic-force microscopy tip [12]. Here the two-component epoxy resin adhesive is used to bond the graphene plate to the AFM tip. Here the standard Si_3N_4 tip for the contact AFM experiment is used. The junction formed between the AFM tip and the graphene should be mechanically rigid enough to measure the elasticity of the graphene sheet during the peeling process. The two-component epoxy resin adhesive satisfies the above condition. If the thickness of the peeled graphene plate is reduced, the comparison between the present simulation and the experiment will become possible.

Therefore, in this paper, ahead of experiment, we have theoretically reported the nanoscale peeling behaviors of the monolayer graphene sheet based on the molecular mechanics

simulation [13, 14]. The peeling force curve exhibits the nanoscale change of the graphene shape from the surface to the line contact. The center position and the left edge are chosen as the lifting position. In Section 3, the peeling of the monolayer graphene sheet with the armchair edge for lifting the center position is discussed. In Sections 4 and 5, the peeling of the monolayer graphene sheet with the armchair- and zigzag-edge for lifting the edge position is discussed, respectively.

2. Model and Method of Simulation

In the simulation, a rectangular-shaped monolayer graphene sheet with each side of $38 \text{ \AA} \times 20 - 21 \text{ \AA}$, comprised of 310 carbon atoms, is peeled from the rigid rectangular graphene sheet (which is called, the “graphite surface,” hereafter) with each side of $164 - 165 \text{ \AA} \times 58 \text{ \AA}$, comprised of 3536 carbon atoms [Figure 1(a)]. First, both the above graphene sheets are separately optimized by minimizing the covalent bonding energy described by the Tersoff potential energy [15], V_{cov} , using the Polak-Rebriere-type conjugate gradient (CG) method [16]. Here the convergence criterion is set so that the maximum of absolute value of all the forces acting on the movable atoms becomes lower than 10^{-5} eV/\AA . Next, the graphene sheet is put and adsorbed onto the graphite surface, so that the AB stacking registry between the graphene sheet and the graphite surface is satisfied as shown in Figures 1(b) and 1(c). Here the green-colored six-membered ring at the center position or the outermost left edge of the graphene sheet is assumed to be attached to the AFM tip apex (Figure 1(a)), and then it is gradually moved upward along the z direction, parallel to the $[0001]$ axis, by 0.1 \AA . For each lifting position of the graphene sheet, z , the total energy $V_{\text{total}} = V_{\text{cov}} + V_{\text{vdW}}$ is minimized using the CG method, where V_{vdW} is the nonbonding vdW interaction described by the modified Lennard-Jones (LJ) potential energy [17, 18], acting between the graphene sheet and the graphite surface. Thus the optimized positions of the movable carbon atoms of the graphene sheet, (x, y, z) , the vertical peeling force F_z , and the lateral sliding forces F_x and F_y , acting on the lifting center, are calculated during the peeling process. In this paper, the graphene sheets with armchair-(Figure 1(b)) and zigzag-edges (Figure 1(c)) are discussed.

3. Center-Lifting Case of Armchair-Edge Graphene

When the six-membered ring located at the center position of the monolayer graphene sheet is lifted, the graphene sheet exhibits the characteristic transition of its shape during the peeling process within the $x - z$ plane as illustrated in Figures 2(A)–2(J), corresponding to Figures 3(A)–3(J), the vertical force acting on the lifting center position F_z plotted as a function of the displacement from the initial position along z -direction, z . At first the monolayer graphene sheet takes an initial planar structure parallel to the rigid graphite surface (Figure 2(A): $z = 0 \text{ \AA}$). Here the surface contact is formed between the graphene sheet and the graphite

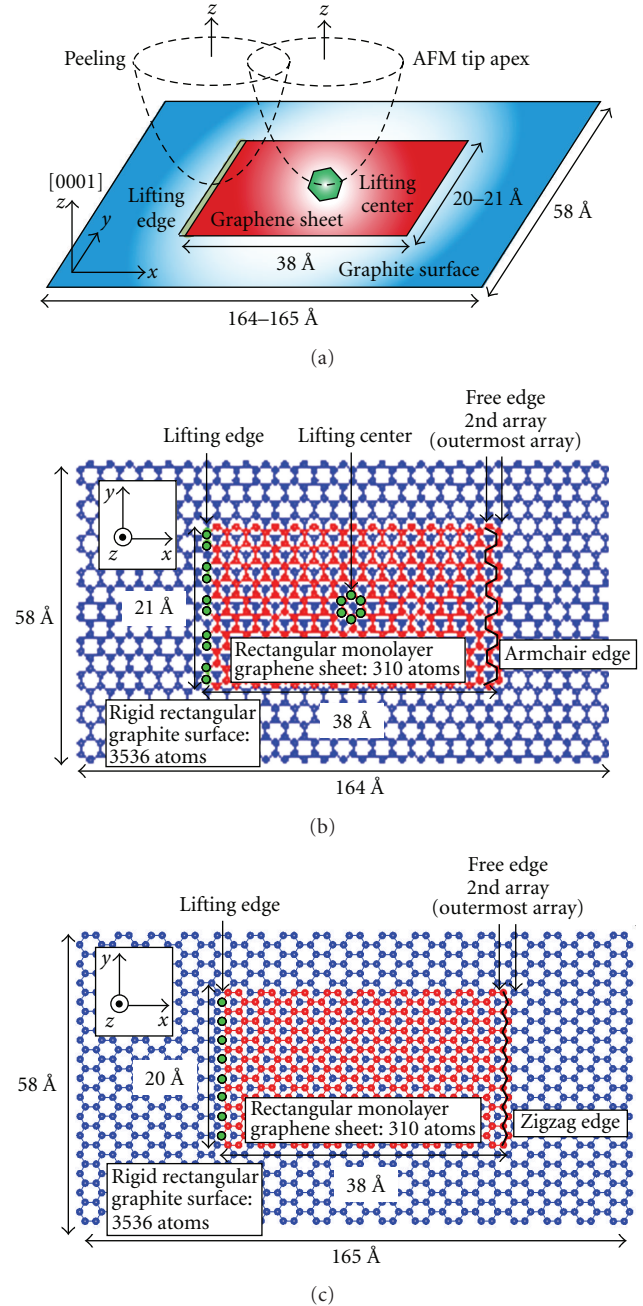


FIGURE 1: (a) The schematic illustration of the model of the monolayer graphene sheet physically adsorbed onto the rigid graphite surface used in the simulation. The green-colored six-membered ring at the center position or left edge of the graphene sheet is assumed to be adsorbed onto the atomic force microscopy tip apex indicated by broken lines, and it is moved upward along the z (or $[0001]$) direction, by $z = 0.1 \text{ \AA}$. Initial AB stacking registry of the red-colored graphene sheet with (b) armchair and (c) zigzag edge adsorbed onto the blue-colored graphite surface within the $x - y$ plane.

surface. The vertical force F_z is zero (Figure 3(a)). Just after the beginning of the peeling (Figure 2(B): $z = 2.0 \text{ \AA}$), the attractive interaction force takes the minimum value, -3.1 eV/\AA (Figure 3(B)).

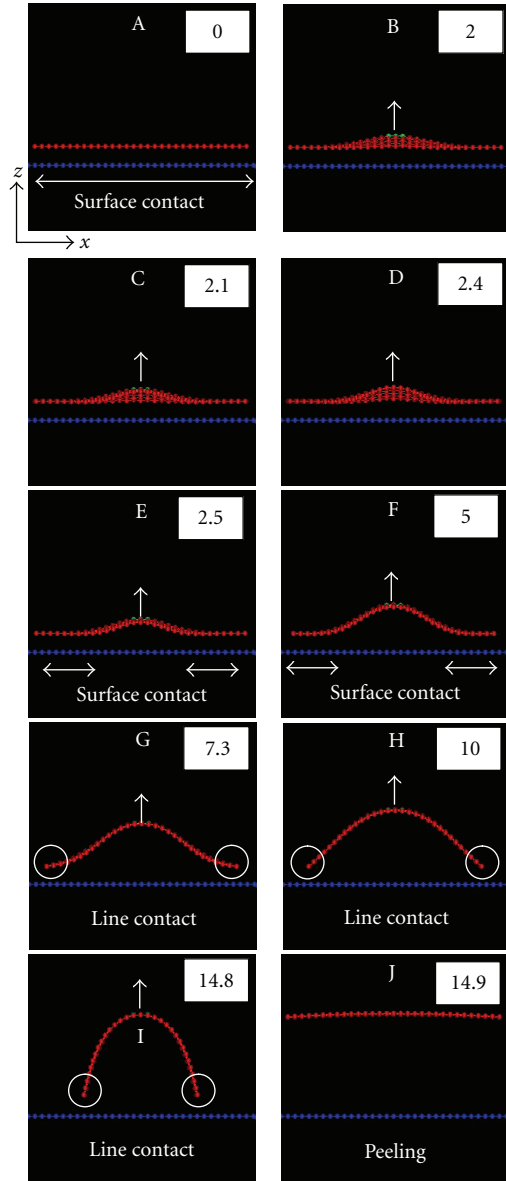


FIGURE 2: The transition of the shape of the monolayer graphene sheet during the peeling process from A to J within the x - z plane. The red-colored graphene sheet and blue-colored graphite surface are shown. The displacement of the lifting center position from the initial position, $z(\text{\AA})$, is indicated on the upper-right positions of each picture.

Between $z = 2.0 \text{\AA}$ and 2.1\AA , the first discrete partial peeling of the graphene occurs (Figures 2(B) \rightarrow 2(C)), which produces the 1st discontinuous jump in the force curve (Figures 3(B) \rightarrow 3(C)). The partial peeled area around the lifting center of the graphene is shown in Figures 4(B) \rightarrow 4(C). Then, between $z = 2.4 \text{\AA}$ and 2.5\AA , the second discrete partial peeling of the graphene occurs (Figures 2(D) \rightarrow 2(E)), which produces the 2nd discontinuous jump in the force curve (Figures 3(D) \rightarrow 3(E)). The partial peeled area of the graphene is shown in Figures 4(D) \rightarrow 4(E). Which of these two areas is peeled first is expected to be actually the

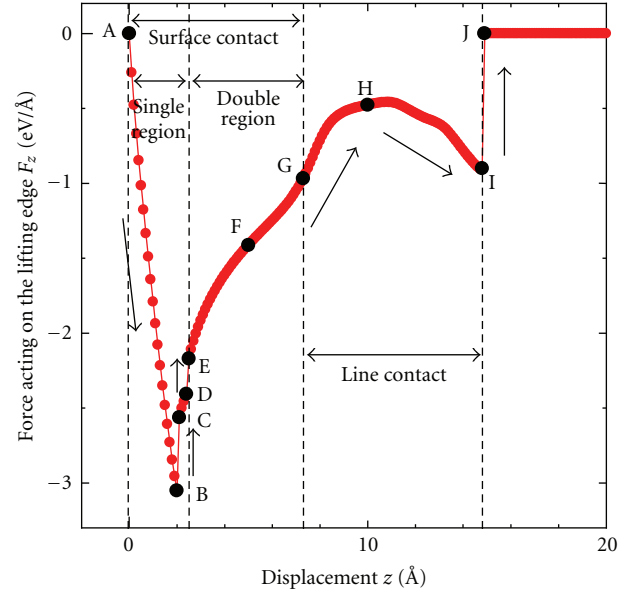


FIGURE 3: The vertical force, F_z , acting on the center six-membered ring, plotted as a function of the lifting displacement z . The positions A-J correspond to those of Figure 2.

stochastic process under the room temperature condition. Now the surface contact region is split into the left and right sections (Figure 2(E)). After the two discrete jumps, F_z increases as the peeling proceeds, since the attractive surface contact region gradually decreases (Figure 2(F): $z = 5.0 \text{\AA}$). Then the surface contact continuously turns into the line contact at $z = 7.3 \text{\AA}$ (Figure 2(G)). Here the 'line contact' is defined by the following two criteria: (1) The carbon atoms on the left and right outermost arrays of the graphene sheet (Figure 1(b)) receive the repulsive interaction force from the graphite surface. (2) The carbon atoms on the second arrays (Figure 1(b)) next to the outermost arrays receive the attractive interaction force. As illustrated in Figure 5, the average forces acting on one carbon atom on the outermost and the second arrays satisfy the above criteria at $z = 7.3 \text{\AA}$, which corresponds to Figure 2(G).

Once the line contacts are formed between the free edges (outermost arrays) of the peeled graphene sheet and the graphite surface, they clearly slide on the graphite surface as indicated by a circle in Figures 2(G) \rightarrow 2(H) \rightarrow 2(I) with a rapid increase of the bending of the graphene sheet. Within x - y plane, the right outermost array of the graphene sheet slides nearly straightforward along $-x$ direction, not so sensitive to the lattice structure of the surface as illustrated in Figures 6(a) and 6(b), which show the trajectories of the two carbon atoms on the right outermost array illustrated in Figure 1(b). The sliding of the outermost arrays during G and I appears much more clearly than that during A and G. During H and I, the decrease of F_z (Figures 3(H) and 3(I)) can be explained by the decrease of the repulsive force acting on the carbon atoms on the left and right edges of the graphene sheet as shown in Figure 5, that is to say, the relative increase of the effect of the attractive interaction force.

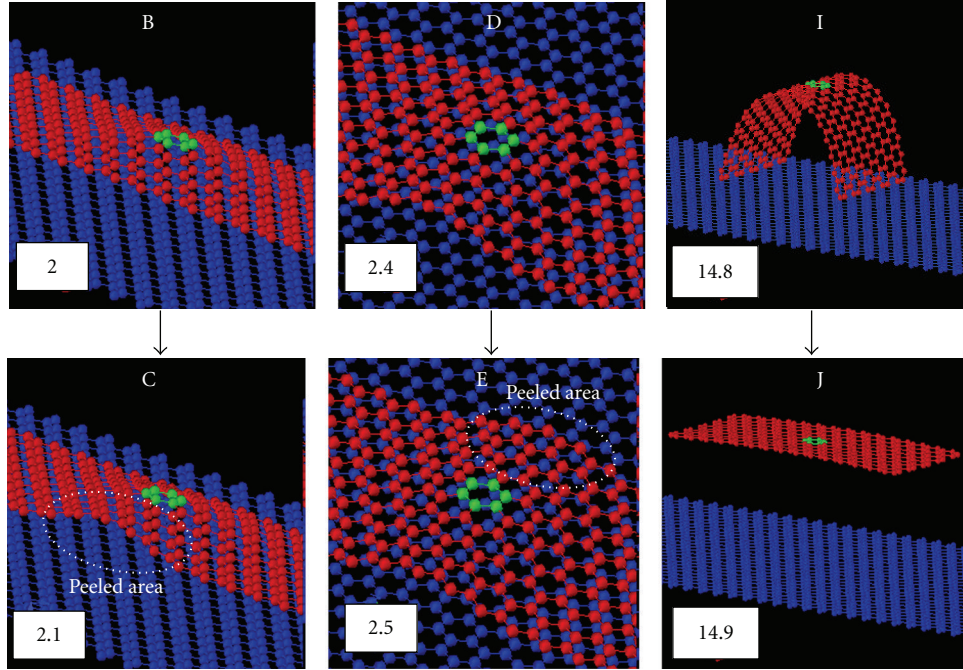


FIGURE 4: The atomic structures of the graphene sheet just before and after the discrete change, $B \rightarrow C$, $D \rightarrow E$, and $I \rightarrow J$. The regions surrounded by dotted ellipses show the partial peeled areas.

When the bending of the graphene sheet becomes larger than a certain range, both the left and right line contacts break and the graphene sheet is completely peeled from the surface (Figures 2(I) \rightarrow 2(J): $z = 14.8 \text{ \AA} \rightarrow 14.9 \text{ \AA}$), which produces the 3rd discontinuous jump in the force curve (Figures 3(I) \rightarrow 3(J)). As illustrated in Figures 2(I) \rightarrow 2(J) and Figures 4(I) \rightarrow 4(J), the graphene sheet exhibits the transition from the arched shape to the planer shape.

Thus the vertical peeling force F_z exhibits the characteristic shape as shown in Figure 3, which reflects the transition from the surface to the line contact between the graphene sheet and the graphite surface. On the other hand, the lateral sliding force F_x is zero due to the structural symmetry of the system. However, the lateral sliding force F_y shows a finite value with an oscillation whose period and amplitude decrease as z increases. This oscillation of Figure 7 reflects the trajectory of the graphene edges illustrated in Figure 6 at the graphene-substrate interface during the peeling process. The maximum lateral force $F_y \simeq 0.1 \text{ eV/\AA}$ which is only about 3% of the absolute value of the maximum adhesion force $|F_z| = 3.1 \text{ eV/\AA}$.

4. Edge-Lifting Case of Armchair-Edge Graphene

4.1. Nanoscale Peeling along Vertical Direction. When the left edge of the monolayer graphene sheet with armchair edge (Figure 1(b)) is lifted, the shape of the graphene sheet markedly changes during the peeling process within the $x-z$ plane as illustrated in Figures 8(A)–8(J), corresponding to

Figures 9(a)A–9(a)J, the vertical force acting on the lifting edge F_z plotted as a function of the edge height z .

4.1.1. Surface-Contact Region. At first the monolayer graphene sheet takes an initial planar structure parallel to the rigid graphite surface (Figure 8(A): $z = 0 \text{ \AA}$), and the vertical force F_z is zero (Figure 9(a)A), which means the graphene sheet completely takes the surface contact with the graphite surface. Just after the start of the peeling (Figure 8(B): $z = 1.1 \text{ \AA}$), the attractive interaction force $|F_z|$ becomes the maximum, 0.74 eV/\AA (Figure 9(a)B). After that the surface contact area gradually decreases as the peeling proceeds (Figures 8(C)–8(E)), where Figure 9(a) exhibits the atomic-scale zigzag structures (Figures 9(a)C–E), which will be explained in the Section 4.2.

4.1.2. Line-Contact Region. After the surface contact vanishes, the line contact appears (Figure 8(F)). Here the “line contact” is defined by the following two criteria similar to the case of the center-lifting peeling. (1) The outermost array of the free edge of the graphene sheet (Figure 1(b)) receives the averaged repulsive interaction force per one carbon atom from the graphite surface. (2) The second array next to the outermost array (Figure 1(b)) receives the averaged attractive interaction force per one carbon atom. As illustrated in Figure 9(b), the edge height $z = 31.3 \text{ \AA}$ satisfies the above criteria (Figure 8(F)). Here the free edge adsorbed onto the graphite surface is nearly fixed even if the left edge is lifted (Figure 8(F) \rightarrow Figure 8(G): $z = 33.9 \text{ \AA}$). As a result, the in-plane bending of the graphene sheet markedly decreases,

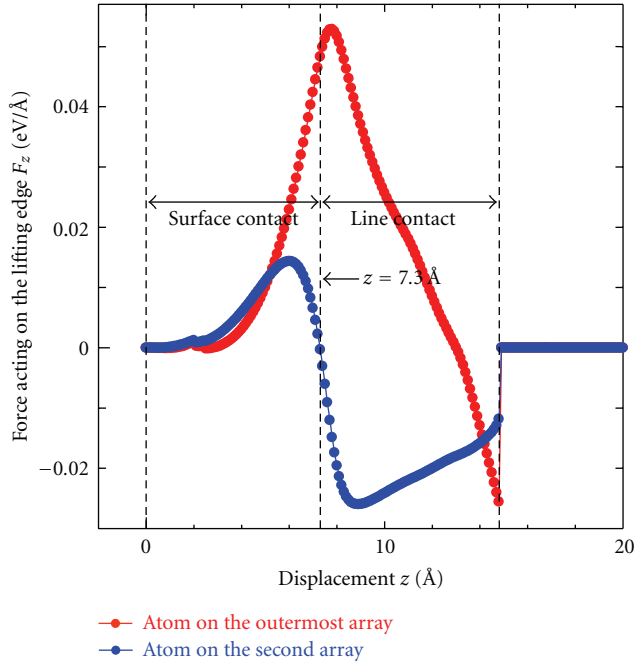


FIGURE 5: The averaged forces acting on one atom on the left and right outermost arrays (red-colored) and those on the left and right second arrays (blue-colored), as a function of the displacement of the lifting center position from the initial position, z (Å).

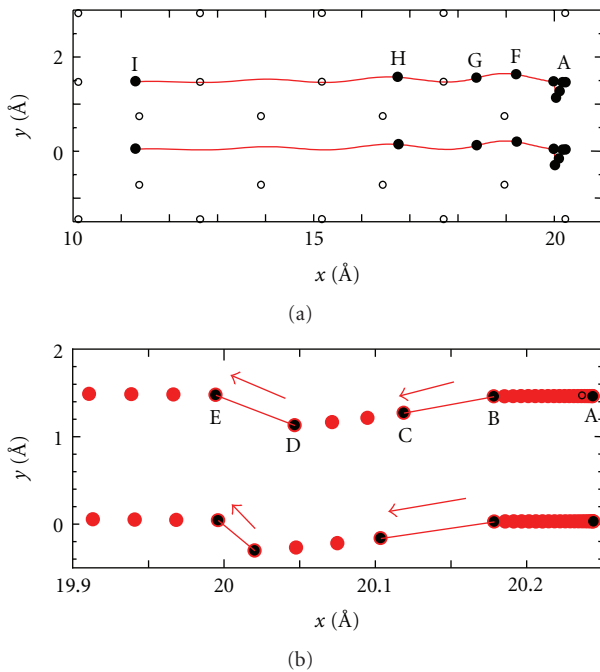


FIGURE 6: The trajectory of the two carbon atoms on the right free edge (outermost array) indicated by white circles in Figure 1(b). (a) The whole trajectory A → I, and (b) the part of the trajectory A → E, including the discrete jumps, B → C and D → E, are indicated. White circles mean carbon atoms of the graphite surface. The indices A–I correspond to those in Figure 2.

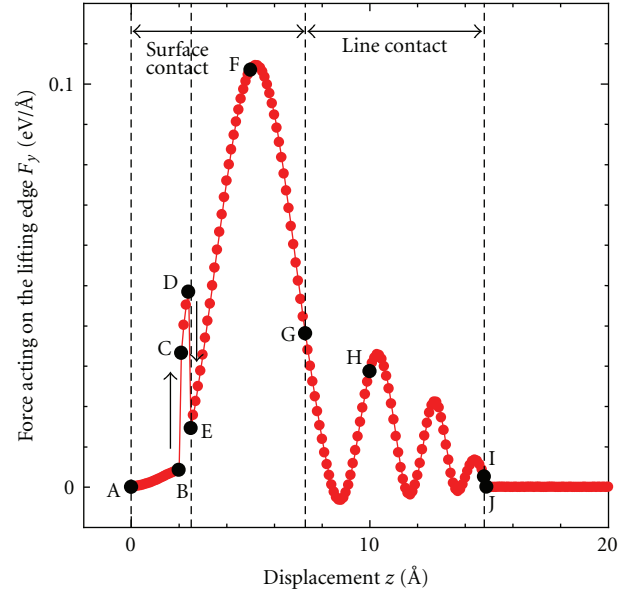


FIGURE 7: The lateral force, F_y , acting on the center six-membered ring, plotted as a function of the displacement z . The positions A–J correspond to those of Figure 2.

and $|F_z|$ decreases to zero (Figures 9(a)F–G). After that the free edge slides on the surface until the graphene sheet takes planar structure within the y - z plane (Figure 8(H): $z = 37.9$ Å), where $|F_z|$ increases again (Figure 9(a)H).

4.1.3. Toward Complete Peeling. Then the graphene sheet is continuously moved upward (Figure 8(I): $z = 38.0$ Å → Figure 8(J): $z = 38.4$ Å) and is completely peeled from the surface. It is noted that the line contact clearly vanishes at $z = 38.0$ Å (Figure 9(b)I). The attractive interaction force $|F_z|$ increases to take the maximum value (Figures 9(a)I → J), and then it gradually decreases to zero toward the complete peeling.

4.2. Atomic-Scale Sliding within Lateral Plane. Figure 9(a) shows the atomic-scale zigzag structures within the surface- and line-contact regions, which can be explained by the following atomic-scale sliding motions of the graphene sheet within the x – y plane.

4.2.1. Surface-Contact Region. During the surface contact region between C and E in Figure 9(a), z – F_z curve takes the atomic-scale zigzag structures from I to VII. The zigzag behaviors exhibit the transition from the continuous (Figures 10(a)I–II) to the sawtooth shapes (Figures 10(a)III–VII). First Figures 10(a)1 → 2 → 3 → 4 → 5 correspond to Figures 10(b)1 → 2 → 3 → 4 → 5, which show that the graphene sheet continuously slides passing over the nearest neighboring AB stacking sites with the graphite surface. The trajectories of the graphene sheet exhibit the continuous zigzag paths as shown in Figure 10(b)5. Next Figures 10(a)6 → 7 → 8 → 9 → 10 correspond to Figures 10(c)6 → 7 → 8 → 9 → 10 which show that the graphene sheet takes the zigzag stick-slip

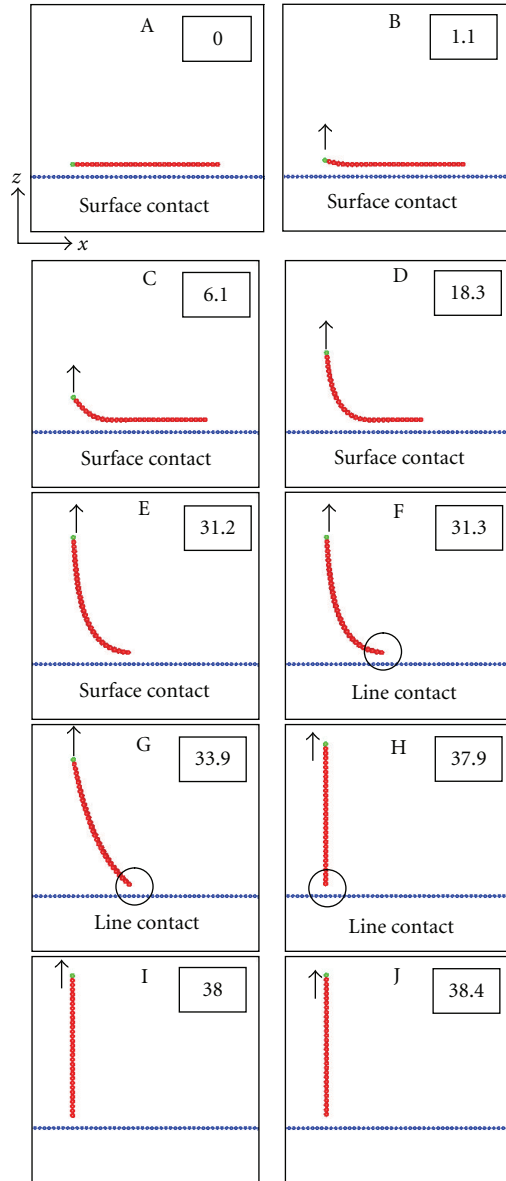
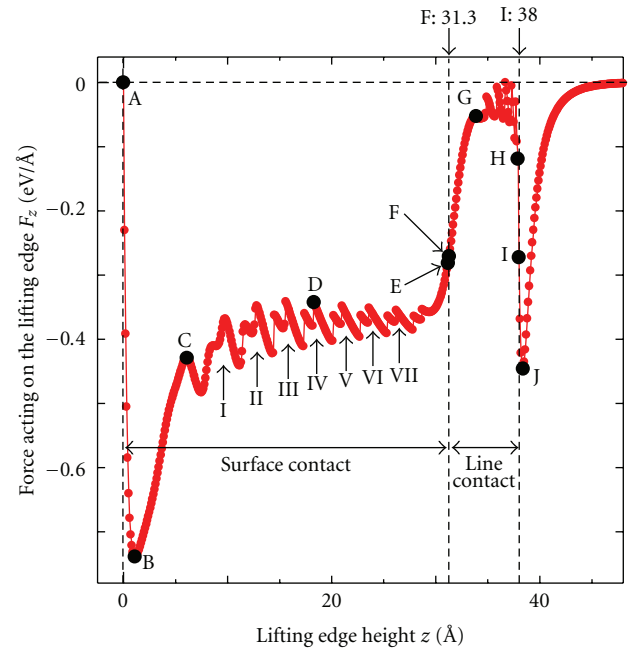
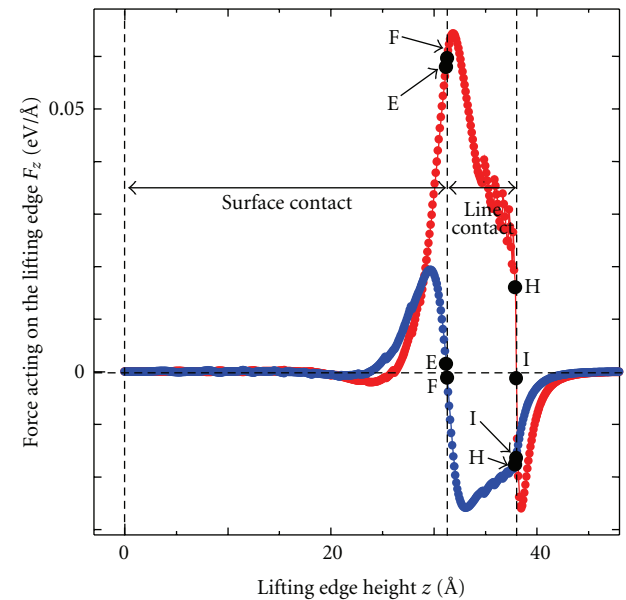


FIGURE 8: The transition of the shape of the monolayer graphene sheet with free edge of armchair-type during the peeling process from A to J within the $x-z$ plane. The red-colored graphene sheet and blue-colored graphite surface are shown. The height of the lifting left edge $z(\text{\AA})$ is indicated on the upper-right positions of each picture.

motions between the nearest neighboring AB stacking sites. Just before the slip, the graphene sheet deviates quite a little from the AB-stacking site (Figure 10(c)6: $z = 17.3 \text{\AA}$). Then it discretely jumps or slips to the neighboring AB-stacking site (Figure 10(c)7: $z = 17.4 \text{\AA}$). As the peeling proceeds, the graphene sheet continuously slides quite a little (Figure 10(c)8: $z = 18.2 \text{\AA}$), then it discretely slips again to the neighboring AB stacking site (Figure 10(c)9: $z = 18.3 \text{\AA}$). After that the graphene sheet continuously slides quite a little again (Figure 10(c)10: $z = 20.1 \text{\AA}$) until the next slip toward the neighboring AB stacking site occurs. As a result



(a)



—●— The outermost array
—●— The second array

(b)

FIGURE 9: (a) The vertical force, F_z , acting on the lifting edge, plotted as a function of the lifting edge height z for the graphene with armchair-type free edge. The indices A–J correspond to those of Figure 8. (b) The red-colored averaged force per one atom acting on the outermost array, and the blue-colored one acting on the second array, as a function of the lifting edge height $z(\text{\AA})$. The indices E, F, H, and I correspond to those of Figures 8 and 9(a).

the trajectories of the graphene sheet exhibit the discrete zigzag paths connecting the nearest neighboring AB-stacking sites as shown in Figure 10(c)10. The period of the zigzag

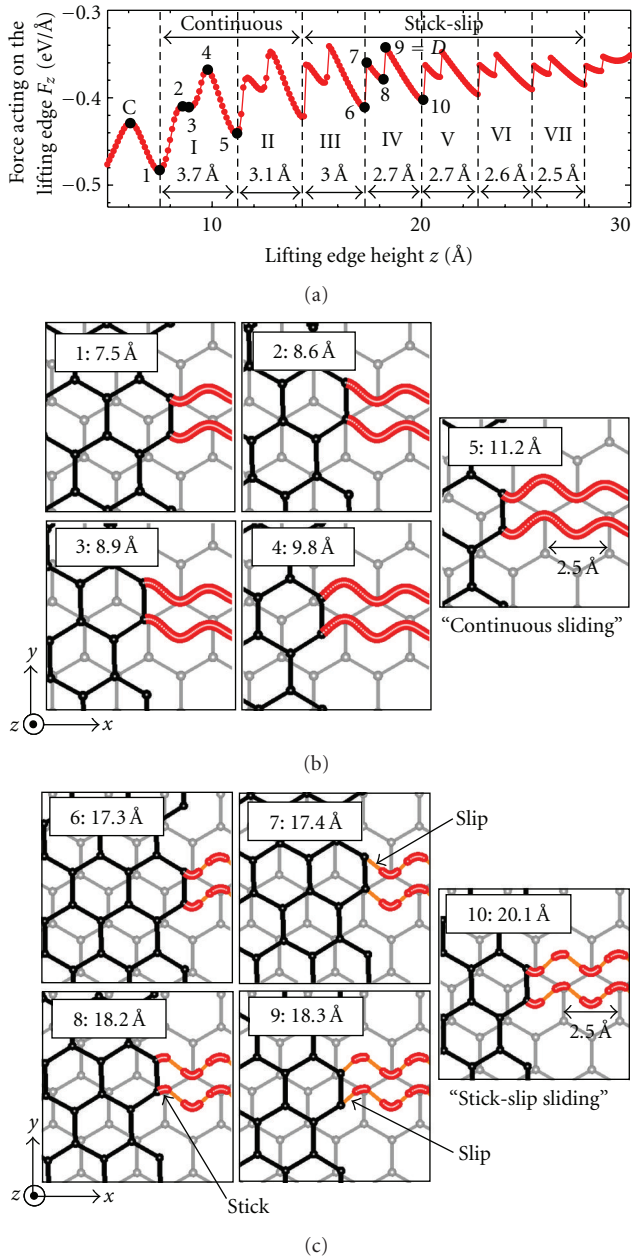


FIGURE 10: (a) Enlargement of part of the $z - F_z$ curve (Figure 9(a)) corresponding to the continuous and stick-slip process during the surface contact. (b) The trajectories of the two carbon atoms on the free edge from 1 to 5 indicated in (a). (c) The trajectories of the two carbon atoms on the free edge from 6 to 10 indicated in (a).

behavior of the F_z curve decreases from 3.7 Å to 2.5 Å as shown in Figure 10(a) as the peeling proceeds. The lattice spacing of the graphite surface, 2.5 Å, appears in the peeling force curve particularly for the stick-slip region.

4.2.2. *Line-Contact Region.* During the line contact region between G and H in Figure 9(a), $z - F_z$ curve takes another atomic-scale zigzag structures as shown in Figure 11(a). One of the zigzag behaviors in the force curve (Figures 11(a)1 →

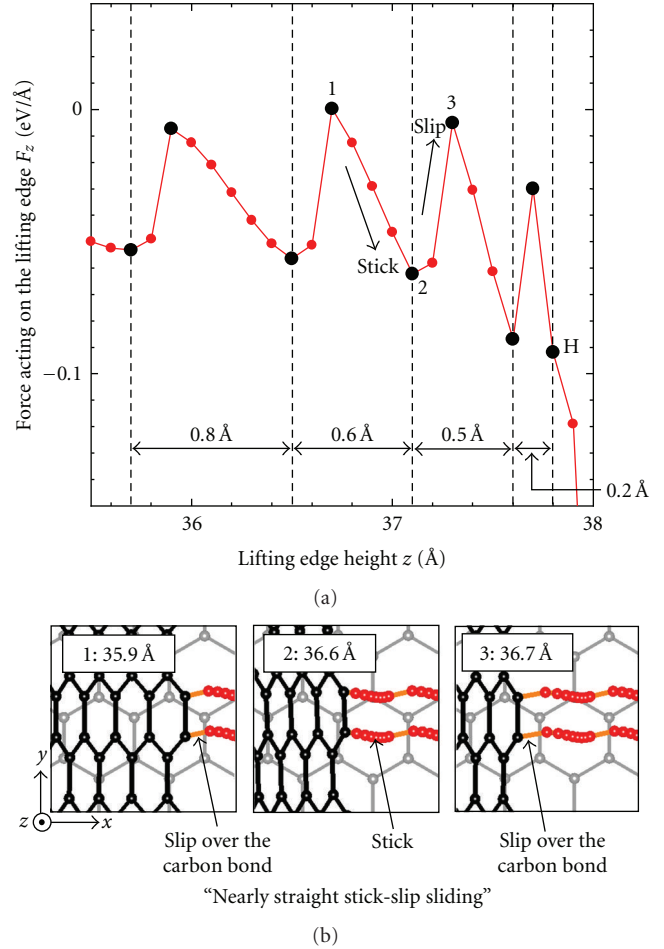


FIGURE 11: (a) Enlargement of part of the $z - F_z$ curve (Figure 9(a)) corresponding to the nearly straight stick-slip region during the line contact. (b) The trajectories of the two carbon atoms on the free edge from 1 to 3 indicated in (a).

2 → 3) corresponds to the stick-slip sliding motion of the graphene sheet (Figures 11(b)1 → 2 → 3). Here the free edge of the graphene sheet slides with nearly the straight stick-slip motions. One of the carbon atoms on the free edge passes over the carbon-carbon bonds as shown in Figures 11(b)1 and 3.

5. Edge-Lifting Case of Zigzag-Edge Graphene

Recently it has been reported that the edge structure of the graphene sheet plays quite an important role in electronic, magnetic, and optical properties of graphene, which can be also expected to give influences on the mechanical properties such as, the peeling process. Therefore, in this section, the peeling process of the graphene sheet with zigzag edge is discussed. In the simulation, the model obtained by rotating Figure 1(b) by 30° is used (Figure 1(c)), and the left zigzag edge is lifted to simulate the peeling process, while the right free edge is zigzag type. As a result, the nanoscale peeling process within the $x - z$ plane and the global shape of the

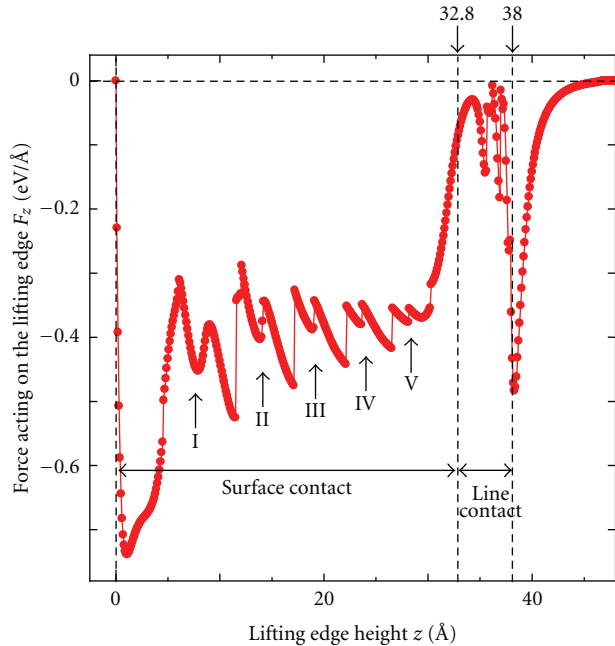


FIGURE 12: The vertical force, F_z , acting on the lifting edge, plotted as a function of the lifting edge height z for the graphene with zigzag-type free edge.

force curve (Figure 12) is similar to that of Figures 8 and 9, respectively. The qualitative tendency of the decrease of the period and amplitude of the force curve (Figure 12(b)I-IV) is similar to that for Figure 9(a)I-VII. However, the details of the atomic-scale mechanics of the zigzag edge are clearly different from those of the armchair edge as follows.

During the surface contact, the graphene sheet first takes zigzag (Figures 13(b)1-6) and then straight stick-slip motions (Figures 13(c)7-11), passing over the nearest neighboring AB-stacking site along $[10\bar{1}0]$ direction. It is noted to avoid AA-stacking registry, the graphene sheet takes zigzag slip toward the nearest neighboring AB-stacking site as shown in Figure 13(b)1 \rightarrow 2, although it takes straight slip as shown in Figure 13(c)7 \rightarrow 8. The minimum period of the force curve of 4.4 \AA (Figure 13(a)IV) reflects the lattice period of the graphite surface along the $[10\bar{1}0]$ direction, while 2.5 \AA for the armchair-type edge (Figure 10(a)VII) reflects that along the $[12\bar{3}0]$ direction. Thus the edge structure gives the marked effects on the atomic-scale dynamics depending on the lattice orientation of the surface.

During the line contact, the difference between the armchair- and zigzag-type edge is enhanced. Figure 14(a) reflects the zigzag stick-slip motion of the graphene sheet (Figures 14(b)1-9) unlike nearly the straight stick-slip motion (Figures 10(b)1-3). Important point of the line-contact sliding is that each carbon atom on the free edge takes stick-slip motion between the nearest neighboring six-membered rings. When each atom is located on the hollow site of the six-membered ring, the graphene sheet does not deform along the y direction (Figures 14(b)1, 4-5, and 8-9). However, when each atom is located a little far from

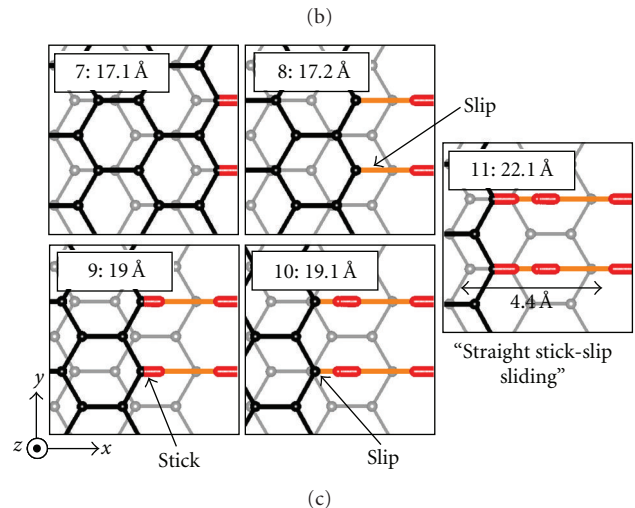
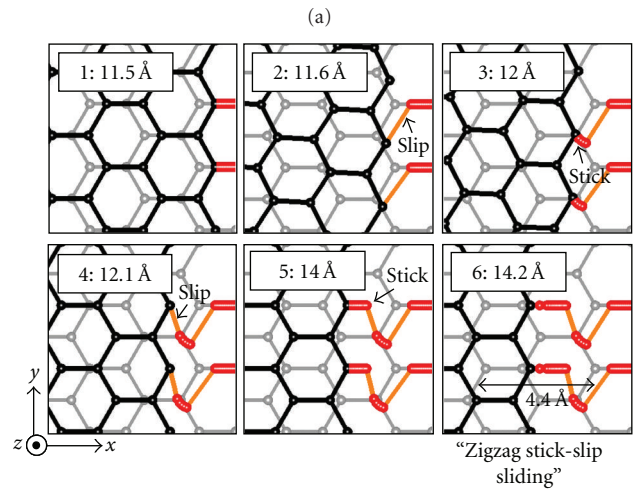
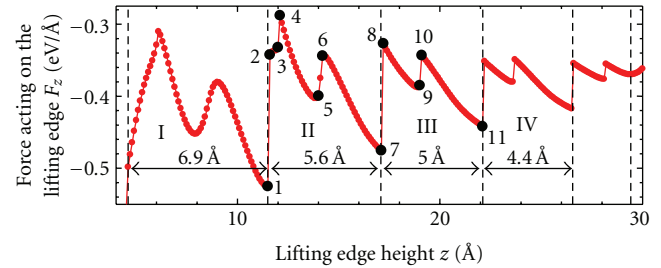
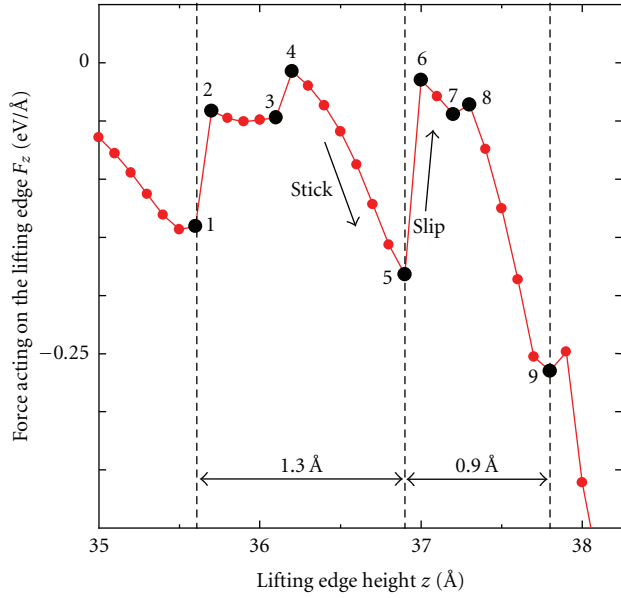
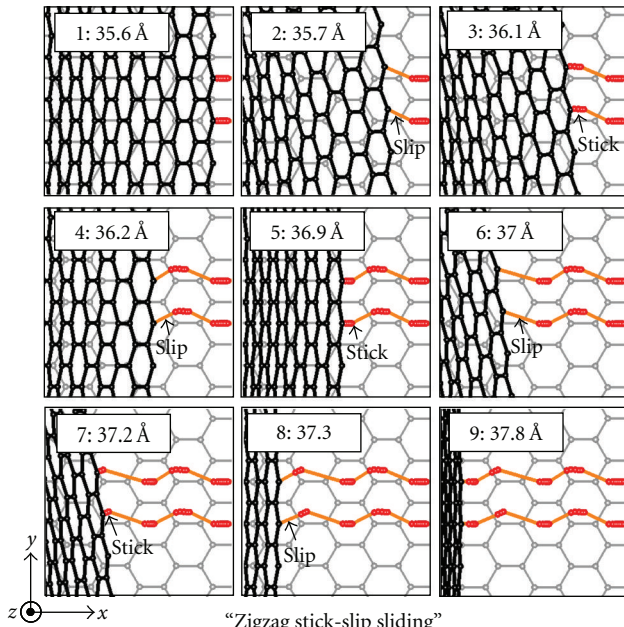


FIGURE 13: (a) Enlargement of part of the $z-F_z$ curve (Figure 12(b)) corresponding to the zigzag and straight stick-slip process during the surface contact. (b) The trajectories of the two carbon atoms on the free edge from 1 to 6 indicated in (a). (c) The trajectories of the two carbon atoms on the free edge from 7 to 11 indicated in (a).

the hollow site or near the carbon bond, the graphene sheet bends toward the y direction to decrease the total interaction energy (Figures 14(b)2-3 and 6-7). Thus, in the case of the zigzag-type edge, collective motion of the single carbon “atom” on the free edge nearly dominates the graphene mechanics together with its deformation. On the other hand, for the armchair-type edge, collective motion of the single carbon “bond” is dominant.



(a)



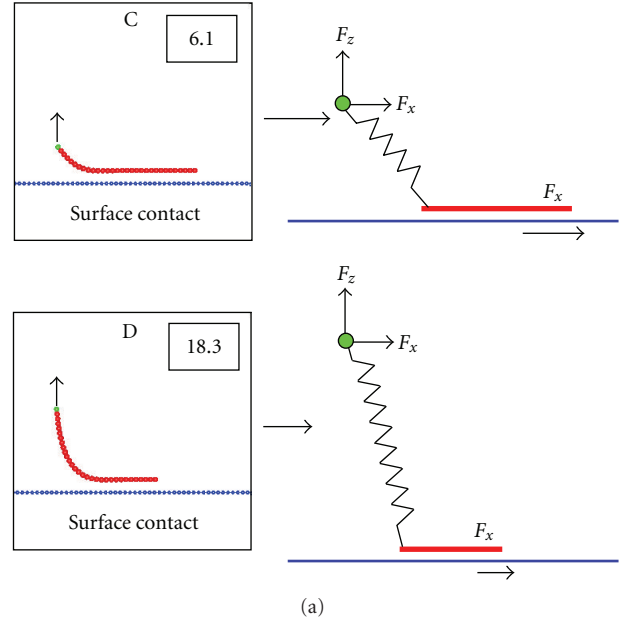
(b)

FIGURE 14: (a) Enlargement of part of the $z-F_z$ curve (Figure 12(b)) corresponding to the zigzag stick-slip process during the line contact. (b) The trajectories of the two carbon atoms on the free edge from 1 to 9 indicated in zig (a).

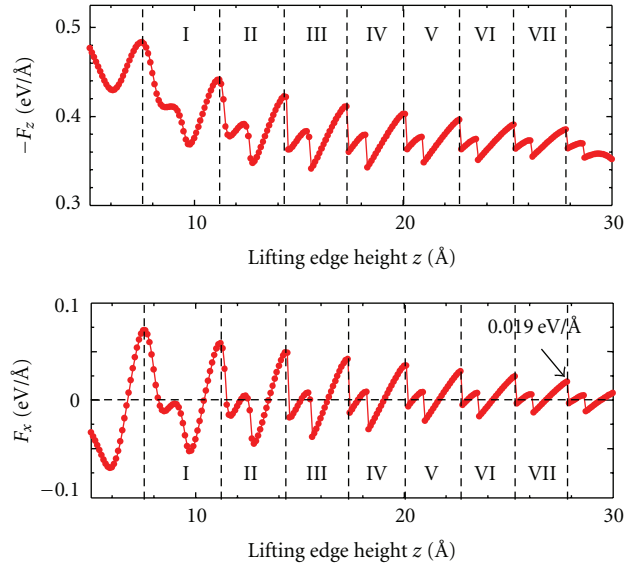
6. Discussions and Conclusions

In this work molecular mechanics study of the nanoscale peeling of the monolayer graphene sheet has been performed. The peeling force curve clearly exhibits the change of the graphene shape from the surface- to the line-contact.

In Section 3, the peeling of the monolayer graphene sheet with the armchair edge for lifting the center position is discussed. It is noted that the maximum lateral sliding force



(a)



(b)

FIGURE 15: (a) Schematic illustration of the increase of the peeled area and the decrease of the surface contact area from C ($z = 6.1 \text{ \AA}$) to D ($z = 18.3 \text{ \AA}$) for the graphene sheet with armchair-type free edge. (b) $-F_z$ and F_x plotted as a function of the edge height z , show qualitatively the same behavior to each other for the graphene sheet with armchair-type free edge.

$F_y \simeq 0.1 \text{ eV/\AA}$ is only about 3% of the absolute value of the maximum adhesion force $|F_z| \simeq 3.1 \text{ eV/\AA}$. This small sliding force F_y is derived from the superlubricity at the interface between the graphene sheet and the graphite surface [13] and atomic-scale wear [19]. There is a possibility that such anisotropy between the vertical force F_z and the lateral sliding force F_y can be applied to the adhesives, which can be strongly adhered to the substrate but can easily slide on it. Our AFM measurement exhibits that the maximum pull-off

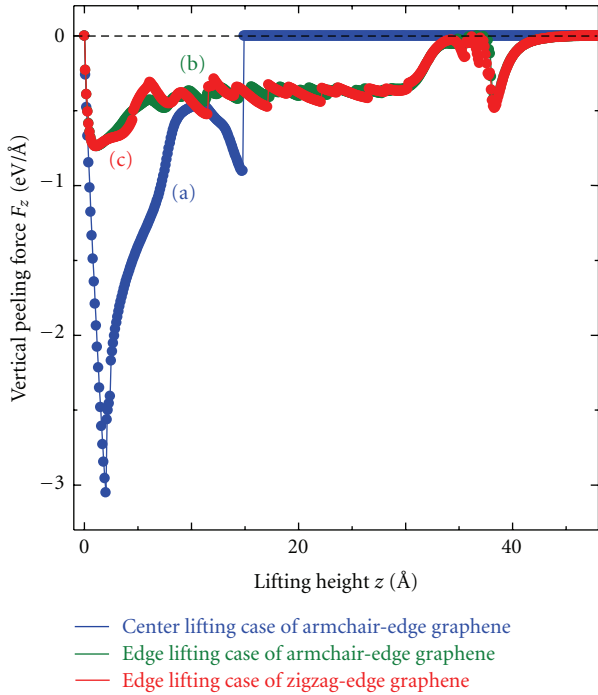


FIGURE 16: Comparison of the vertical forces, F_z , among (a) center-lifting case of the armchair-edge graphene sheet, (b) edge-lifting case of the armchair-edge graphene sheet, and (c) edge-lifting case of the zigzag-edge graphene sheet.

force is about several hundreds of nN, which is clearly much larger than the binding force, $3 \text{ eV}/\text{\AA} \simeq 4.8 \text{ nN}$, assumed in our simulation.

In Sections 4 and 5, the peeling of the monolayer graphene sheet with the armchair- and zigzag-edge for lifting the edge position is discussed, respectively. The atomic-scale sliding motion of the monolayer graphene sheet during the peeling process is found. For the graphene sheet with armchair edge, the transition from the continuous to the stick-slip motion of the graphene sheet is found, which can be explained as follows. The peeling process induces the increase of the peeled area of the graphene sheet and the decrease of the surface contact area. Considering that the peeled area of the graphene sheet acts as an effective spring as shown in Figure 15, the increase of the peeled area makes the effective spring softer, and the decrease of the surface contact area decreases the energy barrier to slide the graphene sheet. Finally the peeling process induces the transition from the continuous to the stick-slip sliding motion of the graphene sheet, together with the decrease of the period and amplitude of the $z - F_z$ curve. An important point is that the period of the peeling force curve for the armchair-edge graphene for the surface contact region corresponds to the lattice spacing of the graphite surface along $[12\bar{3}0]$ direction, 2.5 \AA . On the other hand, for the zigzag-edge graphene, the period becomes the lattice spacing along $[10\bar{1}0]$ direction, 4.4 \AA . This means the sliding length of the graphene sheet along x direction becomes nearly equal to the peeled length along z direction. The zigzag

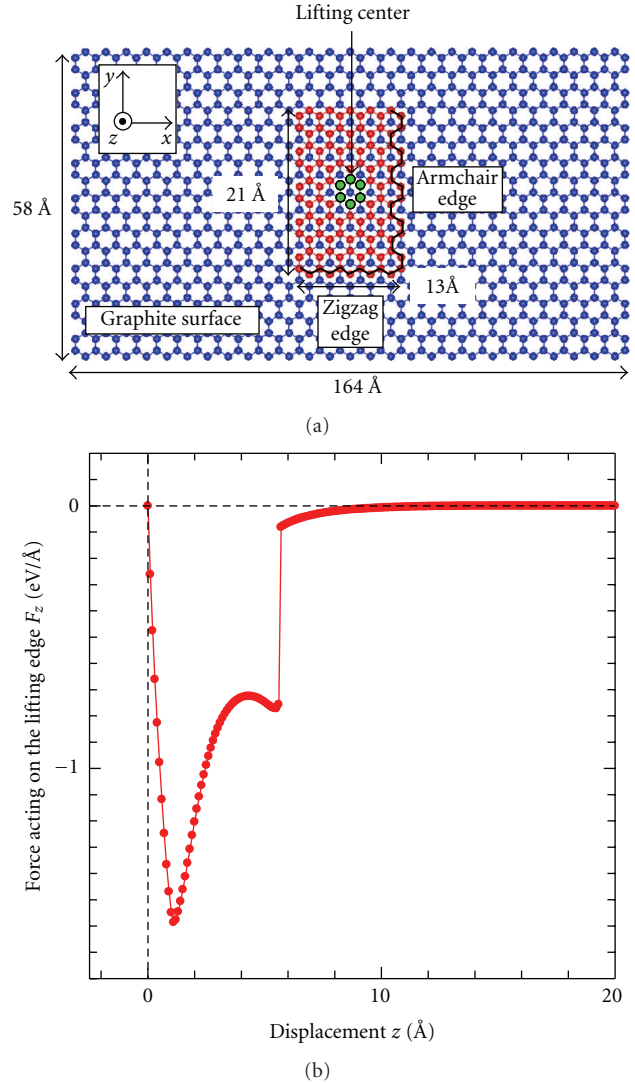


FIGURE 17: (a) The model of the red-colored monolayer graphene sheet physically adsorbed onto the blue-colored rigid graphite surface within the x - y plane. The green-colored six-membered ring at the center position is moved upward along the z (or $[0001]$) direction, by $z = 0.1 \text{ \AA}$. Initial AB stacking registry of the red-colored graphene sheet with the blue-colored graphite surface is assumed. (b) The vertical force, F_z , acting on the center six-membered ring, plotted as a function of the lifting displacement z .

structures of the peeling force curve with the same period of about several \AA have been also observed by our preliminary experiments using the multilayered graphene, which will be reported elsewhere [12]. Of course, if the number of the peeled graphene sheets is reduced, the direct comparison between the present simulation and the experiment will become possible.

As a result, the center-lifting case requires the largest attractive peeling force, $-3.1 \text{ eV}/\text{\AA}$, in order to peel the graphene sheet as shown in Figure 16(a). On the other hand, the edge-lifting case requires only $-0.74 \text{ eV}/\text{\AA}$, about 20% of that for the center-lifting case as shown in Figures 16(b) and

16(c). The edge structures give little influences on the basic features of the force curve. However, the sliding direction and the edge structure clearly give marked influences on the surface- and line-contact regions, respectively.

Another important point is that the behavior of the lateral force curve ($F_x(z)$) is qualitatively the same as that of the vertical force curve ($F_z(z)$) during the surface contact as shown in Figure 9(b). Therefore, it can be said that the peeling force curve, $F_x(z)$, directly reflects the atomic-scale friction force, $F_x(z)$, which decreases to $0.019 \text{ eV}/\text{\AA} \simeq 30 \text{ pN}$ for $z = 27.8 \text{ \AA}$ (Figure 9(b)). This ultralow friction force, F_x , is derived from the superlubricity at the interface between the graphene sheet and the graphite surface [19–21]. Furthermore, effect of the edge structure on the peeling process is clarified by comparison of the free edge between the armchair- and zigzag-types. As mentioned above, the atomic-scale structure of the force curve during the surface contact reflects the lattice spacing of the graphite surface. So the minimum period of the atomic-scale structure of the force curve can tell us the atomic-scale lattice orientation and structure of the free edge of graphene. Such information can be used for the control of the electronic properties of the graphene sheet adsorbed onto the substrate. Therefore, this paper indicates the possibility of the identification of the lattice orientation and the edge structure of the graphene sheet.

In this paper, we discussed the importance of the dynamics of the free edge during the peeling process. On the other hand, we also found the importance of the shape of the graphene sheet. Additional simulated model and results are shown in Figure 17. As shown in Figure 17(a), rectangular graphene sheet whose aspect ratio is different from that of the graphene sheet of Figure 1(b) is used. The basic shape of the vertical force curve, Figure 17(b), is similar to that of Figure 3. However, the armchair-type edge is peeled first for Figure 10(a), although the zigzag-type edge is peeled first for Figure 1(b) as discussed in Section III. This means that the shape of the graphene sheet plays an important role for deciding which edge is peeled first. Effect of the graphene shape on the peeling process will be discussed in detail somewhere in the near future.

Lastly it should be noted that the peeling process discussed in this paper is closely related to the atomic-scale wear of the graphite and the graphene tip formation in the friction force microscopy [22]. When the tip is pushed onto the surface for less than the critical tip height, the outermost graphene layer is attached to the FFM tip, which results in the formation of the graphene tip. In that case, the graphene sheet takes the surface contact with the second layer graphene, and it takes the two-dimensional stick-slip motion. However, it is difficult to observe directly the stick-slip motion during the scan process, due to the very small gap between the FFM tip and the graphite surface. On the other hand, if the peeling process is used, it can be expected that the contact at the AFM tip/graphite interface has a wider space to be observed directly by ex Transmission Electron Microscopy (TEM). This paper indicates the possibility of a direct observation of the stick-slip motion of the graphene sheet, that is to say, the elementary process of the atomic-scale

friction or superlubricity which occurs at the tip/graphite surface interface.

Acknowledgments

This research was supported by a Grant-in-Aid for Scientific Research (B) from the Japan Society for the Promotion of Science (no. 20360022). This work was also supported by the Ministry of Education, Culture, Sports, Science and Technology through a Grant-in-Aid for Building Strategic Research Infrastructures.

References

- [1] N. Sasaki, A. Toyoda, H. Saitoh, N. Itamura, M. Ohyama, and K. Miura, "Theoretical simulation of atomic-scale peeling of single-walled carbon nanotube from graphite surface," *e-Journal of Surface Science and Nanotechnology*, vol. 4, pp. 133–137, 2006.
- [2] N. Sasaki, A. Toyoda, N. Itamura, and K. Miura, "Simulation of nanoscale peeling and adhesion of single-walled carbon nanotube on graphite surface," *e-Journal of Surface Science and Nanotechnology*, vol. 6, pp. 72–78, 2008.
- [3] N. Sasaki, H. Saitoh, N. Itamura, and K. Miura, "Analysis of lateral orientation of single-walled carbon nanotube on graphite," *e-Journal of Surface Science and Nanotechnology*, vol. 7, pp. 48–52, 2009.
- [4] M. Ishikawa, R. Harada, N. Sasaki, and K. Miura, "Visualization of nanoscale peeling of carbon nanotube on graphite," *Applied Physics Letters*, vol. 93, no. 8, Article ID 083122, 2008.
- [5] M. Ishikawa, R. Harada, N. Sasaki, and K. Miura, "Adhesion and peeling forces of carbon nanotubes on a substrate," *Physical Review B*, vol. 80, no. 19, Article ID 193406, 2009.
- [6] K. Autumn, Y. A. Liang, S. T. Hsieh et al., "Adhesive force of a single gecko foot-hair," *Nature*, vol. 405, no. 6787, pp. 681–685, 2000.
- [7] K. Autumn, M. Sitti, Y. A. Liang et al., "Evidence for van der Waals adhesion in gecko setae," *Proceedings of the National Academy of Sciences of the United States of America*, vol. 99, no. 19, pp. 12252–12256, 2002.
- [8] L. Qu, L. Dai, M. Stone, Z. Xia, and Z. L. Wang, "Carbon nanotube arrays with strong shear binding-on and easy normal lifting-off," *Science*, vol. 322, no. 5899, pp. 238–242, 2008.
- [9] K. S. Novoselov, A. K. Geim, S. V. Morozov et al., "Electric field in atomically thin carbon films," *Science*, vol. 306, no. 5696, pp. 666–669, 2004.
- [10] K. S. Novoselov, A. K. Geim, S. V. Morozov et al., "Two-dimensional gas of massless Dirac fermions in graphene," *Nature*, vol. 438, no. 7065, pp. 197–200, 2005.
- [11] A. K. Geim and K. S. Novoselov, "The rise of graphene," *Nature Materials*, vol. 6, no. 3, pp. 183–191, 2007.
- [12] M. Ishikawa, N. Sasaki, and K. Miura, in preparation.
- [13] N. Sasaki, H. Okamoto, N. Itamura, and K. Miura, "Peeling of graphene sheet—simulation study," *e-Journal of Surface Science and Nanotechnology*, vol. 7, pp. 783–786, 2009.
- [14] N. Sasaki, H. Okamoto, N. Itamura, and K. Miura, "Atomic-scale friction of monolayer graphenes with armchair- and zigzag-type edges during peeling process," *e-Journal of Surface Science and Nanotechnology*, vol. 8, pp. 105–111, 2010.

- [15] J. Tersoff, "Empirical interatomic potential for carbon, with applications to amorphous carbon," *Physical Review Letters*, vol. 61, no. 25, pp. 2879–2882, 1988.
- [16] W. H. Press, S. A. Teukolsky, W. T. Vetterling, and B. P. Flannery, *Numerical Recipes: The Art of Scientific Computing*, Cambridge University Press, New York, NY, USA, 2nd edition, 1992.
- [17] J. P. Lu, X.-P. Li, and R. M. Martin, "Ground state and phase transitions in solid C_{60} ," *Physical Review Letters*, vol. 68, no. 10, pp. 1551–1554, 1992.
- [18] S. D. Stoddard and J. Ford, "Numerical experiments on the stochastic behavior of a lennard-jones gas system," *Physical Review A*, vol. 8, no. 3, pp. 1504–1512, 1973.
- [19] N. Sasaki, N. Itamura, and K. Miura, "Simulation of atomic-scale ultralow friction of graphite/ C_{60} /graphite interface along $[10\bar{1}0]$ direction," *Japanese Journal of Applied Physics Part 2*, vol. 46, no. 45–49, pp. L1237–L1239, 2007.
- [20] N. Itamura, K. Miura, and N. Sasaki, "Analysis of mechanism of low lateral stiffness of superlubric C_{60} bearing system," *Japanese Journal of Applied Physics*, vol. 48, no. 3, Article ID 030214, 2009.
- [21] N. Itamura, K. Miura, and N. Sasaki, "Simulation of scan-directional dependence of superlubricity of C_{60} molecular bearings and graphite," *Japanese Journal of Applied Physics*, vol. 48, no. 6, Article ID 060207, 2009.
- [22] N. Sasaki, H. Saitoh, K. Terada, N. Itamura, and K. Miura, "Simulation of atomic-scale wear of graphite—nanotip induced graphene formation," *e-Journal of Surface Science and Nanotechnology*, vol. 7, pp. 173–180, 2009.